Mechanical characterisation of

Micro-stereolithographic materials

By

Dun Xu

A thesis submitted in partial fulfilment of the requirements
for the degree of Doctor of Philosophy

School of Engineering

THE UNIVERSITY OF
WARWICK

Dec. 2011

Table of Contents

List of Figures

List of Tables

List of Acronyms

AFM	Atomic Force Microscope
ASTM	American Society for Testing and Materials
BS	British Standards
CAD	Computer-aid Design
CCD	Charge-coupled Device
CVD	Chemical vapour deposition
DAQ	Data Acquisition
DMD	Digital micro-mirror device
ERM	Enhanced Resolution Module
FEM	Finite Element Methods
GCD	Green Creep Distortion
IC	Integrated Circuit
IH	Integrated Harden
LCD	Liquid Crystal Display
LIGA	Lithographie, Galvanoformung and Abformung
MEMS	Micro-Electro-Mechanical System
MSL	Micro-Stereolithography
N.A	Neutral axis
PPF	Propylene fumarate
PT	Lead titanate
PZT	Lead zirconate titanate
PVD	Physical vapour deposition

SCS	Single-Crystal silicon
SEM	Scanning Electron Microscope
SL	Stereolithography
TPP	Two-Photon Polymerisation
TEM	Transmission Electron Microscope
UV	Ultra-violet

Acknowledgement

First of all, I would like to express my special thanks to my supervisor, Professor Derek Chetwynd, for his academic guidance, constant encouragement, constructive advice and extremely valuable support throughout the whole my study. I am also grateful to Dr James Covington for his advice and help in many parts especially in Micro-stereolithography fabrication. Special thanks are due to my colleagues in Precision Engineering and Surfaces Group for their fruitful discussions and valuable advices.

I would like to thank my parents for their financial and moral support which made possible of my PhD study. I would not complete this work without their support and encouragement.

I would also like to take the opportunity to thanks Dr Zhaoyang Yue, Dr Xiaokang Yin, Mr Chris Purssell, Dr Simon Leigh and Miss Marina Talib from the University of Warwick for their academic support and valuable discussions. Thanks also go to Dr Xuqin Li, Dr Bao Zhao, Miss Xisha Chen and Dr Weiming Yang, for their valuable advices and suggestions. I am also indebt for Mr David Robinson and Mr Martin Davis for their meticulous supports in the laboratory.

Declaration

This thesis is submitted in partial fulfilment for the degree of Doctor of Philosophy under the regulations set out by the Graduate School at the University of Warwick. The work described in this thesis was conducted by Dun Xu, except where stated otherwise, under the supervision of Prof. Derek G. Chetwynd and Dr. James A. Covington in the School of Engineering, University of Warwick between the dates of Jan 2008 and Dec 2011. No part of this work has been previously submitted to any institution for admission to a higher degree.

List of Publication:

Xu, D, Chetwynd, D.G. and Covington, J.A. (2011) “A method for tensile testing of delicate polymeric parts”, H Spaan *et al*. (eds) *Proc. 11th* ***euspen*** *Int. Conf.*, V1 175-178, Como, June 2011.

Abstract

Promising techniques such as micro-stereolithography (MSL) are opening up practical potential for exploiting new ideas for specialized polymer-based Micro-Electro-mechanical systems (MEMS) through small-batch production. As the field matures and grows, substantial research and commercial development demands better understanding of mechanical properties of MEMS materials to fully explore the potential of this technology. Bulk properties derived from conventional testing of large specimens (at 10 mm order) cannot be trusted. However, small-scale specimens (less than 1 mm) introduce major challenges, such as handling and mounting.

The aim of this study was to contribute towards an improved understanding of the mechanical properties of the polymers (MSL materials) with a strong emphasis on developing new metrology. It proposed and described a special form of test-rig and compatible special MSL specimen design. A uniaxial tensile approach was chosen, partly because it offered simpler uncertainty models. The prototype used deadweight loading through a notch flexure, which acted both as a spring in parallel sharing the same displacement with the specimen and as a linear guideway. The specimen was integrally fabricated with large clamping regions and support bars released by cutting. Stiffly constrained mounting and loading surfaces were used to clamp MSL specimens to the flexure, protecting them against parasitic motions during the test in combination. Strain was measured through an elongation measurement by high-sensitivity capacitive micrometry, knowing the specimen dimensions. Verification tests on the clamping conditions showed no significant evidence of sudden slip or creep.

MSL specimens were fabricated by a projection-based Envisiontec Perfactory system using a commercial acrylate-based R11 resin. Substantial shrinkage and curl distortion had been observed, which greatly reduced the fabrication accuracy of the MSL specimens. Specimens with different UV exposures and different sizes were fabricated and tested for better understanding of the MSL fabrication process. Typically, Young's Modulus was a little smaller than expected and certainly dependent on both size and process parameters (in the region studied).

Chapter 1: Introduction

1.1 The impact of MEMS technology

Micro-Electro-Mechanical Systems (MEMS) is the integration of mechanical elements, sensors, actuators and electronics on typical silicon substrates to produce small size devices (Goel 2008). It is an enabling technology that merges and augments the computational ability of micro-electronics with the sensing and actuation capabilities of micro-sensors and micro-actuators to sense and control the physical properties at a miniaturized level. Typical examples of current successful MEMS device are simple optical switches, pressure sensors and inertial sensor while microfluidics and photonics devices were identified as the major growth areas of MEMS devices (Gardner 2005). These MEMS devices usually exhibit high resolution, electronic accuracy and miniature size as MEMS fabrication techniques are growing more and more sophisticated and progressing all the time (Zhang 2005). They are also relative low cost due to batch fabrication methods. Modern MEMS technology allows more functionality to be placed in a given space at relatively low cost, and is expected to have enormous opportunities in various markets other than micro-electronics, such as biomedical, chemistry, fluidic applications.

MEMS technology brought entirely new concepts to the system design, materials selection, fabrication processes, generated functionality and production methodologies. It opened up great potential for incorporating different types of small scale devices such as motors, pumps, sensors and actuators. A highly functional device could be well fabricated within a compact space where conventional fabrication equipment might experience difficulties due to, e.g., insufficient precision. Moreover, these fabrication

techniques significantly improve the efficiencies of micro-manufacturing. Small devices of complex structures could be well prepared by the flourishing MEMS fabrication techniques. MEMS technology is also a technology embracing new conceptions and designs every day. New applications are continually brought forward by regular innovations and further challenge any strict definition of micro-electromechanical systems.

This chapter briefly describes the background knowledge of MEMS technology in terms of fabrication techniques, materials and applications. The current challenges and research interests in MEMS technology are also discussed, suggesting a growing need for mechanical characterisation of some MEMS technology. As one of the representative novel techniques, Micro-stereolithography (MSL) was chosen for its promising ability to fabricate 3D complex micro-structures.

1.2 MEMS fabrication techniques

MEMS fabrication techniques had mostly grown out of the infrastructure which was developed in the batch production of micro-electronics. The traditional MEMS technology shares the same fabrication techniques commonly used for standard Microelectronic technologies including wafer fabrication, monolithic processing and signal interconnect packaging. (Gardner 2005) Most of these techniques were based on the process of silicon as it was the most common semi-conductor materials and also the most important material for fabricating micro-transducers and the integrated circuit (IC). Besides, silicon also offers some excellent mechanical characteristics (Petersen 1982). A

great diversity of mechanical complex structures could be formed on top of silicon chips by silicon micromachining techniques comprising silicon bulk micromachining and surface micromachining. The former is widely utilized in the manufacturing of mechanical structures within bulk single-crystal silicon (SCS) wafer by selectively removing the wafer materials. Etching and wafer bonding are the key technical steps in bulk micromachining. The latter technique mainly deals with thin films located on the surface of a silicon substrate which is usually an order of magnitude smaller in thickness than the bulk micromachining structures. Surface micromachining possesses a great advantage in integrating with the IC components, as the silicon wafer could also be employed for fabricating microelectronics.

The standard microelectronic technologies as well as silicon micromachining had enabled the rapid growth of MEMS research based on silicon. However, the increasing miniaturization trend of products poses challenges to conventional silicon technologies: some can affect precision, but most crucially they concerns moving from planar to true 3D devices. Moreover, the emergent nature of MEMS technology have prevailed in a variety of industrial fields or triggered new markets nowadays where silicon materials are not capable to meet the particular demands. New fabrication techniques are continually investigated and developed and a great diversity of materials is employed. A general review about MEMS fabrication techniques at an important point in their history was given by Kovaks (1998) while a general review of newly developed MEMS techniques could be found by Gardner (2005). Several novel techniques, such as Micro-stereolithography (MSL) technology and the LIGA process, had been developed and

commonly employed for new generation of micro-fabrication to facilitate the increasing performance demand of MEMS products in the past decade.

MSL and LIGA processes are developed for high-precision fabrication for MEMS parts, especially for high aspect ratio micro parts. MSL technology builds the small parts by using UV sources to selectively solidify a polymeric resin in a layer-by-layer accumulation fashion (Figure 1.1). It permits the fabrication of true 3D complex structures, on micrometre to millimetre scales (Gardner 2005). Recently developed two-photon MSL systems (Lee *et.al* 2008) significantly enhance the accuracy of MSL fabrication and more materials are continually been investigated for novel applications. LIGA is a German acronym representing "Lithographie, Galvanoformung, and Abformung" which is based on deep X-ray techniques. In a typical LIGA process, the individual mechanical components are created by deposition of material into moulds which are micro-fabricated using deep X-ray lithography, followed by assembling the micromachine elements into a MEMS device (Figure 1.2). A general review about LIGA process and its application were given by Malek (2004). LIGA processes are compatible to a wider range of materials including metal, silicon, polymer, ceramic, and usually have higher precision than MSL processes (Prasad 2004). However, the expensive cost of LIGA processes and limited industrial accessibility to suitable synchrotron sources have restrained it from many industrial fields. Furthermore, complex 3D objects are often difficult to fabricate in LIGA process. Therefore, the MSL technique had attracted a great deal of research interest. It was commonly used for prototyping MEMS components, and was being seriously considered for manufacture of functional products.

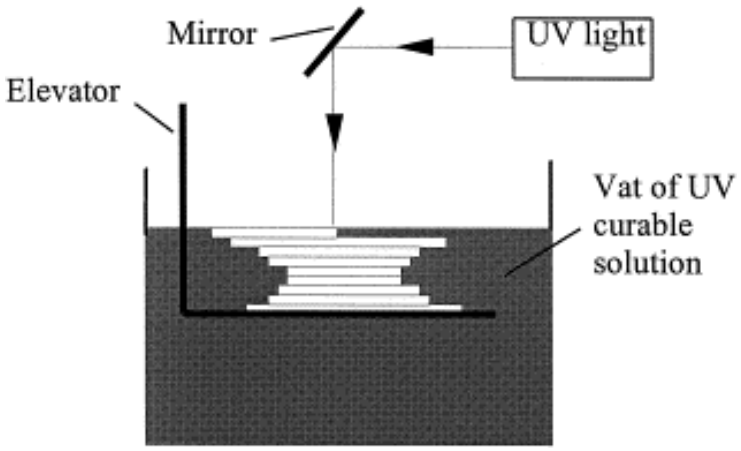

Figure 1.1: The schematic illustration of MSL fabrication, from Zhang (1999)

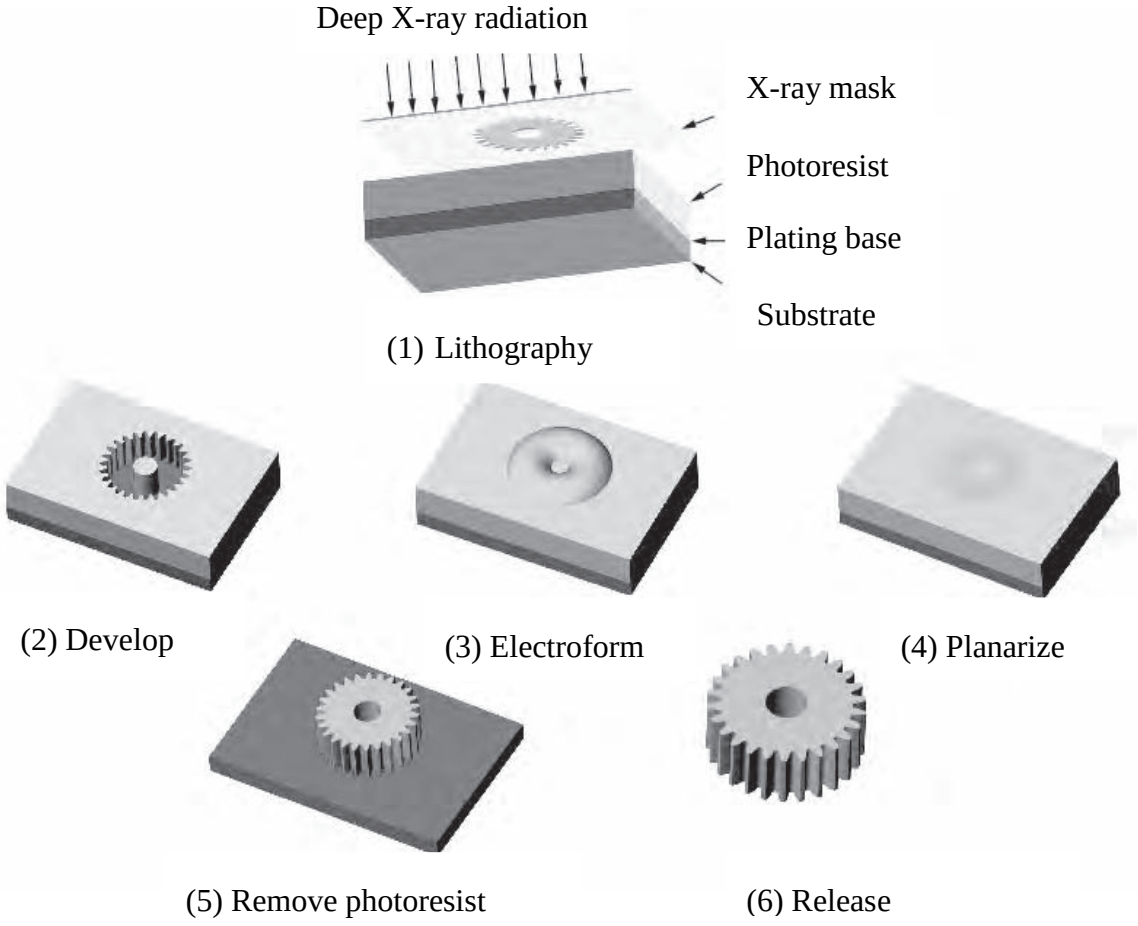

Figure 1.2: The schematic illustration of typical LIGA microfabrication steps (Prasad 2004)

1.3 MEMS materials

The early developing stages of MEMS technology mainly relied and flourished on silicon technology since it could take great advantage of the existing integrated circuit (IC) fabrication techniques designed for silicon processing. In the search for much greater range of mechanical, electrical and other properties, more and more materials had been introduced as MEMS applications moved to various industrial fields. Common materials involved in MEMS applications are silicon materials, polymers, ceramics, metals and composites. A general overview of these materials is provided in the following sections with description of their general roles in MEMS technology.

1.3.1 Silicon materials

Silicon is by far the most widely used and also the most tested material in MEMS technology. It is the essential material of IC technology as well as MEMS technology. It was first introduced into the microelectronic industry in the middle of 20th century and later become a principal material for integrated circuit (IC) technology due to its well understood and controllable electrical properties. A very influential and still highly relevant general overview about the mechanical properties of silicon along with its fabrication techniques was given by Petersen (1982).

For Microsystems purpose, silicon could be classified into three forms: single-crystal silicon (SCS), amorphous silicon and polysilicon. Grown as an almost perfect crystal, SCS behaves close to a theoretical ideal material and remains the most important and widely used form of silicon. Many of its mechanical properties are anisotropic and thus

determined by the orientation of the crystal axis. It is almost ideal elastic brittle (i.e., linearly elastic until sudden fracture), lighter than Aluminum and had a Young's modulus near to that of stainless steel (Table 1.1). A mature technique for growing single-crystal silicon at reasonably low cost had been made available during the evolution of standard micro-electronic technologies. The reliable and reproducible mechanical and electrical properties of SCS make it highly desirable for implementing Micro-Electro-Mechanical devices (Petersen 1982). Amorphous silicon is the opposite of single-crystal silicon. The non-crystal form of amorphous silicon may cause many defects, but it also offers some unique electrical properties useful for some specific applications. For instance, amorphous silicon has been extensively studied in large-scale electronics and solar cells (Rech 1999). Apart from these two forms, polysilicon (polycrystalline silicon) consists of many small crystals in random orientations. Its properties are therefore something of average across orientation, but some are dominated by grain boundary effects. Its ability of deposit semiconductor layers on a wide range of substrates has led to various successful applications such as polysilicon gate MOS, polysilicon emitters and a range of passive devices. Moreover, it is simple to control polysilicon deposition, making it extra attractive whereas its properties are adequate. A detailed description about polysilicon along with its application was given by French (2002).

Other materials in this family include epitaxial silicon, silicon nitride and silicon dioxide. These materials are commonly employed in MEMS fabrication as they can be conveniently grown by chemical vapour deposition (CVD) or physical vapour deposition (PVD). They are frequently formed as insulators for the standard microelectronic

technology. A detailed review of the deposition of these materials could be found by Beeby (2004).

Table 1.1: Properties of Silicon and Selected Other Materials (Beeby 2004)

Properties	SCS	Stainless steel	Al	Al_2O_3 (96%)	SiO_2	Quartz
Young's Modulus (GPa)	190	200	70	303	73	107
Poisson's Ratio	0.22	0.3	0.33	0.21	0.17	0.16
Density (g/cm^3)	2.3	8	2.7	3.8	2.3	2.6
Yield Strength (GPa)	7	3.0	0.17	9	8.4	9
Thermal coefficient of expansion (10^{-6}/K)	2.3	16	24	6	0.55	0.55
Thermal Conductivity at 300 K (W/cm·K)	1.48	0.2	2.37	0.25	0.014	0.015
Melting temperature (℃)	1414	1500	660	2000	1700	1600

One of the most significant roles of silicon in MEMS was forming semiconductors. It has been the most utilized elemental semiconductor in micro-electronics since the early 1970s, and several sophisticated approaches had been developed to change its electrical, mechanical and optical properties for various applications. Just as silicon had already spread widely over the microelectronic industry over the past decades, so too has it dominated in MEMS. The excellent mechanical properties and important electrical properties of silicon as well as its abundance have made it the primary material since

almost the beginning of IC technology and it remained so in MEMS technology. Besides, there is a larger number and variety of well-developed conventional silicon fabrication techniques available such as silicon-wafer manufacture, bulk silicon micro-machining and surface silicon micro-machining. A general review about silicon fabricating techniques was published by Lang (1999) with later development described by Gardner (2005). Although the emerging applications of MEMS has expanded to a vast field where sometimes they requires a unique material behaviour that silicon could not fully support, for example, biomedical applications, silicon is still usually considered as the routine material for most MEMS applications.

1.3.2 Polymers

Polymers are organic materials which consisted of long molecular chains or networks of small molecular units called *monomers*. The process of monomers chemically combining with each other to form polymers is called *polymerisation* (see Chapter 2 for detail). Most polymers are long chain structures or random networks, thus they are usually non-crystalline. But some of the polymers can grow as a single crystalline phase by chemical reaction which had important effects on mechanical, thermal and optical properties. These single-crystal polymers were widely used for electronics and optoelectronics (Chilton and Goosey 1995).

Besides silicon materials, polymers have been the most commonly employed materials in MEMS technology. One of the over-riding reasons is that polymers offer unique mechanical properties with great versatility to meet different system demands. The

distinctive properties of polymers are mainly due to their macromolecular nature. Since the early 1920s, large research efforts had been continuously devoted to investigating the structure and properties of polymers to explore their promising potential, see Meijer (2005). The common polymers applied in MEMS applications; including epoxies, acrylate, polyesters and other photo resins, possesses some desirable properties for various applications. They tend to have moderate strength (5 to 50 MPa), high ductility and relative low density. Many polymers display good electro-insulating ability and could be used as an insulator in MEMS.

Traditionally, polymers were frequently used as passive materials in MEMS applications, such as substrates, insulation layers, and packaging materials. This was mainly because these polymers are generally inexpensive and exhibit good mechanical properties. In the past decade, functional polymers had come to the fore in MEMS research as they not only met the demands of the rapid developing technology but also urge new designs and products for fast-growth industries. Typical successful examples were reported in designing and fabricating low cost organic electrical devices or 'plastic electronics' by either forming thin film transistors or phosphorescent light emitting diodes (Kelley 2004, and Zheng 2003). Functional polymers have been further explored to create smart sensors. An instance of these applications was the use of an electroactive polymer, such as polypyrrole, to build chemoresistive sensors for an electronic nose (Gardner 1999). Besides, more and more scientists believe that the polymeric materials could function as a key component in biochemical applications, such as drug delivery or vaccine delivery (Fréchet 2005). Other functional polymers show great potential in medical applications, such as for cornea regenerative medicine (Lai 2007).

1.3.3 Ceramics, Metals and Composites

Ceramics are quite commonly used in MEMS fields for special purposes and offer a range of properties significantly different to polymers. They are inorganic compounds which are often prepared by heating and cooling mixed metallic and non-metallic materials subsequently. The most common ceramics are Alumina, Zirconia, Non-metallic nitrides, metallic silicides and ceramics superconductors. However, their processing is usually not compatible with traditional MEMS fabrication.

Due to their diverse nature, the physical properties of ceramics vary to a great extent. Most ceramics showes high compressive strength but rather low tensile strength, high hardness though usually mechanical brittleness, high elastic modulus and modest density. More significantly, they have excellent resistance to high temperature and wear, which are high desirable for energy-intensive MEMS systems, such as micro-engine (Epstein *et al.* 1997) or micro-turbines (Mcdonald 2008) applications. One well-known role of ceramics in MEMS is the use of piezo-ceramics as transducers. Piezo-ceramics, such as lead zirconate titanate (PZT), lead titanate (PT) and lead metaniobate ($PbNb_2O_6$), produce a voltage in response to an applied uniaxial force, and *vice versa*. Thin films of many piezoelectric materials can be deposited, making them attractive as both sensors and actuators in MEMS. Hence, these materials are frequently found in microphones and speakers, micro-sensors and precision actuators, *etc*. They are usually poor electrical conductors, and could be generally treated as an electrical insulator. Nevertheless, some ceramics can become more conductive when experiencing high temperature.

Besides silicon, polymer and ceramics, there are some other MEMS materials widely used, such as metal and composite. Metals are strong and ductile material at room

temperature and could be used as structural materials in MEMS for robust and stable mechanical behaviour. Thin metal films sometimes are also formed by metallisation process for interconnection, ohmic contacts, and so on (Gardner 2005). Metals may dominate much macroscopic manufacture, but they take a comparatively minor role in MEMS, mainly because of issues with fabrication. A composite material is a physical combination of two or more different types of materials. It is often sophisticatedly engineered by mixing selected matrix materials, e.g. reinforcing materials. In typical composite materials intended for high strength/density ratio, the matrix material surrounds and supports reinforcing materials by bonding them together while the reinforcing materials imparted their special mechanical and physical properties to obtain desired material characteristics. Composites are also commonly employed as passive materials in MEMS products in place of metal because it is equally strong strength but much lighter. Composite materials are not only used to gain strength. There is rapidly growing interest in ‘functionalized’ composite where small or nano-particles are introduced to create specific magnetic, optical, thermal or other properties.

1.4 MEMS applications

The driving forces for miniaturization of electro-mechanical systems include cost, size, weight and precision. These MEMS products are inherently smaller, lighter, cheaper and faster than their bulk conventional counterparts, leading to enormous opportunities in various industrial fields. In general, MEMS technology has the potential to revolutionize the fabrication in many industrial fields. Since it has brought more and more advanced fabrication techniques, sophisticated functional devices can be fabricated within a smaller

space than was possible before. Its capability of fabricating micro-structures, micro-sensors or micro-actuators has been investigated by many researchers. Recently, new applications in automotive, industrial and biomedical research have drawn various interests.

MEMS technology had evolved from standard electronic technologies and it was natural to use it in designing and manufacturing micro-system components such as micro-sensors and micro-actuators to make them more efficient and less expensive. An early successful example of MEMS micro-sensor was the pressure sensor based on a thinned silicon diaphragm (Kung and Lee 1992). More successful MEMS sensors or actuators such as mechanical sensor, inject printhead, fluidic controls, data storage device, and communication device followed to convince the industry that the new generation of MEMS micro-sensors and micro-actuators are better and more reliable than the existing counterparts made using fine mechanics. This advanced MEMS technology has led to a further reduction in size but a higher functionality.

As one of the most lucrative industrial businesses, the automotive field was frequently involved with MEMS technology (Figure 1.3). This technology could produce smaller size devices with the required reliability and was well suited to fabricate a class of micro-machined sensors and actuators in the automotive system (Eddy 1998). Moreover, the involvement of MEMS techniques altered the design, materials, fabrication processes, generated functionality and production methodologies of existing automotive industry, and can significantly reduce the cost of commercial parts. For instance, the mechanical accelerometer used to trigger the safety airbag which cost about $18 originally, was replaced by the new generation electromechanical on-chip micro-accelerometer which

cost less than $3 (Gardner 2005). Other successful MEMS applications had been reported on fuel injector pressure sensor, brake pressure sensor and GPS navigation systems, *etc*. A general review and discussion about MEMS application in automotive field was given by Ueno (2007).

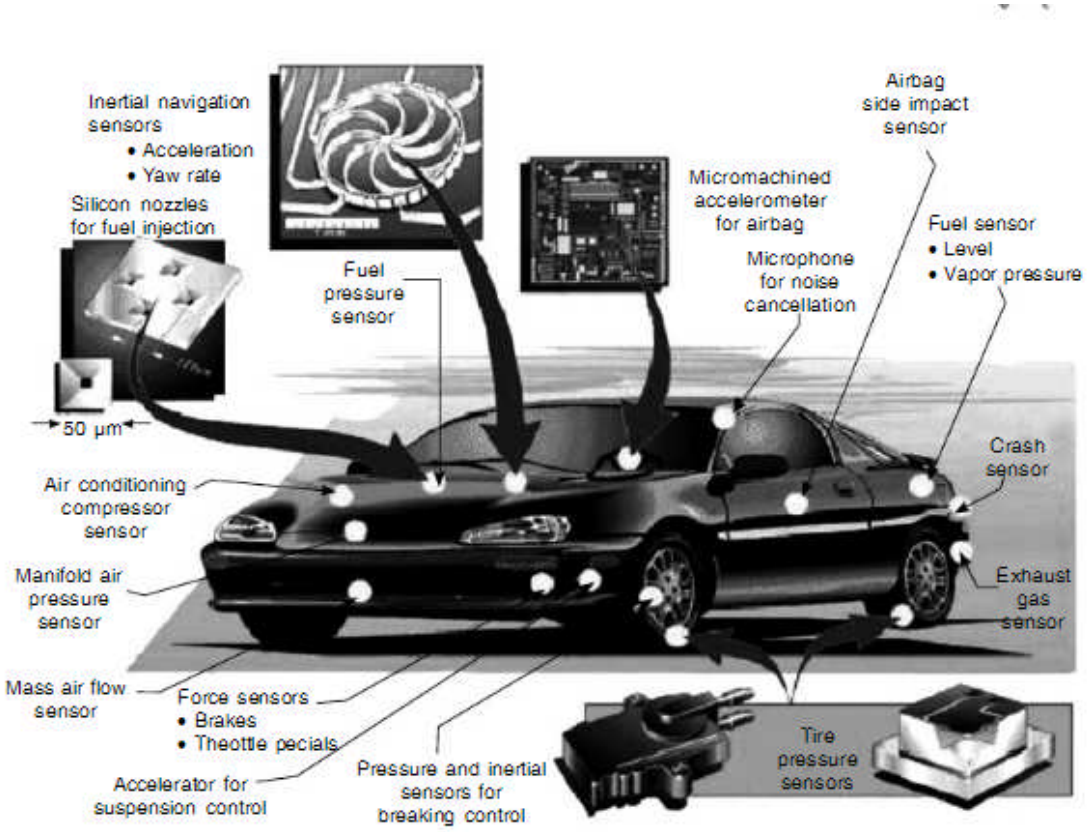

Figure 1.3: MEMS products in automotive fields (Michalicek 2000)

Biomedical applications are one of the most promising new areas in MEMS technology. Recently, a great deal of interest has been drawn to using MEMS devices as human implants (Kotzar *et.al* 2002). Their micro-size iss naturally suitable for small implants inside human, having high-sensitivity sensing and high-precision controlling. Other

biomedical applications such as drug delivery monitoring, spine research and internal nano-robot control had also been reported (Tsai 2007, Nisar 2008 and Glos 2010).

MEMS technology forms a basis for large radical or discontinuous innovations. Its applications are manifested in a variety of industrial markets indicating great potential of market entry for products but accompanied by high risk of failure. Most MEMS products are only now starting to be pushed to the commercial markets and the insufficiency of successful marketing for MEMS technology was evident. The main driving force for MEMS development is still technology rather than market-oriented. It is crucial to investigate and understand the essential information about MEMS technology and to commercialize the products in order to maximize the benefits of this advanced technology. A rapid growth of effort has been devoted into the commercialization of current MEMS technology in parallel with the development of novel fabrication techniques.

1.5 Current challenges and interests of MEMS research

MEMS technology is a disruptive technology, or in another term, involved discontinuous innovation which introduced novel techniques that require upheaval in the existing manufacturing practices. The true revolutionary rather than evolutional MEMS technology had brought significant amounts of innovation to manufacturing processes and design methodologies but still faced various problems, such as insufficient understanding on fabrication processes and material properties. In this section, an overview of current challenges and interests in MEMS research is briefly given. The

focus is on the aspects of mechanical characterisation of materials, methodologies design and commercialization of MEMS technology.

The first entrance of the disruptive MEMS technology was replacing existing products. In the early stages, the emphasis of MEMS research had been on novel micro-system concepts and the fabrication process for them. Study of the fundamental issues (such as the mechanical properties of materials) is usually not synchronous, resulting in an insufficiency of data for safe, cost-effective moving from concepts to products. It has become one of the major obstacles of MEMS production. Besides, MEMS technology brought in brand new processes and methods as well as new materials, leading to great potential for the creation of new production but with a high failure risk commonly related to the mechanical behaviour of the structures. Thus, it is essential to build high-performance tests to obtain the reliable engineering data of new materials for understanding, testing and modelling the mechanical behaviour of MEMS devices. However, it is usually difficult to precisely characterize the mechanical properties of MEMS materials at small scales. It is crucial to obtain data from tests at representative scale because much behaviour cannot be directly inferred from large scale bulk tests: dimensional scaling may be inaccurate for reason of basic physics, quantization within production processes or when there are phenomena such as the well-known volume to surface relationships. For example, a subtle form of the latter can manifest in an increasing dominance of surface properties that are not typical of bulk ones.

Another impediment to MEMS take-up nowadays is the lack of maturity of design methodologies and tools. Various new ideas as well as novel design are emerging daily but there is hardly a systematic review of MEMS design and fabrication processes. Most

of the research had investigated individual designs on particular fabrication processes and it exhibited a great diversity in results. Some excellent results had been reported but still suffer questions of reliability as they were heavily dependent on the experience and knowledge-level of designers. It was very difficult for researchers to use these results for understanding, designing and assessing new MEMS systems when different methodologies and fabrication tools were selected. Scientists have recently devoted increasing efforts towards establishing standard procedures to assess MEMS design and fabrication process (Zhang 2005). Vast amount of work such as frame design, principle analysis and data interpretation could be simplified or even eliminated during the design.

To date, considerable MEMS products have been brought to the market successfully. However, the present MEMS market is staid contrasts with the enormous potential. Again, this is mostly related to the disruptive nature of MEMS technology which brings new concepts of design and manufacture and so requires new investment in infrastructure entirely different from the previous manufacture practices (Da Silva 2002). Moreover, the insufficient basic understanding of MEMS behaviour leads to high-marketing risks. Considerable effort had been devoted to encouraging the commercialization of MEMS technology by establishing collaborative design methodologies and frameworks (Zhang 2005 and Walsh 2002).

In summary, disruptive MEMS technology created a new revolution for precision manufacturing and opened up many potential applications for industry. Several impediments including insufficient knowledge of materials properties, lack of standard processes / flows, low maturity of design methodologies and tools and relatively slow progress in commercialization constituted the major challenges in MEMS development.

Thus, this work aimed to contribute to better understanding of MEMS fabrication processes by performing mechanical characterisations on specimens fabricated by novel representative MSL processes. A prototype test-rig had been built because conventional measurement systems have difficulties in dealing with small and fragile specimens.

1.6 Aims and Objects

There were significant signs that MSL would soon allow manufacture of micro-mechanical devices of considerable complexity by directly addressed photo-curing of polymeric resins. Such systems open up practical potential for exploiting new ideas for specialized polymer-based MEMS devices through small-batch production. The main hurdles to realizing this hope are poor current knowledge of the mechanical properties of the materials and considerable uncertainties in the practical mechanical characterisation methods. The conventional measuring systems experienced difficulties in dealing with small specimens and bulk properties derived from testing large specimens (10 mm level) cannot be trusted. Thus the aim of this study is to contribute towards improved understanding of the MSL fabrication process and the mechanical properties of its materials with a strong emphasis on developing new metrology technique for mechanical characterisation at small scales (less than 1 mm).

In order to achieve the aim, the following research objectives have been identified:

1) To review and gain the general understanding of MSL technology and its characteristics and difficulties.

2) To investigate various methods and identify practical challenges in order to search a reliable methodology for mechanical characterisation of MSL specimens.
3) To inspect and the general behaves of small specimens fabricated by MSL machine and to identify the difficulties and challenges in fabricating these specimens.
4) To build a novel test-rig along with compatible specimen design to performance mechanical tests of MSL specimens.
5) To use the test results to provide a better understanding of the MSL processes and materials properties.

Thus this research addressed three areas currently constraining commercial viability of MEMS techniques: better understanding of the mechanical properties of the MSL materials (polymers) at small scales; better knowledge of MSL fabrication processes and the development of new metrology techniques to gain this data.

1.7 Outline of thesis

This study begins by reviewing the state of the art in Micro-stereolithography (MSL) technology, a novel fabrication technique of MEMS parts. The principles of MSL system are introduced in Chapter 2, followed by discussion of different development in the MSL materials and apparatus. The current interests and limitations of MSL technology are also described, indicating a need for better understanding of the mechanical properties to fully explore its potential. A comparison of approaches to mechanical (elastic) characterisation methods is given in Chapter 3. The emphasis is on the challenges of building accurate

mechanical characterisation for small MEMS parts. Several testing methods are examined, suggesting possible solutions for building an accurate mechanical characterisation testing on small MEMS materials.

Chapter 4 deals with the fabrication process of MSL specimens. It describes the basic fabrication process using a customized Envisiontec Perfactory MSL system with a commercial acrylate-based resin. The two major hurdles in fabricating small MSL specimens, shrinkage and curl distortion, are studied and briefly discussed.

Chapter 5 presents the design and implementation of a special form of tensile test-rig and compatible specially designed specimens for small scale measurement. Brief discussion of the rationale for choosing these concepts and an outline of the actual design is followed by preliminary results illustrating the practicality of the method. The calibration and the validation of test methods with verification of the preliminary data against results using a commercial Deben tensile device are also included. The results of geometry measurement and tensile testing on the resulting specimens under different fabrication conditions are given and briefly discussed in Chapter 6.

Chapter 7 thereafter discusses the test results of MSL specimens in a broader context. An analysis of the performance of the tensile test-rig is also included with discussions on critical parts of the design. Chapter 8 concludes this PhD study with a summary of its highlights and recommendations for future work.

References

Beeby, S., Ensell, G., Kraft, M. and White, N. (2004). *MEMS Mechanical Sensors*, Chapter 2, 7-38, Artech House, London. ISBN: 1580535364.

Chilton, J.A. and Goosey, M.T., eds. (1995). *Special polymers for Electronics and optoelectronics*, Chapter 3, 65-87, Chapman and Hall, London. ISBN: 041258400X.

Da Silva, M.G., Giasolli, R., Cunningham, S. and Deroo, D. (2002). "MEMS design for Manufacturability," *Sensors Exp and Conference 2002*.

Eddy, D.S. and Sparks, D.R. (1998). "Application of MEMS Technology in Automotive Sensors and Actuators," *Proceedings of the IEEE*, **86**(8), 1747-1755.

Epstein, S.D., Senturia, S.D., Al-Midani, G., *et.al*. (1997). "Micro-heat engines, gas turbines and rocket engines- The MIT microengine project," Transducers ’97, The 9th International Conference on Solid-State Sensors and Actuators, Chicago, IL.

French, P. J. (2002). "Polysilicon: a versatile material for microsystems." *Sensors and Actuators A: Physical*, **99**(1-2), 3-12.

Fréchet, J. M. J. (2005). "Functional polymers: from plastic electronics to polymer-assisted therapeutics," Progress in Polymer Science **30**(8-9): 844-857.

Gardner, J. W. and Bartlett, P. N. (1999). *Electronic Noses: Principles and Applications*, Oxford University Press, Oxford, p. 245. ISBN: 0198559550.

Gardner, J.W., Varadan, V.K, and Awadelkarim, O.O. (2005). *Microsensors MEMS and smart Devices*, JOHN WILEY & SONS, Chichester. ISBN: 047186109X.

Glos, D.L., Sauser, F.E., Papautsky, I. and Bylski-Austrow, D.I. (2010). "Implantable MEMS compressive stress sensors: Design, fabrication and calibration with application to the disc annulus," *Journal of Biomechanics*, **43**, 2244-2248.

Goel, V. K. and Ferrara, L. (2008). "Basic Science Symposium II: MEMS Technology." *SAS Journal*, **2**(2), 120-129.

Jacobs, P.F. (1996). *Stereolithography and other RP&M Technologies*, Society of Manufacturing Engineering, Dearborn, MI. ISBN: 0872634671.

Kelly, T.W., Braude, P.F., Gerlach, C., Ender, D.E., Muyres, D., Haase, M.A., Vogel, D.E. and Theiss, S.D. (2004). "Recent progress in Organic Electronics: Materials, Devices and Processes," *Chem. Mater.*, **16**, 4413-4422.

Kotzar, G., Freas, M., Abel, P., Fleischman, A. *et.al* (2002). "Evaluation of MEMS materials of construction for implantable medical devices," *Biomaterials*, **23**, 2737-2750.

Kovaks, G., (1998) *Micromachnined Tranducers Sourcebook*, New York: WCB/Mc Graw-Hill. ISBN: 0072907223.

Kung, J. T. and Lee, H-S. (1992). "An integrated Gir-gap-capacitor pressure sensor and digital read-out with sub-100 attofarad resolution," *Microelectromech. Syst.*, **1**, 121–129.

Lang, W. (1996). "Silicon microstructuring technology," *Materials Science and Engineering: R: Reports*, **17**(1), 1-55.

Lai, J.-Y. and Hsiue, G.-H. (2007). "Functional biomedical polymers for corneal regenerative medicine," *Reactive and Functional Polymers*, **67**(11), 1284-1291.

Lee, K. S., Kim, R.H., Yang, D.Y. and Park, S.H. (2008). "Advances in 3D nano/microfabrication using two-photon initiated polymerisation," *Progress in Polymer Science*, **33**(6): 631-681.

Malek, C.K. and Saile, V. (2004). "Applications of LIGA technology to precision manufacturingof high-aspect-ratio micro-components and -systems: a review," *Microelectronics Journal*, **35**, 131-143.

McDonald, C.F. and Rodgers, C. (2008). "Small recuperated ceramic microturbine demonstrator concept," *Applied Thermal Engineering*, **28** (1), 60-74.

Meijer, H.E.H. and Govaert, L.E. (2005). "Mechanical performance of polymer systems: The relation between structure and properties," *Progress in Polymer Science*, **30**(8-9), 915-938.

Michalicek, M.A. (2000). *Introduction to Microelectromechanical Systems*, Air Force Research Laboratory, New Mexico. ISBN: 0890065810.

Nisar, A., Afzulpurkar, N., Mahaisavariya, B. and Tuantranont, A. (2008), "MEMS-based micropumps in drug delivery and previous termbiomedicalnext term applications," *Sensors and Actuators B: chemical*, **130**, 917-942.

Petersen, K. (1982). "Silicon as a mechanical material," *Proc. IEEE*, **70**(5), 420–457.

Prasad, S. V., M. T. Dugger, et al. (2004). "LIGA Microsystems: Surface Interactions, Tribology, and Coatings." *Journal of Manufacturing Processes*, **6**(1), 107-116.

Rech, B. and Wagner, H. (1999). "Potential of amorphous silicon for solar cells," *Applied Physics A: Materials Science & Processing*, **69**(2), 155-167.

Tsai, N.-C. and Sue, C.-Y. (2007). "Review of MEMS-based drug delivery and dosing systems," *Sensors and Actuators A*, **134**, 555-564.

Ueno, Y. and Kawahara, N. (2007). "Microsystem Technologies for Automotive applications," *Towards synthesis of Micro-/Nano-systems*, Part 1, Springer London, 21-27.

Walsh, S., Linton, J., Grace, R., Marshall, S. and Knutti, J., (2000) MEMS, microsystems, micromachines: commercializing an emergent disruptive technology. In: Rai-Choudry, P., Editor,. *MEMS and MOEMS Technology and Applications*, SPIE–The International Society for Optical Engineering Development, Billingham, WA, 479–514.

Zhang, X.F, (2005). Manufacturing advisory service system for concurrent and collaborative design of MEMS devices. In *MEMS/NEMS Handbook Techniques and Applications*. Springer, USA. Chapter 1, 1-34.

Zhang, X., Jiang, X.N., et al. (1999). "Micro-Stereolithography of polymeric and ceramic microstructures," *Sensors and Actuators A: Physical*, **77**(2), 149-156.

Zheng, S. and Shi, J. (2003). "Novel polymers for light emitting diodes", *Handbook of Luminescence, Display Materials, and Devices,* **vol. 1** ,in: Nalwa, H.S., Rohwer, L.S. Editors, American Scientific Publishers, Stevenson Ranch, CA, 197–260.

Chapter 2: Micro-stereolithography Technology

2.1 Introduction to SL system and MSL system

Stereo-lithography (SL) was first introduced as a rapid prototyping technology a few decades ago (Kodama 1981). The key concept of SL is to create three-dimensional free-form prototypes directly from designed engineering models. This attractive feature made SL system ideal for prototyping new products before batching production in the conventional manner. Hence the SL technology was widely used in both automotive and aerospace industries for prototyping the production of new concepts at low cost. A new view on characteristic features and applications of SL system could be found by Melchels (2010).

The typical SL fabrication begins with a computer-aid design (CAD) model in computer. The build data is converted to *stl* files which describes the surface geometry of design objects in triangular representations. These data are then passed to the computer and transferred to a three-dimensional virtually sliced SL model layer by layer where each layer contains the desired geometrical patterns. A block diagram of typical SL system is shown in Figure 2.1. A UV laser beam is directed and focused down onto the surface of a photopolymeric resin by galvanometric x-y scanner to initialize the photopolymerisation in a selected pattern. After completing curing the first layer, the three-dimensional solid microstructure is built bottom-up in layer by layer fashion with the aid of computer-driven supporting platform. The part taken directly from the SL building and of relatively low cohesion after draining and washing-off the excess resin is only partially cured and usually require either UV or thermal post-cure procedure to ensure useful rigidity and ruggedness.

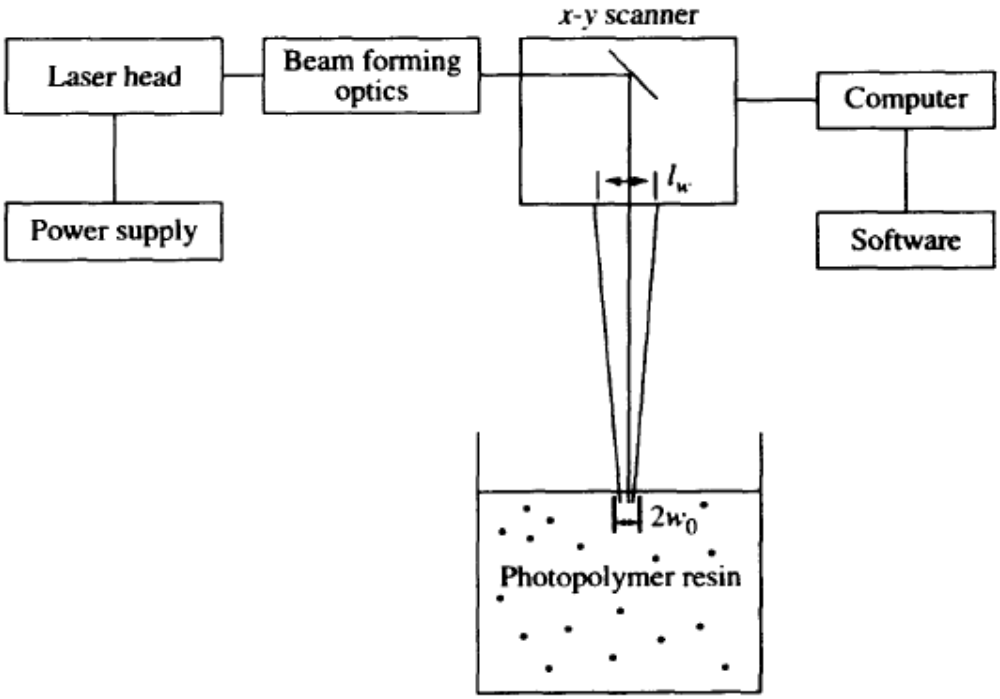

Figure 2.1: A block diagram of an SL system, from Jacobs (1992)

The term micro-stereolithography (MSL) generally referred to an SL system employed to manufacture micro-parts. MSL usually has great advantages over other rapid fabrication technology regarding to accuracy, thus it was first developed and introduced as an additive process to the bulk and surface-micromachining technology to make small parts for MEMS (Gardner 2005, Ikuta and Hirowatari 1993). Small complex 3D objects could be fabricated directly from digital designs with no milling or moulding (Figure 2.2). Another great advantage of this technology is simply process operation. Most of the processes are conveniently operated in the PC. This technique allows for the fabrication of custom small complex components in a matter of hours rather than days or months.

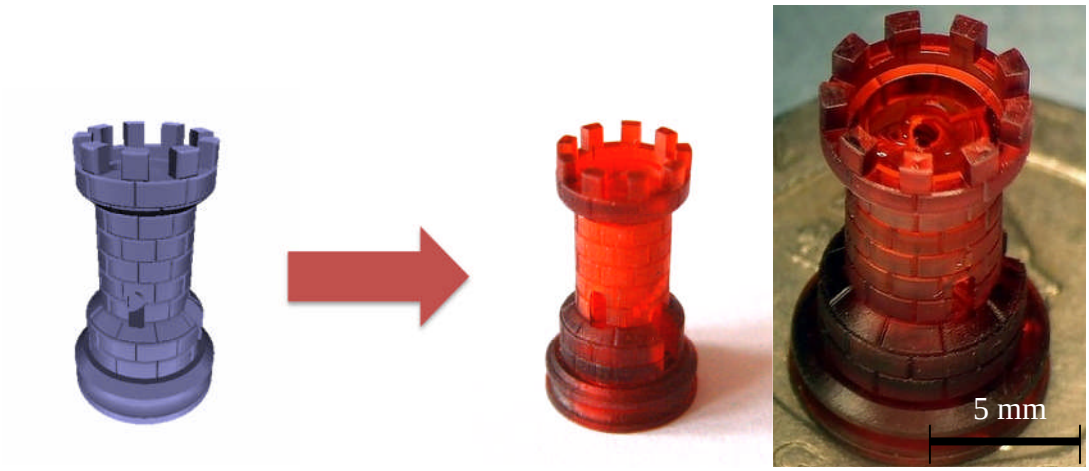

Figure 2.2: An example of MSL fabrication on a 20 penny scale by Warwick Microsensors and Bioelectronics Laboratory (2007)

However, MSL technology was still subjected to several technical limitations, such as it being time-consuming to fabricate a complex three-dimension part, low reliability of the resulting micro-structures, and a limited range of commercially available resins. Lately, TNO group developed an improved micro-stereolithography system, which was 6 to 10 times faster than conventional MSL systems (TNO 2007). This system was capable of fabricating high precision products of 0.005 mm planar resolution, making it possible to accurately manufacture complex MEMS components. Current research interest has been heavily devoted to introducing more MSL resins for high-efficiency polymerisation and new setup approaches for increasing both precision and reliability.

2.2 The MSL materials

The key process of MSL is the photopolymerisation. This is a process that joins a number of small molecules together to form large molecules when exposed to incident light (usually UV radiation). Three major types of photopolymer systems, either based on free-radical photopolymerisation or cationic photopolymerisation, are acrylate, epoxy, and vinyl ether (Figure 2.3 Jacobs 1996).

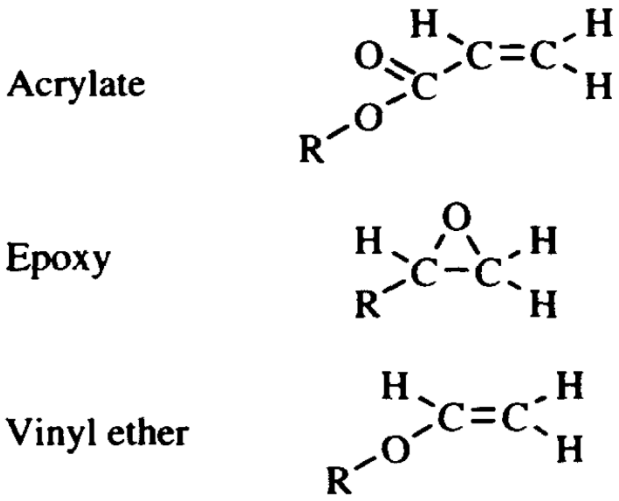

Figure 2.3: The three main types of photopolymer, from Jacobs (1996)

During photopolymerisation, the C=C double bond (acrylate and vinyl ether) or the ring (epoxy) breaks when absorbing the incident UV laser radiation and so enables monomers or pre-polymers in the resin to link up to form long-chain structure or cross-linked network. The photopolymerisation usually involves three steps: chain initiation, chain

propagation and chain termination. A free-radical photopolymerisation, for example (Figure 2.4), begins with an additional photoinitiator in the resin being excited by the radiation of UV laser. The excited photoinitiator generates a free-radical and breaks the C=C double bond to enable the chain initiation. The subsequent rapid chain propagation forms cross-linked polymers; photopolymerisation is complete when the propagation is terminated. Cationic photopolymerisation is similar to free-radical photopolymerisation except that the polymer chain growth is enabled by a cationic initiator transferring bonds and charge to a monomeric unit.

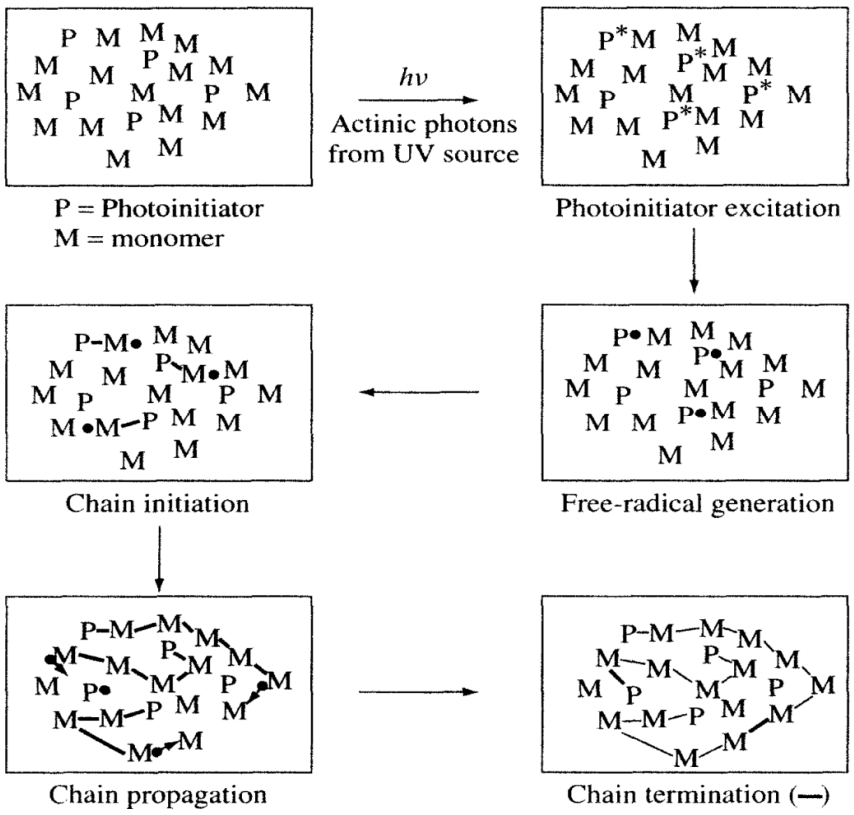

Figure 2.4: An example of simplified free-radical polymerisation process, from Jacobs (1996)

According to the type of chemical reaction responsible for enabling chemical linked to hold the monomers together, the photopolymer system for MSL could be categorized into acrylate, epoxy and vinylether. The acrylate-base system is polymerised via a free-radical mechanism. It usually possesses a high photospeed and was the first commonly used photopolymer systems. However, acrylic resins usually have problems in severe linear shrinkage and curl distortion. Epoxy and vinyl ether systems used cationic polymerisation and usually have relatively slow speed due to their relatively high activation energies of monomer propagation for cationic reactions as opposed to the low values for free-radical reactions (Odian 1981). Nevertheless, the vinyl ether base systems usually have low viscosity and are easy to clean and epoxy-based photopolymers show greatly reduced effective linear shrinkage and negligible curl distortions, which are highly desirable for accurate MSL fabrication (Jacobs 1996).

Photopolymeric resins are the most common routine MSL materials employed nowadays. Unfortunately, they commonly experience shrinkage and curl distortion, which significantly limits their performance in fabricating small size specimens (usually less than 1 mm See Chapter 4 for detail). New polymer systems with greater flexibility, higher polymerisation speed and improved resistance to shrinkage and curl distortion are continually being investigated. As the MSL applications expanded and required the integration of various functional materials, several MSL processes based on different materials other than polymers, such as ceramic MSL (Epstein *et al.* 1997) and Metallic MSL (Cabrera 1998), were developed for their particular applications. These MSL processes attracted a great deal of interest in micro-fluidic applications, micro-engine and micro-sensors applications, where the traditional silicon and polymer structure cannot

fulfil the demanding requirements and gave a new impetus to material research. Small but complex biomedical structures such as biocompatible or biodegradable micro-scaffolds could be delicately fabricated by an MSL system using the novel photopolymeric materials Poly (propylene fumarate) (PPF) (Choi 2009). In another example, a micro-turbine was built up with 110 layers of 4.5 μm thickness (Beluze 1999).

2.3 The Micro-stereolithography fabrication system

Micro-stereolithography (MSL) is one of the most representative and attractive technologies for rapid prototyping of MEMS components at present, offering a promising solution for future batch production of functional micro-systems where traditional SL systems generally cannot. It shares the same principle with SL systems, but it includes a sub-micrometre precision x-y-z stage and a precise laser delivery system. In a typical MSL system, the laser beam is usually focused down to a few micrometres spot and the thickness of each curing resin layer is usually at the order of 10 μm.

A classic design of MSL apparatus is shown in Figure 2.5. The laser beam is directed by the galvanometric *X*-*Y* mirror and focused by a lens onto the surface of photo-polymeric resin to initialize the photopolymerisation. An acousto-optical shutter is employed to switch the laser beam on and off and selectively solidify the resin. The designed pattern is thereby cured in this layer. After finishing the first layer, the computer-controlled *Z*-stage moves downward to allow new resin to flow over the cured pattern and so proceed to curing the next layer and so on, to construct the whole part layer by layer eventually. This MSL system is capable of fabricating small objects, up to a few hundred micrometres, but

the laser focus kit needed to be further improved to obtain micro-parts with precision less than 100 µm.

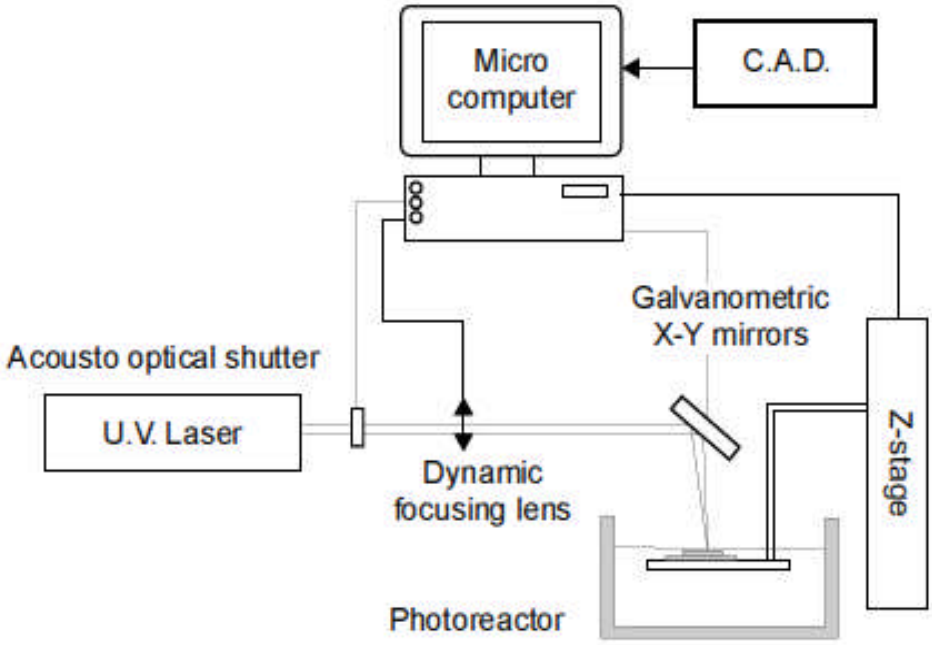

Figure 2.5: Schematic diagram of a classic MSL apparatus (Bertsch *et al* 1997)

In classical MSL setups, the laser beam is directed to the surface of the resin from above to cure the resin. After then, the platform move downwards to cure the new layer above the cured layers (Bottom-up fashion). This approach usually required a large volume of resin tank and the surface of finished layers are often stressed due to the fluctuation of the resin. Lately, the top-down MSL approaches have been increasingly employed. In this method, the laser beam illuminates the resin through a transparent vessel from underneath (Figure 2.6). The layers are cured inside the resin container and the cured layers are adhesive to the platform, therefore, the platform moves upward to proceed with curing

new layers beneath the cured layers. Despite the larger mechanical forces required to separate the structure from the bottom plate, this approach possesses advantages over the bottom-up ones in several aspects: smooth illuminated surface; smaller amounts of resin required; and limited oxygen inhibition.

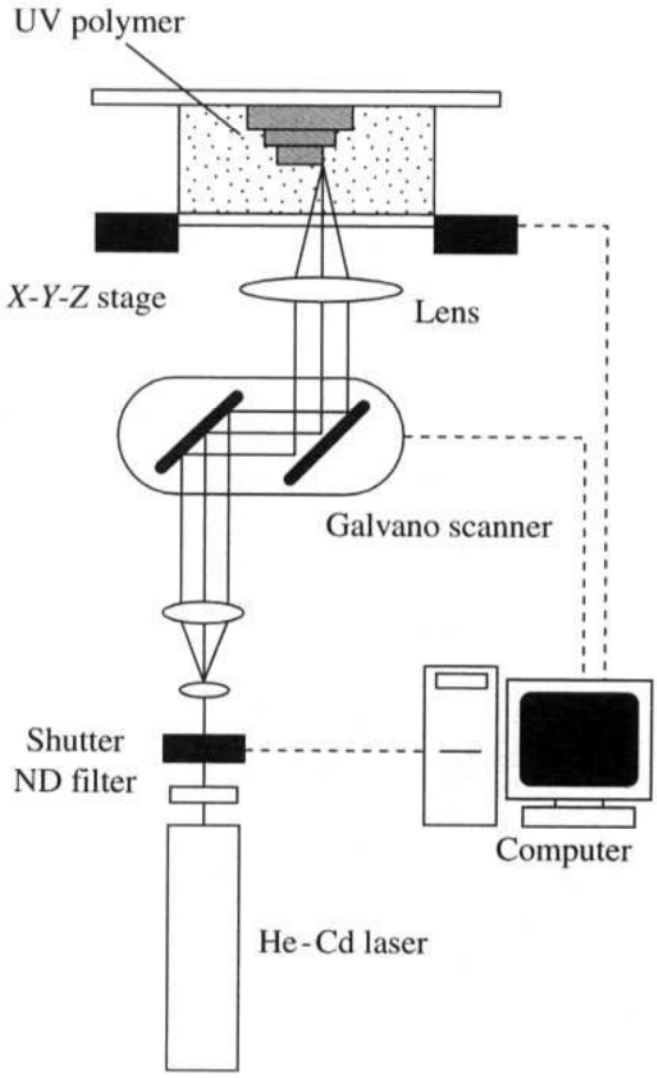

Figure 2.6: A top-down approach of MSL, from Ikuta (1998)

2.4 MSL arrangement and development

Based on the different beam delivery systems employed, an MSL apparatus is usually categorized as either a scanning MSL or a projection MSL. In scanning MSL, A well-focused laser beam is focused by dynamic lens and directed by galvanometric mirrors to draw selective patterns while the projection MSL utilises either a real photographic mask or a dynamic mask (*Liquid crystal display* (LCD) mask or micro-mirror arrays) to project the UV patterns. Both types have been modified for high-performance. In recent years, two-photon MSL apparatus have been designed in order to achieve higher precision products in the anticipation of future products.

2.4.1 Scanning MSL

Most MSL machines had evolved from the classical scanning method. As described in the preceding section, the classical MSL used an acousto-optical shutter, dynamic lens, and galvanometric mirrors to control, focus and deflect laser beam to form the desired patterns (see section 2.2). It was generally believed that, too many optical components are involved in the classical MSL (Figure 2.5), which brought a non-negligible uncertainty in laser metrology and results in poor focus (Bertsch *et al.* 1997). Thus, it was necessary to decrease the number of active operating elements to achieve higher precision. Despite the focus issue which prevented it from delivering high-resolution fabrication, the classic MSL is still extensively used in industry for its relatively fast manufacturing speed.

In order to pursue high-precision MSL fabrication, constrained-surface or free surface techniques were integrated into conventional MSL apparatus. Based on the classical MSL

method, Integrated Harden (IH) polymer processed design by Ikuta and Hirowatari (1993), which utilised constrained surface method to improve laser focusing, had been developed to address the beam-focusing issues (Figure 2.7). The laser beam was firstly focused and kept fixed onto the surface of resin through a glass window which was attached to the *Z*-stage. The dynamic lens was not required as the focal point is fixed. The resin container was placed onto an *X*-*Y* stage which provided the scanning instead of previous galvanometric mirrors. After manufacturing the first layer vector by vector by scanning the *X*-*Y* stage, the *Z*-stage moved the focal point upward to the cure next layer. In IH process, the x-y stage carried the resin to selective harden the polymer rather than using dynamic lens and galvanometric mirrors to focus and direct laser beams. A smaller focal point (hereby a higher precision) could be obtained. It was also reported that this approach reduce manufacture time significantly (Bertsch *et al.* 1997). Furthermore, the thickness of each layer could be well controlled using glass windows.

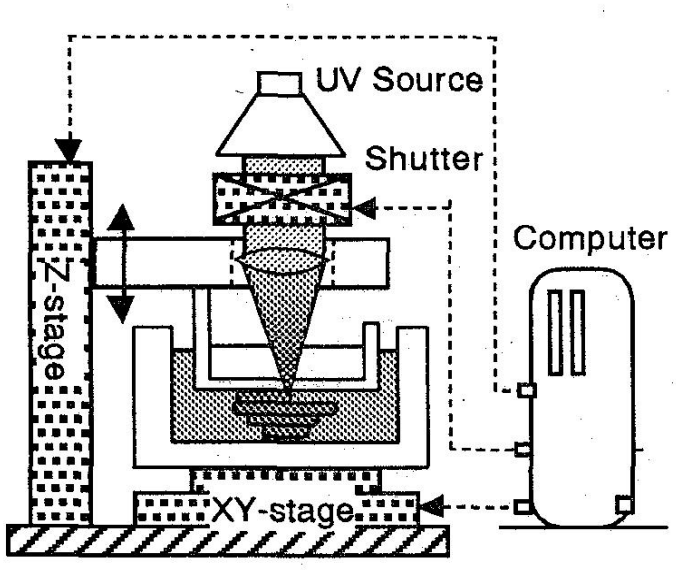

Figure 2.7: Schematic diagram of the IH apparatus, from Ikuta and Hirowatari (1993)

However, one major disadvantage of using a constrained surface (glass windows) is that the formed polymer was likely to be damaged due to the adhesion to the glass. A free surface MSL was invented to avoid the damage issues in the IH process (Ziss *et al.* 1996, Zhang *et al.* 1999). Similar to the IH process, this free surface MSL (Figure 2.8) replaces galvanometric mirrors with *X*-*Y* stages and also keeps all the laser beam delivery optics fixed. Instead of using glass windows, free-surface method is adapted to prepare the layer. The *Z* position of the focal point is carefully calibrated to be set at the same height as the plane of free surface of the resin. The fabrication procedure proceeds with the *Z*-stage moving downward to cure a fresh horizontal layer on the top of a cured layer. Because in the free-surface MSL, the fabrication time of curing each layer is only determined by the rheological properties of the resin, resins with low viscosity were selected. Therefore, light-absorbing medium is usually added into the resin formulation, and the resolution of width and depth is decreased.

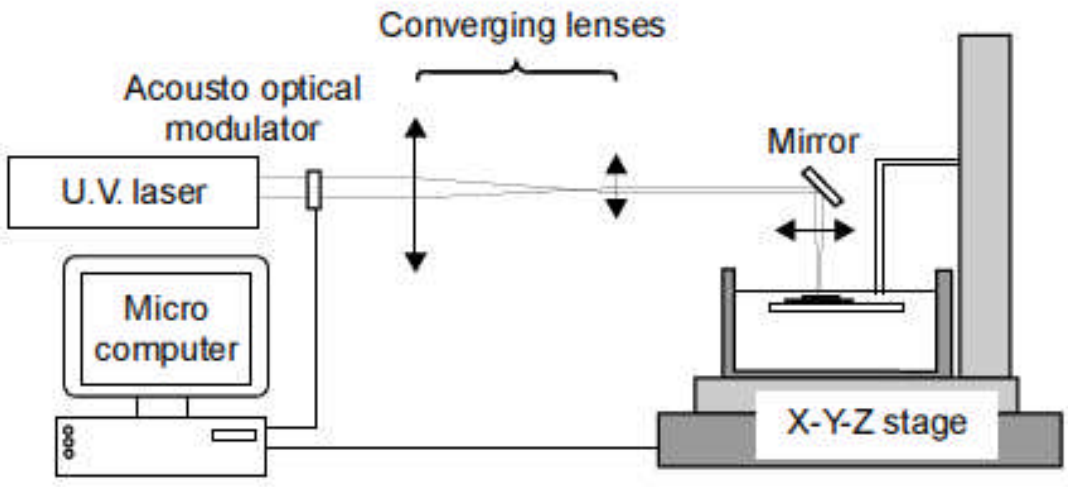

Figure 2.8: Schematic diagram of free surface MSL apparatus, from Bertsch (1997)

In summary, the conventional scanning MSL machines employs a set of optical components to direct a laser beam to formed desired micro-structures. The precision of this apparatus could be pushed further to micro level in *z*-direction and sub-micrometre level in *x-y* direction by applying additive techniques such as constrained surface technique or free surface technique at the sacrifice of fabrication time. (Ikuta and Hirowatari 1993, Ikuta *et al*. 1996) Although the recent developed scanning MSL is competent to fabricate micro or sub-micrometre level complex microstructure, the slow fabrication speed of building a three-dimensional product remains as one major drawback. This method hereby is most utilized in prototyping fine and high-aspect-ratio micro MEMS parts in research laboratories rather than for commercial high-resolution fabrication.

2.4.2 Projection MSL

Scanning MSL machines build the micro structures in a vector by vector and layer by layer manner which produces fine micro parts but took a long time. On the other hand, projection MSL, which employed a patterned mask to illuminate the whole resin layer and cure pixels in parallel rather than scanning the layer line by line (Figure 2.9), was proposed by Suzumori (1994) for a more rapid fabrication solution. Based on the different masks used, two types of projection MSL have been developed: real-photographic mask projection MSL and dynamic mask projection MSL.

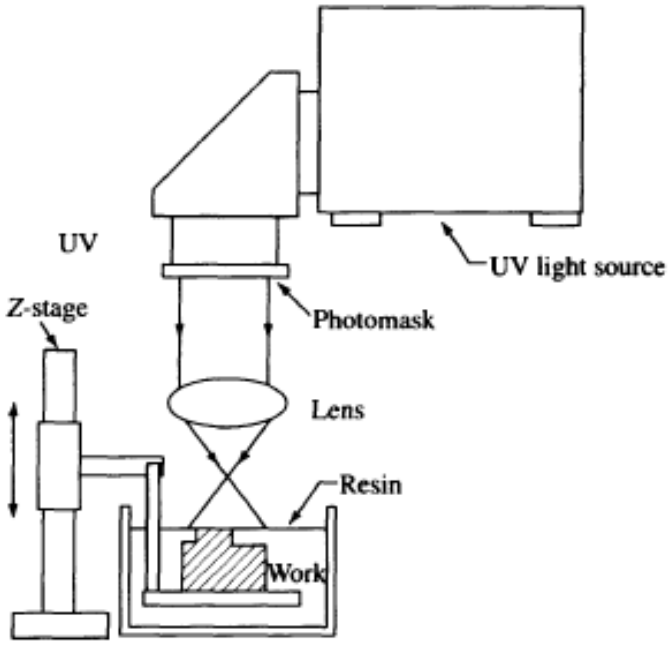

Figure 2.9: Schematic diagram of mask-projection MSL, from Suzumori (1994)

As with scanning MSL, projection MSL builds structures in a layer-by-layer fashion. Instead of laser scanning optics, photographic masks which contained the geometrical features of each layer are utilised to transfer the patterns to curing layers. In this approach, each layer is built by employing a laser or other UV light exposure through the masks to selectively cure patterns. The time of curing each layer is only dependent on the required exposure time but not the *X*-*Y* plane size and construction numbers, which dramatically reduces the fabrication time.

Although real-mask projection MSL saves significant fabrication time in producing complex three-dimensional objects, a larger amount of pre-work is required to produce layer masks; this is not only time consuming but also expensive. Thus, a dynamic pattern generator is sometimes used to replace these real-photographic masks. A typical

schematic diagram of this dynamic mask-projection MSL is shown in Figure 2.10 (Yang. 2008).

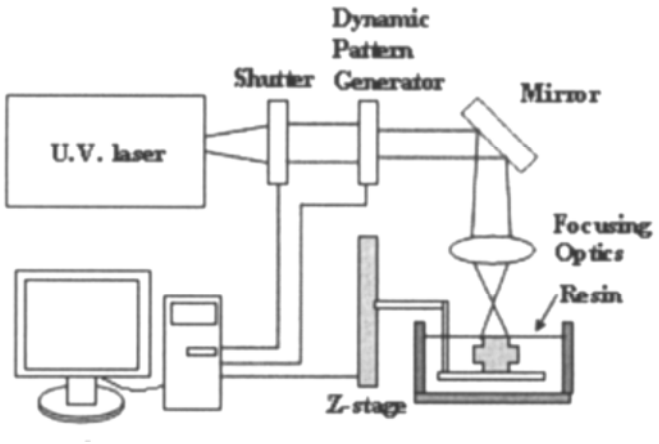

Figure 2.10: The schematic diagram of dynamic mask-projection MSL, from Yang (2008)

In dynamic mask projection MSL, a computer-controlled *liquid crystal display* (LCD) or micro-mirror arrays projection device, which controls on/off transmission of the incident light on each pixel, is used to transfer the images. Light passes through the activated pixels of the LCD device and is focused on the selected exposure areas of the resin surface for the polymerisation. Using the LCD projectors to deliver the patterns not only cuts the expensive cost of multiple masks but also skips the procedure of physically replacing masks for each layer. The rest of the procedure is similar to the other MSL apparatuses, and the microstructure is also formed in layer-by-layer accumulating fashion. This method significantly reduces the fabrication time without making massive real photographic masks, thus shows a great potential in batch manufacture of complex three-dimensional micro-structures in various industries.

However, this LCD mask comes with some intrinsic drawbacks, such as large pixel sizes, low filling ratio (51%), low switching speed (20 ms), the low optical density of refractive elements during the OFF mode and higher light absorption during the ON mode (Sun, 2005). Moreover, the UV radiation is often sufficiently energetic that the dynamic masks tend to accumulate damage and have a fairly short life in real applications. Recently, the Digital micro-mirror devices, which moderate the radiation by flipping micro-mirror arrays, have been increasingly employed for their advantages in smaller pixel size, higher filling ratio (91%) and faster responding time (20 μs). More significantly, they are compatible to high UV radiation (lasers) which gives a promising future for high-precision fabrication.

2.4.3 Two-photon MSL

Despite the rapid progress in developing high-precision MSL, these conventional MSL systems still experience difficulties in fabricating sub-micrometre structures. The main technical limitations of conventional MSL systems are in terms of the minimum thickness of resin layers due to the viscosity and surface tension effects and the small spot size especially as some part of the focus radiation is penetrated into the resin. In contrast, the two-photon MSL is a true three-dimensional process whereas the conventional MSL is a planar process which builds structure layer-by-layer and the focus spot is much smaller than the conventional ones. Thus, this technology avoids the minimum thickness problem as the resin does not need to be layered and has better focus spot resulting in a better manufacturing precision (Wu 2006).

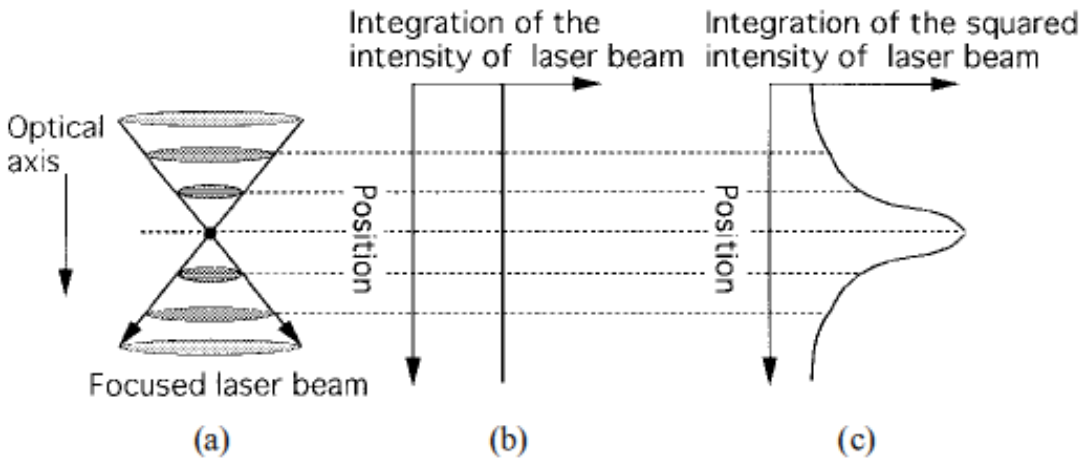

Figure 2.11: Single-photon absorption and two-photon absorption generated by a focus laser: (a) schematic diagram of a focused laser beam; (b) total single-photon absorption per transversal plane which is calculated by integrating the intensity over the plane, versus optical axis. (c) Total two-photon absorption per transversal plane, which is calculated by integrating the squared intensity over the plane, versus optical axis (Maruo 1998)

The two-photon MSL setup is built based on two-photon polymerisation (TPP). In TPP, when an UV beam is closely focused on the volume of a liquid state resin, the photoinitiators are excited by the simultaneous absorption of two photons and the polymerisation began. The polymerisation occurs at the highly localized area around the centre of focused beam as a result of the absorption of the threshold energy. An overview of two-photon polymerisation could be found by Lee *et al*. (2008) As shown in Figure 2.11, the density of photons decreases with the distance away from the focal plane, but the polymerisation rate at each cross section remains the same as well as the light intensity in single-photon MSL (Maruo and Kawata 1998). Thus, the resin is cured completely in the illuminating area and even beyond focal plane which resulted in a poor spatial resolution. On the other hand, the polymerisation rate in two-photon MSL is

proportional to the square of the laser intensity. Thus the polymerisation is concentrated only at the close vicinity of the focal spot and as a result of high precision of less than 100 or 200 nm could be obtained (Lee *et al*. 2008). High power pulsed lasers are required to obtain two-photon polymerisation.

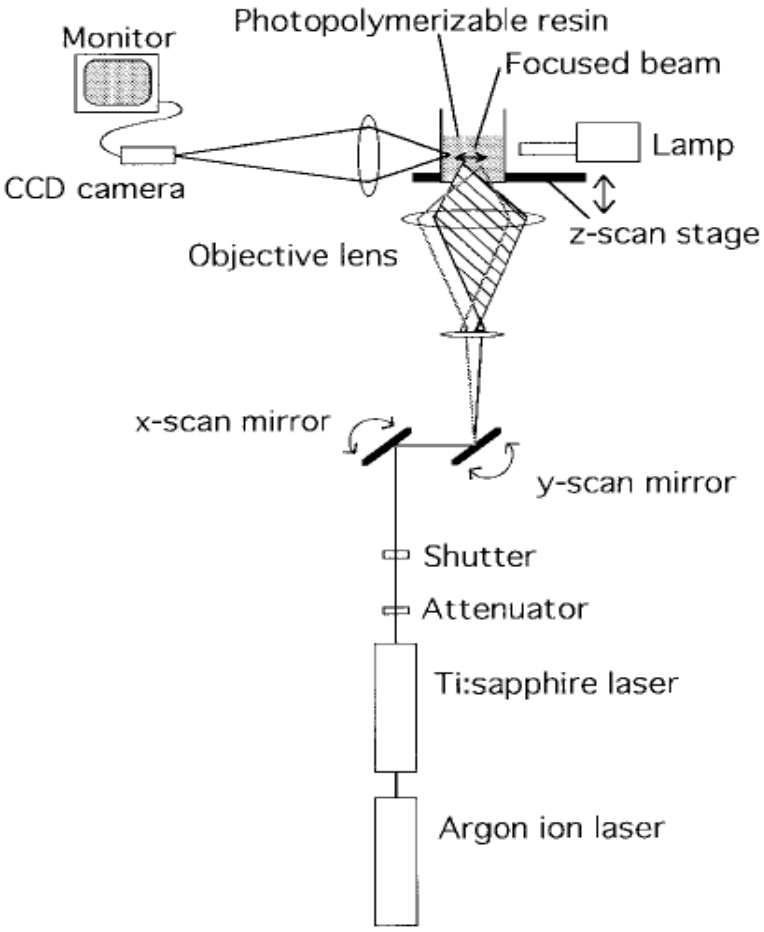

Figure 2.12: Schematic diagram of two-photon MSL setup, from Maruo and Kawata (1998)

A two-photon MSL apparatus is shown in Figure 2.12 (Maruo and Kawata 1998). In order to meet the high radical density requirement of two-photon absorption, a mode-locked Titanium sapphire laser is employed to provide a high intensity focus-spot. The

beam is directed by two-galvanic scanning mirrors and focused with an objective lens into the resin. A *Z*-stage is employed to move the sample vertically along the optical axis for multilayer fabrication while a high-magnification charge-coupled device (CCD) is also used to aid the laser focus and monitor the fabrication process.

In principle, a two-photon MSL is a scanning MSL which transfers designed patterns to photopolymeric resin either by galvanometric mirrors or *X*-*Y* stage scanning. The two-photon polymerisation could be initiated within the volume of resin rather than being restricted to the surface (single-photon polymerisation). Thus, two-photon MSL is a true three-dimensional fabrication technique which evades the difficulties of minimum layers and the oxygen induced polymerisation suppression. Moreover, the focus beam spot in two-photon MSL is much smaller than the conventional MSL, allowing the capability of fabricating sub-micro/nano complex structures.

The two-photon MSL has great advantage in the precision of fabricating small MEMS parts. The lateral and depth resolution of two-photon MSL apparatus was reported to be 0.62 and 2.2 μm respectively by Maruo and Kawata (1998). There were a few potential applications of the two-photon MSL in various fields, such as fabricating tips for scanning-probe microscopy, nano-imprinting and micro-pillars for mechanical properties evaluation (Lee *et.al* 2008). The most obvious drawback of the two-photon MSL is that it is also time-consuming in curing each layer, and hence is mostly chosen for prototyping specimens of high aspect ratio. In addition, it is more expensive than other types of MSL apparatus.

2.5 Current interest in MSL technology

It is widely accepted that the MSL technology is a particularly attractive choice of making small 3D MEMS parts where silicon had been ruled out. Nevertheless, the MSL product development is still insufficient due to lack of reliable material data, low-precision of thickness control and relative low fabrication speed. A current interest of MSL research focuses on: 1) the mechanical characterisation of material in parallel with new material investigation; 2) enhancing the thickness control; 3) modification of fabrication system for higher fabrication speed.

As one of the promising fabrication techniques of MEMS technology, the MSL technology shares the same obstacle of lack knowledge of mechanical properties. A few traditional MSL materials have been commonly employed but these were seldom enough for MSL development. A great deal of interest has grown in using MSL system to fabricate functional MEMS parts where the insufficient understanding of material properties, especially the mechanical properties, is preventing MSL production from moving from traditional structural role to functional parts. Moreover, the fabrication of new generation of MEMS devices requires the integration of different materials other than polymers such as ceramics, metals and metal alloys. The development of Multi-materials MSL technology also urges a reliable characterisation work for engineering data in order to assess the performance of products.

The standard MSL technology is an actually two and half dimension fabrication method. The lateral dimension is completed with the layer by layer accumulation, hence is largely dependent on the minimum curing thickness controlled by the system. Increasing the laser wavelength would enhance the accuracy of the lateral thickness but would also raise

the exposure time and cost to a great extent. Recently work has been investigated with applying additive techniques such as constrained surface technique or free surface technique to the classic MSL apparatus to further push the *Z*-directional accuracy. The two-photon MSL is also a novel technique where near nano-meter fabrication accuracy could be realized (Lee *et.al* 2008).

Another disadvantage of MSL technologies is the relatively low fabrication speed which prevents it from large batch-production. It is usually time-consuming to build a complex 3D micro-structure in scanning MSL system except the new developed TNO machines. A few designs such as mass-IH process (Ikuta 1996) had been brought up to increase the fabrication speed through the use of an array of optical fibres. For alternative, the Projection MSL (PμSL) approach, which forms each layer by one laser exposure through a patterned mask instead of laser scanning, could significantly reduce the fabrication time. The intensity distribution of the patterned light in the Projection MSL had a negative effect on the accuracy of the microstructure, but it is still an attractive option as the fabrication speed is always the first consideration of production.

2.6 Conclusion

As one of the primary fabrication techniques for MEMS components, MSL is a free-form technique which offered an attractive potential for fabricating MEMS parts. Micro or sub-micrometre fabrication accuracy has been achieved with the continuous development and combining of techniques and an increasing numbers of materials can be applied in the process. The materials mostly employed for MSL system are acrylate, epoxy, and

vinyl ether while materials other than traditional polymeric materials have also been introduced and investigated in MSL system for multi-materials needs. Whereas conventional SL is limited to a prototyping tool, MSL system also offers great potentials in the future industrial manufacture.

However, the MSL technology still has technical limitations in fabrication speed and high cost in high-precision applications. Most current MSL systems are applied for prototyping purpose rather than for batch-production. Another impediment of MSL fabrication systems is insufficient knowledge of the mechanical, physical and chemical properties of MSL materials. Significantly, many new materials have been proposed in MSL fabrication research, but only a few of them had been proved reliable. Thus, it is of great interest to investigate the properties, especially the mechanical properties, of MSL materials in order to further push the applications of MSL products.

References

Beluze, L., Bertsch, A. and Remaid, P. (1999). "Microstereolithography: a new process to build complex three-dimensional objects, " *Pro.SPIE*, **3680**, 808-817.

Bertsch, A., Lorenz, H. *et al.* (1999). "3D microfabrication by combining microstereolithography and thick resist UV lithography," *Sensors and Actuators A: Physical*, **73**(1-2), 14-23.

Bertsch, A., Zissi, S., Jézéquel, J.Y., Corbel, S. and André. J.C. (1997). "Microstereolithography using liquid crystal display as dynamic mask-generator," *Microsyst. Technol*., **3**, 42-47.

Cabrera, M. *et al.* (1998). "Microphotofabrication of very small objects: pushing the limits of stereolithography," *Mol. Cryst. Liq. Cryst.*, **315,** 223–234.

Choi, J.-W., Wicker, R., Lee, S.H., Choi, K.H., Ha, C.S. and Chung, I. (2009). "Fabrication of 3D biocompatible/biodegradable micro-scaffolds using dynamic mask projection microstereolithography," *Journal of Materials Processing Technology*, **209**(15-16), 5494-5503.

Epstein, A.H. et al. (1997). "Power MEMS and Microengine," *Proc. Int. Conf. Solid-State Sensors Actuators*, **2**,753-756.

Gardner, J.W, Varadan, V.K, and Awadelkarim, O.O. (2005). *Microsensors MEMS and smart Devices*, JOHN WILEY & SONS, Chichester, ISBN: 047186109X.

Ikuta, K. and Hirowatari, K. (1993). "Real three-dimensional microfabrication using stereolithography and metal moulding," *Proc. IEEE MEMS*, 42-47.

Ikuta, K., Maruo, S. and Kojima, S. (1998). "New microstereolithography for freely moved three dimensional microstructure-super IH process with submicron resolution," *Proc. IEEE MEMS,* 290–295.

Ikuta, K., Ogata, T., Tsubio, M. and Kojima, S. (1996). "Development of mass productive microstereolithography (Mass-IH process), " *Proc IEEE MEMS*, 301-305.

Jacobs, P.F. (1992). *Rapid prototyping and manufacturing: Fundamentals of stereolithography*, 1st edition, Society of Manufacturing Engineering, Dearborn, MI. ISBN: 0872634256.

Jacobs, P. F. (1996), *Stereolithography and other RP & M technologies: from rapid prototyping to rapid tooling*, Society of Manufacture Engineers, USA. ISBN: 0872634671.

Kodama, H. (1981). "Automatic method for fabricating a three-dimensional plastic model with photo-hardening polymer," *Rev. Sci. Instrum*., **52**, 1770-1773.

Lee, K. S., Kim, R.H., Yang, D.Y. and Park, S.H. (2008). "Advances in 3D nano/microfabrication using two-photon initiated polymerisation," *Progress in Polymer Science*, **33**(6): 631-681.

Maruo, S. and Kawata, S. (1998). "Two-photon absorbed near infrared photopolymerisation for three-dimensional microfabrication," *J.Microelectromech. Syst.*, **7**, 411-415.

Melchels, F.P.W., Feijen, J. And Grijpma, D.W. (2010). "A review on stereolithography and its applications in biomedical engineering," *Biomaterials*, **31**(24), 6121-6130.

Odian, G. (1981). "Chain copolymerisation," Chapter 6, *Principles of polymerization*, Wiley-Interscience Publication, New York. ISBN: 0471274003.

Sun, C., Fang, N., Wu, D., and Zhang, X., (2005). "Projection micro-stereolithography using digital micro-mirror dynamic mask, " *Sensors and Actuators A*, **121**, 113-120.

Suzumori, K., Koga, A. and Haneda, R. (1994). "Microfabrication of integrated FMAs using Stereolithography," *Proc. IEEE MEMS*, 136-141.

TNO. (2007). "Improved micro-stereolithography Faster and more accurate 3D printing", TNO science and Industry. Eindhoven. The Netherlands.

Warwick Microsensors and Bioelectronics Laboratory, (2007). University of Warwick. UK.

Wu, S., Serbin, J. and Gu, M. (2006). "Two-photon polymerisation for three-dimensional micro-fabrication," *Journal of Photochemistry and photobiology:A Chemistry*, **181**, 1-11.

Yang, H., Tsiklos, G., Ronaldo, R., Ratchev, S. (2008). *Micro-Assembly Technologies and Applications*, eds. Ratchev, S., Koelemijer, S., in IFIP International Federation for Information Processing, Volume 260, Boston: Springer, 171-176.

Zhang, X., Jiang, X.N. and Sun, C. (1999). "Microstereolithography of polymeric and ceramic microstructure," *Sensors and Actuators A*, **77**, 149-156.

Zissi, S., Bertsch, A., Jezequel, J.Y., Corbel, S., Andre, J.C. and Lougnot, D.J. (1996). “Stereolithography and microtechnologies,” *Microsyst. Technol.*, **2,** 97-102.

Chapter 3: Review of Micro-tensile test method and Methodology

3.1 Introduction

The importance of mechanical properties in MEMS technology was recognized in 1990 by Muller. He concluded that it is essential to build mechanical engineering data bases of MEMS materials at the appropriate scaling of mechanical design to make it possible to fully exploit the advance development of MEMS technology. Later expanded conclusion were made in the report of a National Research Council committee that test-and-characterisation methods and methodology were required to facilitate consistent evaluation of material and properties at required scales and to help fabrication facilities define MEMS materials for potential users (Muller 1997). As the fields of MEMS technology underwent rapid growth and the range of applied materials increases, the need for reliable mechanical material data also rose greatly. However, most of the MEMS materials have not been well characterized regarding their mechanical properties at small scales (particularly under 1 mm) yet. The most prominent explanation for the insufficient characterisation work is the difficulty in testing at this size scale (Tsuchiya 2008). In the past decade, sustained research work has been devoted to characterisation of silicon materials for better understanding of fundamental mechanical properties such as Young's modulus, fracture strength and Poisson's ratio. A summary of mechanical characterisation results about silicon materials and other structural materials in MEMS could be found by Sharpe (2001). The fabrication of new MEMS device requires various functional and structural materials, which spurs the development of materials research for MEMS (e.g. polymers, ceramic, metallic, composite, *et al.*).

This chapter summarises a variety of important mechanical properties and several general characterisation methods for MEMS materials at small scale. Particular emphasis is placed onto the uniaxial tensile test approach and bending test approach since they are the most widely used approaches for mechanical characterisation. A comparison of the tensile test and the bending test is given, leading to a practical preference to the tensile approach for its simplicity in data conversion and existing practical fabrication limitations. An analytic overview of existing MEMS-based tensile tests as well as their challengers is also given to explore potential methods to develop a suitable tensile test-rig for MSL polymeric materials.

3.2 Test Methods of micro-characterisation

3.2.1 Definitions of MEMS mechanical properties

There are several standards in developing standard methods for mechanical characterisation, such as ASTM (American Society for Testing and Materials) standards, British Standards, IEC (International Electrotechnical Commission) and MMC (Micromachine Centre) (Tsuchiya 2008). Generally, these standard test procedures are developed for bulk material tests which may not suitable to MEMS-based characterisation at small scales. Nevertheless, it is useful to use these standards as a guide to understanding the mechanical properties of MEMS.

The mechanical properties of materials characterise the response of a material when they are subjected to loads. In terms of assessing elastic behaviour and reliability of MEMS materials, the following aspects of mechanical properties are usually evaluated:

Elastic response – Young's modulus and Poisson's ratio,

Design strength – yield strength and ultimate strength,

Fatigue life prediction – stress-life (*S*-*N*) curve.

The elastic response of a material enables engineers to determine the deflection of components when subjected to forces. The elastic properties which describe the general material behaviour under load can only be obtained by experimental methods (e.g. tensile test and bending test). This is mostly because the real materials are structurally too complicated and the elastic behaviour is difficult to be precisely predicted with current insufficiently sophisticated theoretical determination. Important properties of this category include Young's modulus and Poisson ration, *etc*. The Young's Modulus (also known as tensile modulus) denotes the slope of the linear section of the stress-strain curve of the test material, in other words, it stands for the material stiffness. From the definition, the Young's modulus (*E*) is given by

$$E = \frac{\sigma}{\varepsilon} \tag{3.1}$$

where σ and ε denotes the tensile stress and tensile strain respectively. According to BS EN 10002-1 (2001), the standard procedures of obtaining Young's modulus are derived by measuring the stress and strain simultaneously when a uniaxial load is applied to the tensile specimen either incrementally or continuously. The Poisson's ratio (γ) is another important parameter that described the elastic behaviour of materials. It is defined as the ratio of transverse contraction strain to longitudinal extension strain, referenced to the direction of the stretching force:

$$\gamma = -\frac{d\epsilon_{trans}}{d\epsilon_{axial}} \tag{3.2}$$

where ϵ_{trans} stands for the transverse strain and ϵ_{axial} is the axial strain. The standard procedures to obtain Poisson's ratio are derived from strains resulting from uniaxial stress in a tensile test (ASTM E132). The values of Young's modulus and Poisson's ratio vary when different directional forces with respect to material structure are applied to anisotropic materials.

The elastic properties of materials are essential in predicting the deflection of structures subjected to external forces and building reliable MEMS components. They also provide essential information for micro-mechanical sensors where the mechanical structures function as transducers. As one of the most widely used materials for MEMS, the Young's modulus of silicon is also the most tested by various researchers via a variety of methods. Other silicon related materials such as single-crystalline silicon, silicon dioxide, silicon carbide and silicon nitride are extensively characterised in the semiconductor industry as well (Sharpe, 2001). However, the knowledge of mechanical properties of MEMS materials especially the newer materials, such as polymeric materials and biomedical materials, are rarely sufficient to firmly establish design data in handbooks.

The material strength shows the critical boundary points in the stress-strain curve derived from a uniaxial tensile test as illustrated in Figure 3.1. Several terms are used to describe the material strengths, such as yield strength, ultimate strength and fracture strength. The yield strength represents the upper limit point of stress where a material begins to deform plastically and the ultimate strength is peak stress before complete failure. Acknowledgement of yield strength is vital in structural engineering to assess the

maximum load before plastic deformation. Therefore it provides a valuable foundation for system reliability analysis especially for delicate complex structures. On the other hand, the ultimate strength (known as tensile strength) is also indispensable to assure the mechanical reliability of structure. The tensile strength of a material depends on several factors such as material preparation, the natural material defects, temperature or other environmental effects, etc. Thus, the measurement of the ultimate strength of materials plays a significant role as a guide value for preparing and testing MEMS materials. In addition, fracture strength, defined as 'the normal stress at the beginning of fracture' in ASTM E6, is the stress when the materials break via fracture. The fracture strength is often lower than the ultimate strength for ductile materials and it is equal to yield strength and ultimate strength for brittle materials such as polysilicon.

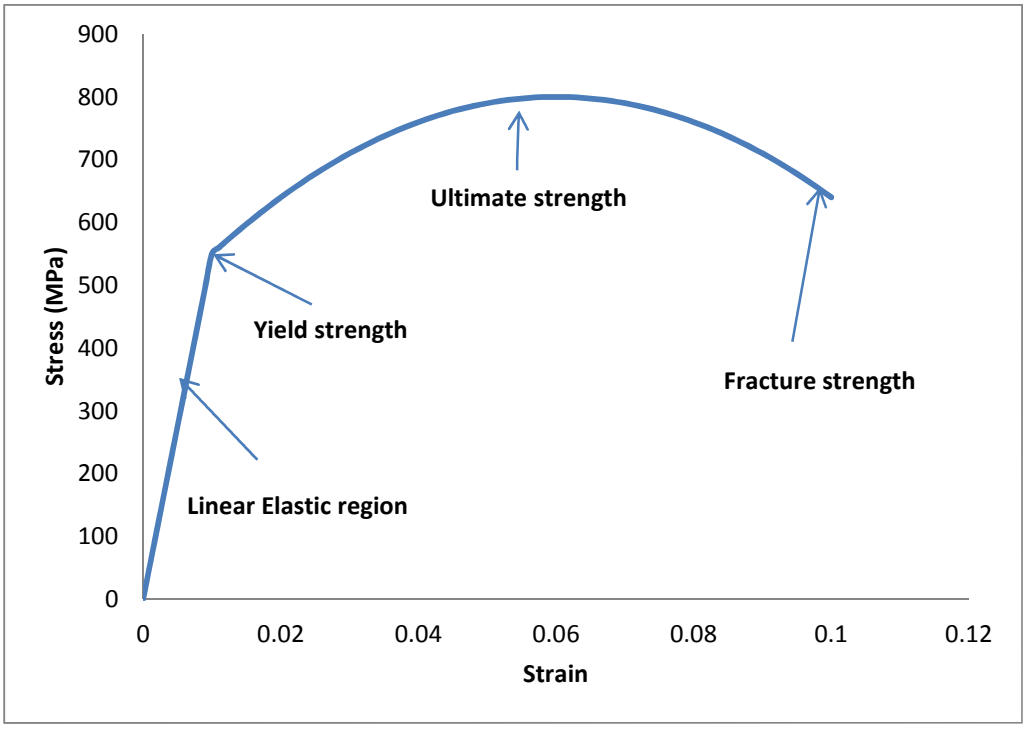

Figure 3.1: A stress-strain curve of a ductile metal, derived after Smallman (1999)

Understanding the materials strength is essential to evaluate the mechanical reliability of structures. As new MEMS material fabrication techniques are continuing to emerge, it is essential to be aware of practical bounds for the stress limits of these materials before applying them into real parts design. The strength of many MEMS materials exhibits considerable difference in real applications and this makes establishing the strength data base crucial in selecting adequate strength materials and building reliable structures. (Chen 2004) Besides, the strength of materials is also important for quality control purpose in the manufacture processes.

The term “fatigue-life” reflects the fatigue responses of a material subjected to cyclic loads and can be critical to the reliability and life endurance of products. It is defined by ASTM as the number of stress cycles of a specified character that a specimen sustained before failure. Other important properties related to the fatigue life are fatigue strength, fatigue limit and endurance limit. The fatigue stress is the stress value when the failure occurs and the fatigue limit is the limiting value of stress before failure occurs when life cycle becomes a certain large number. Similar to the fatigue limit, the endurance limit is cyclic stress value which a material could survive for a larger number of cycles (usually 10’s millions). Usually, these properties are illustrated in the S-N curve plot which is the graphic representation of relationship between the applied cyclic stress and numbers of life cycles, derived from test on the specimens of the material to be characterized (Figure 3.2).

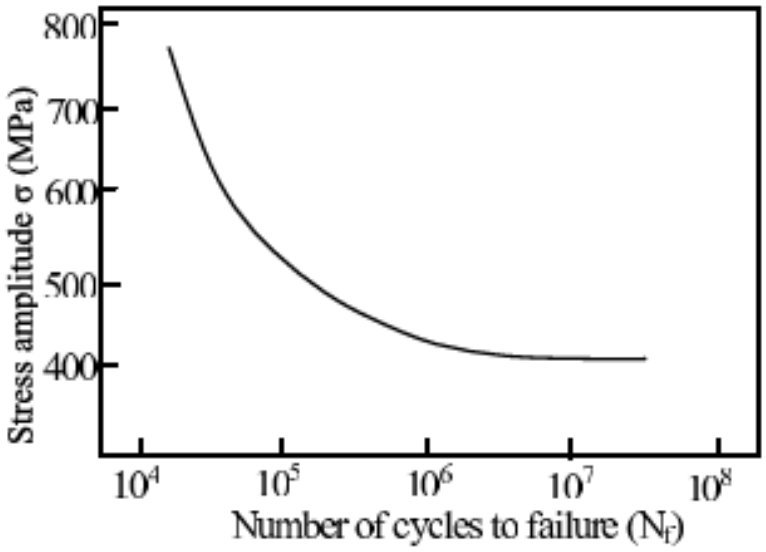

Figure 3.2: A typical S-N curve plot of a ductile material, from Illston (1979)

Most MEMS products are designed to have millions or more cycles of operations and years of product life-cycles. Understanding of the fatigue properties not only helps to understand how the materials behave along with long-time usage but also how to develop an economical product. Ultimately commercialization of MEMS products would require testing of prototypes before the batch-production. In this context it may be affordable to re-design if problems arise. However, all conventional MEMS processes are associated with large set-up cost, so it is desirable to obtain a few prototype designs and test at the cost of a few designed prototypes. Even so, obtaining accurate fatigue behaviour of small MEMS parts required conducting tests on large number of samples which is usually time-consuming and expensive.

Overall, a comprehensive understanding of the mechanical properties is difficult but particularly important in the development of multi-disciplinary MEMS technologies. A brief review of important mechanical properties is presented, mostly according to BS or ASTM standards. Most BS or ASTM standard definitions and procedures only apply to their own respective material categories and standards for metals are applied here as guidance to understand the definitions of mechanical properties since metals have broadly similar mechanical behaviour to the most common MEMS materials, silicon. However, the method of characterisation of other materials such as polymeric materials might greatly differ from those of the metal; modification or amendment of the methodology is need for accurate results (Czichos 2006). In all, it is still quite an early stage in establishing standard test procedures for MEMS materials, and more experimental characterisation work on a wide range of materials should be continued, driven by academic interest and the vigorous market forces.

3.2.2 Review of mechanical characterisation methods on MEMS materials

A few attempts towards mechanical characterisation of MEMS materials had been made in the past decades, but none of them has been standardized yet. This section provides a brief overview of recent developments of mechanical characterisation methods for MEMS materials. Most of these methods were based on two primary types of tests: tensile test and bending test. Others, such as membrane tests, indentation tests and resonant beam tests, were usually designed and applied to their own specific applications.

Among various methods for obtaining mechanical properties including bending test, indentation test, resonance beam test, *etc*., tensile test is an effective approach commonly employed in small scale characterisation tests as it allows direct data conversion to provide essential information of materials such as Young's modulus, fracture strength and Poisson's ratio. As the mechanical properties of the materials may still be subject to a considerable theoretical uncertainty under small scale conditions, the tensile test which could measure these properties without any conversion using special equations possesses great advantages in simplicity and was thus by far most investigated approach in MEMS characterisation. Typical procedures for tensile tests on MEMS materials starts with specimen fabrication and mounting, followed by precise dimension measurement, continued by applying a force or a displacement, and ended with force and displacement measurement. The general restrictions and major uncertainty source in MEMS-base tensile tests are regarding specimen mounting and alignment due to the miniaturized specimens. A general overview on the recent progress of MEMS-based tensile test was given by Sharpe (2003). Tensile tests on small specimens are commonly used in different loadings (fatigue), for different materials (polysilicon, silicon carbide and silicon nitride), and in different environment (high temperature). Meanwhile, new technologies are continually introduced and developed in order to refine the methodology and test procedures and to acquire a substantial engineering database of mechanical properties.

The bending test is another common method for measuring mechanical properties for MEMS materials. In general, the bending test has the advantage of being simple in the instrument setup and force loading as it is relatively free of problems of specimen handing and alignment that occurs in tensile test. It requires a significantly smaller force

to yield a lateral displacement which can more easily be picked up by various displacement detection techniques such as optical microscopy. Furthermore, the bending test is free of the misalignment issue which generally is the major concern in tensile tests, and the loading mechanism hereby could be much simplified. Thus, specimens with smaller dimensions than tensile specimens can be easily accommodated in bending tests. Three types of bending setups used for MEMS material are commonly used in this field: out of plane cantilever bending, built-in beam bending and in-plane bending. Experiments based on these three arrangements are extensively carried out to obtain the elastic behaviour of silicon-related materials in the past two decades and provided substantial experimental data.

Other MEMS-based characterisation methods are generally designed for acquiring particular mechanical data. For instance, the membrane tests are developed to obtain the stress data on thin membranes by measuring the deflection when subjected to pressure; the indentation tests could be used to determine the hardness of thin films on substrate; and various shapes of beam attached to a capacitive comb actuator could be used to obtain accurate Young's modulus in resonant beam tests. A summary of these approaches along with their applications was given by Sharpe (2001). These material tests had their own advantage in determining specific mechanical values via their unique techniques, but it was generally difficult to relate their particular value to other material properties due to the lack of knowledge of all potentially relevant factors.

In summary, the mechanical testing of MEMS materials is still at its very first stage where no method had distinguished itself as a standard procedure yet. Tensile test and bending test have been the most extensively investigated methods for MEMS scale

characterisation, offering some specific advantage and will be discussed in section 3.2.3. Other approaches employing innovative techniques to investigate particular mechanical properties are subject to propagating relative uncertainties due to the indirect manner and complexity of experimental setup.

3.2.3 A comparison between tensile test and bending test

The contradiction of increasing demand for accurate engineering data and insufficient existing knowledge on mechanical properties has motivated a great deal of research into the MEMS characterisation fields. Substantial research and commercial development have been made in the past years towards establishing reliable approaches for mechanical characterisation. However, common problems associated with small size of specimen of MEMS material such as sample fabrication, sample measurement and sample loading, have been major drawbacks and have led to a considerable variation among mechanical values.

Prior to designing a mechanical characterisation test-rig for MEMS materials, it is necessary to determine suitable experimental methodologies. In the past decades, most work had been devoted to developing the two primary types of characterisation tests: tensile test and bending test, which made them much more mature candidates for general mechanical characterisation than other approaches. A theoretical analysis of both tensile test and bending test is therefore presented here in order to justify the preferred practical experimental designs for this work. Two main material properties – Young's modulus and fracture strength are focused on as they provide the most valuable information for

most occasions. A rectangular beam (with length L, width b and depth h) was chosen as the specimen for each case. In the tensile test, a point force F_t is applied along the centreline of the beam while the concentrated bending force F_b is applied at the mid-span of a built-in beam (Figure 3.3).

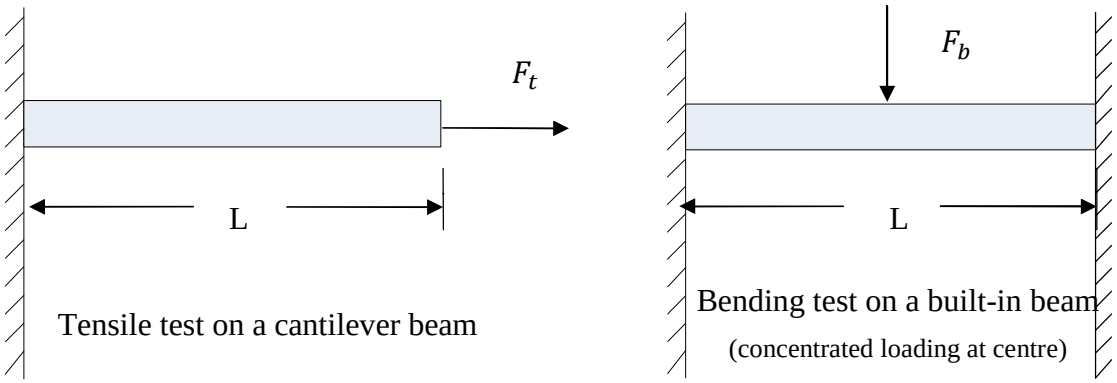

Figure 3.3: Basics of a tensile test (left) and a built-in bending test (right)

From classic strength of materials, the tensile stress (σ_t) and the end deflection (δ_t) of the test beam in the uniaxial tensile test are easily deduced as

$$\sigma_t = \frac{F_t}{bh} \tag{3.3}$$

$$\delta_t = \frac{\sigma_t}{E} L = \frac{F_t}{Ebh} L \tag{3.4}$$

where E denotes the Young's modulus of the material. In the bending test, it is assumed that the plane cross-sections remain planar (also known as St Venant's principle) and the effect of shear stress is negligible. From simple beam bending theory, it is obtained that

$$\frac{M}{I} = \frac{\sigma_b}{y} = \frac{E}{R} \tag{3.5}$$

where *M* is the applied bending moment at a transverse section, *I* is the second moment of area of the beam cross-section about the neutral axis (N.A.) of the beam, σ_b is the bending stress at a distance of *y* from the N.A and *R* is the radius curvature at the cross-section. Thus

$$\sigma_b = \frac{My}{I} \tag{3.6}$$

The measurement of built-in bending test is usually taken place at the mid-span where the maximum deflection occurred. The bending moment diagram of a built-in beam carrying a concentrate load at the mid-span could be as given in Figure 3.4. The total bending moment diagram of a built-in beam is a superposition of a 'free' moment diagram and a fixing moment diagram.

By symmetry, the bending moment at the mid-span can be concluded to be

$$M = \frac{F_b L}{8} \tag{3.7}$$

The N.A of the rectangle cross section is located at the central line and the second moment of area $I = \frac{bh^3}{12}$. Hence the maximum stress occurs at the edge of mid-span where x=*L*/2, $y=h/2$ is given by:

$$\sigma_b = \frac{3F_b L}{8bh^2} \tag{3.8}$$

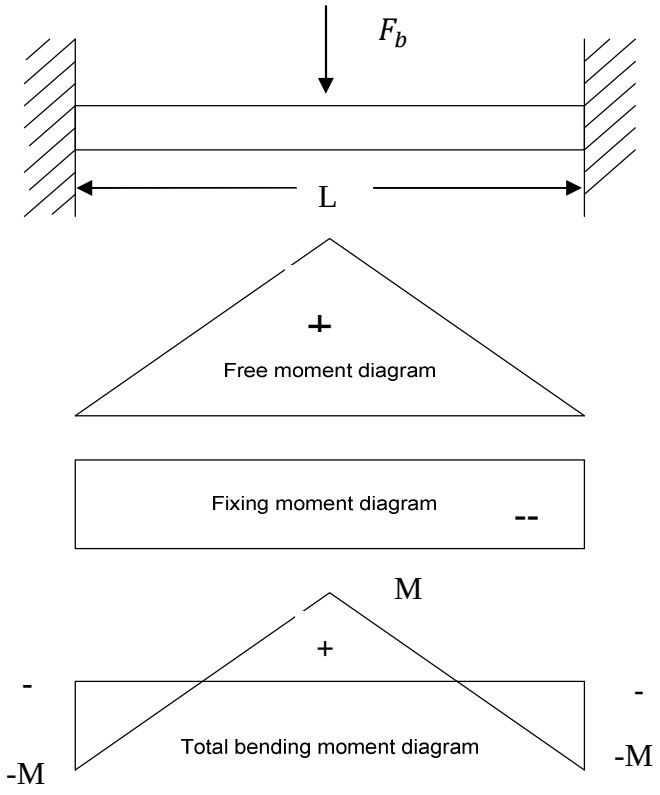

Figure 3.4: The Bending Moment (B.M) diagram of a built-in beam

Then Mohr's second theorem can be applied for the deflection at mid-span, thus the defection at the mid-span relative to the ends is given as

$\delta_b = \frac{1}{EI} \times [first\ moment\ of\ area\ of\ bending\ moment\ diagram\ between\ mid - span\ and\ one\ end\ about\ the\ centre]$

Thus, from the B.M. diagram in Figure 3.4,

$$\delta_b = \frac{1}{EI}\left(\frac{F_b L^3}{96} + \frac{-ML^2}{8}\right) = -\frac{F_b L^3}{16Ebh^3} \tag{3.9}$$

Thus, a summary of the result of uniaxial tensile test and built-in bending test is concluded in Table 3.1.

Table 3.1: Maximum Stress and Maximum deflection of the tensile test and the bending test

	Maximum Stress	Maximum Deflection	Young's Modulus
Tensile test	$\sigma_t = \frac{F_t}{bh}$	$\delta_t = \frac{F_t}{Ebh}L$	$\mathrm{E} = \frac{\mathrm{F_t L}}{\delta_t bh}$
Bending test **(Built-in beam central load)**	$\sigma_b = \frac{3F_b L}{8bh^2}$	$\delta_b = -\frac{F_b L^3}{16Ebh^3}$	$\mathrm{E} = \frac{F_b L^3}{16\delta_b bh^3}$

From Table 3.1

$$\frac{\sigma_t}{\sigma_b} = \frac{8F_t h}{3F_b L} \tag{3.10}$$

For same materials, it is presumed that: $\sigma_{\mathrm{critical}} = \sigma_{\mathrm{t}} = \sigma_b$ Thus

$$\frac{F_t}{F_b} = \frac{8L}{3h} \tag{3.11}$$

In the case of linear simple bending beam theory, the length L is usually much larger value than h in typical designs of test beams (usually ten times more). Thus, equation 3.11 also emphasizes that a smaller force (usually an order of magnitude smaller) is required to generate the critical stress in the bending test. Another great advantage of bending test is that the maximum deflection at failure is much larger than that of a tensile test on a similar beam and can be conveniently detected with various techniques.

On the other hand, according to Table 3.1, accurate measurements of applied force, specimen dimensions and displacement are required to determine Young's modulus. Hence

$$\mathrm{E} = \frac{\mathrm{F_t L}}{\delta_t bh} = \frac{F_b L^3}{16\delta_b bh^3} \tag{3.12}$$

According to equation 3.12, the main uncertainty in the tensile metrology is likely to originate from the measurement of elongation δ_t because of its small magnitude compared with the tension force F_t, while the dominant factor in the cantilever bending metrology is likely to be the depth of height h due to the high exponent (h^3) in the denominator and the relatively small force F_b. Therefore, an accurate measurement of the specimen's dimensions is critical in bending tests while a precise measurement of elongation is the top priority in tensile tests.

The primary object of this research is to conduct a solid mechanical characterisation for polymeric MEMS materials, mainly MSL materials. The major difficulties in mechanical characterisation on MEMS materials were insufficient precise models for interpreting data and the metrology errors in establishing the geometry of test devices (Senturia 1998). Hence data conversion and metrology errors were the main concerns in selecting proper characterisation methods.

In principle, the tensile test is a more straightforward method to obtain Young's modulus or stress level than the bending test. The tensile tests are the standard procedures in ASTM and BS standards and are similar in concept to the standard definition of mechanical properties where the testing theory of bending is derived from classic bending theories based on general assumptions which may be questionable under small scales and

the interpretation of test results is much more complicated and susceptible to the uncertainties of measured quantities. A few tensile tests on MEMS materials had been carried out and exhibits high agreement of values of mechanical properties with other material tests (e.g. membrane test) (Sharpe 2003). The tensile test is therefore the preferred method for more direct data interpretation and more reliable results would be expected in general mechanical characterisation of materials.

On the other hand, the bending test has the advantage of lower requirements for force implementation and displacement measurement. However, the spatial and lateral accuracy of most MEMS specimens fabricated using MSL systems is usually limited by the nature of this technology, especially the thickness. Furthermore, it is also practically difficult to precisely measure the dimensions of typical high-aspect-ratio MEMS specimens (fibres and thin-films) at small scale. Since the accuracy of specimen dimension is crucial in bending tests, uncertainty in the geometry can result in significant errors in the whole bending metrology loop. Moreover, the surface residual stress of MSL specimen, which commonly exists but is hard to detect, also has significant effect on the strength characterisation in bending tests. Thus, the bending test is not a desirable candidate for testing MSL specimens as the dimensional error and surface residual stress in MSL specimens usually introduce severe metrology errors.

In all, because the data interpretation and metrology errors were the major concerns in designing a mechanical characterisation test-rig for MSL material, the tensile test was finally selected as the characterisation approach in the present research.

3.3 Considerations for building a tensile tester for MEMS materials

Although the tensile test is an effective method for characterizing mechanical properties, it remains challenging to build up a precise experimental MEMS-based tensile test. The difficulties arise relative to the increasingly small scale of specimens (usually only a few tens to hundreds micrometres for MEMS applications). The test results from macro-material characterisation cannot be fully trusted as the measurement set-up cannot be miniaturized to the small scale of specimen (Tsuchiya 2008). The small and fragile nature of MEMS specimen makes it difficult for them to be properly handled and transferred to test-rigs without either damage or introducing metrology uncertainties. Apart from uncertainties over specimen dimensions and specimen handling, inherent imprecision in the macro-system force and metrology loops would not scale down and may become dominant. Moreover, the surface-to-volume effect also makes it unsafe to simply apply properties under macro-scale test.

Two families of MEMS-based tensile test-rigs had been developed: force-based tensile test and displacement-based test. The first approach applies controlled force to specimen and measures the corresponding elongation to derive the elastic properties. The other approach uses both force and displacement sensor to control the deformation of specimen while asserting a movement and enable an *in situ* test. The latter approach usually integrates the specimen design into the actuator and managed to avoid the technical difficulties of specimen gripping and alignment. For example, a novel displacement-base tensile setup developed by Haque and Saif (2001b) to allow on-chip and *in situ* testing in both SEMs and TEMs. Nevertheless, this methodology could only be applied to limited MEMS materials characterisation (mostly metal or metal like material) because the

specimen was co-fabricated on chip with the force actuators. Thus, for general MEMS materials characterisation, the first approach is commonly employed.

A typical tensile test procedure includes several steps: specimen design and fabrication, specimen mounting and alignment, measuring the dimensions of specimen, applying force or displacement to deform it, measuring the force and displacement (preferably direct strain if possible). General requirements for MEMS-base tensile testing are precision fabrication of specimen, sophisticated specimen handling strategy, accurate measurement of specimen dimension, high-performance force actuator, and precise strain gauges, all of which are hard to meet in practical experiments. Thus, it is generally challenging to apply tensile tests to gain mechanical values of MEMS materials at small scales.

3.3.1 Specimen design and fabrication

Preparing a small scale MEMS specimen for tensile test is difficult despite a few fabrication techniques already being available. Unlike the bulk tensile samples precisely cut from bulk materials, MEMS specimens are usually created from deposition and etching processes which place limitations on the spatial resolution. The small features of a designed specimen could be of the order of a micrometre which may exceed the capability of many commercial MEMS fabrication devices. Precise measurement of each specimen is usually needed to minimize the uncertainties in the specimen geometry, which is itself not an easy task. Moreover, it is crucial but demanding to prepare an initially stress-free test beam as pre-stress can significantly deviate the results of

mechanical tests. The pre-stress on the MSL specimen is difficult to identify unless direct strain measurement is employed in the tensile test. Hence, the design of MEMS specimen should take the consideration of the fabrication limitations and the preservation of specimen from external stress.

The MEMS tensile specimens are often made in forms of low dimensional materials, such as fibres and thin films. A fibre specimen has the advantages over a thin-film specimen of easy alignment and stable gripping. The fibre specimen can be well aligned and gripped by clamping down the two ends to the load system (Hua 2007). However, it is generally difficult to fabricate uniform fibres at small scale in many of the materials commonly used in MEMS field. On the other hand, the thin film tensile specimens can be well prepared by standard silicon MEMS techniques combining etching and deposition. A few other MEMS fabrication techniques, such as MSL, LIGA and electroplating techniques, had been developed to produce high-quality thin-film specimens. Nevertheless, thin film tensile specimens introduce several practical issues mostly regarding specimen mounting and loading. The common self-alignment methods in material tests (such as pin loading, universal joints, *etc.*) are difficult to apply to MEMS specimen as small but unwanted realignments can be easily introduced without notice at the present of relative large loading forces. Moreover, the small backlash and other motion uncertainties in the joints become unacceptable in the metrology loops since it is ultimately difficult to build metrology work between those joints when came to small deflections. Besides, a free-standing thin film tensile specimen without pre-stressing during the fabrication or mounting is genuinely difficult as the thickness decreases.

Protection structures are usually required for delicate specimens during fabrication and mounting to prevent initial stress or damage.

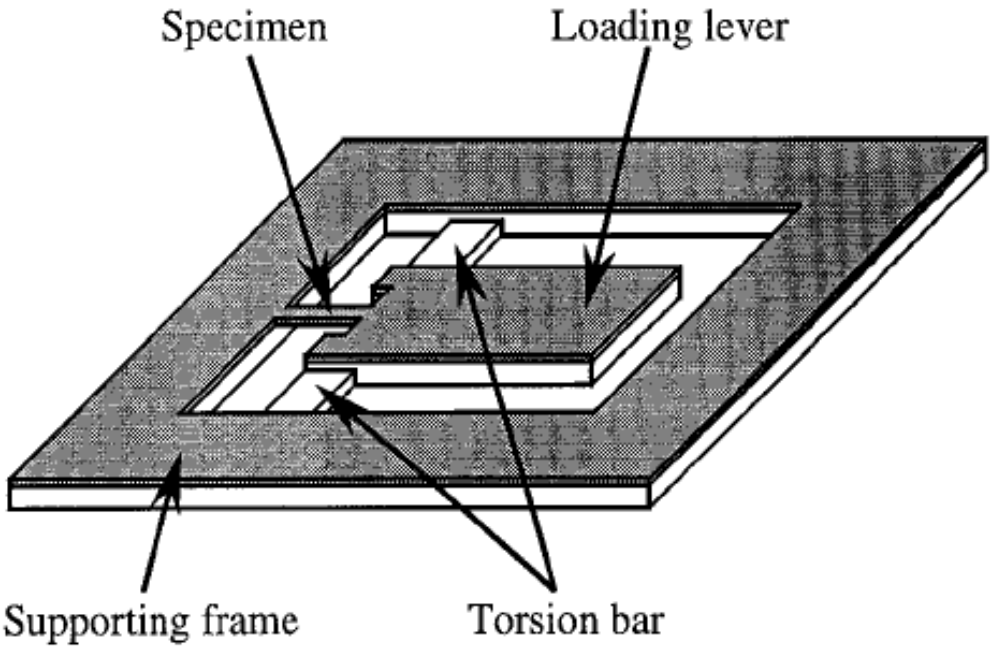

Figure 3.5: A typical specimen design with protection bars (Sato 1996)

One of the common strategies in small-scale sample design is to alleviate or minimize the specimen mounting and alignment issues by adding a specific aid structure. Several research efforts had been made to overcome these constraints by fully integrating the specimens into the test-rigs. For instance, Sato *et al* (1996) fabricated a specimen monolithically with an aid structure to protect it from damage and minimize the misalignment between the specimen and test-rig (Figure 3.5). Most of the specimen handling problems could be avoided by making the entire system including the loading

actuator on a chip. Haque and Saif (2001b) integrated the specimen and loading system into a chip for a novel *in situ* testing in TEM (also see Haque and Saif 2002). However, the on-chip integration of specimen and loading system has stringent requirements on fabrication techniques and high-performance calibration of force actuator which limits its potential applications. It is also very expensive and not suitable for general mechanical testing.

3.3.2 Specimen mounting and alignment

The tensile specimen is generally designed to have one end fixed to a stationary point while the other end is attached to its force actuator or lead screw. The common strategy of specimen mounting in macro-scale tensile tests is using mechanical grippers (e.g. threaded grip, pin-grip and wedge-grip (Czichos 2006)). However, firm mechanical gripping without over-stressing or damaging the specimen is hard to achieve in micro scale tensile tests because either slip or over-stress issues can easily occur. As the stiffness of specimen is usually much less than that of the loading system, it is hard to establish whether the specimen is pre-stressed by the loading system. As the conventional mechanical gripper for macro-tensile test usually fails to handle the delicate MEMS specimen, several alternative gripping systems were proposed by various researchers. An adhesive was used by Koskinen (1993) to fix the specimen to the grippers which produces a reliable specimen gripping but experiences difficulties in releasing the specimen. Another testing method using electrostatic attraction force to hold specimen during the tensile loading was developed by Tschiya *et al.* (1997). And a novel

piezoelectric micro-manipulator was developed by Perez *et al* (2006) for handling the specimen and applying force.

Another common strategy is using robust specimen design by either integrally fabricating specimens with protection structures in a bulk carrier (Tsuchiya 1997) or combing them with rigid mechanical support structures (Read 1999) to protect them during mounting and alignment. By offering protection to delicate specimen, it allows more robust handling with potential advantage for both challenges discussed in the previous proposal. It is also important but challenging to acquire a good alignment between specimens and test-rigs, especially for fracture strength measurement. These protection or support structures can also provide solid geometry reference for alignment and minimize the unwanted bending moments or shear introduced by misalignment between the specimen axis and loading direction. These structures are usually removed after mounting. Some of the specimens are even integrally fabricated with the loading system on chip and hence alleviate the issue of mounting and alignment (Haque and Salif 2001b).

3.3.3 Applying and measuring the test load

The forces applied in MEMS-based tensile tests are larger than in bending test but still very small. Acquiring small forces of high resolution and accurately applying them to the specimen are critical but difficult for MEMS characterisation. High sensitivity versions of force actuators tend to be simultaneously delicate and bulky, while they can add underlying level of series uncertainties into the metrology loop. These issues are sometimes hard to predict and increase the uncertainties in to the designed systems. Many

commercial force actuators for bulk tests, such as step-motors, cannot yet fully meet the high requirement. Several new techniques for implementing small scale force in tensile test have been made available in the past decades. For example, piezo-electrical transducers (usually using PZT) are frequently employed in mechanical characterisation of MEMS materials for their precise displacement control. However, the non-linearity and hysteresis phenomenon of PZT actuator have limited their performance. A PZT actuating type tensile test-rig using compensating nonlinear control was constructed by Kim (2005) to acquire linear behaviour of PZT transducers. Another type of commonly utilized force transducer in MEMS characterisation is the electromagnetic actuators which has several distinct advantages such as linear operation, fast response time and larger deflection at quite low drive voltage (Reyne 2002 and Hua 2007). The drawbacks in electromagnetic actuators are thermal dissipation, relative bulk of the mechanism and high requirements for the power supply. Other force transducers such DC servo motor (Ogawa *et al* 1997), hydraulic pressure systems (Hamza 1987), electrostatic comb driver systems (Haque and Salif 2001a) are also used in MEMS tensile tests.

Beside force actuators with inherent force sensors, the task of measuring tensile load is commonly completed by loadcells of low capacity. Commercial load cells can provide small loadcells with maximum capacity as low as 0.2 N. Load cells which are much stiffer than the tensile specimen are preferred so as to reduce the uncertainty in force calibration. However some researchers often preferred to build up their own load-cell to accommodate specific needs for their loading frame (Yi 1999). For instance, Suwito (1997) built a thin plate with a distance sensor is to measure the tensile load. The thin

plate functioned as a flexure spring and the tensile load was calculated from the bending stiffness of the thin plate and its deformation.

3.3.4 Strain measurement

The common strategy for strain measurement in MEMS-based tensile testing is to measure the specimen dimension and elongation separately. Most traditional MEMS fabrication techniques have limited performance in the spatial resolution of specimens; therefore the geometry of resulting specimens for tensile tests needs to be explicitly measured as well as their elongation. There are a few well-developed displacement sensors, such as capacitive gauges, inductive gauges, eddy current sensors, which had generally good performance in measuring either the specimen dimensions or elongation at the microscale. These sensors should be carefully integrated into the system as it is easy to pick up metrology errors. These displacement sensors needs to be carefully calibrated before test and the metrology loop should be kept small as any other introduced metrological error would significantly affect the test results. A review of performance of displacement sensors for MEMS characterisation was provided by Bell (2005). Since the MEMS specimens are usually fragile and extremely subjective to external forces, non-contact detecting techniques, SEM (scanning electron microscopy), AFM (atomic force microscopy), or TEM (transmission electron microscopy), were sometimes used to determine the elongation of gauge length (Sharpe 1997a 1997b, Yi and Kim 1999). Since the specimen length in even these tensile tests is usually large enough for most techniques (such as optical microscope), the difficulties mostly occurs in determining the geometry of the cross-section of small test beams. This technical issue

not only occurs before the tensile test but also after the deformation. The deformation of the tensile beams makes it even more difficult to establish the edge information. Important mechanical properties, such as Poisson's ratio, which depend on the accurate measurement of the dimensional change, are extremely difficult to measure under small scale.

Another strategy for strain measurement is defining the gauge length by depositing gauge marks and measuring the elongation optically. Several efforts had been made towards employing optical microscopy to measure the mechanical deflection of MEMS specimen. Tsuchiya (1997), Chasiotis (1998) and Haque (2001a) had used the SEM (scanning electron microscopy), AFM (atomic force microscopy), and TEM (transmission electron microscopy) respectively to conduct strain measurement for tensile test respectively. These approaches created surface gauge marks on the specimen, spot them on microscopy, captures them using CCD (charge-coupled device) camera and analyse them using image-correlation techniques. The elongation could also be picked up by interferometer for higher resolution strain measurement. Sharpe *et al* (1997a and 1997b) developed a two-slit optical interferometer approach to pick up the gauge marks by examining the fringe patterns generated by illuminating light through the slits. However, none of these techniques had been extensively studied for MEMS based mechanical characterisation.

In summary, it is difficult to establish standard MEMS-base tensile test for various materials. Several technical issues imposed by the small size of specimen, such as specimen mounting, alignment and loading, have not yet been resolved. A common strategy for constructing a MEMS-based tensile test was to design a special form of test

apparatus and compatible specimens that are less prone to the difficulties mentioned above. Most current designs have taken the advantage of either unique measurement technology or material fabrication techniques to overcome these limitations. Therefore, tensile tests for universal MEMS materials is not well established due to the limited solutions to these technical problems, but tensile tests for some specific MEMS applications are reasonably well developed.

3.4 Discussion and conclusion

Mechanical tests are of great importance in the development of both material science and engineering design. Currently insufficient mechanical engineering data of MEMS materials at small scale imposes a critical obstacle to designing and fabricating reliable MEMS parts. A review of mechanical properties and test methods has been presented. As the main error sources in MEMS-based mechanical characterisation are data interpretation and geometrical metrology errors, uniaxial tensile test is the preferred choice for straightforward data conversion and relatively low requirement on the dimensional accuracy of specimens. The common practical issues accompanying tensile test for MEMS materials such as specimen handling and loading are usually dealt with by integrating sample and test-rig designs along with modern strain technologies. In the following chapters, a general-purpose tensile measurement system primary aim for polymeric materials (particularly Micro-stereolithography materials) at small scale will be developed. It is designed to cover a wide range of common MEMS materials such as silicon, ceramic and polymeric materials and to deal with small specimens (with small dimensions at 0.1 mm level).

References

A.S.T.M. (2011). *Metals: Mechanical testing; Elevated and low-temperature Tests; Metallography*, Vol **03.01**, Annual book of ASTM standards, American Society for Testing and Materials, New York: ISBN: 9780803184657.

Bamberg, E. et al. (2006). "A tensile test device for in situ atomic force microscope mechanical testing," *Precision Engineering*, **30,** 71-84.

Bell, D.J., Lu, T.J., Fleck, N.A. and Spearing, S.M. (2005). "MEMS actuators and sensors observations on their performance and selection for purpose," *J. Micromech. Microeng.*, **15**, S153-164. ISBN: 1580535364.

British Stands (BS EN) (2001). *Tensile testing of metallic materials Method of test at ambient temperature*, London. ISBN: 0580384594.

Chen, K.S. and Ou, K.S. (2004). "Equivalent strengths for reliability assessment of MEMS structures," *Sensors and Actuators A*, **112**, 163-174.

Chasiotis, I. and Knauss, W. (1998). "Mechanical properties of thin polysilicon films by means of probe microscopy," *Proc. SPIE*, 3512, 66–75.

Czichos, H., Saito, T. and Smith, L. eds. (2006). *Springer handbook of materials measurement methods*, Chapter 7, 281-397, Springer, Heidelberg. ISBN: 3540207856.

Hamaz, A.A., Fouda, I.M., El-Farhaty, K.A. and Helaly, S.A. (1987). "Stress birefringence in polypropylene fibres," *Polym. Testing*, **7**(5), 329-343.

Haque, M.A. and Salif, M.T.A. (2001a). "Microscale materials testing using MEMS actuators," *J.Microelectromech.Syst*, **10**(1), 146-162.

Haque, M.A. and Salif, M.T.A. (2001b). "In *Situ* Tensile testing of nanoscale specimen in SEM and TEM," *Experimental Mechnics*, **42**(1), 123-128.

Haque, M.A. and Salif, M.T.A. (2002). "Application of MEMS force sensors for in situ mechanical characterisation of nano-scale thin films in SEM and TEM," *Sensors and Actuators A*, **97-98**, 239-245.

Haque, M.A. and Salif, M.T.A. (2003). "A review of MEMS-based microscale and nanoscale tensile and bending test," *Experimental Mechnics*, **43**(3), 248-255.

Hua, T., Xie, H., Pan, B., Qing, X., Dai, F. and Feng, X. (2007). "A new micro-tensile system for measuring the mechanical properties of low-dimensional materials—Fibers and films," *Polymer Testing*, 26, 513-518.

Illston, J.M., Dinwoodie, J.M. and Smith, A.A. (1979). *Concrete, Timber and Metals*, Van Nostrand, Reinhold, Crystal City, VA. ISBN: 0442301448.

Johnson, G.C., Jones, P.T. and Howe, R.T. (1999). "Material characterisation for MEMS: a comparison of uniaxial and bending test," *Proc. SPIE*, **3874**, 94-101.

Kim, S.S., Lee, H.J., Lee, H.W., Lee, N.K., Han, C.S. and Hwang, J.K. (2005). "Development and verification of PZT actuating micro tensile tester for optically functional materials," *International journal of Control, Automation and Systems*, **3**(3), 477-485.

Koskinen, J., Steinwall, J.E., Soave, R. and Johnson, H.H. (1993). "Microtensile testing of free-standing polysilicon fibers of various grain sizes," *J. Micromech. Microeng*, **3**(1), 13-17.

Modlinski, R., Puers, R. and Wolf, I.D. (2008). "AlCuMgMn micro-tensile samples Mechanical characterisation of MEMS materials at micro-scale," *Sensors and Actuators A*, **143**, 120-128.

Muller, R.S. (1990). "Microdynamics," *Sensor and Actuator. A (Phys.),* **A21-A23**, 1-8.

Muller, R.S. (1997). *Microelectromechanical Systems*, National Academy of Science, Washington, D.C.

Ogawa, H., Suzuki, K., Kaneko, S., Nakano,Y., Ishikawa, Y. and Kitahara, T. (1997). "Measurement of mechanical properties of microfabricated thin films," *Proc. of IEEE Micro Electro Mechanical Systems Workshop*, 430-435.

Perez, R., Chaillet, N., Domanski, K., Janus, P. and Grabiec, P. (2006). "Fabrication, modeling and integration of a silicon technology force sensor in a piezoelectric micro-manipulator," *Sensors and Actuators A*, **128**, 367-375.

Read, D.T., Cheng, Y.W., Keller, R.R. and McColskey, D.J. (2001). "Tensile Properties of Free-Standing Aluminum Thin Films," *Scripta. Mater.*, **45** (5), 583-589.

Reyne, G. (2002). "Electromagnetic actuation for MOEMS, examples, advantages and drawbacks of MAGMAS," *Journal of Magnetism and Magnetic Materials*, **242-245**, 1119-1125.

Sato, K., Shikida, M., Yoshioka, T., Ando, T. and Kawabata, T. (1996). "Micro tensile-test of silicon film having different caystallographic orientations," *Proc. Int. Conf. Solid-State Sensors and Actuators, Chicago, 1L, June*, 595-598.

Senturia, S.D. (1998). "CAD challenges for microsensors, microactuator, and microsystems," *Proc. IEEE*, **86**, 1611-26.

Smallman, R.E. and Bishop, R.J. (1999). *Modern physical Metallurgy and materials Engineering*, Chapter 7, 197-258, Butterworth-Heinmann, Oxford. ISBN: 0750645644.

Sharpe, W. N. Jr. (2001). "Mechanical Properties of MEMS Materials," Chapter 3, in the MEMS Handbook, CRC Press, 3-33.

Sharpe, W. N. Jr., Bagdahn, J., Jackson, K. and Coles, G. (2003). "Tensile testing of MEMS materials – recent progress," *Material science*, **38**, 4075-4079.

Sharpe, W. N. Jr., Yuan. B. and Edwards, R.L. (1997a). "A new technique for measuring the mechanical properties of thin film," *J. Microelectromech. Syst*, **6**, 193-199.

Sharpe, W. N. Jr., La Van, D.A. and Edwards, R.L. (1997b). "Mechanical properties of LIGA-deposited nickel for MEMs transducers," *Proc. Int. Conf. Solid-state Sensors and Actuators Chicago June 1997,* 607-610.

Sharpe, W. N. Jr., Yuan. B., Vaidyanathan. R. and Edwards, R. L. (1996). "New test structures and techniques for measurement of mechanical properties of MEMS materials," *Proc. SPIE*, **2880**, 78–91.

Suwito, W., Dun, M.L. and Cunningham, S.J. (1997). "Mechanical behaviour of structures for microelectromechanical systems," *Proc. Int. Conf. Solid-state Sensors and Actuators Chicago June 1997*, 611-614.

Tsuchiya, T., Tabato, O., Sakata, J. and Taga, Y. (1997). "Specimen size effect on tensile strength of surface-micromachined polycrystalline silicon thin films," *Journal of microelectromechanical systems*, **7**, 106-113.

Tsuchiya, T. (2008) "Evaluation of Mechanical Properties of MEMS Materials and Their Standardization," in *Reliability of MEMS: Testing of Materials and Devices* (eds O. Tabata and T. Tsuchiya), Wiley-VCH Verlag GmbH & Co. KGaA, Weinheim, Germany.

Yi, T. and Kim, C. J. (1999). "Measurement of mechanical properties for MEMS materials," *Meas.Sci. Technol*, **10**, 706-716.

Yi, T. and Kim, C.J. (1999) "Microscale material testing: etchant effect on the tensile strength," *Proc. Int. Conf. Solid-State Sensors and Actuators*, Sendai, June 1999, 518–521.

Chapter 4: The specimen fabrication process

4.1 Introduction

Specimen fabrication is a prominent factor in the mechanical characterisation of MEMS materials. Most specimen fabrication techniques are limited by the practical specification of particular MEMS fabrication equipment. The MSL fabrication technique possesses a unique advantage of converting complex 3D small structures directly from the model, but has limited performance in spatial fabrication accuracy, particularly the thickness, since it builds specimens in a layer-by-layer fashion. Moreover, much of the MSL materials research is still at the preliminary stage. Only a few materials have been made commercially available and even then usually with scarce knowledge about their mechanical properties. Besides, the common parameter settings in the fabrication process are mostly derived from empirical tests but hardly extensively studied yet. Thus, the fabrication of specimens should be considered an intrinsic feature of MSL material testing and should be experimentally tested.

In this study, the tensile specimen was fabricated by an Envisiontec Perfactory SXGA+ stereolithography system using a commercial acrylate-based resin R11 from Envisiontec. The Perfactory system had a 20 μm resolution in *X*-*Y*-direction and 25 μm in *Z*-direction. The description of the basic principle of Perfactory machine and its applied resin are presented in detail in this chapter. Emphasis is focused on the fabrication procedures and the critical parameter settings in Perfactory system. A critique of the resulting specimens is given at the end, with the main issue being curved surfaces occurring commonly in the thin-film specimens.

4.2 R11 MSL Resin

The MSL resin used for fabricating tensile specimens is a commercially available resin formulation R11 from Envisiontec. This material is an accurate and functional acrylate-based resin formulation. It is mostly used for producing robust and durable parts on all Perfactory® systems and suitable for fabricating rubber moulding parts, electrical housing, medical parts, and small parts in automobile applications (Envisiontec 2007). For instance, King (2009) fabricated a novel micro-actuator entirely using R11 resin (Figure 4.1). The device employed a single pneumatically actuated membrane and examined in long-term tests, which proved the high reliability of the device. A few other high-resolution small-scale parts have been fabricated using R11 resin formulation by the Microsensors & Bioelectronics Laboratory of University of Warwick (Figure 4.2).

Figure 4.1: A novel monolithic micro-actuator fabricated using R11 resin on a 5 p coin

Figure 4.2: Small objects fabricated in resin R11 on a 5p coin for scale (Leigh, 2010)

The R11 resin formulation is composed of an acrylic oligomer, cross-linking agents, a photoinitiator and a dye (Leigh 2010). The acrylic oligomer, similar to 1,6 hexanediol-ethoxylate diacrylate, is the basic monomer and the cross-linking agents (dipentaerythritol pentaacrylate and propoxylated trimethylpropane triacrylate) are used to promote intermolecular covalent bonding between monomers, linking them together to create more rigid parts. Commercially available 2-benzyl-2-(dimethylamino)-4´-morpholinobutyrophenone is used as the photoinitiator suitable for visible light radiation and the dye is used here to prevent the resin from being over-cured and thus to increase the fabrication resolution in all axes.

The MSL parts manufactured with R11 resin exhibit superior fatigue strength properties and excellent tolerance to a broad temperature and humidity environment during and after build. It also offers excellent chemical resistance and a good balance of properties between rigidity and functionality. A summary of materials properties is provided within the Envisiontec datasheet (Envisiontec 2007) and major ones are reported in Table 4.1. These mechanical properties are mostly evaluated at relatively large scale (ten millimetre scale) specimens and may not be applicable for small specimens (sub-millimetre scale) (See section 3.3). There is still insufficient knowledge about the mechanical properties of R11 resin under small scales. Also, these quoted values vary to a substantial extent in different methods. In the later tensile characterisation, the elastic behaviour of MSL specimens within small deflection is focused on.

Table 4.1: The mechanical properties of Envisiontec R11 (Envisiontec 2007)

ATSM METHOD	Material properties	Envisiontec R11
D638M	Young's modulus	1.245～1.510 GPa
D638M	Tensile strength	50 MPa
D638M	Elongation at break	13%
D638M	Elongation at yield	8%
D790M	Flexure strength	75 MPa
D790M	Flexure Modulus	2450 MPa
D2204	Hardness (Shore D)	85 Shore

4.3 The principle of Envisiontec MSL system

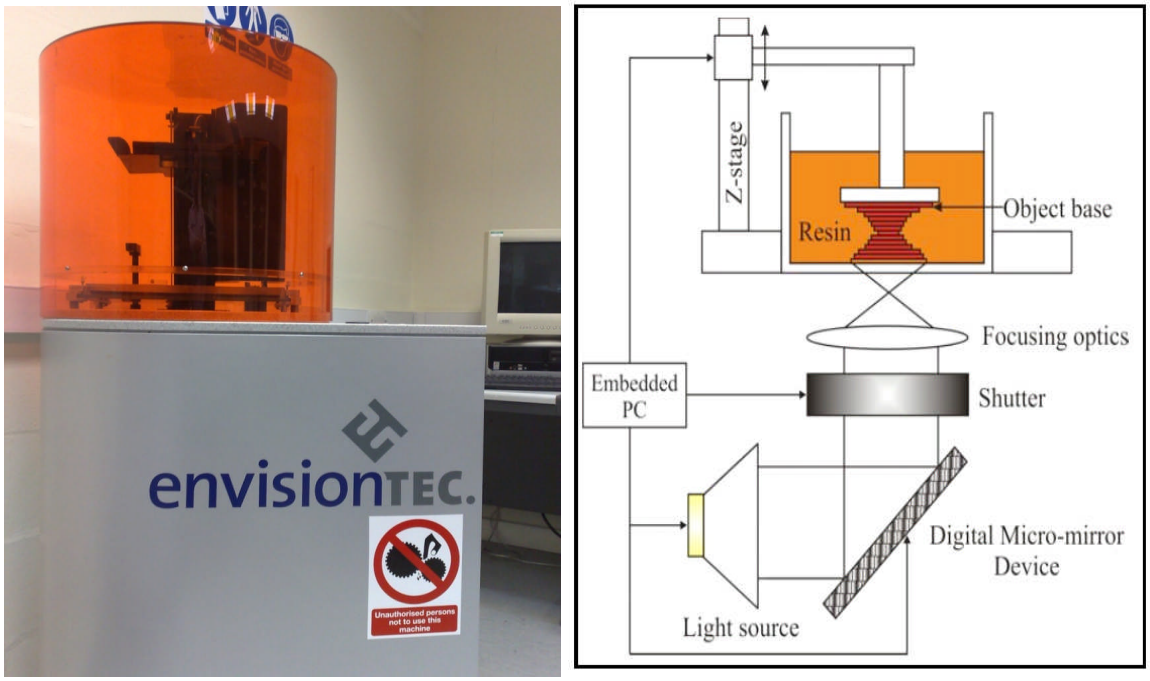

Figure 4.3: The Perfactory machine (left) and the principle of the machine (right)

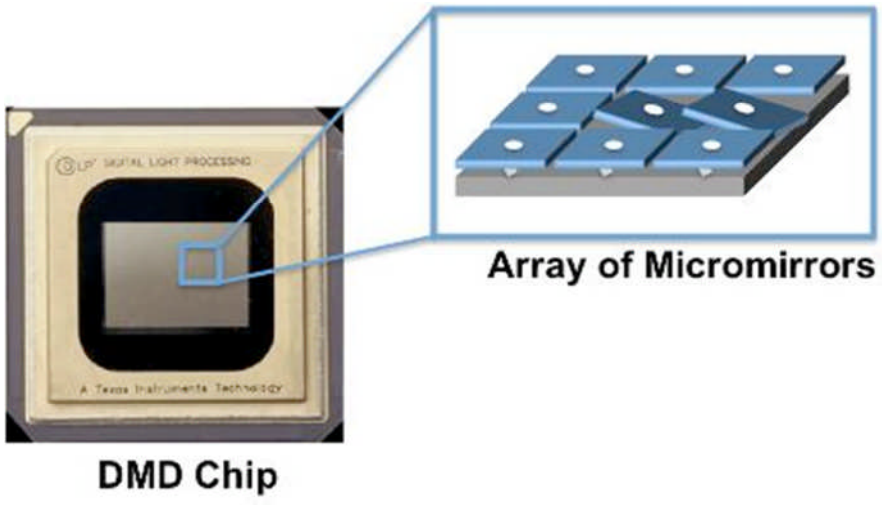

Figure 4.4: The Digital micro-mirror device (DMD) chip

The MSL specimen for tensile test was fabricated using a customized German Envisiontec Perfactory SXGA+ (Figure 4.3 left). The Perfactory system included six parts: A blue LED light source (ENFIS (UK) Uno AIR LE) to cure R11 resin (maximum wavelength of 465 nm), a digital micro-mirror device (DMD chip from Texas Instruments) to form mask, focus optics to adjust the building size, a shutter to turn on/off the UV exposure, a transparent glass tray to contain the resin and a Z-directional stage. The key component of the Perfactory system was the DMD chip (Figure 4.4), consisting of 1400x1050 micro-mirrors arranged in a rectangular array on the surface which correspond to the pixel in the image cross-section. It was independently controlled by the embedded PC, functioned as a mask generator. Figure 4.3 (right) illustrates the principle of Perfactory machine used. For each layer, the DMD device moderated the light by flipping the mirrors (±10-12°) towards or away from light source to form the mask. The light generated from a blue LED light passed through a DMD chip to selective cure the rein. A thin layer of R11 resin was thereby cured and sandwiched between a Z-axis mobile platform and the bottom of the transparent tray. This process was repeated for next curing layer and so on to finish the whole fabrication.

The typical building size of envelope for small specimens was 27.96 × 20.98 mm, with 1400 × 1050 corresponding pixels. This planar resolution (19.97 × 19.98 μm) could be further improved by turning on ERM (Enhanced Resolution Module) and using half-pixel shifting method (Covington 2006). This ERM doubled the precision using ½ pixel shifting methods (illustrated in Figure 4.5). In this method, each curing layer was cured twice through two masks with one mask ½ pixel shifting to another, thus small features of ½ pixel size on the edge could be formed. However, this method was not applicable to

the fabrication of tensile test beams since the edge of specimens were cured twice which would significantly decrease the uniformity of the cross section and change the resultant mechanical properties of test beams. On the other hand, the minimum thickness (the vertical resolution) was usually set to be a few tens of micrometres (in balance between high precision and sufficient mechanical strength).

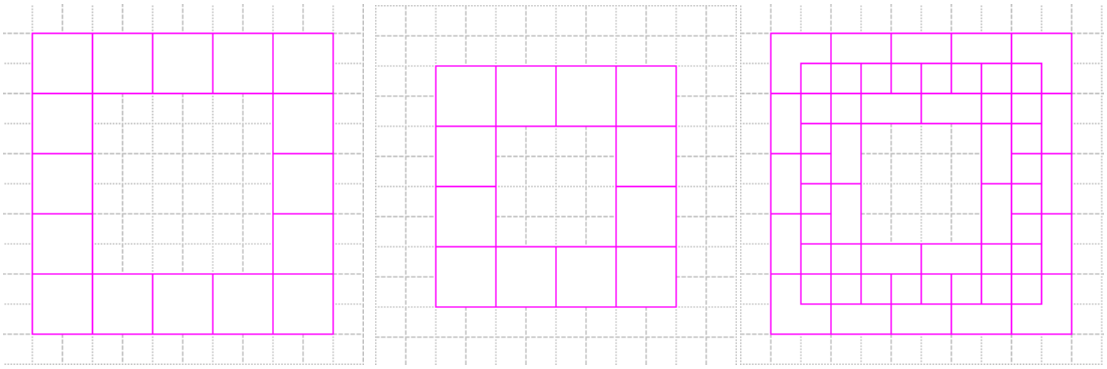

Figure 4.5: The principle of ERM system: ½ pixel shifting using ERM

The recommended parameters (e.g. exposure time and waiting time) for Perfactory machine were mostly empirically derived (Envisiontec 2003). The standard radiation exposure time was 3.5 s for normal curing layer and the first few layers deposited on the platform, defined as the burn-in range, were over-exposed to UV radiation (recommend value of 9.0 s) to ensure a sufficiently robust mechanical behaviour for the finished device to be safely removed from the platform. After finishing a layer, the system waited for a few seconds (normally 30 s) to let the cured layer finish curing and then proceeded

for the next curing layer. The whole build speed was dependent on the UV exposure and the thickness. Normally the building time for thin specimens that were used here was approximately 40 minutes for the thin specimen cells (e.g. 1 mm) and 90 minutes for the thick specimen cells (e.g. 2 mm) under standard exposures. These important parameters could be set in Perfactory Software suit (Figure 4.6). A summary of the Perfactory machine is given in Table 4.2.

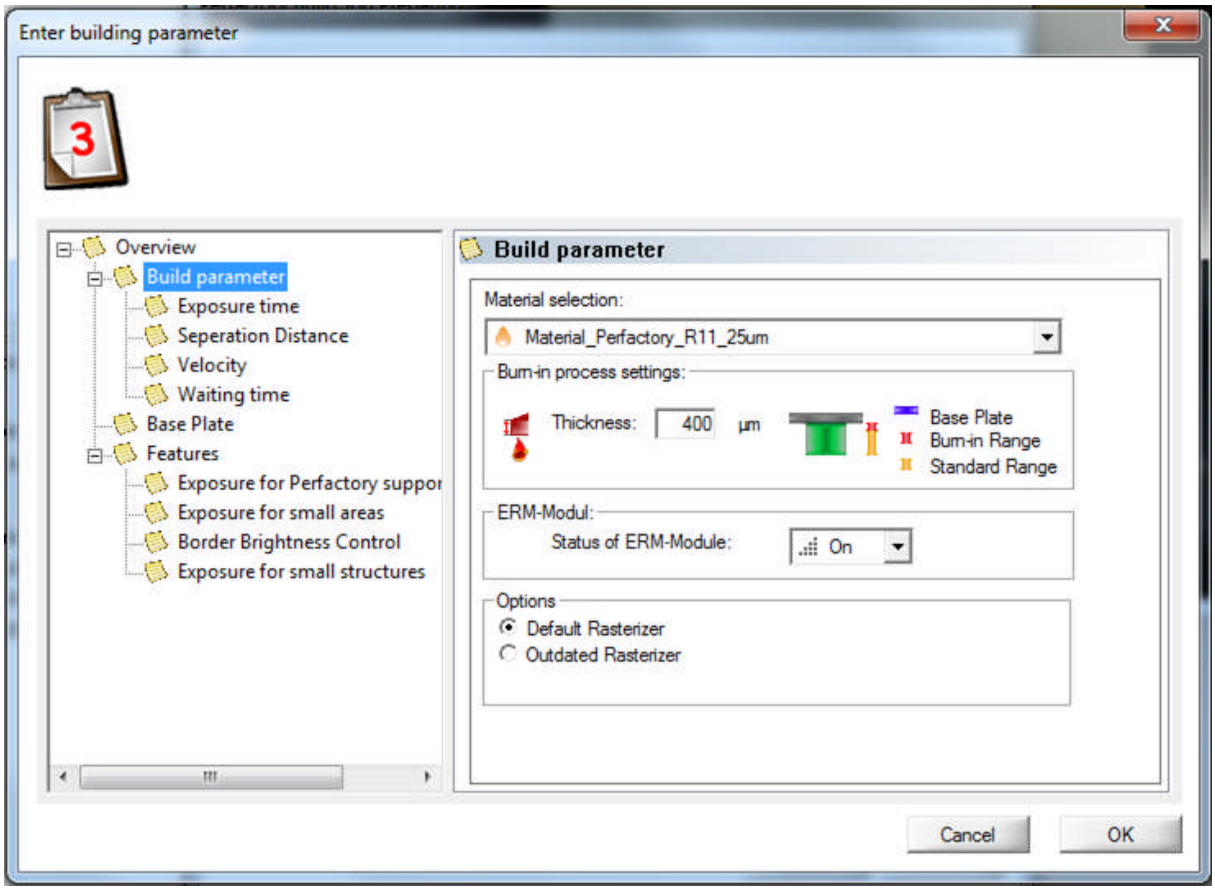

Figure 4.6: The building parameters in the Perfactory machine

Table 4.2: The summary information of Perfactory MSL fabrication system

Based Machine	Envision Tec Perfactory SXGA+
UV source	ENFIS (UK) Uno AIR LE, Spectral output maximum at 465 nm
DMD chips	Texas instruments MP1800
Building size	27.96 x 20.98 (mm)
Building resolution (per pixel)	19.97 x19.98 (µm)
Layer thickness	25-100 (µm)
Recommended exposure time	3.5 (s)
Burn-in range	≥100 µm
Burn-in range exposure time	9.5 (s)

4.4 The procedures of the fabrication

A typical flow chart of fabrication steps for the Perfactory MSL system is given in Figure 4.7. It was usually categorized into three stages. The first stage included building the CAD model, setting the fabrication parameters and generating the full set of digital pattern masks before curing starts. The curing stage for thin MSL specimen usually divided into normal curing layers and the over-exposed curing of burn-in range layers. After finishing curing of the whole set pattern layers, the specimen was removed from the platform (in a soft 'green body' state), passed through a chemical rinse and post-cured for a high cure-ratio of the final parts.

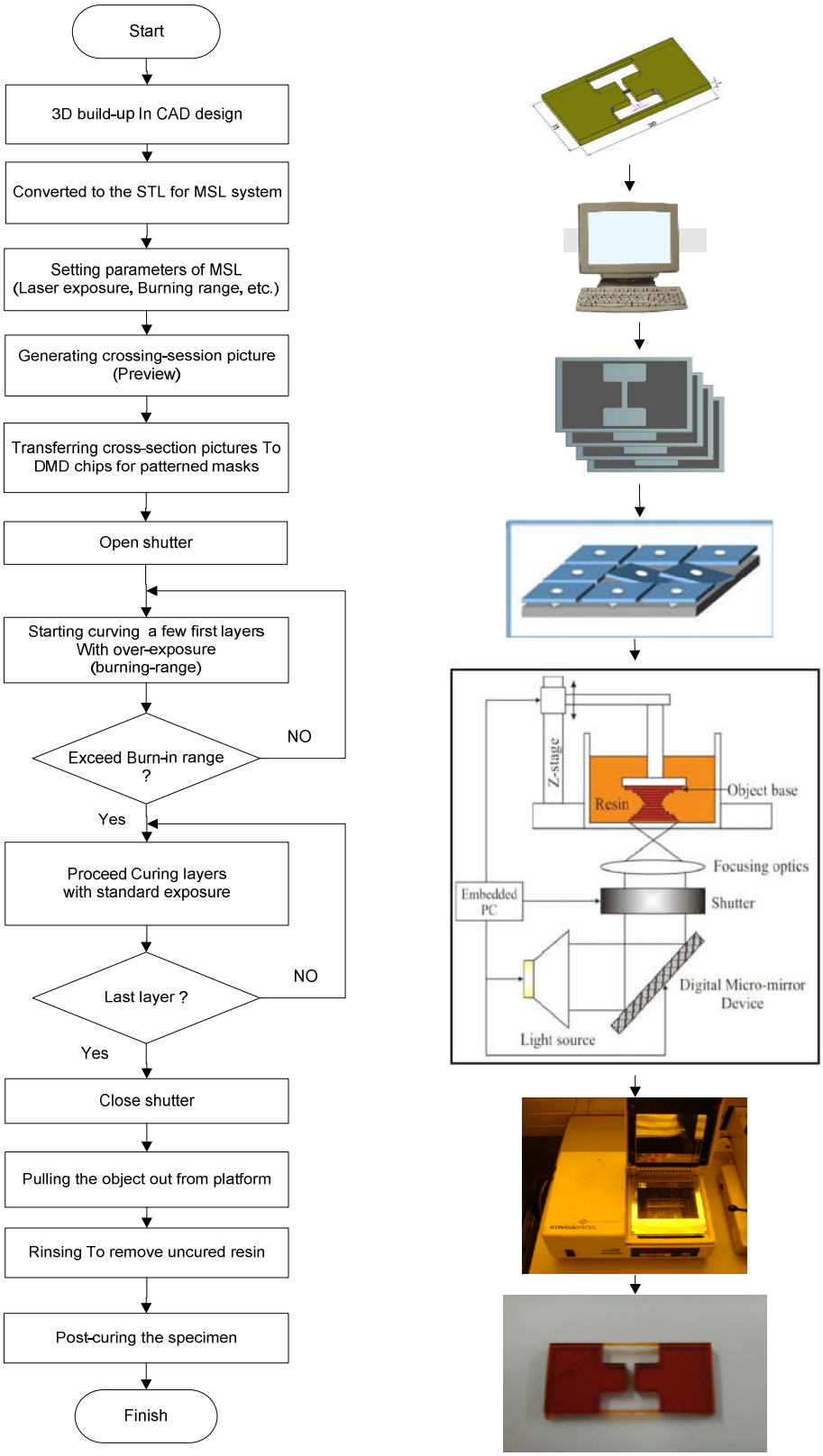

Figure 4.7: Flowchart of the MSL fabrication procedures

The fabrication procedure of MSL specimens began with building CAD models of specimens in CAD softwares, such as Solidworks 2011. The CAD model was then converted to the commonly used *stl* file format file in the Perfactory system. Crucial fabrication parameters, such as standard UV exposure, burn-in range *etc.*, were also set in the Perfactory® Software Suite before the fabrication process begins. There had not been much study on how these parameters affect the properties of final parts yet; and most of the standard or recommended parameters were empirically derived from laboratory works (Envisiontec 2003). The standard radiation exposure for curing layers and burn-in range were 3.5 s and 9.5 s respectively. Specimens with different radiation exposure were also fabricated and tested in the later experiments here. The *Z*-voxel thickness, namely the thickness of every layer was set to be 25 μm in order to reach high fabrication resolution in *Z*-direction with relatively high strength to resist curl distortion and the burn-in range was set to be 200 μm (8 layers) to ensure a success specimen removal without interference to the properties of test beam. After setting all the fabrication parameters, the Perfactory system generated a set of sliced cross-section images that would be passed to the DMD chips to form corresponding masks pixel-by-pixel.

The curing process was remotely started and monitored in the imbedded PC of Perfactory system. The building stage was first moved down towards the resin tray to give a 25 μm gap between them to start curing first layer. The system then controlled the DMD chips to form the first projection mask by flipping the mirrors toward or away from the light source. The resin was thus selectively cured by opening the shutter to allow the light illuminating through the DMD chips to the layer of resin trapped between the stage and resin tray. After curing a layer, the system stopped for a few seconds (recommended

value of 30 s) to let the photo-polymerised resins further cured and adhesive onto the build-stage. The platform was then lifted after finishing curing the first layer and lowered back to leave the same 25 μm space between the top of existing cured layer and the resin tray to proceed curing the next layer below. The first few layers within the burn-in range was curing with extra UV exposure of 9.5 s, resulting in a harder mechanical properties to prevent specimens from removal damage when the specimen is pulled away from the platform. After curving 8 layers within burn-in range, the system proceeded with a standard UV exposure of 3.5 s, the building process was then completed by repeating this curing process for all masks generated from the CAD model.

After curing all layers of the specimen, the green-state body was pulled away from the platform using a sharp knife. The specimen was then rinsed with isopropanol to remove any uncured resin. It was a quick wash for only a few seconds since the tensile specimens were quite thin and the test beam could be easily deteriorated in the isopropanol solution. After rinse, the specimens were post-cured in an Otoflash G171 UV flash box (Figure 4.8) for a few seconds (20 seconds for 1 mm specimen and 1 minute for 2 mm specimen). The flash box had two flash bulbs at the bottoms, which generated intense light radiation (range 300 nm to 700 nm) at a frequency of 10 flashes per second (Otoflash manual 2010). After post-cured, the overall cure-ratio was largely increased and the tensile specimens became more rigid. The specimens were then stored at a dark cupboard for two days. All these fabrication processes were carried out in a filtered amber light laboratory to prevent the pre-polymerisation of photo-sensitive materials (Figure 4.9).

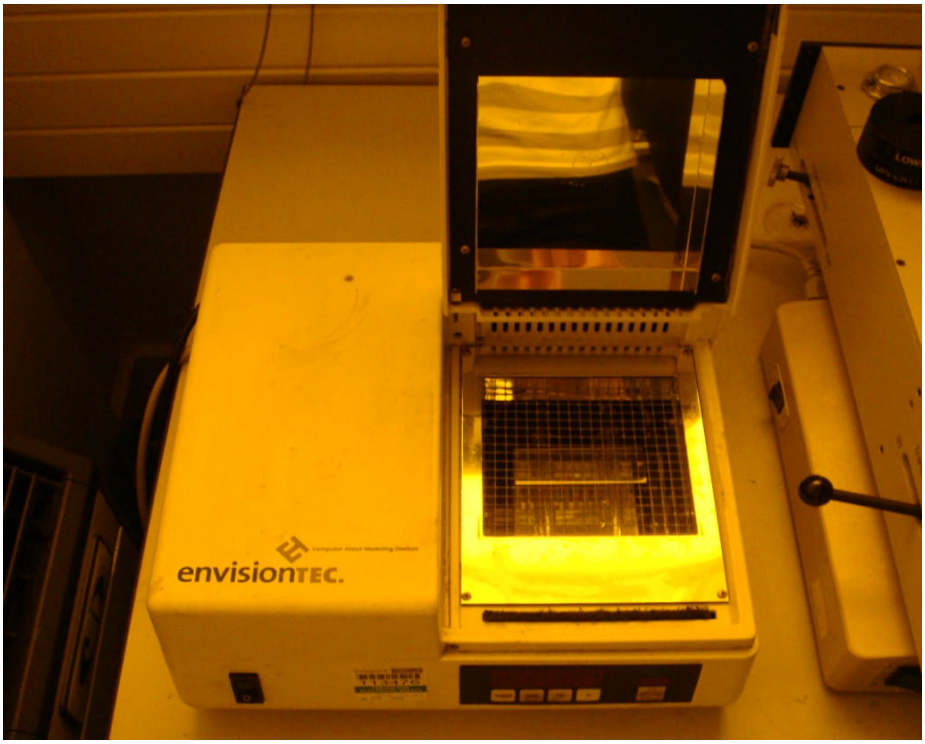

Figure 4.8: The Otoflash post-cured flash box for post-curing processes

Figure 4.9: The laboratory with filtered amber light and safe chemical facility

4.5 The Resultant specimens

4.5.1 The shrinkage and curl distortion

The significant amount of specimen shrinkage and curl distortion encountered in both polymerisation and post-curing stages were major error sources in the SL process. They were commonly the main reasons accounting for the discrepancies between the designed geometry and the dimension of final products. Particularly, shrinkage and curl distortion in SL systems became a more serious issue for fabricating small scale MSL specimens as these specimens were more fragile and small.

Shrinkage and curl distortion of MSL parts were mainly related to the properties of resin itself and to building parameters such as UV power, radiation exposure, scanning speed and burn-in range. Several researchers had endeavoured to investigate the factors affecting the shrinkage and curl distortion in order to improve the accuracy of SL process. Jacobs (1992) firstly conducted a systematic investigation the process accuracy and interpreted the general relationship of SL process parameters and the final SL parts. Later several studies had been carried out to study the influence of process factors on stereolithography part deformation. Narahara (1999) performed an experimental analysis about the effect of fabrication parameters on the linear shrinkage of the cured resin while Wang (1996) performed an investigation on the relationship between the fabrication factors and post-curing shrinkage. Huang (2003) and Bugeda (1995) had studied the curl distortion in SL processes by means of Finite Element Methods (FEM). Such research was devoted to discovering the crucial factors for process control and predicting how they affect the accuracy of products in terms of shrinkage and distortion. However, there were still insufficient studies on SL processes, particularly MSL processes, to establish

any sophisticated model of relationship between process parameters and part shrinkage and distortion.

The basic theory on the shrinkage of SL green part is illustrated in Figure 4.10. The shrinkage and the photopolymerisation occurred simultaneously in the SL process. When the absorption of radiation energy exceeded a critical quantity, shrink started with the polymerisation actions, and the resin was supplied from the surroundings. The volume of resin increased after polymerisation as it transited to a stable basic state and expanded due to the polymerisation heat. The resin was finally cooled by heat diffusion resulting in a thermal shrink. The green-state specimen also suffered a heating expansion and cooling shrink in the thermal post-curing process.

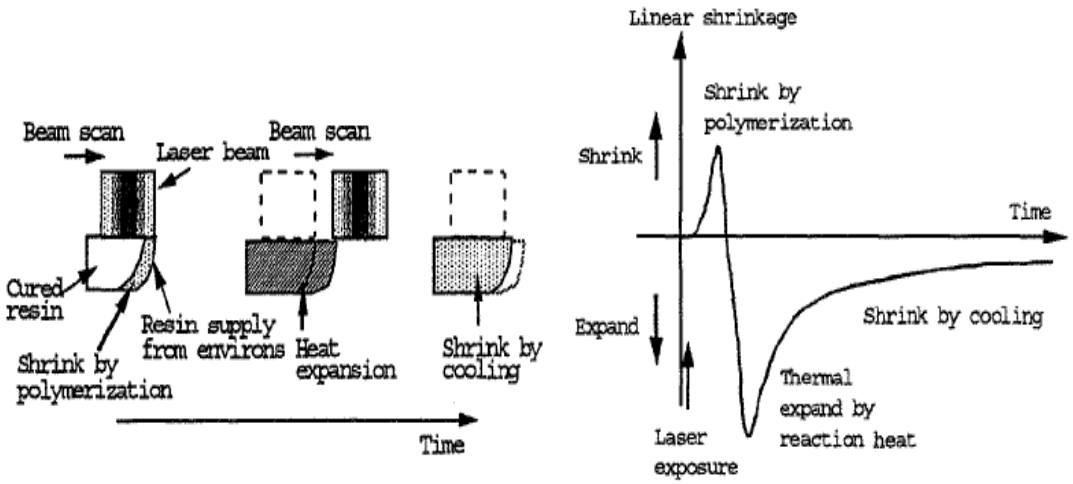

Figure 4.10: The shrinkage of a single layer in SL process, from Narahara (1999)

The shrinkage on MSL specimen had significant impact on the fabrication performance since the small scale MSL specimens require high dimension accuracy. Thus, the

geometry of the resultant specimens was usually smaller than the defined size dimension in the Envisiontec Perfactory system. This significant shrinkage of MSL parts urged a further measurement on the dimension measurement on the final specimens. These shrinkages could be calculated after the measurement of specimen dimension; they are discussed in Chapter 5.

On the other hand, curl distortion was another common problem in SL processes introduced by non-uniform internal stress during the process. Jacobs (1992) and Bugeda (1995) showed the curl distortion issues manifested in a set of sequence steps of building a cantilever as illustrated in Figure 4.11. The first layer of a cantilever was nearly free of distortion stress and retains a high flatness. The second layer was then bonded to the layer below it after curing. Thus the shrinkage occurring at the upper layer later introduced a bending moment to the layer below, causing it to curl upwards. Thin high-aspect-ratio specimens with thin curing layer thickness had relatively low flexure strength and curled severely under the bending moment. However, during curing the upper layers, the layer beneath them underwent re-exposure and additional shrinkage due to the UV penetration, resulting in a less curvature. Hence specimens fabricated with higher exposures usually were less curved.

Besides, the curl behaviour of cantilever beam had warped out of the next layer liquid surface and resulted in a non-uniform curving thickness for the next curing layer. This self-correcting effect occurred and makes the successive few layers of cantilever less curved. Hence cantilevers with thicker sections were better able to resist the curl distortion.

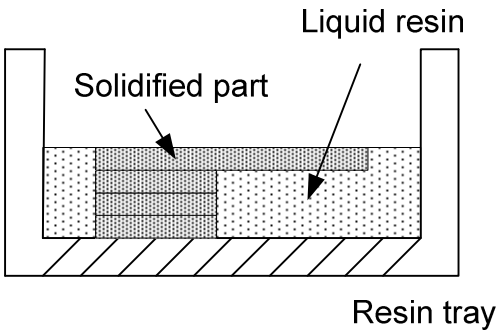

(1) First layer of cantilever

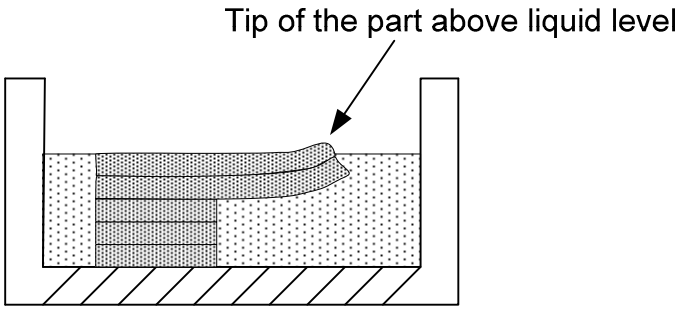

(2) Second layer of cantilever

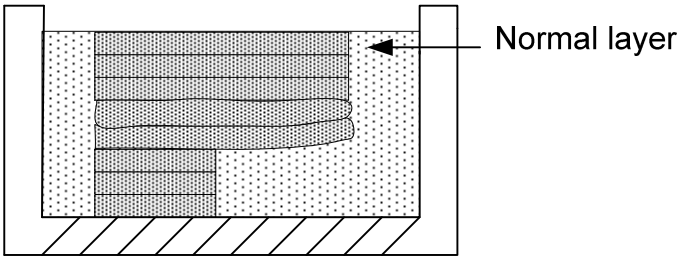

(3) After a few layers

Figure 4.11: Schematic cross section of part building leading to curl distortion (derived after Jacobs 1992)

The curl distortion was more prominent in small scale high-aspect-ratio SL parts and thus became the major disadvantage of MSL techniques in building the tensile specimens. The MSL specimens were far thinner than the SL parts with high aspect ratio and the thickness of the curing layer in MSL process was only tens of micrometres. Thus they were more susceptible to the UV re-penetration and lateral bending moment introduced by shrinkage, resulting in a more significant curl distortion phenomenon. Moreover, the acrylate resin R11 used in the study tended to introduce a much higher curl distortion and lower flatness to the final specimen than the epoxy resin (Jacobs 1996). For fabricating small MEMS specimens where accuracy was critical, the curl distortion in MSL parts not only further limited the fabrication resolution, but also brought significant hurdles to mechanical characterisation test. A CAD drawing of curved thin MSL specimen based on rough measurement is given in Figure 4.12. The curved specimens were more fragile and difficult to process during the specimen transferring and mounting. They also put significant uncertainty into the final result of tensile test as it was hard to precisely predict the curl distortion effect on the result of tensile tests.

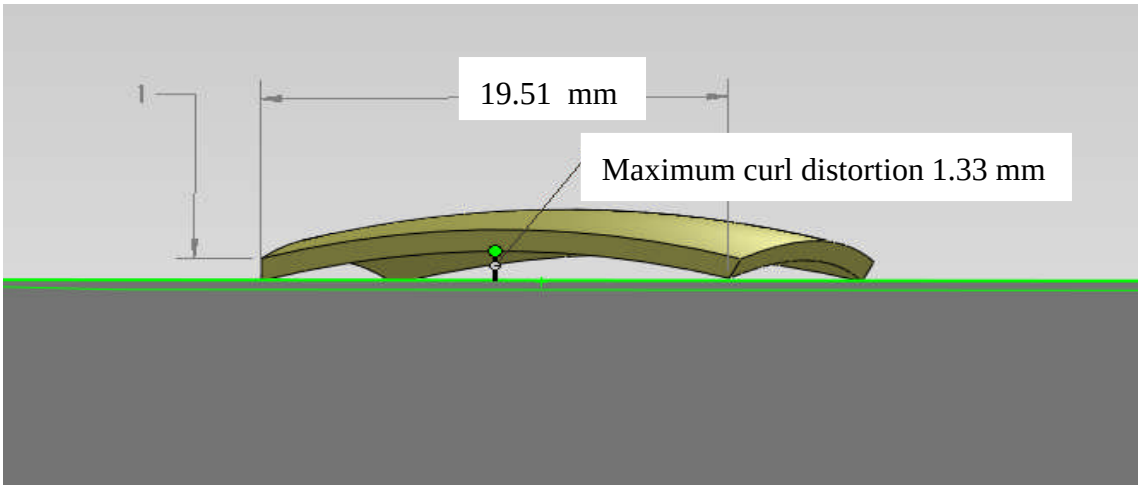

Figure 4.12: The curved behaviour on a MSL specimen

In summary, shrinkage and distortion were critical issues encountered in fabricating small scale high-aspect-ratio specimens. The shrinkage greatly compromised the manufacturing resolution of MSL system while the curl distortion posed an additional challenge on to handling small scale tensile specimens. Detailed results of specimen shrinkage on specimens with different fabrication parameters would be given in Chapter 6 after the measurement of resulting specimen dimensions and some preliminary results of curl distortion were described in the next section.

4.5.2 The resultant specimens fabricated with different parameters

In this study, tensile specimens (see section 5.3 for detail) under different fabrication conditions, particularly under different UV exposures, were fabricated for later characterisation and study of the effect of fabrication parameters on the mechanical properties of final specimens. The standard UV exposure time recommended by the Envisiontec was 3.5 s and 9.0 s for curing layers and burn-in range layers respectively. When using UV exposure time less than 3.0 s, specimens tended to blur and were easily dissolved in the isopropanol cleaning wash due to the insufficient curing ratio of R11 resin. The burn-in range exposure time also should exceed the threshold of 6.0 s otherwise the specimens were hard to remove from the platform without getting stressed or damaged.

The curl distortion issue was of most concern in building small scale high-aspect-ratio tensile specimens. Since the high-aspect-ratio MSL tensile specimens were composed of relatively few layers, they were much more susceptible to the curl distortion than SL

parts. As mentioned in section 4.5.1, specimens with thicker cross-sections were better able to resist the distortion force due to the self-correcting effects. It was observed that specimen cells with thickness less than 1 mm were observed with severe curl distortion while specimen cells with thickness of 2 mm exhibited a higher flatness for tensile test (Figure 4.13).

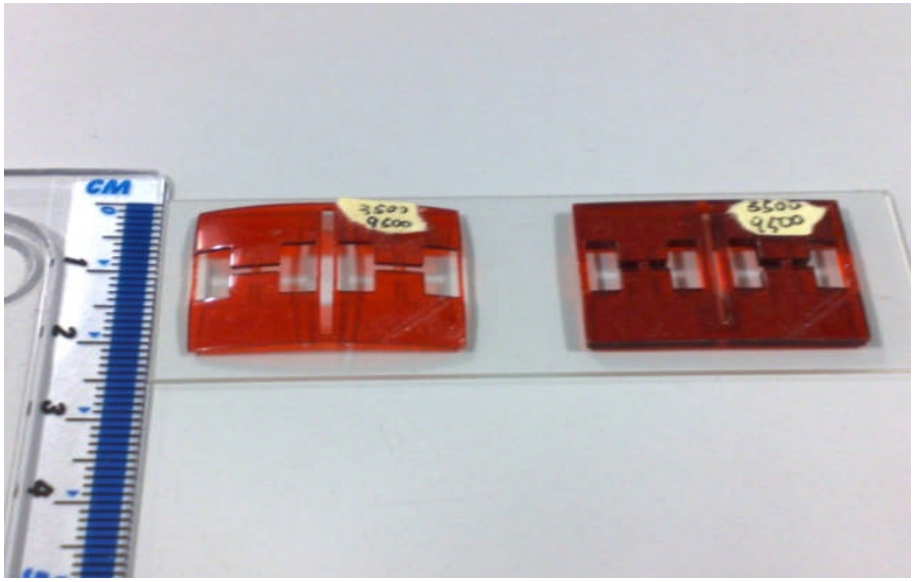

Figure 4.13: Specimens fabricated using standard UV exposure (left: 1 mm thickness; right: 2 mm thickness)

The burn-in range layers were often over-exposed to ensure a safe removal from the platform. Usually this did not cause significant impact on the overall properties of MSL parts. However, these layers became more prominent during the fabrication process of high-aspect-ratio specimens. The different UV exposure time between standard curing layers and burn-in range layers had resulted in a significant non-uniform internal stress of MSL parts and eventually severe curl distortion (Figure 4.14). The (thin) 1 mm specimen under UV exposure for both curing layers of standard 3.5 s and burn-in range layers of

9.5 s showed a high flatness. The specimen retained a high flatness when the overall UV exposure is reduced to 6.0 s (Figure 4.15). Thus the difference of UV exposure between the burn-in range layers and curing layers was another major factor contributing to the curved behaviour of the thin MSL specimens.

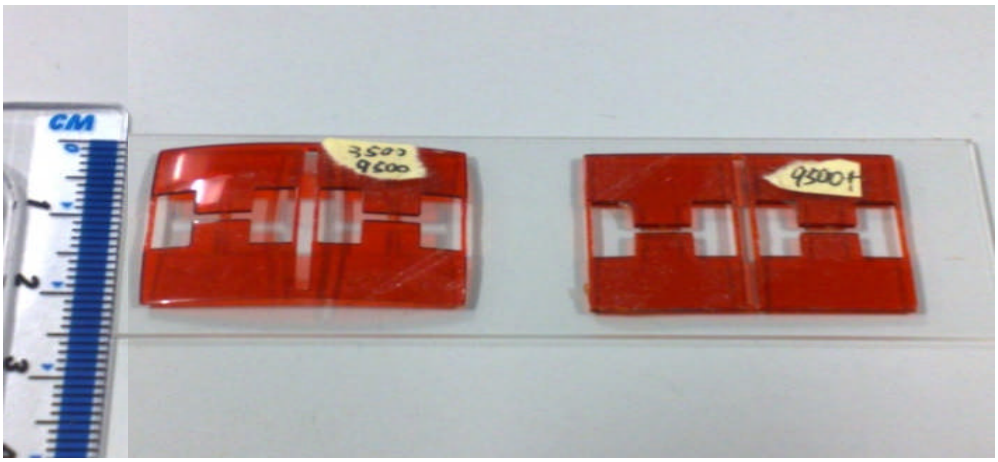

Figure 4.14: Specimens (1 mm thickness) under standard and overall high exposure UV radiation (left: standard exposure 3.5 and 9.5 s; right: overall 9.5 s curing)

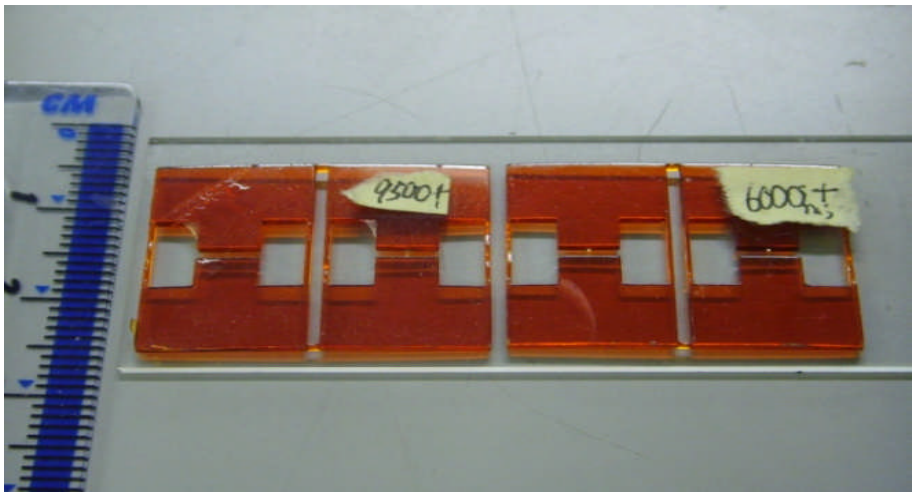

Figure 4.15: Specimens (1 mm thickness) with uniform overall UV exposure (left: 9.5 s overall curing; right: 6.0 s overall curing)

From Figure 4.16, specimens under 3.0 s UV exposure displayed much less curl than at the standard 3.5 s exposure. Although the specimen under 3.0 s UV exposure had greater difference with the burn-in range layers, the lower light penetration effect made it less curled than the standard 3.5 s specimen. Moreover, the specimen under a 3.0 s UV exposure had relatively low curing-ratio, and the material strength was also relatively low and was easy to deform under the shrinkage stress.

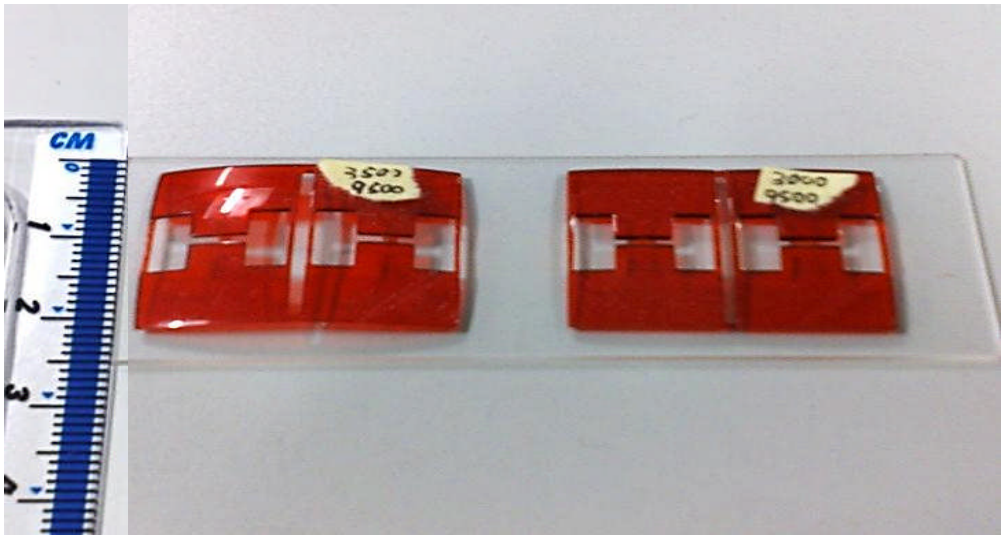

Figure 4.16: Specimens (1 mm thickness) with 3.5 and 3.0 s UV exposure (left: 3.5 and 9.5 s curing; right: 3.0 and 9.5 s curing)

4.6 Conclusion

In this study, a projection-based Envision Tec Perfactory ® SXGA+ stereolithography system using Envisiontec R11 acrylate-based resin had been employed to fabricate the MSL tensile specimens. This system had a resolution of 20 µm in X-Y direction and 25

μm in the Z-direction. This machine also had an ability of producing specimens rapidly and cheaply with different specifications in various materials. However, this machine had limited performance in producing small scale MSL tensile specimens in terms of dimension accuracy and curl distortion. The preliminary results of this fabrication test indicated that the small value of thickness and the difference of UV exposure between curing layers and burn-in range layers were the main factors of curl distortion in thin tensile specimens. Specimens with different dimension and UV exposure were fabricated for later tensile test.

References

Bugeda, G., Cervera, M., Lombera, G. and Onate, E. (1995). "Numerical analysis of stereolithography processes using the finite element method," *Rapid prototyping journal*, **1**(2), 13-23.

Covington, J.A. (2006). "Rapid Manufacturing for Micro-engineering: The Development of a Portable Electronic Nose," *TCT rapid manufacturing Conference.*

Envisiontec (2003). Envisiontec Perfactory manual, Edition 2003, Envisiontec GmbH, Gladbeck, Germany.

Envisiontec (2007). Envisiontec Perfactory R5 – R11 Material Documentation, Edition 2007, Envisiontec GmbH, Gladbeck, Germany.

Huang, Y-M. and Jiang C-P. (2003). "Curl distortion analysis during photopolymerisation of stereolithography using dynamic finite element method," *Int. J. Adv. Manuf. Technol*, **21**,586-595.

Jacobs, P.F. (1992). *Rapid prototyping and manufacturing: Fundamentals of stereolithography*, 1st edition, Society of Manufacturing Engineering, Dearborn, MI. ISBN:0872634256.

Jacobs, P.F. (1996). *Stereolithography and other RP&M Technologies*, Society of Manufacturing Engineering, Dearborn, MI. ISBN: 0872634671.

King, P. and Covington, J.A. (2009). "A novel monolithic microactuator fabricated by 3D rapid direct manufacture," *Proceedings of Eurosensors XXIII conference, Procedia chemistry*, **1**, 1163-1166.

Leigh, S.J. and Purssell, C.P (2010). "Snapshots of Science 2010 Picture Competition 2010 – Winner," Birmingham, UK.

Leigh, S.J., Purssell, C.P., Hutchins, D.A., Covington, J.A. and Billson, D.R. (2011). "A miniature flow sensor fabricated by micro-stereolithography employing a magnetite/acrylic nanocomposite resin," *Sensors and Actuators A: Physical*, **168**(1), 66-71.

Marutani, Y. and Nakai, T. (1989). *Laser research*, **17**, 410-480.

Narahara, H., Tanaka, F., Kishnami, T., Igarash, S. and Saito, K. (1999). "Reaction heat effect on initial linear shrinkage of stereolithography resins," *Rapid Prototyping Journal*, **5**(3), 120-128.

Otoflash G171 instruction manual, (2010). NK-Optik GmbH, Germany.

Wang, W.L., Cheah, C.M., Fuh, J.Y.H. and Lu, L. (1996). "Influence of process parameters on stereolithography part shrinkage," *Materials & design.* **17**(4), 205-213.

Chapter 5: The tensile set up for MSL materials

5.1 Introduction

The rising interest in Micro-stereolithography (MSL) and associated materials has further expanded to various industrial sectors recently. This makes even more urgent the need for the knowledge of mechanical properties of MSL materials and so spurs the development of MEMS-based characterisation tests. Important mechanical properties, such as Young's modulus, play a vital role in the function of many MSL parts and solid data on them is essential to exploring full potential of the MSL technology. But it is genuinely a challenging task to conduct a precise mechanical characterisation on an MSL specimen due to the small size. Among the few commonly developed characterisation methods for MSL materials, the tensile approach distinguishes itself with simple test geometry and direct data conversion, which makes it less affected by the complexity inevitably introduced by miniature specimens. It is the preferred choice for this study.

The primary aim of this phase of the research was to build an effective test-rig for measuring the mechanical properties of small samples made by MSL techniques. The initial specimens were fabricated on an Envisiontec Perfactory SXGA+ using a commercial acrylate-based R11 resin formulation. It was important that no feature unique to this machine was required for specimen fabrication and the R11 resin used was generally a good all-round MSL resin. The typical tensile strength of R11 resin was about 50~60 MPa with elongation of 13 %, hence the maximum strain was safely set to be 5%. Preliminary results from Envisiontec datasheet also suggested that the Young's modulus of R11 was around 1 GPa (Envisiontec 2007). Meanwhile a practical compromise between preparing small specimens and not being overly vulnerable to the machine

resolution suggested the typical size of MSL specimen of 1/0.5/0.1 mm (L/W/T). The maximum specimen cross-section might be 2.0 x 0.5 mm^2 when the maximum tensile force before break was about 25 N. The typical testing area was 10 times smaller, thus the maximum force on specimen was set to be 2 N in the design for higher resolution, which would introduced about 4% strain over the specimen. A general specification of the MSL specimen and test region was therefore chosen as:

Maximum specimen size: 5/2/0.5 mm (L/W/T)

Minimum specimen size: 1/0.2/0.1 mm (L/W/T)

Maximum strain: 5%

Maximum tensile force on specimen: 2 N

Typical specimen size: 1/0.5/0.1 mm (L/W/T)

Typical strain: 2% - 5%

In this chapter, a new tensile test-rig developed for the mechanical characterisation of small specimens (particularly Micro-stereolithography materials but could also be applied to other MEMS materials) of a few hundred micrometres is presented. This approach is based on establishing a robust, easy to use method for determining the stress-strain behaviour of MSL materials but simultaneously developed special forms of both instrument and specimens. The design of a suitable complete system is iterative,

especially between specimen shape and clamping requirements, or where requiring robust clamping to a delicate (mostly sub-N) force imposition system. Reporting cannot readily reflect this process and no attempt is made to do so. Instead the four main sub-systems including specimen design, force imposition mechanism, strain measurement, and specimen mounting and alignment will be described separately in the following sections, with explicit cross-reference only included where essential. Each considers anticipated operating constraints leading to concept design and broad operating strategies, and, then, to the further analysis and the details of the design actually implemented. The calibration and the validation of test methods are also included with verification of the preliminary data against results using a commercial Deben tensile device.

5.2 The overall principle and implementation

The schematic configuration of the test-rig is presented in Figure 5.1. The tensile test system consisted of a notch hinge flexure monolithically machined from solid aluminium plate, a pair of clamping devices for specimen mounting and a pair of capacitive probe electrodes for strain measurement. In this Figure, load was applied by standard deadweight, which had the advantage of metrological simplicity and high reliability, and was excellent for calibration. However, it had several drawbacks, such as only applying distinctly quantized load, risking dynamic overload by clamping operation, *etc*. These were not fundamental since the operation would be essentially the same if the weights were replaced by, e.g., a linear voice-coil force actuator. A key point was that the tensile load was not directly applied to the sample clamps (See details in section 5.4). Instead, to

add robustness, it drove the flexure mechanism and that was attached to one end of the specimen. The principle of force gauge system is summarised in Figure 5.2.

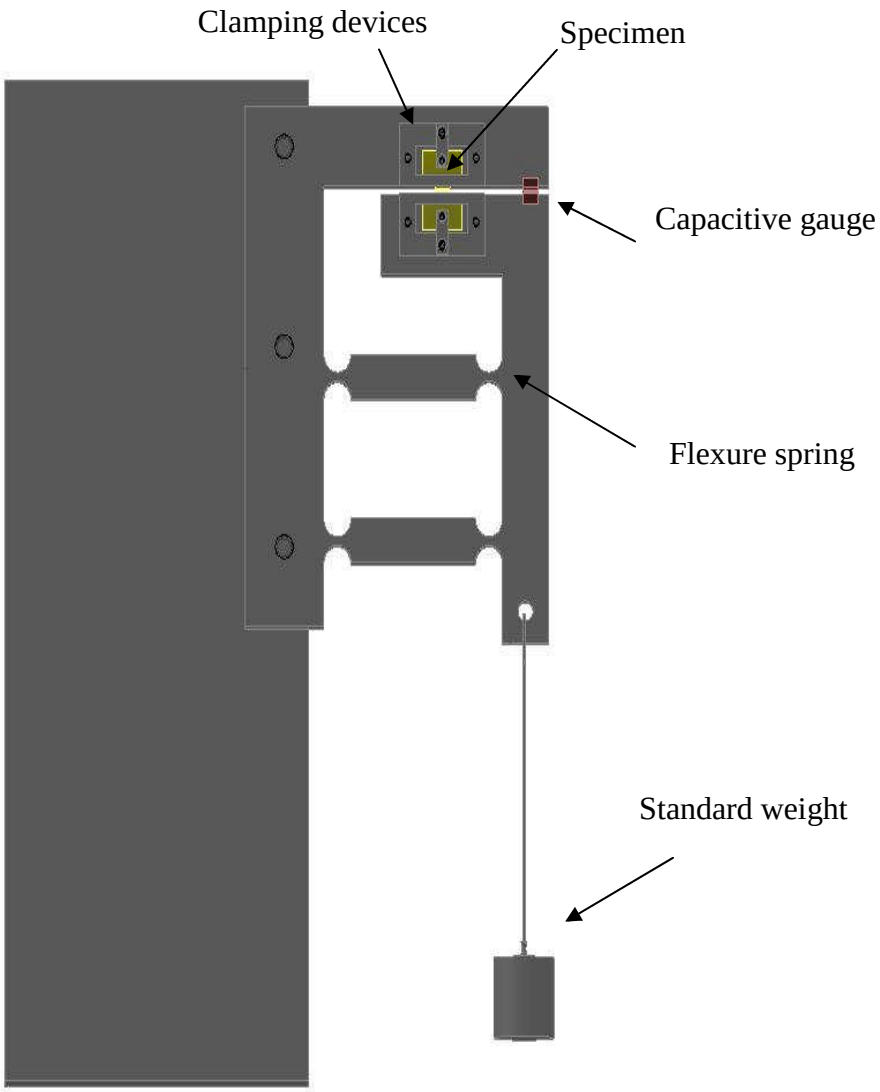

Figure 5.1: The schematic configuration of the test-system

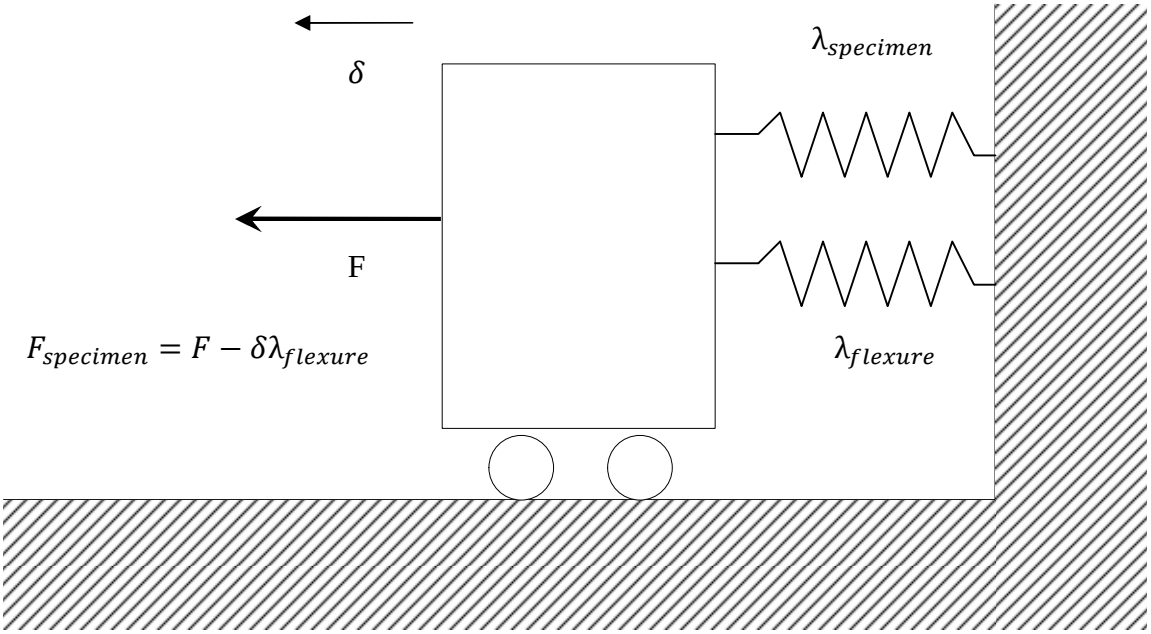

Figure 5.2: The two parallel springs concept

In principle, the specimen and flexure spring functioned as two parallel springs sharing the same displacement δ under an applied load F (Figure 5.2). Thus, the tensile force applied on the specimen, F_s, related to the force of the notch flexure, F_f, by

$$F_s = F - F_f \tag{5.1}$$

Clearly, $F_f = \lambda_f \delta$ where λ_f was the stiffness of notch flexure and can be calibrated before the test. From the basic definition of Young's modulus

$$\mathrm{E} = \frac{\sigma}{\varepsilon} = \frac{F_s l}{\delta A} \tag{5.2}$$

where l, A represented the critical length and cross-section area of the specimen respectively. Thus the Young's modulus of the specimen was given by

$$E = \left(\frac{F}{\delta} - \lambda_f\right)\frac{l}{A} \tag{5.3}$$

This parallel spring concept allowed a “force gearing” in which only a controlled fraction of the applied load was distributed across the specimens. This may be advantageous for interfacing to existing larger force systems (or even for allowing convenient dead weights) and it tended to protect against damage and other effects from unintended load transients. However, a major purpose was that the stiff flexure acted as a parallel motion guide to allow a large area for specimen clamping and eased the task of measuring very small elongations on small and delicate specimens. The robust guideway also allowed robust handling during system set-up.

An accurate strain measurement was another imperative aspect of the tensile test. The uniaxial tensile strain was defined as the ratio of specimen extension and length. Two common strategies of strain measurements have been developed for high precision strain measurement. The first strategy defined a particular gauge length by setting gauge marks to the specimen and usually employed optical or other probes to spot the strain change. A few novel applications employing this direct strain measurement methodology had been developed by various researchers. For instance, Sharpe (1997a, 1997b) had developed an elegant method using two-slit interferometry to examine the fringe pattern generated by a gold strip deposited on the specimen. This approach had the advantage in high-precision direct strain measurement that it skipped the measurement of the characteristic length of specimen. However, these approaches required high quality and consistency of specimen manufacture and a reliable approach of delicate and accurate forming of the gauge marks. Also, this approach was ideally integrated with optical microscopy techniques of specific gauge ranges; thus it was generally difficult to combine the bulk optical microscopy into the test-rigs. An alternative approach was measuring the specimen dimension and

elongation separately. This approach did not possess stringent requirements on specimen manufacture (although an adequately uniform cross-section was always implied where the stress was determined in term of stress) and could be implemented with various displacement measurement techniques which granted substantial flexibility to the system design. It was thereby more suitable for general purpose material tests rather than characterisation of specific materials at particular range. In this research, the strain measurement was the combination of measuring specimen displacement and specimen dimension.

The specimen shared the same displacement with the flexure, thus, it was convenient to measure the deflection of the flexure rather than to measure the elongation of specimen due to the stringent space constraints. Among various displacement sensors, capacitive gauges were commonly used in small distance detection. It can be conveniently integrated into the test-rig to produce sub-micrometre resolution results. Nevertheless, although the geometry of resulting MSL specimen was pre-defined in the CAD modelling, it was severely subjected to the shrinkage and the curl distortion and should be further examined (See section 5.6).

5.3 Tensile test specimen design

The most important factors in designing MSL tensile test specimens were to facilitate the metrology process while coping with the small size specimen. The specimen usually contained characteristic features of far less than 1 millimetre. This awkward size imposed a significant difficulty in both fabrication process and specimen handling. It was

genuinely challenging to accurately build small scale MEMS specimens and then to preserve their original status before the characterisation took place. Thus, the most important considerations in the specimen design were accommodating specimen fabrication limitations and providing for a reliable specimen handling implementation before the test.

The basic specimen design chosen here was an adaptation of the traditional dog-bone like tensile tester in which a closely uniform cross-section was maintained over a gauge length, while larger integral end regions of standard form and size made easier its mounting in the clamping devices of an instrument. Other approaches had been also used with micro-tensile testing (e.g. Marsh (1961) glued the specimen whisker onto the instrument jaws), but they were generally slow and required extra precautions in preventing delicate specimens from pre-stress or partially distortion.

The tensile specimens were fabricated using the Envisiontec Perfactory MSL system, as described in chapter 4, which was capable of directly converting an engineering model into real parts in tens of micrometres fabrication resolutions and gave substantial flexibility in designing the specimen geometry. However, the MSL system had intrinsic drawbacks, e.g., the limited Z-direction accuracy which defined the smallest value of high aspect-ratio specimens. The shrinkage of these MSL specimens during and after curing further limited the accuracy of resultant specimens. The curl distortion commonly found on thin specimens brought extra difficulties in handling small scale specimens since most of the traditional specimen mounting required good flatness of specimens.

Moreover, both forces during the manufacture (especially layer peeling) and during handling and clamping to the instrument cannot in practice be controlled to low enough

levels to avoid severe risk of damage to typical sizes of test beams. This was especially so if extra mass was added at the ends to allow reasonably sized clamping area. Also, the curvature behaviour of thin MSL specimen was a potential problem and was best rectified by making the larger ends of specimen relatively thick (e.g. 2 mm). Therefore, a design decision was taken to use very large clamping area. The clamping area should be at least 10 times larger than the dimension of working section. Considering that the MSL machine had a working platform of 27×21 mm^2, the actual size of specimen cell was set to be 13×20 mm^2 to allow two specimens be made simultaneously. This larger clamping area design made it easier to test different types of clamping arrangements and would probably also be easier for specimen alignment by making physical handling simpler. Given the possible need to investigate different clamping approaches, the clamping lands were further expanded into an extra section, considerably larger. This provided possible location faces for contacting pins for implementing pseudo-kinematic methods for applying tensile forces.

In order to preserve the small work-section specimen, the two bulk end structures must be linked using protection structures (bridges) throughout the fabrication process (which the thinner main specimen section cannot support the whole specimen cell adequately). By designing complete integral support structures, the specimen was sufficiently rigid and surrounds the test section on completion. It was to be mounted on the test instrument in this form, which is quite robust. Then, only when alignment and clamping were completed, these supports were carefully cut through to leave the working section supported between the clamping devices. These concepts led to the final design of tensile specimen cell as depicted in Figure 5.3.

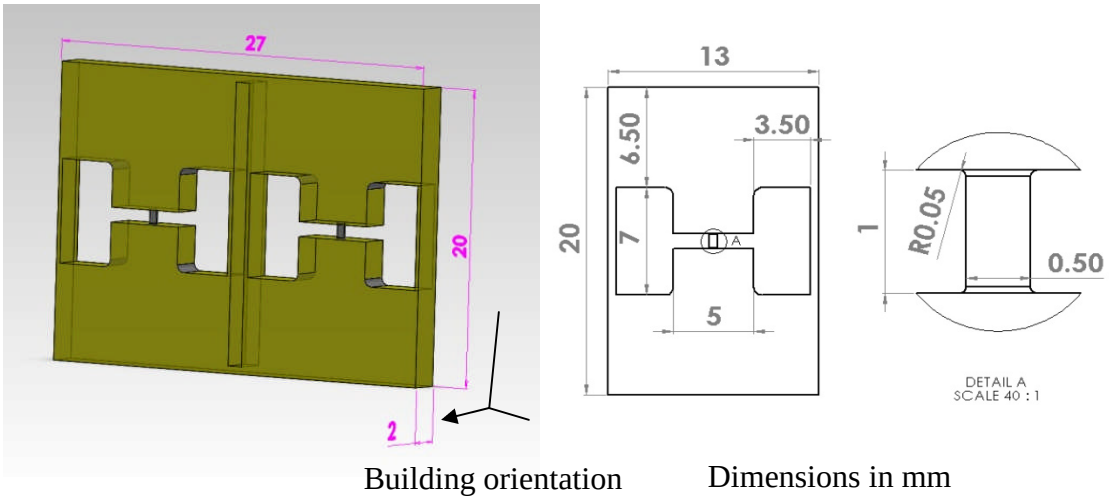

Building orientation Dimensions in mm

Figure 5.3: A typical fabrication cells with central test cross-section of 1/0.5/0.1 mm (L/W/T) (Left: building cell; Right: individual specimen cell)

The typical size of specimen cell was 27×20×2 mm^3 comprising two individual specimen cells (13×20×2 mm^2, Figure 5.3 right). The dimensions of specimen cell were fixed except for the working sections located in the central region. The test cross-section had a typical dimension of 1.0/0.5/0.1 (L/W/T) mm and was rounded near the ends to avoid sharp edges (local stress concentration). Particularly, the thickness of specimens should be the integral multiple of the minimum thickness of the curing layer, as specimens were formed in layer-by-layer accumulation from either side due to the symmetric structure design.

The specimen cell was designed to have the test-beam section in the central region with bulk parts at two sides providing space for specimen mounting and alignment in a way that leaves the test-beam stress free. Two thin bars (but thick enough to provide good support) at each side of the specimen cell were included to prevent the pulling off damage after the MSL system finished curing the specimens. These bars also played an

important role in preventing the pre-axial stress and torsion during mounting and are removed afterwards.

5.4 Force Measurement Method

The small size of MSL specimens implied small forces. That was certainly the case here where the main target material was polymer. Any extra guiding system was likely to provide a parallel path in the force loop, making the actual force applied to the specimen uncertain. Therefore, the force implementation mechanism in the characterisation of small MSL specimen needed to precisely produce small forces to deform the specimens and it should also guide the specimens to prevent lateral shear stress. A notch hinge flexure mechanism, which can be monolithically fabricated in aluminium at relatively low cost, could readily provide sufficiently large places to accommodate specimen mounting and strain measurement and produce smooth and precisely controlled displacement corresponding to the net applied force within the linear elastic region. The standard deadweight could be easily used for either calibration or applying the tensile load. Other load mechanisms, such as piezoelectric actuators, were stiff (unsuitable for delicate MSL specimens) and had undesirable temperature-sensitive behaviour and hysteresis. Thus, the flexure mechanism was chosen as both a guide to deliver the load to specimens and a robust load cell, meanwhile the deadweight was employed to applied the load since the tensile load could apply to the flexure and the specimen compliantly but could be also be conveniently replaced by an electromagnetic actuator.

As shown in Figure 5.2, the flexure functioned as a spring in parallel with the specimen to share the tensile load. Empirical test results from bulk polymeric tests suggested that the Young's modulus of polymers ranged from 0.1~10 GPa (Cheah 1997 and Chattopadhyay 2005). Given the typical dimension of a test beam was 1/0.5/0.1 (*L/W/T*) mm^3 and the maximum tensile force and strain was about 2N and 2% respectively, the maximum stiffness of the MSL beam would be: $1.0 \times 10^2\ kN\ m^{-1}$. In order to protect the specimen, the stiffness of flexure spring should be a few times larger than the stiffness of specimen to share most of the tensile load, namely a few hundred kN/m.

The stiffness of the hinge spring was calculated as below. According to Smith et al. (1988), the rotation angle of notch hinge was given as

$$\theta \approx \frac{2KRM}{EI} \tag{5.4}$$

where *E, b, L, t,* and *R* were the Young's modulus (Aluminium), the width and the length of spring, and the minimum thickness and the radius of hinge. And K was the correction factor for the notch hinge and could be empirically determined by mean of finite element method (Smith 1988) for $t < R < 5t$ as

$$K = 0.565 \times \frac{t}{R} + 0.166 \tag{5.5}$$

I was the second moment of area of the rectangular section ($b \times t$) at the thinnest part of the notch defined as $I = \frac{bt^3}{12}$. The tensile force was ideally applied in the central line of the platform, otherwise, the tension and compression stresses would build up in the notches to balance the moments. Thus the moment at each hinge was:

$$M = FL/4$$

For small angles, the rotational angle of a notch could be treated equalled to the ratio of platform displacement δ and the length of flexure leg: $\theta \approx \sin\theta = \delta/L$. Thus the stiffness of the flexure spring was given by

$$\lambda_{\text{flexure}} = \frac{F}{\delta} \approx \frac{F}{L\theta} = \frac{Ebt^3}{6KRL^2} \tag{5.6}$$

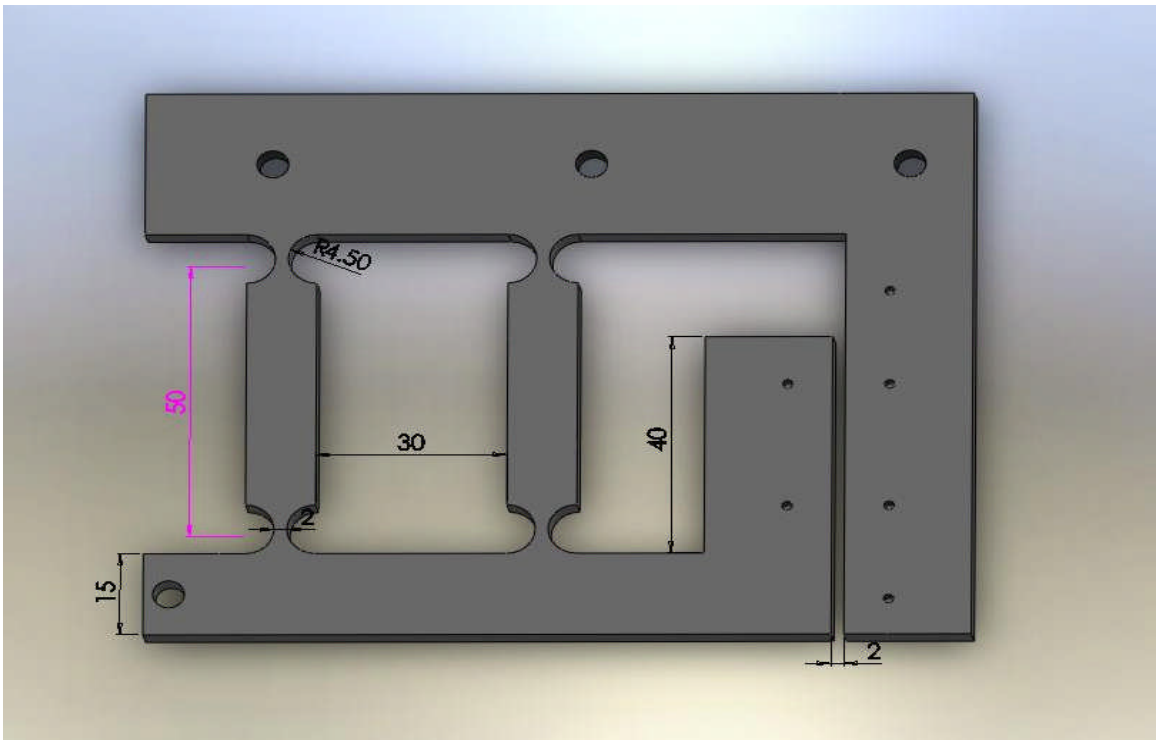

Figure 5.4: The CAD drawing of the notch flexure spring

Thus, the resulting notch hinge flexure was designed as below in Figure 5.4, where E= 7.0×10^{10} Pa, b= 1.0×10^{-2} m, L= 5.0×10^{-2} m, t= 2.0×10^{-3} m, and R= 4.5×10^{-3} m respectively in this case. Substituting these values to equation 5.6, this notch hinge flexure was designed to have a stiffness of 200 kN/m.

The flexure spring also provided both reference base and linear guide for the specimen. The deviation regarding to its parasitic motions and Abbe offset were thus calculated here. A basic form of notch rotation was illustrated in the Figure 5.5 where the lateral parasitic motions of flexure spring could be given as

$$d = L(1 - cos\,\theta) \tag{5.7}$$

Since for small angles, $\theta \approx \delta/L$,

$$d = L(1 - cos\,\theta) = 2\,sin^2\frac{\theta}{2}L \approx \frac{2}{L}\left(\frac{\delta}{2L}\right)^2 = \frac{\delta^2}{2L} \tag{5.8}$$

As the typical maximum uniaxial elongations of specimens were about 50 μm, and L equals to 5.0×10^{-2} m, only 25 nanometres of lateral parasitic motion could occur in the test (nearly 0.05% of the displacement in driving direction). Hence, the shear stress due to the lateral parasitic motions was treated as negligible in the later experiments.

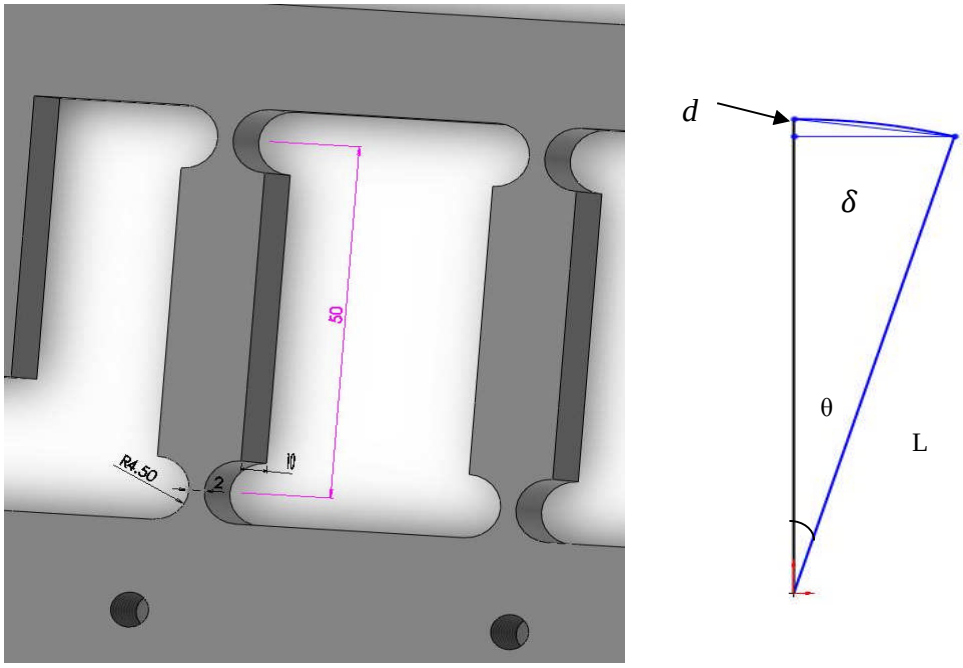

Figure 5.5: The geometry of the notch hinge

According to the Abbe principle, the axis of the capacitive probe should be colinear with the specimen extension axis. In the practical design, as shown in Figure 5.1, the measurement of stage motion was conducted approximately 30 mm away from the specimen loading axis in order to keep a clear zone for specimen mounting. Thus a practical compromise led to an Abbe offset of about 30 mm. An Abbe error was then introduced if the platform was inclined by an angle α, amplified with the perpendicular distance *a* between the two axes (Abbe offset). Therefore,

$$\text{Abbe error} = a\sin\alpha \tag{5.9}$$

A ligament leaf spring mechanism was much more susceptible to lateral stress than a notch hinge subjected to the same stress. It could be considered as the much worse scenario in terms of Abbe error (usually at least 10 times worse). For simplicity, a ligament leaf spring with same cross section of the thinnest part of notch (*b, t*), was analysed rather than the complicated notch hinge flexure. As shown in the Figure 5.6, the Abbe error occurs due to rotational angle α brought by the extension and compression of the spring legs.

The moment at each end of spring leaf was simply $FL/4$, therefore, the tensile force on the leaf spring leg was given as

$$T = \frac{M}{D} = \frac{FL}{4D} \tag{5.10}$$

The strain in the spring leg would be

$$\varepsilon = \frac{\sigma}{E} = \frac{T}{AE} = \frac{FL}{4EDbt} \tag{5.11}$$

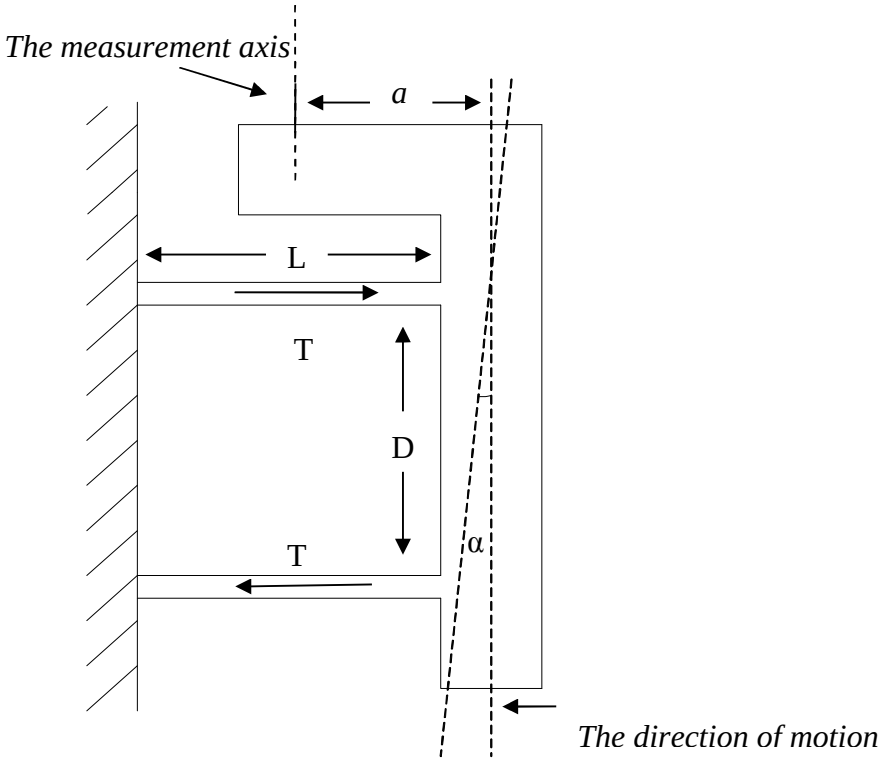

Figure 5.6: The Abbe error in the flexure spring

Thus the maximum elongation in the leaf spring leg when a 5 N tensile load was applied to the platform could be given as

$$\Delta L = \varepsilon L = \frac{FL^2}{4EDbt} = 7.5 \times 10^{-8} m \tag{5.12}$$

Assuming the compression displacement of legs normally equalled the tensile extension, thus, for small angle, the Abbe error was well approximated by:

$$Abbe\ error = asin\alpha \approx \frac{2a\Delta L}{D} \approx 2\Delta L = 1.5 \times 10^{-7} m \tag{5.13}$$

In a practical notch design, the extensional strain was mostly concentrated on the notch rather than distributed over the whole leg in the case of a ligament leaf spring. The strain in the thicker section of notch legs was much less than the strain in the notch which reduces the whole extension by at least, say, 10 times. The real Abbe error would be only tens of nanometres at the very most.

Ideally, the specimen extension measurement axis should be kept in-line or as close as possible with specimen loading to minimize the Abbe error. However, it was necessary to place the strain measurement a few tens of millimetres away from the specimen loading in order to keep the capacitive gauge free of interference during the specimen mounting stage. Typical MSL specimen extension of a couple of tens μm could be obtained with a maximum 10 N tensile load where the Abbe error was only at worst a few of tens nanometres which left it less than 0.1% in the full scale measurement range.

5.5 Specimen mounting and alignment

The MSL specimens were usually at scale of less than 1 mm and delicate. It was difficult but important to preserve the original states of these small specimens during the specimen mounting and alignment stage in order to obtain accurate data. Although the specimen was integrally fabricated with a larger carrier and protection side bars to prevent the small central working section from pre-stress or partial damage, a robust specimen mounting and alignment strategy was still required, especially since the thin MSL specimens were susceptible to severe curl distortion which makes the working-section more vulnerable during handling and mounting.

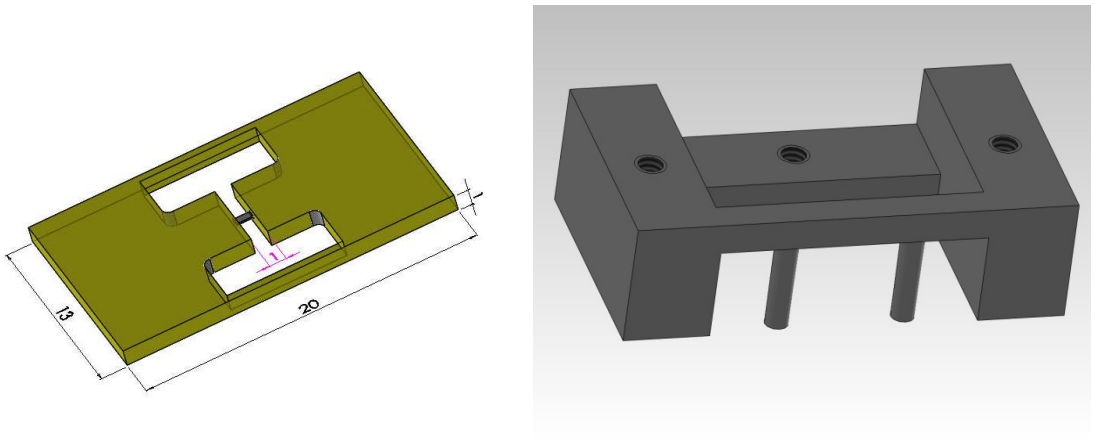

Figure 5.7: The tensile test specimen (left) and the clamping device (right)

The curl distortion on the resulting specimen puts a further hurdle in the way of robust handling and clamping specimens. An initial attempt at specimen mounting was made using the pin-block methods in order to seek a near-kinematic solution and alleviate the curvature issues in MSL specimens. As mentioned in section 5.3, the larger flanged side of specimen (Figure 5.7) could be used to accommodate the pin-block approach. Stiff pins embedded in the clamping device were touched against the vertical of the outer land such that under tensile load the stage movement imposed near-kinematic coupling to the specimen.

This clamping process is illustrated in Figure 5.8. After placing the specimen onto the mounting area of the flexure (oriented horizontally), the left side of clamping device was mounted onto the flexure and its pins were fixed to contact the left flanged side of the specimen. The right side of clamping device was integrated with slotted holes and was

set to be loose to allow a little sliding distance in the tensile direction. These pins on the right clamping device were set to be close to the right specimen flange but not contacted with it. Then, the flexure mechanism was placed vertically with the left side clamping device on the top with pins still contacting the specimens. The right clamp device slid downward due to its self-weight and contacting the specimens to realize a four pin-contacting clamping. This clamping device was then locked by firmly screwing down the bolts on the sliding slot. The specimen can be well aligned since the four pins could provide a rigid reference for specimen alignment.

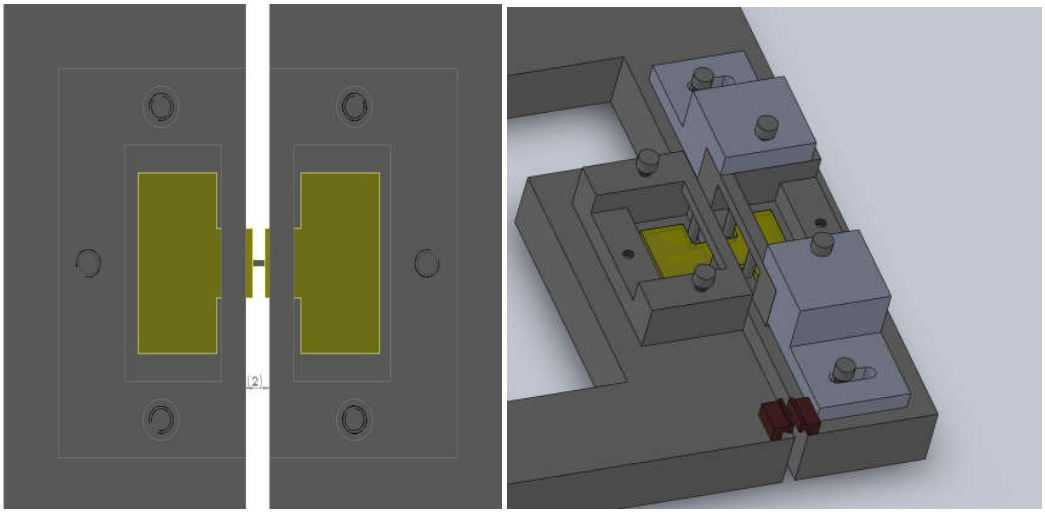

Figure 5.8: The procedures of pin-block specimen mounting

The rigid pin-block method possessed a great advantage in dealing with the curved nature of thin MSL specimens because it avoided the conventional clamping difficulty of flattening the curled surfaces. Another great benefit of this approach was that the specimen could be well aligned by gravity during the mounting process. However, initial

trials of pin-block test experienced severe practical difficulties. The size of these pins was restricted to small values (typical ϕ 1.5 mm) due to the restrained space between the specimens cell. Since the typical stiffness of a test beam was about 100 k$N\ m^{-1}$, it would be difficult to manufacture such small pins with considerably higher stiffness to ensure a stable pin block when the tensile load was applied. Significant wobble had occurred at the small aluminium pins when larger forces (5-10 N) were applied to the flexure. Another impediment of this approach was that the contacting pins may slide a little over the flanges of specimens causing out-plane torsion when the flexure was lifted to apply the vertical tensile load and it was very difficult to observe and measure the tilt angle of the specimen during the tensile test. Substantial slip of specimen flanges along the pins resulting in out-plane shear stress had also been observed occasionally when the mounting device was fastened down to the spring or the tensile load was applied.

This problematic initial pin-block trial tests led to a preference for friction gripping by hard-clamping to the flats of the test rig using screws acting through flexible brackets. A simple screw-driven flexure clamp device was employed as shown in Figure 5.9. The bulk ends of the specimen cell which was about 10 times larger than the test beam could provide sufficient bases for hard, frictional clamping while a screw-driven clamping flexure was employed to firmly hold the specimen. This clamping flexure was deformed by driving the screw down and thus clamping down firmly to the specimen. Rubber was glued at the contacting clamping end as the soft material to prevent direct surface damage and increased the friction force to hold down the specimen. However, because of the curved surface issues in MSL specimen, the thickness of bulk ends in specimen cell needed to be set relatively large (e.g. 2 mm) in order to achieve a relatively good flatness

of the specimen base. Even so, a small area point clamping rather than full area clamping was employed with soft materials on the clamping end to minimize the stress to the specimen introduced by hard clamping. Thus, this led to a practical compromise of setting the clamping area of 3 x 4 mm^2 over the 6.5 x 13 mm^2 of specimen bulk ends that granted sufficient friction force for tensile testing but did not introduce too much stress to affect the central work section of the specimen. The surface of the specimen needed to be well prepared in order to ensure a stable friction clamping.

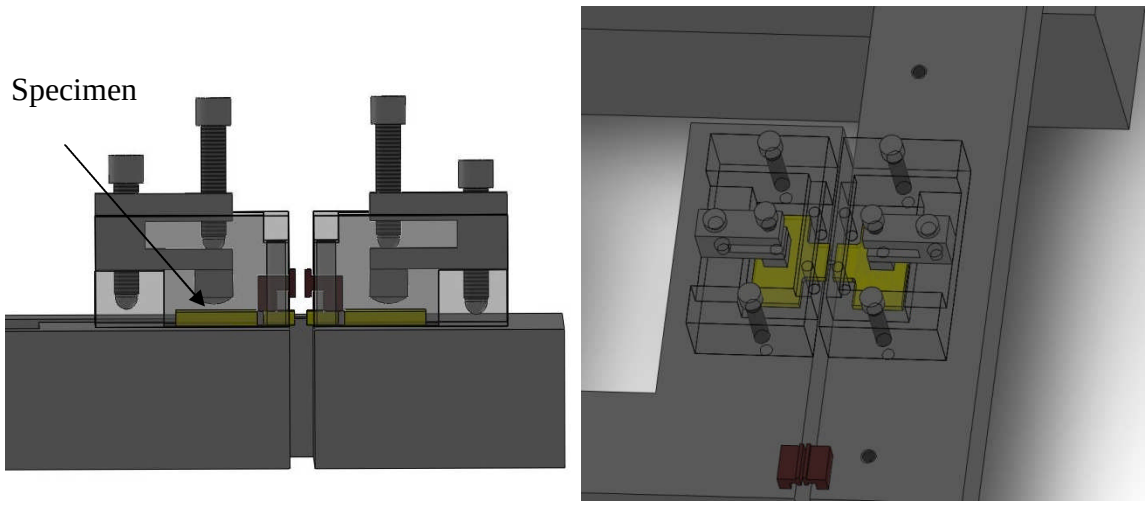

Figure 5.9: The schematic diagram of clamping setting

As mentioned in chapter 4, the test beam was small and embedded in the central region of specimen cell. The specimen alignment should be completed with the aid of bulk end of specimen cell. A line in parallel with the driving axis was drawn and the edge of the specimen cell was carefully set to be coincided with the line. Slight misalignment angles

would not introduce significant errors in the tensile test, since the 1st order errors of the net load and elongation were cancelled out and the shear forces would normally be only less than 1% the tensile ones. The specimen was then clamped down to the surface of flexure spring to ensure in-plane tensile stresses.

In summary, both the two specimen mounting strategies were initially trial-tested to explore for stable and reliable specimen mounting solutions. The first approach could alleviate the curved issues on thin specimens but put a stringent requirement on the fabrication of the rigid pins. The other method took screw-driven clamping approaches and could provide robust specimen mounting but needed extra precautions on the clamping condition. The screw-driven clamping method was finally chosen and fully implemented for the tensile testing because it was a simple and effective method where as the pin-block approach experienced practical difficulties in fabricating highly stiff but small pins. The clamping device could be integrated with the flexure spring to firmly hold down the specimen and help to obtain good alignment. The disadvantage of this over-constrained approach was that specimen surfaces need to be well prepared to align cleanly to the test-rig mounting flats and only specimen cells with thickness larger than 1mm could be employed in order to ensure stable clamping as well as good alignment.

The specimen mounting had been one of the main uncertainty sources, and thus it was necessary to carry out a verification process for clamping conditions. The main criteria for the clamping condition for specimen mounting were no slip and low clamping load-induced stress. The bulk end design in the specimen ensured that the clamping stress was limited only within the bulk ends of specimen cell and had negligible effect on the specimen beam in the centre. Gross slips from poor clamping could be identified

occasionally during the test. Re-clamping the specimen would remedy this problem and the data will not be corrupted. However, micro-slip or creep that may occur during the test might be hardly appreciable within the output data, which would significantly affect the test results. Therefore, a careful verification of specimen clamping conditions was needed and is fully described in section 5.8.3.

5.6 Strain measurement method

Two basic types of strain measurement were commonly employed for MEMS specimens. One approach deposited gauge marks onto the specimen and measure the change via optical means. This approach usually required high resolution optical microscopy or laser interferometer and precise deposition of gauge marks on the small scale specimens within the small range (usually a few hundreds of μm) of the optical microscopy (Sharpe 1997a and Sharpe 1997b). It posed a practical difficulty in current MSL fabrication equipment. Integrating the microscopy or laser interferometer in line with the small samples would also greatly increase the cost and the complexity of whole tensile system. An alternative approach was using various displacement sensors to measure the elongation and the overall length of the tensile specimen separately. This approach could take advantage of broad range of displacement micro-sensors and provide a relatively flexible range of specimen size. Hence, a decision was made to use the latter.

Among various displacement sensors, capacitive gauges were commonly used in small distance detection. Other micro displacement sensors, such as eddy current sensors and inductive sensors, had practical limitation in the bulk size and resolutions in this

application. The capacitive gauges also had limitations in micrometry, such as high impedances which can add electrical noise sensitivity, relatively large variation in initial setting up and relative high cost of conditioner electronics. However, none of them becomes significantly serious. In this case, the compact size and high resolution of capacitive gauges granted them the great advantage of easier integration to the test-rigs over other displacement sensors. A Queensgate Instruments (QI) commercial conditioner box was used to conduct the displacement measurement and a fine sub-micrometre resolution could be expected in open room circumstance. However, these capacitive gauges needed to be carefully calibrated with high-precision instrument. The calibration of capacitive gauges was completed with the aid of an ultra-precision Renishaw laser interferometer XL 80.

On the other hand, the geometry of specimen was largely dependent on the manufacturing tolerance of MSL fabrication. It was generally difficult to measure the cross-section of thin test beam, especially when the working-section of the specimen is surrounded by protection structures. Due to the delicate nature and stringent space constrain, non-contacting optical methods would be ideal. The specimen length and width could be further confirmed by optical microscopy. The thickness of specimens was measured by a Keyence laser confocal sensor which is capable of measuring the thickness of thin transparent objects, by detecting front and back surface reflection.

5.6.1 Displacement measurement

5.6.1.1 The principle of capacitive gauge

The capacitive gauge was a high precision non-contact displacement sensor best suited to applications with a range from a few micrometres to a few millimetres. It worked by measuring changes in the electrical property of capacitance between a pair of target electrode and probe surface. An alternating voltage excited the charges which continually reversed their position (See *Wilson* 2005) and so produced electric current which could be detected by the sensor electronic. The amount of circuit current was determined by the capacitance which was governed as

$$C = \varepsilon \times \frac{A}{d} \tag{5.14}$$

where ε denoted and dielectric constant of the material (generally air) between conductors and *A*, *d* denote the superposition area of two conductors and the distance between them. Capacitive micrometry in which the plate size *A* is kept constant while the distance between parallel plates was varied gave the highest sensitivity at small gaps, *d*, and is employed here. As described in section 5.5, the change of probe area due to the parasitic error motion of flexure spring was relative small during the test and could be ignored. The temperature and other environmental change were kept at small value under a constant-temperature precision laboratory. Thus, the value of capacitance was only depending on the distance between the probe and target.

5.6.1.2 The capacitive gauge build and installation

In the tensile test, the specimen elongation under the tensile load was measured by the two capacitive gauge comprising a pair of thin gold electrodes (8×5 mm^2) deposited on glass pads. The glass pads were then glued to a support aluminium structure to form the capacitive probe while Agon silver paint was used to connect wiring without introducing stress or damage to the gold surface (Figure 5.10).

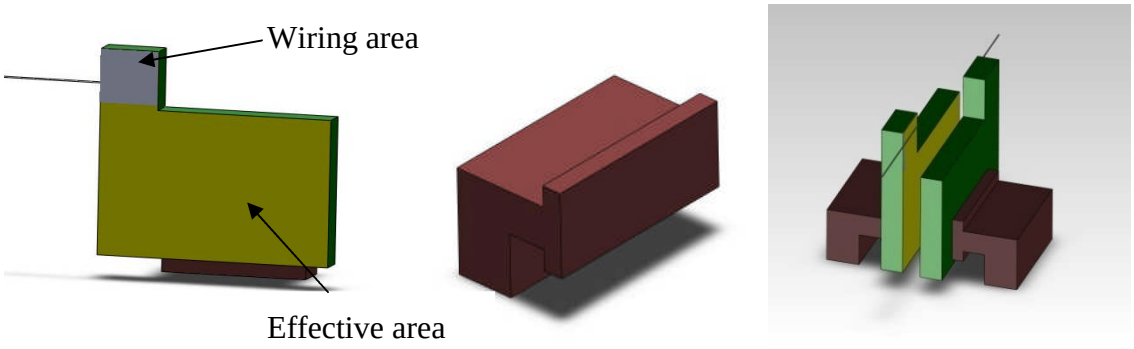

Figure 5.10: The capacitive probe setting: (left) electrode (mid) the support structure (right) overview

The design of the capacitive gauges required specifying a nominal gap *G* between the electrodes. Theoretically, the setting of the nominal gap should be kept in balance between range and sensitivity: the larger nominal gap the larger range with lower sensitivity. As the extension of specimen was never larger than 40 µm, the nominal gap should be kept as small as possible to maximize sensitivity. As a rough rule derived empirically, capacitive micrometry was best used with a displacement range of ±50 % of the nominal gap. In the previous sections, the nominal gap was normally kept to be a few

hundred micrometres after the capacitive pads were installed onto the flexure spring. In order to produce the optimal performance, the reference capacitor in the conditioning electronics should be adjusted to a value close to the detected capacitance between the probes. In practice, the nominal gap was designed to match the reference capacitor, here 10 ρF.

For installation, a pair of capacitive electrodes were clamped together within a thin foil between them and transferred to the flexure spring (Figure 5.11).The thin foil was carefully removed after the probes have been glued in place and left a nominal gap of a little larger than the thickness of the foil, nearly 200～300 micrometres. The capacitive pad glued onto the stage of the flexure spring was referred to as the target surface while the other glued onto the based was called the probe surface.

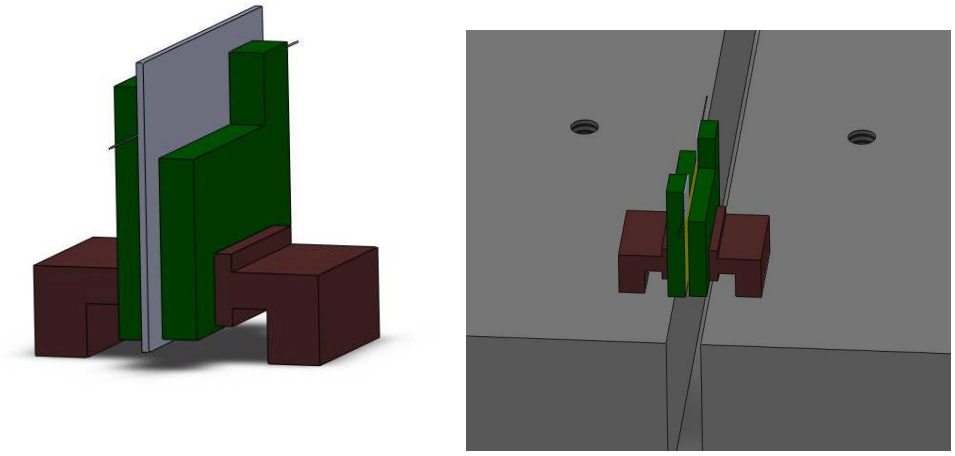

Figure 5.11: The installation of capacitive probes

5.6.1.3 The Queensgate parameter setting

The Queensgate Instrument (QI) NS 2000 is a high-precision capacitive conditioner powered by ±15 voltage at 70 mA producing an analogue output voltage which reflected the displacement of measured gap. The QI box was connected to a stable power supply at the rear panel where the output could be accessed at the socket marked O/P. The target and probe socket was located in the front panel and connected to the capacitive probes. An adjustment screw for tuning the reference capacitor was also embedded between the two input sockets (Figure 5.12) at the front panel. The bandwidth and gauge factor switches were situated at the side of the box.

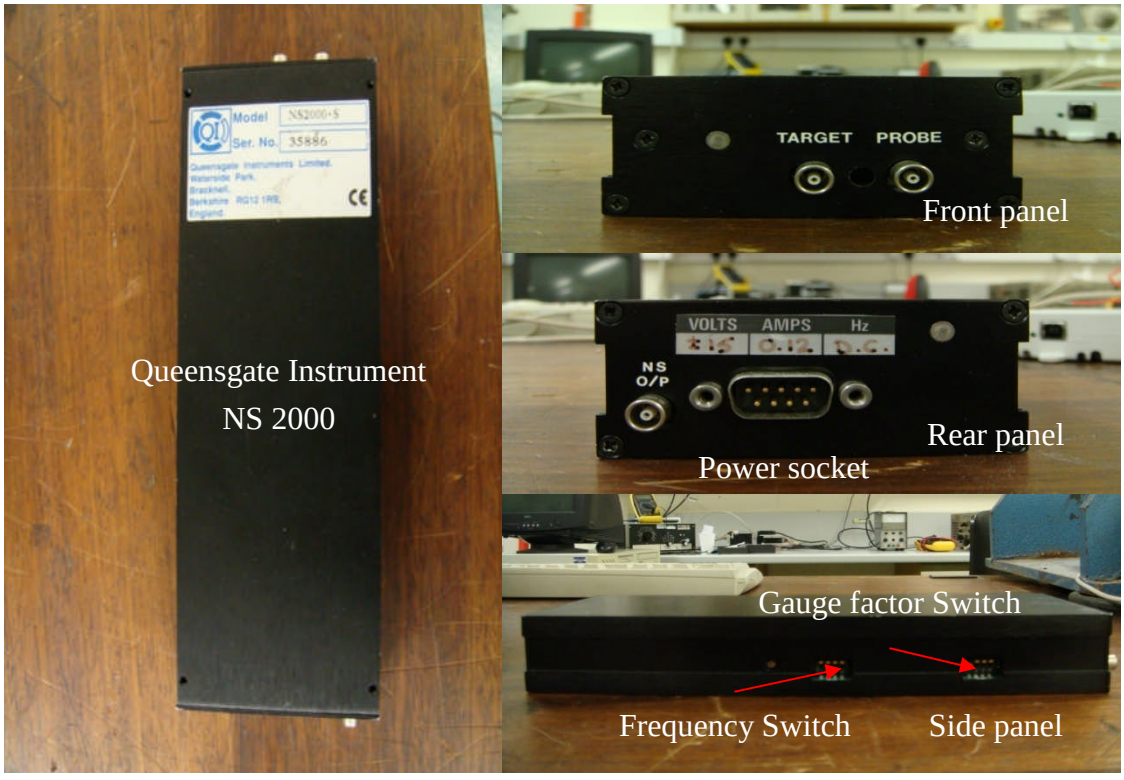

Figure 5.12: The Queensgate instrument conditioner shown in various views

In the Queensgate conditioner, two crucial parameters, gain factor and the bandwidth, could be set on the side panel to get the optimal performance of the capacitive gauge. The gain factor of QI NS2000 is factory set for 1 V for 0.1 *G*. For correct operation, the nominal gap was numerically equal to the displacement range to be measured, thus, the scale factor would be tens of μm for 1 V. High scale factors were inherently preferred in the pursuit of high precision, thus, the default gain factor was chosen other than the alternative 0.01V/G choice.

The QI box module can be set to a bandwidth of 50 Hz, 500 Hz and 5 KHz (factory default). The choice of bandwidth depended on the specific application and was a compromise between response speed and noise level. High bandwidth was related with greater noise but faster response. According to the handbook of QI instrument guide (Nano Positioning system 2000 User's guide 1993), the total noise level was related to the bandwidth defined as

$$\mathrm{N_{electrical}} = \mathrm{N_f}\sqrt{\mathrm{B}} \tag{5.15}$$

where *B* was the bandwidth and N_f was the noise factor pre-set in the QI box which was only affected by the nominal gap *G* and the thermal change. As the nominal gap was about hundreds of μm, the thermal drift was 2.5 $\mathrm{ppm\,K^{-1}}$ and $\mathrm{N_f}$ was about 0.1 $\mathrm{ppm\,Hz^{-\frac{1}{2}}}$ (ppm refers to part per million of nominal *G*), hence the theoretic electrical noise level for 50 Hz would be less than a nanometre from the room temperature drift. Electrical noise picked up by the unshielded electrodes and fine connecting wires totally dominate the actual performance. However, significant larger electrical noise was found in practical setting-up. Typical noise levels of voltage in different bandwidth are

illustrated in the Figure 5.13. A resultant noise level of 2.2 mV, 6.5 mV and 9.3 mV were observed at the bandwidth of 50 Hz, 500Hz and 5 kHz respectively.

The monitor bandwidth should be set higher than the frequency of gap change between capacitive pads. In the design, as the tensile instrument was normally used quasi-statically, 50 Hz was chosen for minimum noise level and higher precision where a noise level of approximately 2 mV was achieved. The noise level was much larger than the theoretical calculation because of the presence of external noise. It corresponded to a displacement of about a couple of hundred of nanometres (see section 5.8.2).

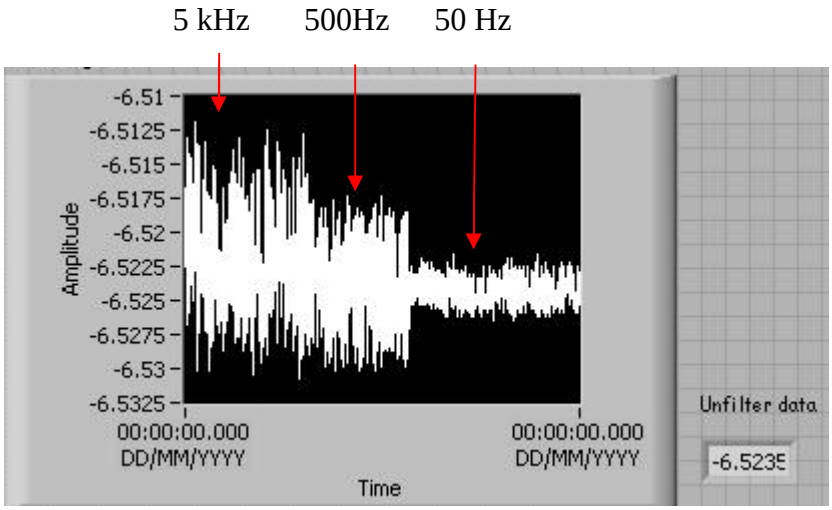

Figure 5.13: The capacitive gauge noise level at different bandwidth (5kHz, 500 Hz and 50Hz)

5.6.1.4 The data process

The capacitive measurement data was recorded to a PC *via* a National Instruments BNC-2010 DAQ (Data Acquisition) device and processed in DAQ (data acquisition) software Labview 7.1 and Matlab 2009. A Butterworth filter was added in Labview to further reduce the electrical noise for better solution. The typical cut-off frequency was set to be 400 Hz with 1000 Hz sample frequency (Figure 5.14). The noise level was calculated in mean (DC) level over 100 ms and recorded for further process in Matlab programs.

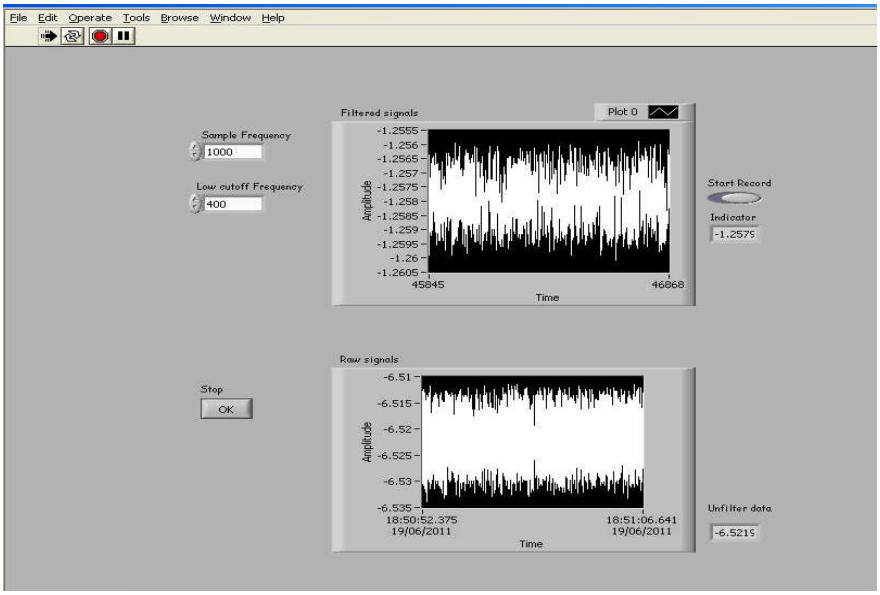

Figure 5.14: The Labview user interface for the capacitive gauge

5.6.2 Dimension Measurement

The dimensions of test specimens were pre-set in the fabrication process of the MSL system, but subjected to the manufacture tolerance and, more significantly, shrinkage and curl distortion. The test beam was integrally fabricated within a larger carrier in order to

avoid pre-stresses or damage during the fabrication process and it was necessary to define the characteristic gauge dimension to separate the test beam apart from the rest of the specimen cell.

As described in section 5.4, the stiffness of the specimen was calculated from the dimensions of specimen including the characteristic gauge length and its cross-section area. The characteristic dimension of the test specimen must be further confirmed after manufacture for high precision measurement. The test beam was formed between the bulk ends of specimen, and the characteristic length is defined by the two edges of bulk ends. Thus, the length and width (typical 1x0.5 mm Figure 5.15) of the test specimen could be further ensured by placing the specimen directly under a measuring microscope: a Nikon OPTIPHOT microscope (Figure 5.16 and 5.17). The specimen was measured under this confocal microscope using object lens of 40 x magnitude, calibrated with a 100 x 0.01 mm scale slide provided by Graticules Ltd.

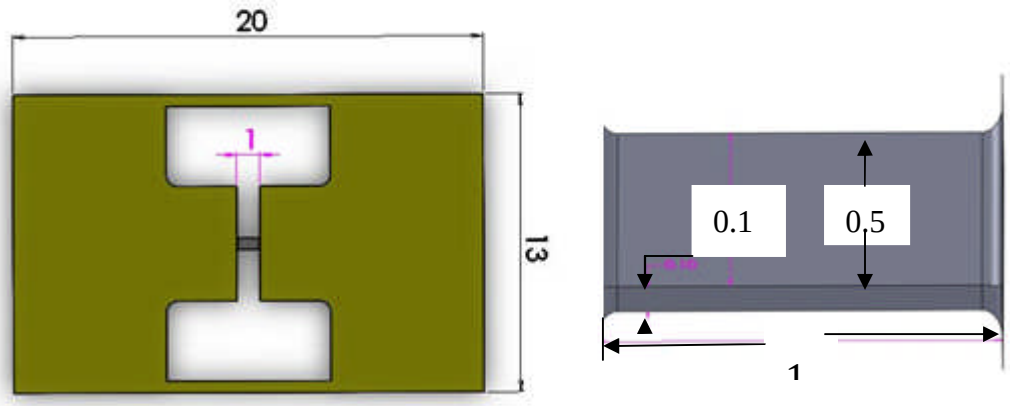

Figure 5.15: The nominal dimensions of test beams (mm)

Figure 5.16: The Nikon digital microscope

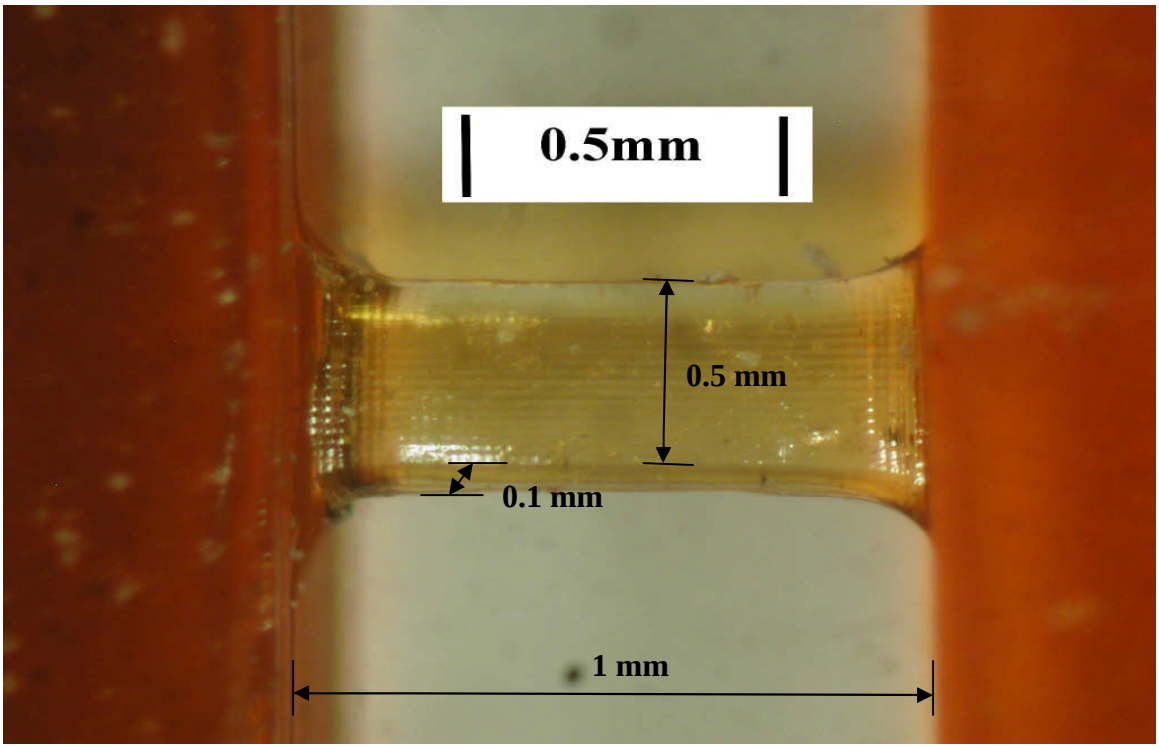

Figure 5.17: Picture of a test beam under the Nikon high-resolution camera

As the smallest dimension, the thickness of the test beam was restricted by the limitation of layer-by-layer MSL fabrication. A Keyence optical confocal sensor LT9010 was used to measure the thickness. The principle of Keyence confocal sensor LT 9010 is shown in Figure 5.18. The objective lens featured a beam towards a target surface which was oscillated back and forth. The beam reflected off the target surface was converged onto a pinhole and then enters the light detector. The variation of target surface position in the vertical direction was determined by measuring the exact position of the objective lens when the light was detected. This sensor was factory calibrated and excellent resolution of 0.3 μm was claimed without being affected by the material, colour, or angle of the target (Keyence 2004). A summary performance of Keyence LT 9010 is given in Table 5.1.

Figure 5.18: The principle of Keyence confocal LT9010 displacement sensor (Keyence 2004)

Table 5.1: The technical specification of Keyence LT9010 (Keyence 2004)

Keyence LT9010	
Laser Source	Red semiconductor laser
Laser wavelength	670 nm
Measurement range	±0.3 mm
Reference distance*	6 mm
Linearity	±0.5% of F.S. *
Resolution	0.3 µm
Temperature characteristics (+20 ~ +30°C)	±0.5% of F.S.

*The reference distance was the distance between the measuring unit and the target surface

*F.S. stands for full scale.

The Keyence LT 9010 was capable of measuring the thickness of transparent specimens, as shown in Figure 5.19. For thin specimens made with Envisiontec R11, the specimen could be treated as transparent or semi-transparent to red light which allowed the laser beams to pass through the top surface of specimen and return to the detector after deflection at the bottom of test beam. The Keyence sensor collected the signal from two reflection surfaces and calculated the height difference, namely the thickness.

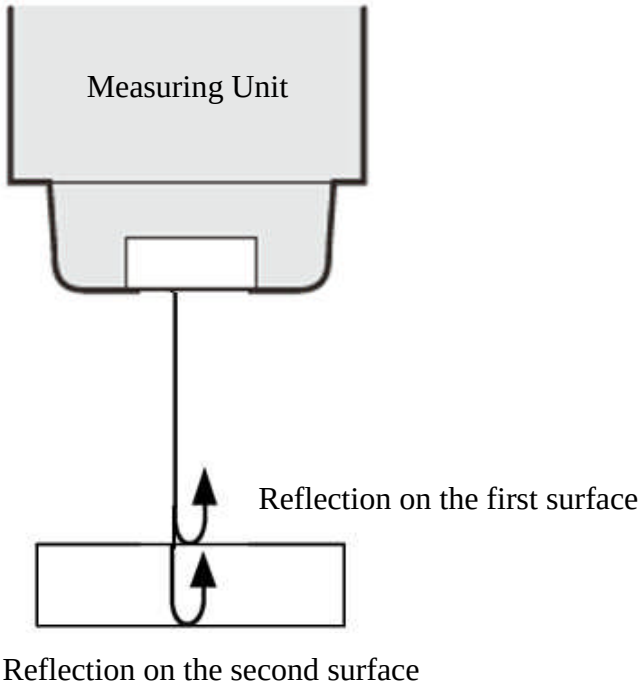

Figure 5.19: The principle of measuring thickness by Keyence LT 9010

A typical dimension repeatability at a typical size specimen size (1/0.5/0.1 L/W/T) made of R11 is given in Table 5.2. The resultant dimension of the specimen was 1/0.47/0.088 mm and the standard deviation value for width measurement and thickness measurement are ±1.45% and ±1.32% respectively. The specimen cell was designed to place the small test beam in the centre between two built-in ends. The length of specimen was closely controllable because most longitudinal shrinkage occurs in the bulk ends. However, the transverse and vertical shrinkage caused significant manufacturing errors to the test beam. Particularly, the discrepancy in thickness became the most prominent. This was because that the high-aspect-ratio specimens only comprised a few thin curing layers hanging above the bulk ends and sometimes the first few thin layers of the test beam may fall off

during the lifting-up due to the weak mechanical strength. This significantly decreased the performance of MSL fabrication and became crucial in designing for fabrication. The effects of different UV exposure on the shrinkage will be discussed in Chapter 6.

Table 5.2: The dimensional measurement on a specimen (1/0.5/0.1 mm (L/W/T))

	Length	Width	Thickness
Measurement 1	1.00 mm	0.48 mm	0.090 mm
Measurement 2	1.00 mm	0.47 mm	0.087 mm
Measurement 3	1.00 mm	0.48 mm	0.089 mm
Measurement 4	1.00 mm	0.48 mm	0.087 mm
Measurement 5	1.00 mm	0.47 mm	0.088 mm

5.7 Summary of the tensile test set-up

The specimen with built-in protection bars was firstly transferred to the horizontal placed flexure spring, then firmly clamped down to the surface of flexure spring and aligned in the clamping devices located approximately 30 mm away from the loading axis. The flexure spring was then attached to the base block and lifted to vertical orientation so that the standard weights provide the tensile load to deform the specimen. For a stable clamping, there was an approximate equality between the flexure displacement and the specimen extension. A pair of capacitive probe was glued onto the flexure spring to monitor the displacement. Data was recorded to a PC *via* a Queensgate Instruments NS2000S conditioner and National Instruments BNC-2010 interface. Control and analysis software Labview and Matlab were used to process the test results.

5.8 Calibration and Verification of testing instrument

The new tensile test-rig imposed externally controlled tensile forces (e.g. weights) and measured the specimen elongation by a capacitive gauge built into the guidance stage. To add robustness, this stage was a flexure mechanism which also shares the imposed force, reducing the actual load across the specimen. Hence there was a need for precise calibration of the spring constant of the flexure stage and of the sensitivity of the capacitive gauge. Besides, the critical specimen clamping condition needed to be carefully observed and further verified by using two pairs of small capacitive electrodes glued on the specimens and flexures to compare the actual elongation of the specimen and the stage displacement.

5.8.1 Calibration of the flexure spring

As shown in Figure 5.20, the calibration of the flexure spring was conducted using the Keyence Laser confocal sensor LT9010. A polished silicon mirror was glued at the end of the flexure spring acted as the target reflector of the optical sensor. This extensional mirror arrangement also allowed about 10 mm Abbe offset, but this was acceptable here for the similar reason discussed in Section 5.4. Standard weights were used as the applying load while the Keyence sensor picks up the displacement. The measurement result was displayed at the LCD monitor.

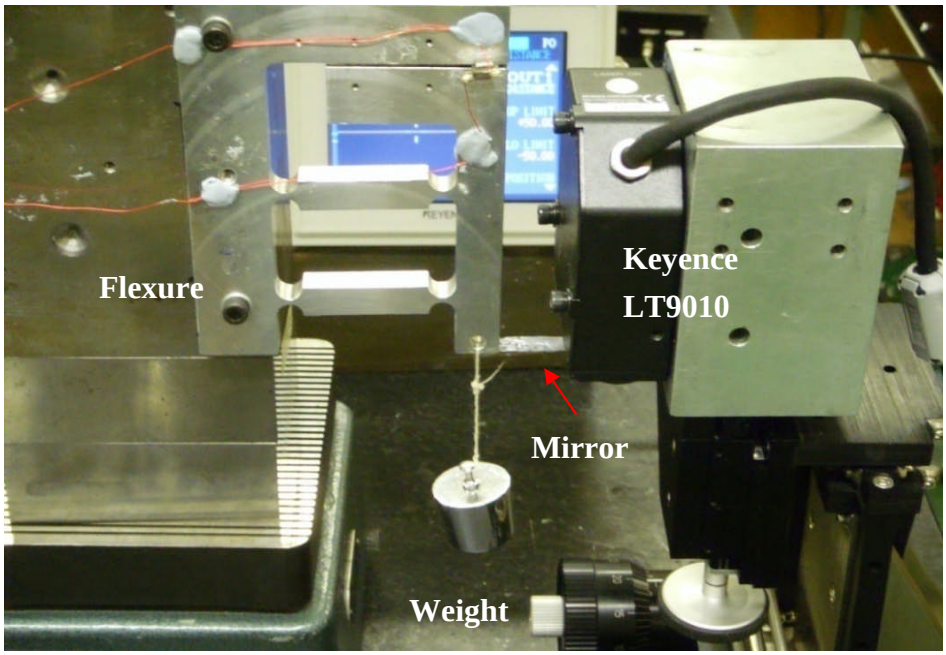

Figure 5.20: The system of calibration hinge spring

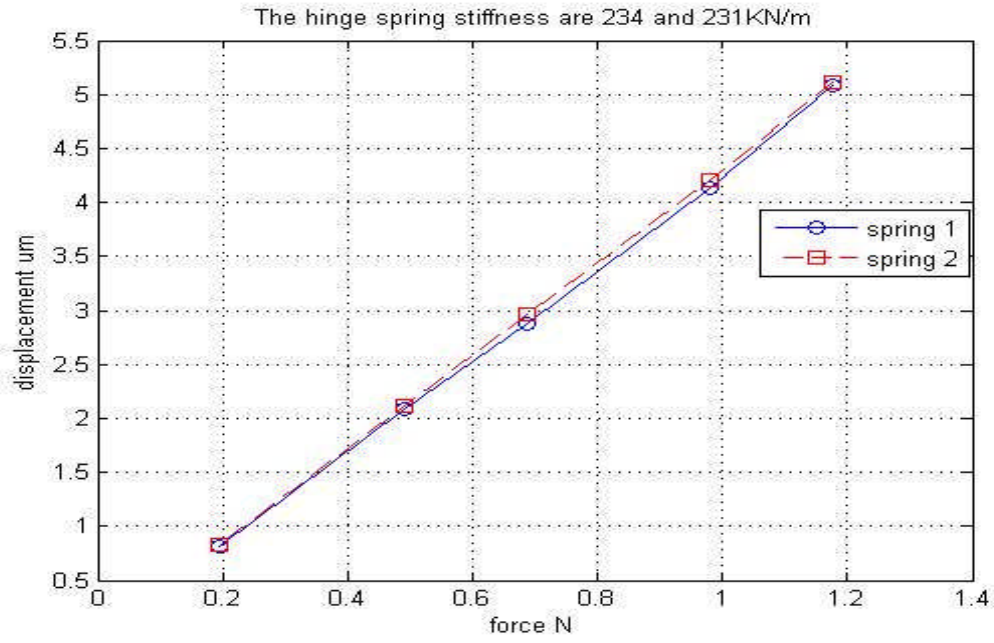

Figure 5.21: The calibration result of two notch hinge springs

Two flexure springs with same parameters were manufactured and calibrated. From Figure 5.21, the two resulting hinge springs were calibrated to have stiffness of 231 and 234 kN/m, close to the designed stiffness of flexure spring of approximately 200 kN/m. The uncertainties in the deadweight were usually 0.01 N, which was only less than 1% of the applying load. Their linearity over 5 μm displacement was also good and more than adequate for current need.

5.8.2 Calibration of the capacitive sensors

The capacitive gauge produces an analogue voltage change corresponding to the displacement, thus it is necessary to calibrate the capacitive sensors using an ultra-precision instrument to determine the sensitivity. Optical interferometer which is capable of ultra-precision and low-electrical noise interference is a preferred candidate. Hence, a Renishaw laser interferometer XL 80 was employed for the task.

The Renishaw interferometry system consists of a laser head housing a laser source and detector, a beam splitter and two retro-reflectors (Figure 5.22). In the system, the XL 80 laser head produces a stable laser beam through the measurement optics which is composed of a 45° beam splitter and a retro-reflector. This retro-reflector is rigidly attached to the beam splitter to form fixed length reference arm while a small mirror is fixed onto the flexure spring to act as the target retro-reflector to deliver the displacement to the Renishaw optics to complete the measurement. The laser beam is half split at beam splitter and travels to the reference retro-reflector and the target retro-reflector respectively and eventually reflected back towards the detector to form either

constructive or destructive interference. The constructive interference results in bright light while the destructive interference results in darkness. Thus, the displacement of target retro-reflector is calculated by counting the peaks and fringes of the returning light.

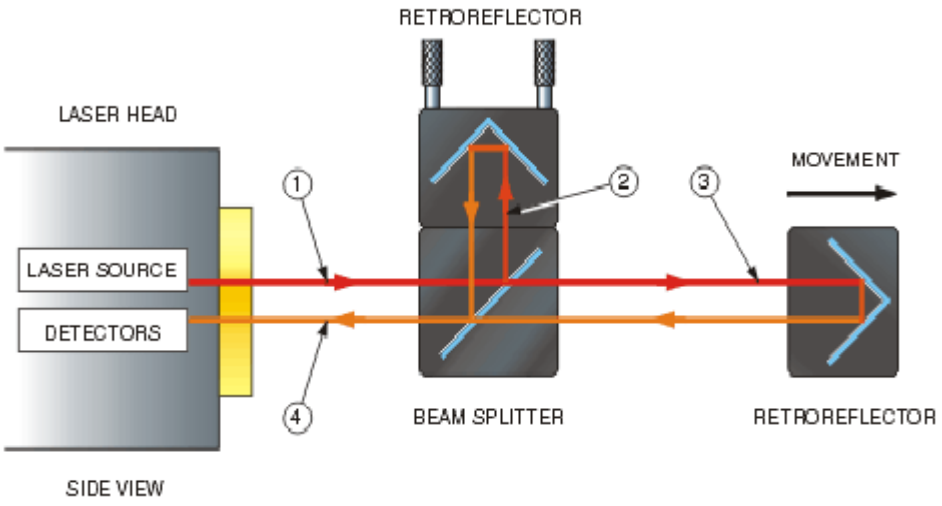

Figure 5.22: The principle of Renishaw laser interferometer (Renishaw 2007)

The Renishaw XL 80 optical interferometer is based on a Michelson configuration. It is a traceable and sophisticated precision meter measuring displacement to the accuracy of the orders of nanometre or better. The system can operate over very long distance (up to 80 m) and so it is easy to ensure that heat source (laser head) remains well away from the capacitive gauge. The data of laser interferometer is restored to the PC *via* a USB device and process in the real-time display software QuickView XL^{TM}. The major specification of Renishaw XL 80 is given in Table 5.3.

Table 5.3: The performance of Renishaw Laser interferometer

Renishaw XL optical interferometer	
Laser source	HeNe laser
Laser power	<1 mW
Laser wavelength	633 nm
Operation temperature	0-40°C
Standard range	0-80 m
Linear measurement accuracy	±0.5 ppm (parts per million)
Resolution	1 nm

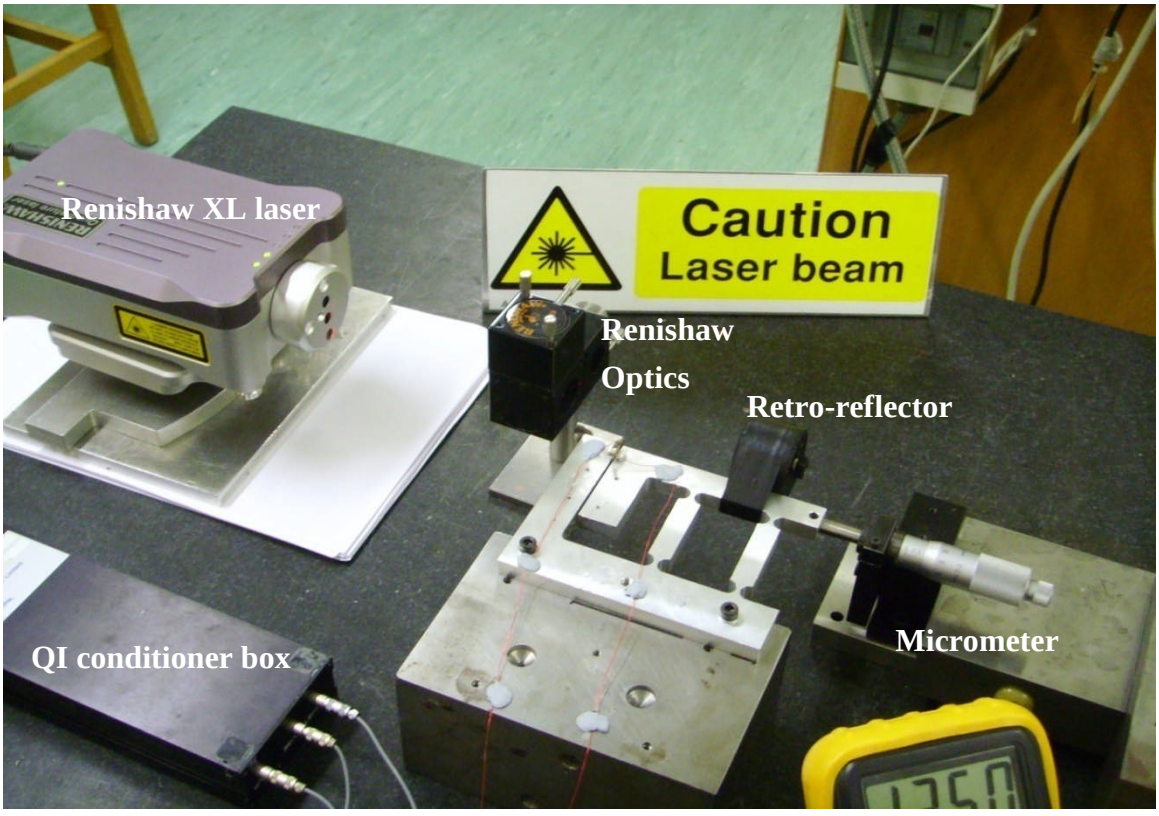

Figure 5.23: The calibration system for capacitive gauges, showing the laser head, remote interferometer and a lightweight retro-reflector taped to the flexure mechanism

For displacement calibration, the flexure spring was placed horizontally with a retro-reflector fixed on its side (Figure 5.23). The laser beam travelled through the measurement optics and back to the detector housed in the laser head. A micrometer was used to apply displacements to the flexure spring, measured by both capacitive gauge on it and the laser interferometer simultaneously. Maximum displacement of 40 μm was achieved during the calibration.

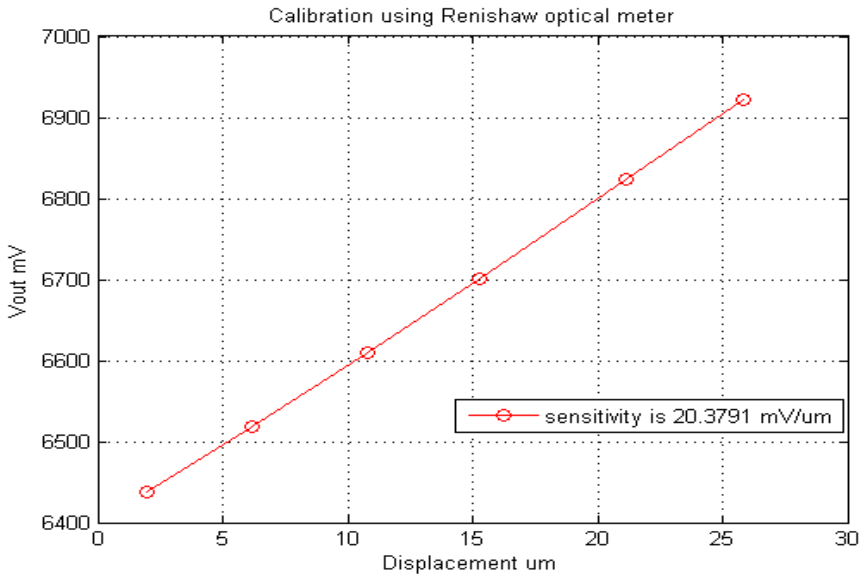

Figure 5.24: The result of capacitive gauge calibration against Renishaw laser interferometry

As shown in Figure 5.24, the capacitive gauge was calibrated to have a sensitivity of 20.38 mV/ μm, with non-linearity better than 0.8%. As mentioned in section 5.6.1.3, 50 Hz was chosen in the QI parameter setting for minimum noise level of about 2.5 mV. This 50 Hz noise level corresponded to around 100 nm, which placed a limit on the working resolution of the system. (Although using the software noise filtering in Labview, a modest improvement could be obtained). The limitation and potential improvement of the capacitive micrometry will be discussed in Chapter 7. Although not ideal, continuing

with the first prototype built was considered a better strategy rather than re-building the entire test-rigs.

5.8.3 Verification of clamping conditions

The performance of most tensile tests at small scale is hampered by the uncertainties in specimen clamping. Thus, verifying the clamping condition is a crucial factor to eliminate the uncertainties in MEMS-based tests and improve the reliability of test results. The clamping force was controlled by driving the screw down manually and left quite an uncertainty in the force applied to the measurement loop. Thus the main concerns in the clamping arrangement in the tensile test were either that the stress applied by the direct-contacting clamping force may affect the test beam or that slight slip occurs due to the insufficient clamping force.

In the clamping arrangement, a relatively large clamping force was required to firmly clamp the specimen to the surface of flexure spring. The basic test concept involved fabricating the specimen with large carrier areas which provided space for hard clamping, so the stress introduced by the hard clamping was likely to be limited to the bulk ends of specimen. The small test beam in the central specimen cell should hardly be affected to the clamping stress. On the other hand, as discussed in section 5.5, the slight slip was difficult to observe but brings significant influence to the test result. The clamping condition was checked by making a pair of extra-light and small ($5\times1\ mm^2$) gold capacitor electrodes (similar to the large ones comprising aluminium support structure and electrodes made by depositing gold layer on glass) and gluing them between the

inner surfaces of a specimen (Figure 5.25). This capacitive probe detected the actual extension of specimen beyond the clamp in a low-stress portion of specimen, albeit with sensitivity less than the main capacitive gauges at approximately 1.3 mV/μm. Another similar pair of small capacitor probes was glued on the flexure spring to measure the stage displacement and provided comparison reference (Figure 5.26). The comparison of the result from ones on the specimen which measured the real specimen deflection and ones on the flexure spring which measured the displacement of flexure spring gave a solid feedback on the clamping conditions.

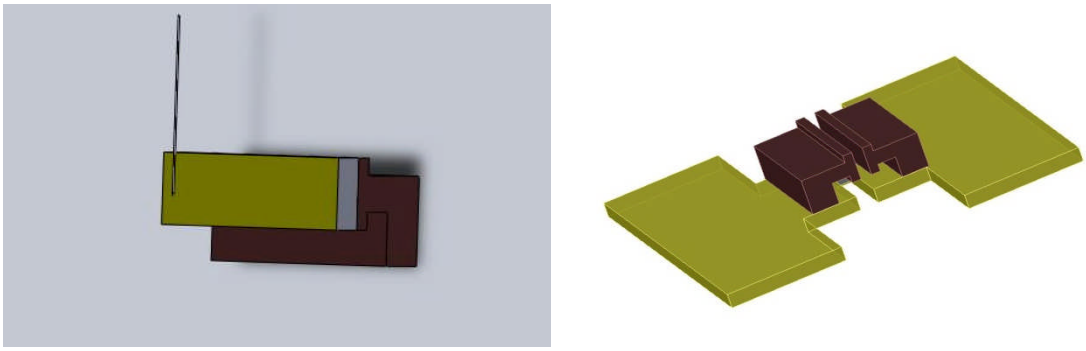

Figure 5.25: the capacitive probe setting on clamping verification

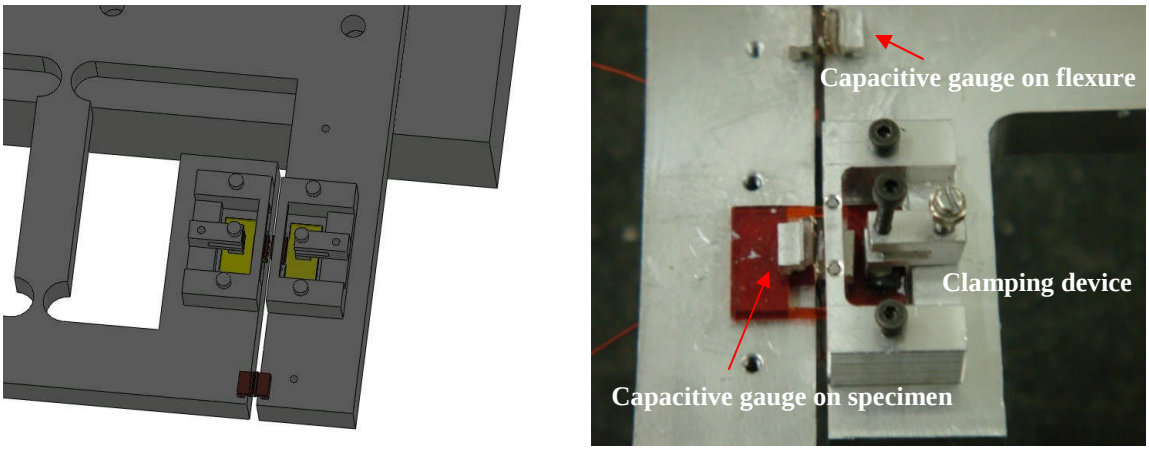

Figure 5.26: The arrangement for verification of clamping condition

In the setting-up of clamping conditions verification, the flexure spring was still horizontally oriented driven by a micrometer. The Renishaw interferometer was used to provide the displacement reading. Two pairs of small capacitive electrodes were mounted and glued (similar installation procedures in section 5.6.1.2 with close nominal gaps between the two capacitive gauges of a few hundred micrometres) to the flexure spring and the test specimen and to measure the stage motion and the actual specimen elongation respectively (The large capacitive electrodes are not included). The clamping device was then carefully placed onto the flexure spring without contacting the small capacitive electrodes on the specimens and the clamping flexure was firmly clamped the specimen by tighten the bolts and driving the screws down. A typical result of clamping verification was shown in Figure 5.27, which plotted the output of this capacitive gauge against actual stage motion.

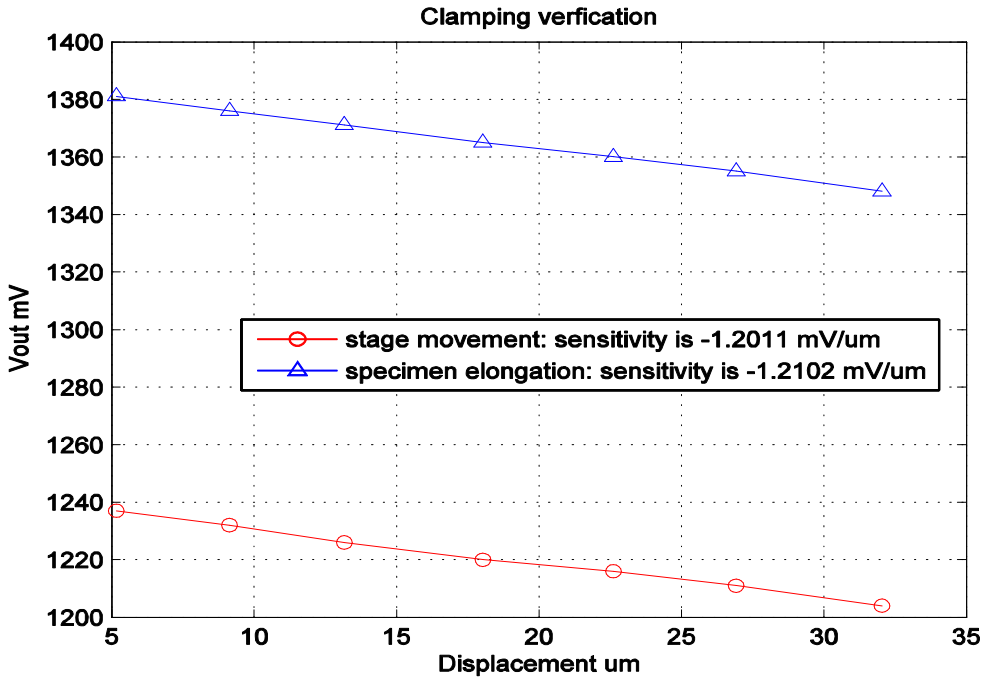

Figure 5.27: The result of two pair of capacitive electrodes in a measurement

The two capacitive gauges displayed similar sensitivities and smooth, consistent slopes. Although the small capacitive gauges suffered with thermal drift over time, there was no evidence of sudden slip. Neither had any pattern consistent with steady creep at clamp been spotted even for heavy loads over displacements of up to 40 µm. A few more specimen clamping verification experiments were performed, showing similar results.

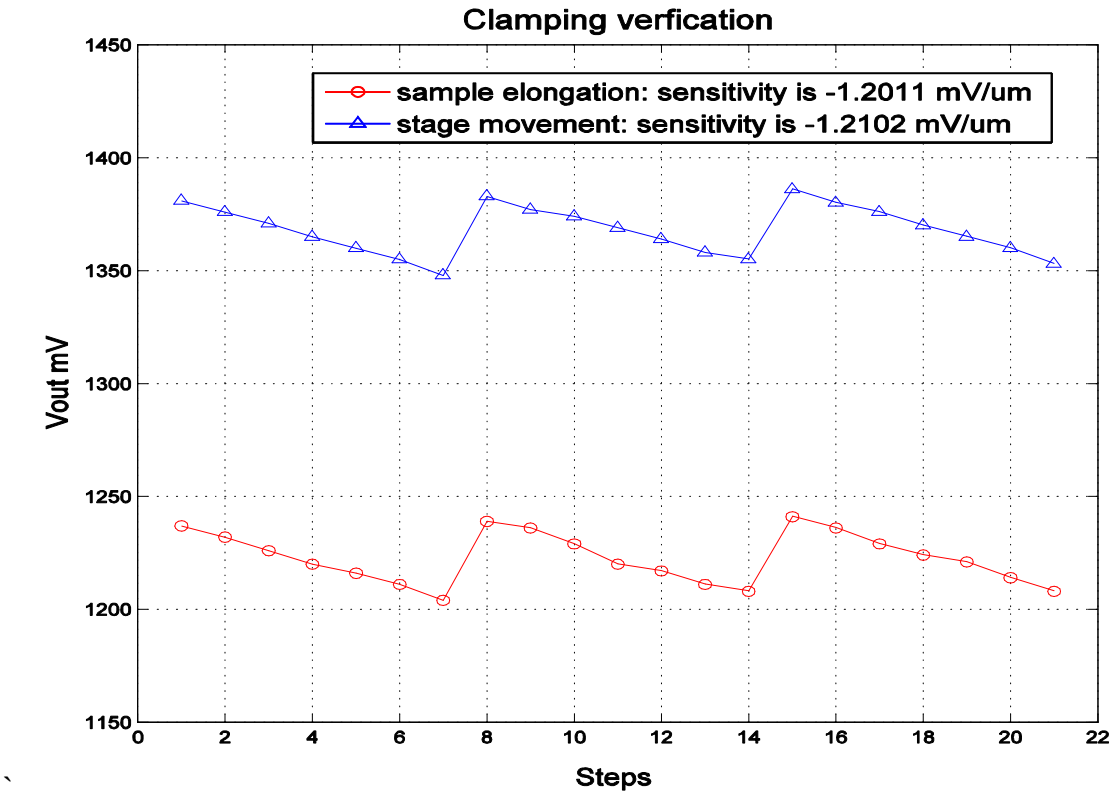

Figure 5.28: The clamping verification by the push-pull method

Figure 5.28 plotted the output of two capacitive gauges under cyclic loads. The tensile load was increased by driving the micrometre approximately 5 µm per steps and after every 7 steps of loading the micrometre was driven back to the origin place and repeated

for another set of similar loads. The consistent pattern of the two capacitive gauges during the back and forth stage motion indicated that no significant creep occurs during the cyclic loading tests and it was mostly likely that no slip had occurred and a stable clamping had been established.

Table 5.4: The result of repeatability tests

mV/μm	Test 1	Test 2	Test 3	Test 4	Test5
Sensitivity	1.2718	1.2544	1.2768	1.2857	1.2990
Sensitivity	1.3339	1.3133	1.2888	1.3343	1.3433
Sensitivity	1.2711	1.3374	1.2527	1.3538	1.3361

In order to further confirm the influence of hard clamping, a repeatability test was carried out. Only one specimen (1-0.5-0.1 mm L/W/T and 2 mm thickness for bulk ends) with capacitive electrodes glued onto the surface to provide reading was used. The clamping device was carefully mounted by driving the screw down to clamp this specimen. After measurement, the clamping flexure was loosened and re-clamped for another similar measurement to ensure that the uncertainty in the specimen mounting and alignment would not introduce significant influence to the test results. This specimen was mounted and tested in five sets, in each set the specimen was loosened and re-clamped three times. After complete measurement in one set, the whole clamping device was removed and the specimen was re-positioned for another set of repeatability test. These test results of the sensitivity of capacitive gauges over 15 μm was listed in the Table 5.4. From Figure 5.29, repeated clamping showed consistent slope with small scale variation in the measurement

sensitivity. Including variations of screw tightness (as long as the screw is driven down enough to fully clamp the specimen) and specimen position, clamping tests showed a maximum divergence within ±3.5% of the mean displacement. While these tests cannot definitively show that there is no variation at all associated with clamping, it was clear that any residual effect was repeatable (as if an elastic effect) and small enough for this clamping technique to be acceptable in practice.

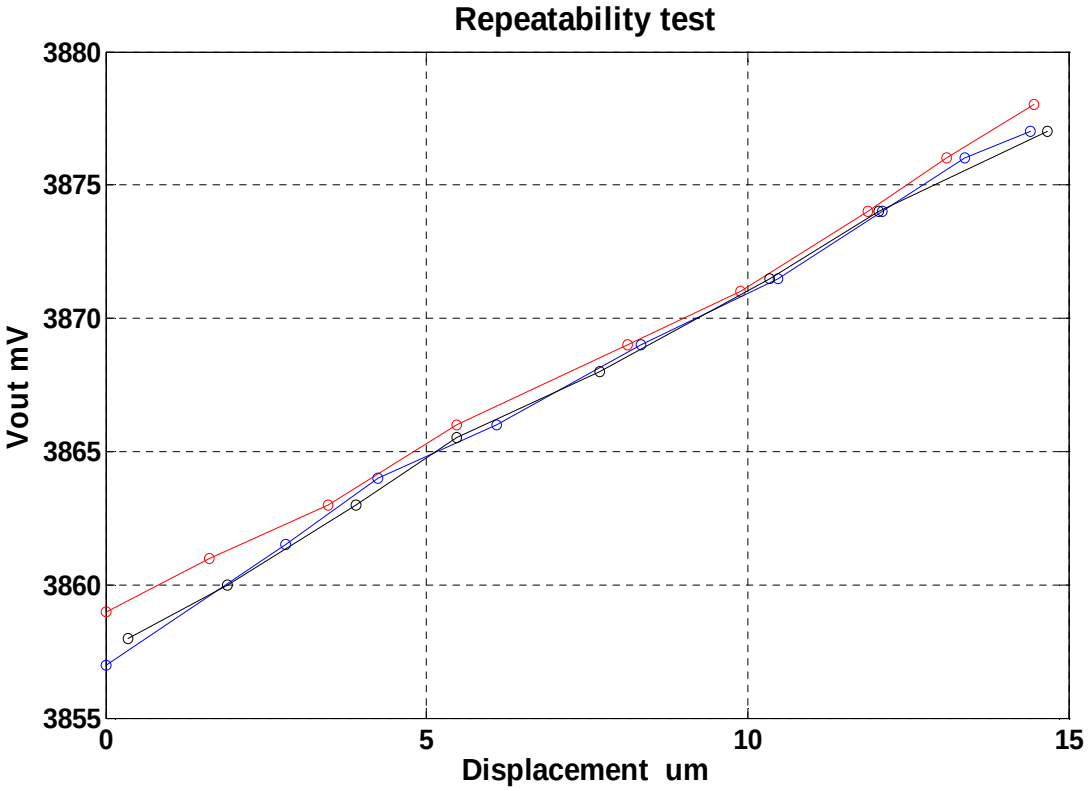

Figure 5.29: Three repeatability test in a set on a specimen (Test 1 in Table 5.4)

5.9 Preliminary results and summarized performance

A typical sensitivity of about 20 mV/µm of the capacitive gauge could be acquired after carefully installing the capacitive electrodes with a nominal gap *G* of a few hundred µm. The linearity error was never exceeding 0.8% where the full scale of calibration was up to 40 µm. The lateral parasitic motion was only a few tens of nanometres and the Abbe offset error introduced by the rotational notch was less than 0.1% of the full scale. The test-rig was run under the constant temperature of 20±2 °C and no significant temperature drift was detected. Table 5.5 summarises the performance of the test-rig.

Table 5.5: The summarized performance of test-rig

Parameters	**Performance**
Sensitivity	20.48 mV/µm
Noise Level	2 mV at 50Hz (After filtering)
Effective Resolution	≤0.1 µm at 50 Hz
Repeatability	93%

The primary determining factor of resolution was the electrical noise which appears in the output voltage causing small instantaneous errors in output. The electrical noise was inherent in electrical components and cannot be eliminated but it can be minimized by careful designs and noise filtering. The aluminium flexure spring was grounded and the wiring around the capacitive gauge was carefully fixed. Extra noise filtering using a Butterworth Filter was carried out in the Labview software. Since the typical sensitivity

of the capacitive gauge was 20.48 mV/µm, and a typical noise level of 2 mV could be obtained at 50 Hz which meant that the output could have an uncertainty of 0.1 µm. Thus, an effective resolution of sub-micrometre could be achieved in the test-rig.

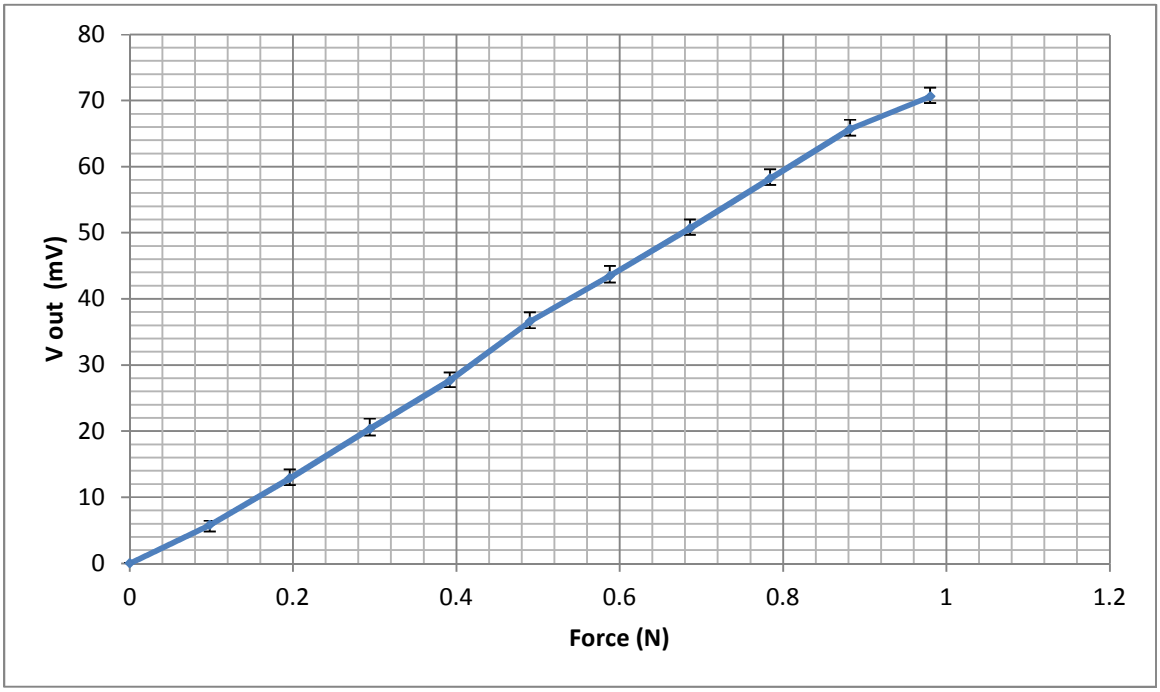

Figure 5.30: The preliminary tensile test results on a typical tensile specimen

The hinge notch spring and the capacitive gauges were calibrated to have a stiffness of 231 kN/m and a sensitivity of 20.48 mV/µm. The typical dimension of a test beam was measured to be 1×0.48×0.087 mm^3 (see Table 5.2). Preliminary repeat testing seven times over an Envisiontec R11 specimen is given in Figure 5.30, indicating a scatter value absolute Δ of about ± 2.5% within maximum load of 0.98 N (See appendix A for detail). Approximately 3.45 µm extensions (corresponding 70.61 mV voltage reading) could be obtain with an overall tensile load of 0.98 N, indicating that about 0.168 N load was applied to the sample. Thus, according to equation 5.3, the Young's modulus of the specimen was given as

$$E = \frac{(F - \lambda_f \delta) l}{\delta A} \approx 1.12 \times 10^9 \text{ Pa}$$

Thus, a typical Young's modulus of 1.12 GPa was measured. This was clearly in the right order compared to the reported polymer values (Cheah 1997) and the test-rig produced a highly repeatable result on a typical specimen (see Appendix A for details). It provided additional confidence that the whole system functions as designed.

5.10 Verification of the tensile results using Deben Micro-test modulus

There is insufficient engineering data about the Young's modulus of R11 resin under small scale conditions, and the elastic value of the material varies to a certain extent from different micro-characterisation methods. In order to provide reference value for the tensile test result, another characterisation was carried out using a commercial Deben microtest module with a similar methodology (Figure 5.31). The Deben microtest module is based on a tensile/compression/bending step motor-driven stage primarily designed for use in confined space such as SEM chamber (Deben 2005).

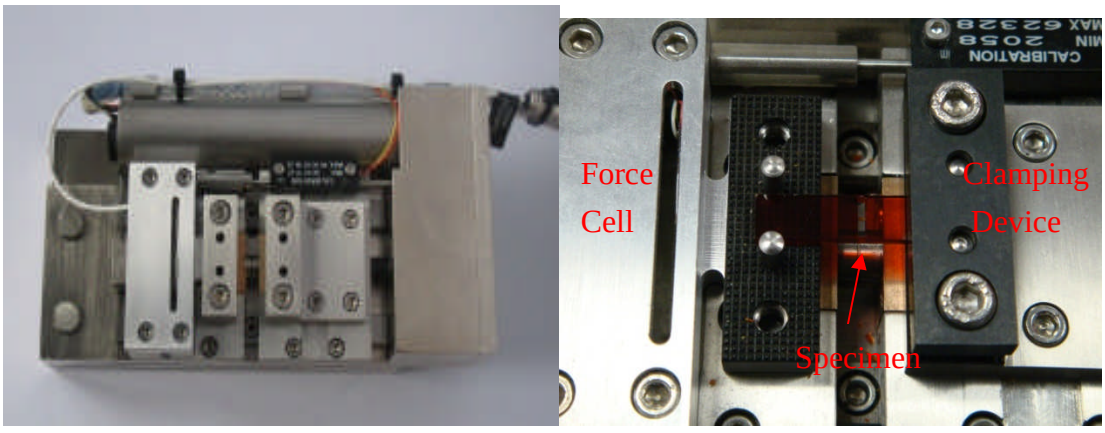

Figure 5.31: The 2kN Deben Tensile compression and horizontal bending stage (left) and specimen mounting (right)

The Deben microtest module employs a stepper motor to applying a tensile load up to 2 kN to deform the specimens. The motor speed is controlled by optical encoders from 0.55µm/s to 6.67µm/s with sample time from 100 ms to 5 s. The force reading comes through a custom miniature load cell of 660 N embedded into one end of the moving stage (Figure 5.31). The strategy for mounting specimen is to use hard mechanical jaws clamping on each ends of the specimen. At first, the specimen is horizontally mounted onto the stage and hard clamped by a pair of mechanical jaws that are supported on stainless steel slide bearings. A dual threaded leadscrew drives the jaws symmetrically in opposite directions, keeping the specimen centrally aligned. A summary about the performance of Deben tensile stage is given in Table 5.6.

Table 5.6: Typical performance of the Deben microtest module

Module type	**2KN tensile tester**
Loadcell calibration value	660 N
Gear box	1526:1
Minimum step motor speed	0.55 µm/s
Minimum sample time	100 ms
Extensometer range	2058 – 62328 µm
Gap distance	10 mm

Applying the same specimen design strategy for the MSL tensile test, the specimens for Deben microtest module (Figure 5.32) was similar to the ones used in the previous tensile test-rig with bulk end regions for clamping and built-in protection bars at each side. The thickness was designed to be 2 mm and the curing exposure was set to be 9.5 s in order to obtain a high flatness. The test-beam in the central had the same dimension of $1\times0.5\times0.1$ mm^3 with bulk end dimension of $27\times6\times2$ mm^3 to fit the dimensions of the mechanical jaws.

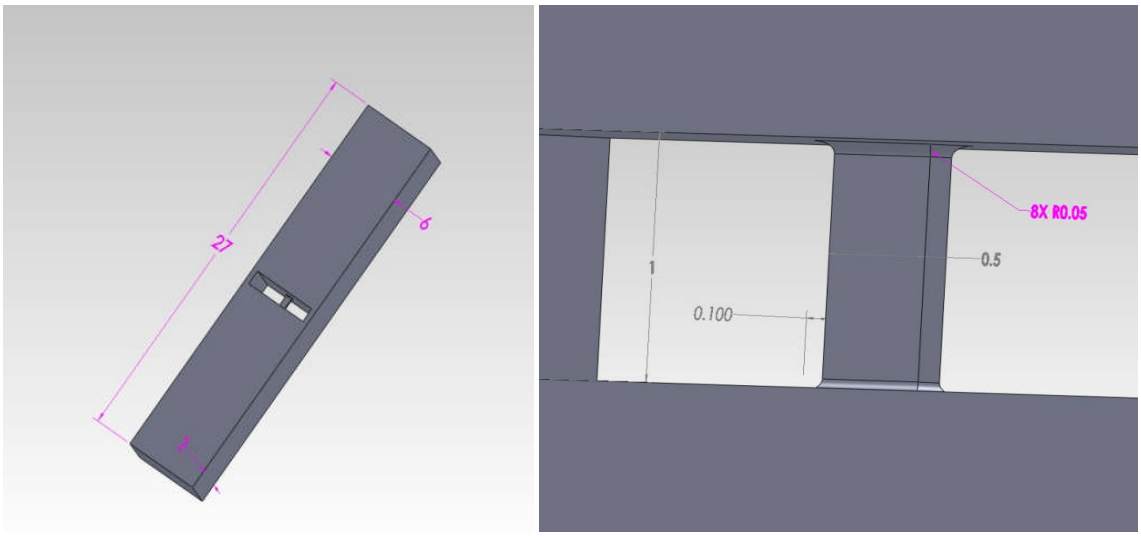

Figure 5.32: The dimensions of a specimen for Deben microtest module

The Deben microtest module allows real time observations of the mechanical behaviour of different samples (Figure 5.33). The rigid hard mechanical jaws clamping in the Deben microtest modules introduce substantial stress to the specimen after the screw is firmly tightened. Therefore, the specimen protected structure should be gently cut-off to release

the specimen and the loadcell offset should also be re-set after mounting. During the test, the step motor runs to exert a steadily increasing force upon the sample.

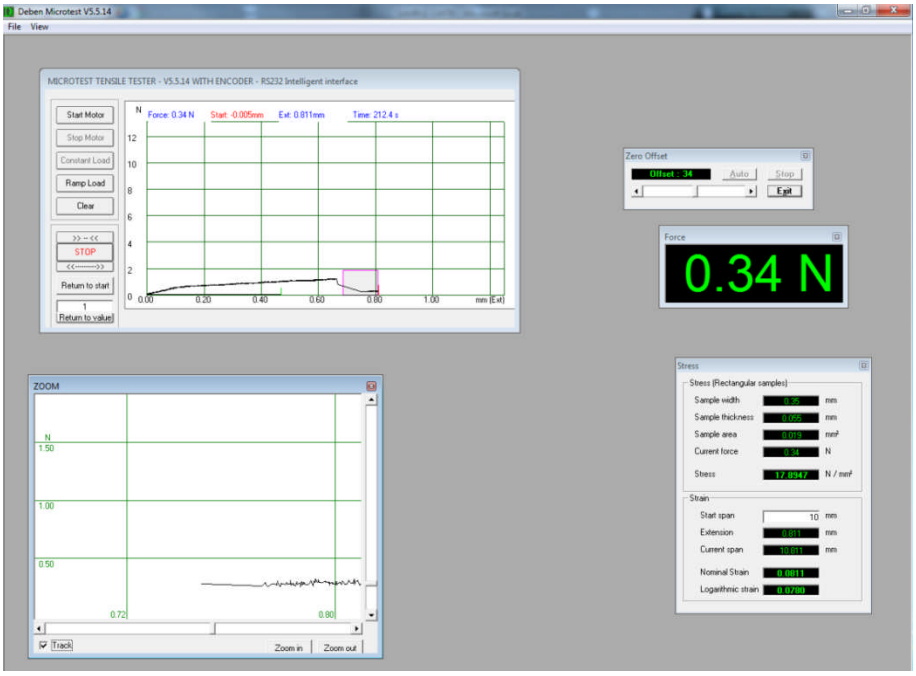

Figure 5.33: The interface of Deben microtest module software

The stress-strain result of the specimen is shown in Figure 5.34. The Young's modulus of the test beam was measured as about 0.8 GPa within the strain of 0.1, namely 100 µm elongation. This test result from Deben microtest module agreed broadly with the value of preliminary result from the new tensile test-rigs. It was observed that with faster rate of increasing load the specimen tended to be broken early.

This additional test can be used only as general confirmation that the new test-rig behaved consistently with these materials, because it had inherent disadvantages as well as good features. The Deben microtest module can take a wide range of loadcells and is capable of producing a full-view of tensile stress-strain behaviour of MSL specimens, where as the new tensile test-rig had limited force range of a few newtons because of the

relatively high stiffness flexure spring. Similar to the previous specimen clamping strategy, the specimen under hard clamping was likely to be subject to large external stress, which might not be so well accommodated by smaller areas. The large face-to-face mechanical jaw clamping required an extremely high flatness and can result in uncertainty in the early off-setting process. Small wobbles had been observed sometimes in the initial stress region due to the uncertainty in the hard clamping. Moreover, the accuracy of this method was limited by the step-motor precision which was only a few tens of micrometre level.

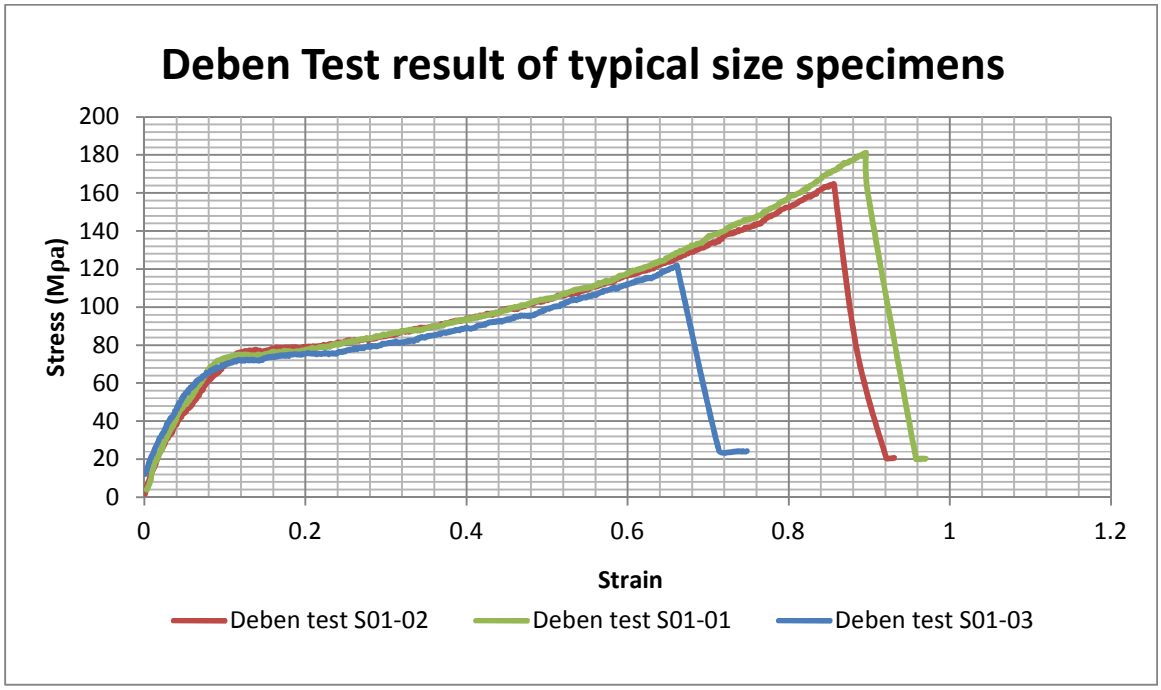

Figure 5.34: The test of typical beam Deben result (S01-02 0.55μm/s; S01-01 1.66 μm/s; S01-03 3.33μm/s)

5.11 Conclusion

The new test-rig offered a practical solution to the unusual challenges of the current measurements. Dividing applied load between the delicate sample and a guide flexure provided robustness to protect the delicate specimen. The flexure allowed an operationally useful Abbe offset in the extension measurement: attaching small capacitors directly to the specimen, as used here for calibration, was impracticably slow and tedious for routine use. The specimen design worked well with friction clamping followed by cutting of the support structures. There was no evidence of slippage at the clamps sufficient to significantly degrade extension measurements. Nevertheless, over-constraint of the specimen was not ideal and further refinements will be explored in parallel with using the instrument to study MSL materials. The results from the Deben microtest module confirmed that this test-rig produced reliable results within small-scale elongations. The details of tensile tests on specimens under various fabricated conditions will be described in Chapter 6.

References

Chattopadhyay, D. K., S. S. Panda, et al. (2005). "Thermal and mechanical properties of epoxy acrylate/methacrylates UV cured coatings." *Progress in Organic Coatings*, **54**(1), 10-19.

Cheah, C.M., Fuh, J.Y.H., Nee, A.Y.H., Lu, L., Choo, Y.S. and Miyazawa, T. (1997). “Characteristics of photopolymeric material used in rapid protypes part II. Mechanical properties at post-cured state”, *Journal of Materials Processing Technology*, **67**, 46-49.

Czichos, H., Saito, T. and Smith, L. eds. (2006). *Springer handbook of materials measurement methods*, Springer, Heidelberg, Chapter 7, 281-397. ISBN: 3540207856.

Deben (2005). 2KN and 5KN tensile compression and horizontal bending stage user manual, Deben UK Limited, Suffolk, UK.

Envisiontec (2007). Envisiontec Perfactory R5 – R11 Material Documentation, Edition 2007, Envisiontec GmbH, Gladbeck, Germany.

Keyence user manual for surface scanning laser confocal displacement meter LT-9001 Series, (2004). Keyence Corporation, Osaka, Japan.

Marsh, D.S. (1961), "Micro-tensile test machine," *Journal of Scientific Instruments*, **38**, 229-234.

Nano Positioning system 2000 User's guide (1993), Queensgate Instruments LtD., Berkshire, England.

Renishaw XL-80 laser system documentation, (2007). Renishaw plc. Gloucestershire, UK.

Sharpe, W. N. Jr., Yuan. B. and Edwards, R.L. (1997a). "A new technique for measuring the mechanical properties of thin film," *J. Microelectromech. Syst*, **6**, 193-199.

Sharpe, W. N. Jr., La Van, D.A. and Edwards, R.L. (1997b). "Mechanical properties of LIGA-deposited nickel for MEMs transducers," *Proc. Int. Conf. Solid-state Sensors and Actuators Chicago June 1997,* 607-610.

Smith, S.T. and Chetwynd, D.G. (1992). *Foundations of ultraprecision mechanism design*, Gordon and breach science publishers S.A, Switzerland, Chapter 4, 95-128. ISBN: 288490019.

Smith, S.T., Chetwynd, D.G. and Bowen, D.K., (1988). "The design and assessment of high precision monolithic translation mechanism", *J. Phys. E: Sci. Instrum.*, **20**, 977-983.

Wilson, J.S. (2005). *Sensor technology handbook*, Elsevier Inc. Oxford, Chapter 8, 193-222. ISBN: 0750677295.

Chapter 6: The tensile results of MSL specimens

6.1 Introduction

The complicated nature of photopolymerisation and the considerable number of variables involved in MSL processes become potentially more difficult under small scales. Thus careful mechanical characterisation of MSL specimens could produce analytical experimental data for better understanding of fabrication processes and material properties. As this chapter reports, different sizes of small MSL specimens made from Envisiontec R11 resin formulation under different UV exposures were fabricated and tested using the tensile test-rig described in Chapter 5. The discrepancy between design dimension and the resulting geometry of MSL specimen is firstly measured and discussed. The tensile test results on the Young's modulus are presented with comments on the mechanical behaviour of different specimens under different UV exposures. It is not within the scope of this work to give a thorough explanation how these fabrication parameters affect the resulting mechanical properties of specimen. Experimental data of representative acrylate-based MSL materials are presented to gain better understandings and useful insights of the fundamental process of MSL technology.

6.2 Dimensional consistency

The dimensions of specimens pre-set in the CAD systems could not be fully trusted due to the significant shrinkage and curl distortion in small size MSL specimens. Since the Young's modulus of the tensile test result is derived from the resulting geometry of specimens (See section 5.2), a precise measurement of the resulting specimens before the

test is required to eliminate the dimensional uncertainty. Specimens under different fabrication conditions and different size were examined and investigated here to give a general idea of specimen shrinkage under different conditions. The length and width of a test beam were measured by placing the specimen cell under a Nikon digital microscope and the thickness was gauged by a Keyence confocal laser sensor, using the techniques discussed in the section 5.6.2.

This section first explores the geometry discrepancy due to the fabrication processes by measurements on test beams having a thin specimen cell (1 mm thickness) in the green-state stage, immediately after post-curing stage and as the final form after a long-time period. It then examines resulting dimension of specimens of different sizes and specimens fabricated under different UV exposures (Table 6.2 Specimen 2.1-2.12). These specimens were used for the later tensile tests.

6.2.1 Geometry discrepancy over the fabrication process

The shrinkage and curl distortion have been the major hurdles in the improving the MSL part accuracy. These effects when using Envisiontec R11 resin formulation significantly changed the dimensions of designed MSL specimens, particularly the thickness. The shrinkage occurred simultaneously when the polymerisation process began and went through the whole build-curing process (Narahara, 1999). These specimens experienced another thermal expansion and shrinkage during the post-curing stage. After post-curing, the specimens were placed in a dark cupboard but still suffered from residual internal stress, resulting in further shrinkage and curl-distortion. In this section, a measurement of

the geometry of test specimens during different fabrication stages was conducted to give general observations of shrinkage and curl distortion effects during the fabrication processes.

Specimens having the same nominal dimensions were fabricated for geometry measurement with curing UV exposures of 3.0, 3.5, 4.0, 6.0 and 9.5 s: in all case the burn-in exposure was 9.5 s. In order to demonstrate the curl distortion effect on thin MSL specimens more clearly, the thickness of the bulk ends was set to be 1 mm so that these specimens are more subjected to curl distortion. The same principle applied to the dimension of test beams, and test beams with small typical size of 1/0/5/0.1 (L/W/T) mm were fabricated, which represented the smallest test beams that could be reliably fabricated. The geometry of these test beams was immediately measured after removal from MSL platform and re-gauged after post-curing the specimens for 20 seconds in Otoflash box. The specimens were then placed in a dark cupboard for at least two days before final dimension measurements prior to the tensile test. The results of dimensional measurements are shown in Table 6.1.

As shown in Table 6.1, the lengths of all test beams in this particular specimen design were close to the designed value during the fabrication processes since most of the longitudinal shrinkage occurs in the bulk ends. On the other hand, the width and thickness were much reduced due to the shrinkage in MSL process. The greatest shrinkage occurs during the build curing process and it reduced the width by about 10% and thickness by about 20%. According to Huang (2003), the shrinkage rate of stereolithographic material is a function of average exposure energy. The dimensions of specimens under higher UV exposures (specimen 1.4 and 1.5) were the most reduced,

particularly the thickness, which was consistent with this research. Specimens under higher UV exposures have absorbed more UV energy, resulting in higher shrinkage ratio during the cooling. It was noticed that specimens of higher exposure showed higher flatness and therefore more consistent values of resultant geometry.

Table 6.1: The resulting geometry of test beams (1/0.5/0.1) at different stages (repeatability is quoted at one standard deviation)

	Measured specimen dimension (L/W/T: mm)				
	Specimen 1.1	Specimen 1.2	Specimen 1.3	Specimen 1.4	Specimen 1.5
Exposure (Cure and burn-in)	**(3.0, 9.5 s)**	**(3.5, 9.5 s)**	**(4.0, 9.5 s)**	**(6.0, 9.5 s)**	**(9.5, 9.5 s)**
After curing	**1.00/0.46/0.081 (0/±1.6%/±1.9%)**	**1.00/0.45/0.080 (0/±1.0%/±0.75%)**	**1.00/0.45/0.076 (0/±1.7%/±1.1%)**	**1.00/0.45/0.070 (0/±1.6%/±0.7%)**	**1.00/0.45/0.072 (0/±1.4%/±0.42%)**
After post-curing	**1.00/0.43/0.080 (0/±2.1%/±2.5%)**	**1.00/0.45/0.078 (0/±0.88%/±1.1%)**	**1.00/0.45/0.072 (0/±1.6%/±0.92%)**	**1.00/0.44/0.070 (0/±1.35%/±1.1%)**	**1.00/0.45/0.072 (0/±1.3%/±0.56%)**
After 2 days	**1.00/0.38/0.077 (0/±1.7%/±2.0%)**	**1.00/0.40/0.077 (0/±1.6%/±1.1%)**	**1.00/0.43/0.071 (0/±1.7%/±1.2%)**	**1.00/0.43/0.068 (0/±1.6%/±1.1%)**	**1.00/0.43/0.071 (0/±1.3%/±0.65%)**

After post-curing these green-state specimens for 20 seconds, the width and thickness of specimen were further reduced. This was partly because specimens absorbed additional UV exposure energy and undergo further shrinkages. There was also noticeable, but smaller, additional shrinkage at the post-curing stage for shorter cure exposures, but less

change after higher cure exposures. The same trend was there (slightly) with the “rested” specimens. These phenomena suggested that low cure exposure specimens were more likely to continue to absorb light energy after curing and suffer additional shrinkage. Overall the high initial exposure seemed to cause more total shrinkage than the total set of process for the low exposure. Another factor accounting for the dimension reduction after post-cure was curl distortion. After the polymerisation, the green-state specimens usually had a good flatness. However, these specimens (particularly specimen 1.1, 1.2 and 1.3) exhibited visible curl distortions after post-curing stage (except for the uniform curing specimen 5). During the thickness measurement, greater non-uniformity on test beam had been spotted in specimen 1.1 and 1.2 by using the Keyence sensor to scan over the gauge length, which further confirmed the occurrence of the curl distortion (The thickness of curled specimens was measured in the mid-span beam when lower values were obtained). The curl distortion further reduced the geometry of test beams, particularly the thickness. This could be a reasonable explanation for why the thickness was more reduced than the width after the post-curing.

After a few days, the shrinkage and curl distortion occurred and further reduced the width and thickness. In the process of polymerisation, the molecular weight and cross-linking of monomer during the phase transition in the photopolymer form liquid state to solid states were likely to increase when the UV exposure rises, resulting an increase of strength of polymers (Huang 2003). Thus, the mechanical strength of specimen 1.1, 1.2 and 1.3 were relative low due to the low cure exposure and these specimens were more vulnerable to curl distortion. Moreover, as mentioned in Chapter 4, the larger difference of UV exposure between the burn-in range layers and curing layers of these specimens was

another major factor contributing to the severe curved behaviour. Severe curl distortion had occurred on specimen 1.1 and 1.2. The test beams were stretched or even significantly deformed. Pictures of specimen 1.2 taken in three stages are given in Figure 6.1 to illustrate the significant effect of curl distortion during the processes.

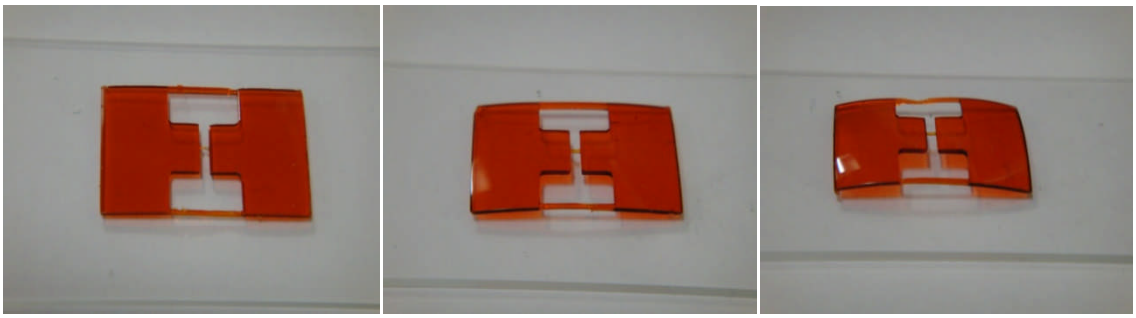

Figure 6.1: Images of specimen 1.2 immediately after curing (left), immediately after post-curing (mid) and after two days of storage (right)

The shrinkage and curl distortion had been significant issues in thin MSL specimens. The shrinkage reduced the geometry of small test beam significantly during the curing stage. The shrinkage ratio rose with increasing UV exposure. After the post-curing stage, the curl distortion became more significantly and further reduces the beam dimensions. The shrinkage and curl distortion continually reduced the geometry of resulting specimens over two days. Specimens with lower UV exposures were more subjected to curl distortion, which could significantly deform or damage the test beams. Thus the test beams in 1 mm thickness specimen cells were not suitable for tensile test and much less curved specimens with bulk ends of 2 mm were fabricated for the later tensile tests and discussed in the rest of this chapter.

6.2.2 Dimensional measurement for MSL tensile specimens

A second set of specimens was made to investigate the tensile properties of MSL specimens under different fabrications conditions (see Table 6.2). In order to obtain specimens without severe curl distortion for later tensile testing, the thickness of whole specimen cell was set to be 2 mm. Specimens 2.1-2.6 were fabricated for investigating the mechanical properties of the test-beams of different size and specimens 2.5, 2.7-2.12 were fabricated for testing specimens under different UV exposures. Each specimen contained two test-beams made in parallel.

Table 6.2: List of test specimens fabricated under different conditions

Specimens	Working-section dimension (L/W/T mm)	Exposure time (s) (curing and burn-in range exposure)
Specimen 2.1	5.0/2.0/0.5	3.5-9.5
Specimen 2.2	2.0/1.0/0.2	3.5-9.5
Specimen 2.3	1.0/1.0/0.2	3.5-9.5
Specimen 2.4	1.0/0.5/0.2	3.5-9.5
Specimen 2.5	1.0/0.5/0.1	3.5-9.5
Specimen 2.6	1.0/0.2/0.1	3.5-9.5
Specimen 2.7	1.0/0.5/0.1	3.0-9.5
Specimen 2.8	1.0/0.5/0.1	4.0-9.5
Specimen 2.9	1.0/0.5/0.1	6.0-9.5
Specimen 2.10	1.0/0.5/0.1	9.5-9.5
Specimen 2.11	1.0/0.5/0.1	3.5-6.0
Specimen 2.12	1.0/0.5/0.1	6.0-6.0

Scaling effects were known to be a potentially major issue in the mechanical characterisation fields. Different kinds of effects of size on the mechanical properties have been reported in literature, but there has not been a unified theory that explained all the effects (Simon 2006). Regarding this complexity, all experimental investigation of the mechanical properties of MSL specimens must include careful geometry measurements of test beams; nominal dimensions cannot be used safely. Specimens with maximum size of 5/2/0.5 (L/W/T) mm and minimum size of 1/0.2/0.1 mm (Specimen 2.1-2.6) were fabricated with the same standard exposure and the geometry of resulting specimens were carefully measured after two days of storage. The measurement of dimensions on the resulting test beam of different sizes is given in Table 6.3.

Table 6.3: The resulting geometry of test beams of different sizes (repeatability is quoted at one standard deviation)

Specimens	Designed dimensions (L/W/T mm)	Resulting dimension (L/W/T mm)	Exposure time (s) (curing and burn-in range exposure)
Specimen 2.1	5.0/2.0/0.5	5.00/1.95/0.368 (0/±0.0070/±0.021)	3.5-9.0
Specimen 2.2	2.0/1.0/0.2	2.00/0.98/0.158 (0/±0.0066/±0.0069)	3.5-9.0
Specimen 2.3	1.0/1.0/0.2	1.00/0.98/0.167 (0/±0.0049/±0.0014)	3.5-9.0
Specimen 2.4	1.0/0.5/0.2	1.00/0.48/0.167 (0/±0.0050/±0.0016)	3.5-9.0
Specimen 2.5	1.0/0.5/0.1	1.00/0.48/0.086 (0/±0.0049/±0.0007)	3.5-9.0
Specimen 2.6	1.0/0.2/0.1	1.00/0.19/0.095 (0/±0.0035/±0.0007)	3.5-9.0

The two test-beams in specimen 2.5 had similar designed dimensions with the test beam 1.2, but their resulting dimensions were much closer to the designed value. The curl distortion was much less significant in specimens fabricated with thicker bulk ends, which increases the fabrication accuracy, particularly the thickness. From Table 6.3, the resulting length of test beams of different sizes remained very close to design values while the width and thickness were reduced. A largely constant reduction ratio had been found in the width measurement, while the reduction of thickness was more significant when the dimension of the specimen increases. This was partly because the first few building layers of the test beam tended to fall off after curing due to the peel effect because a small layer thickness (25 μm) was used (Figure 6.2). This phenomenon became more prominent when building long-span test beams (Specimen 2.1 and 2.2). The typical standard specimen 2.5 had a shrinkage ratio of only about 11% while the specimen 2.1 with maximum size (5 mm long span) had a reduced thickness of about 0.38 mm which was only 75% of its designed value. The long specimen 2.2 (2 mm long span) also had a higher shrinkage of nearly 20%.

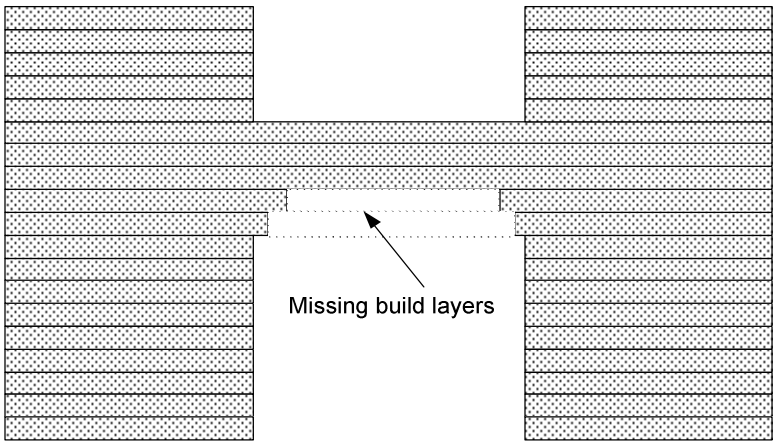

Figure 6.2: The mis build phenomenon in fabricating a test beam

The UV exposure was a significant factor in the polymerisation process. It can be expected that the UV exposure can affect the structure of polymer network being formed and influence the mechanical properties of finished parts (Hunziker 1992). The manufacturer recommended UV exposures were 3.5 s and 9.5 s for the curing layers and burn-in range layers (Specimen 2.5). These values were empirically derived and only ensured a sufficient cure ratio for curing layers and sufficient hardness for the specimen to be safely removed from the platform. There was scarce engineering data about Envisiontec R11 resin at different exposures, thus specimens under different exposures were fabricated and measured in this chapter. The minimum curing exposure was set to be 3.0 s since specimens fabricated with a UV exposure below this level were likely to fail due to the low cure ratio. Alternative burn-in range exposure of 6.0 s was used (Specimen 2.11 and 2.12). These specimens were generally very fragile. The result of geometry measurement on specimens fabricated under different UV exposures was given in Table 6.4.

From Table 6.4, specimens with higher UV exposures (2.10 and 2.9) were likely to have more reduced width and thickness than specimens with lower UV exposures (2.5 and 2.7). Comparing specimens 2.5, 2.7-2.10 with specimens 1.1-1.5, the dimensions of test beams from thick specimen cells (2 mm) were less reduced than those of their counterparts from thin specimen cells (1 mm). However, specimen 2.5 and specimen 2.7 still exhibited a visible curl distortion due to the large difference between curing layer and burn-in range layer. Particularly, the specimen 2.7 had the lowest cure ratio and was likely to have the lowest mechanical strength (among 2.5 2.7-2.10) to resist the curl distortion. Thus,

specimen 2.7 had more severe curl distortion than the typical specimen 2.5, which resulted in a further reduction in the thickness.

Table 6.4: Specimens fabricated under different UV exposures (repeatability is quoted at one standard deviation)

Specimens	Designed dimension (L/W/T mm)	Resulting dimension (L/W/T mm)	Exposure time (s) (curing and burn-in range exposure)
Specimen 2.7	1.0/0.5/0.1	1.00/0.47/0.084 **(0/±3.08 %/±2.28 %)**	3.0-9.5
Specimen 2.5	1.0/0.5/0.1	1.00/0.48/0.086 **(0/±1.03 %/±0.87 %)**	3.5-9.5
Specimen 2.8	1.0/0.5/0.1	1.00/0.47/0.085 **(0/±1.14 %/±1.60 %)**	4.0-9.5
Specimen 2.9	1.0/0.5/0.1	1.00/0.45/0.081 **(0/±1.09 %/±1.02 %)**	6.0-9.5
Specimen 2.10	1.0/0.5/0.1	1.00/0.45/0.080 **(0/±1.10 %/±1.25 %)**	9.5-9.5
Specimen 2.11	1.0/0.5/0.1	1.00/0.40/0.068 **(0/±2.96 %/±3.35 %)**	3.5-6.0
Specimen 2.12	1.0/0.5/0.1	1.00/0.44/0.074 **(0/±1.44 %/±2.15 %)**	6.0-6.0

On the other hand, the dimensions of specimen 2.11 and 2.12 with low burn-in range exposure were much more reduced. These test beams were more likely to be stressed or damaged when the specimens were removed from the platform due to the relative low curing exposure of the burn-in range layers. These two specimens were also tended to be

relatively weak and suffered curl distortion more significantly than their counterparts using 9.5 s (specimen 2.5 and 2.10). Thus, these two specimens were more fragile and curled which required extra precautions in the later tensile testing.

In summary, thin MSL specimens underwent significant shrinkage during the UV curing. After post-curing, the curl distortion became more significant and further reduced the dimension of specimens with shrinkage. These effects continually reduced the dimension over a few days and result in a substantial discrepancy between the design geometry and resulting specimens. The shrinkage ratio of test beams rose when the UV exposure increased and the curl distortion became more prominent when the difference of UV exposure between the curing layers and burn-in layers were larger. The curl distortion effect could be much suppressed by making the specimen cell relatively thicker. Also, specimens with higher exposure tended to have higher mechanical strength to resist the curl distortion.

6.3 The Young's modulus of differently fabricated specimens

In this section, a set of specimens fabricated under different conditions were examined using the tensile test-rig (Figure 5.1). Standard weights ranging from 10 g to 1 kg were used to apply the driving force, F, from 0.098 N to 9.8 N respectively. As discussed in Chapter 5, two parallel spring concept was employed in the tensile test-rig. The flexure notch used for the tensile test was calibrated to have a stiffness λ_f of 231 kN/m. Thus the stress was calculated as

$$\sigma_{Specimen} = \frac{F - \lambda_f \delta}{A} \tag{6.1}$$

where the A was the area of cross-section and δ is the elongation. The strain was simply given as

$$\varepsilon_{specimen} = \frac{\delta}{L} \tag{6.2}$$

The deadweight was firstly increased 10 g per time up to 100 g, and then increased 100 g per time. The stress-strain curve of the first 10 load steps on a typical specimen (specimen 2.5) is given firstly in Figure 6.3. The specimen exhibited a smooth and mostly linear stress-strain curve which would further proved that the clamping was likely to be reliable and without slip. The full view of tensile test result is shown in Figure 6.4 which indicated that the specimen was clearly within the elastic region (Figure 6.4). The Young's modulus of this specimen was approximately 0.9 GPa within 1% strain.

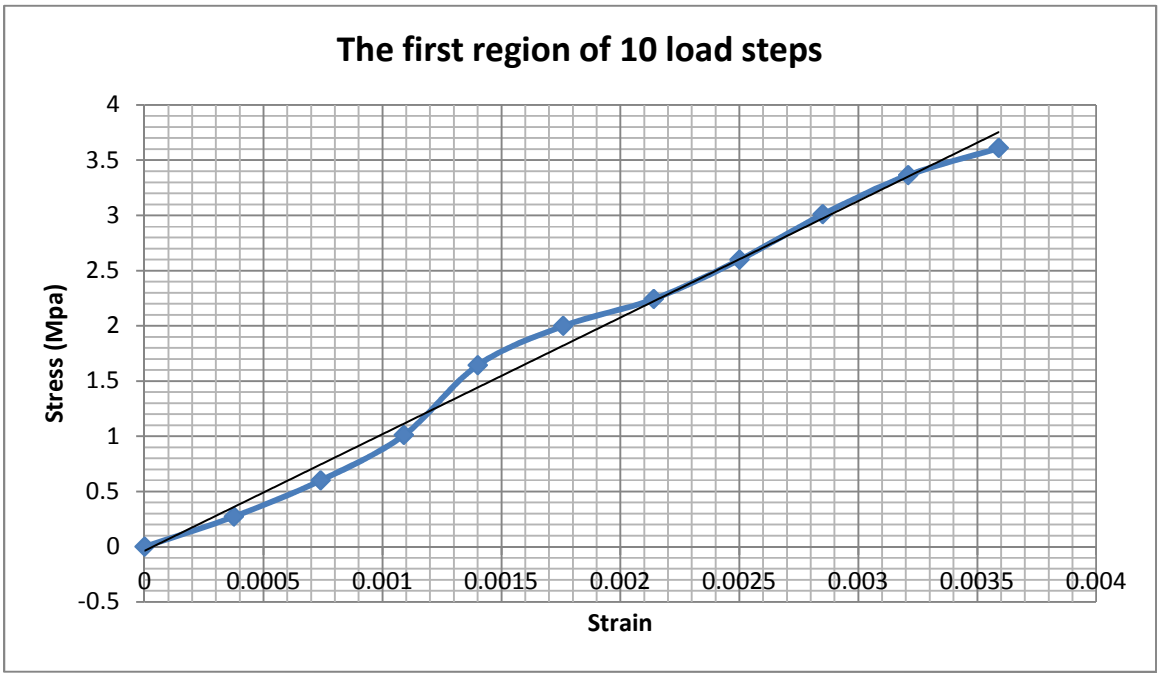

Figure 6.3: The initial stress-strain curve of the first 10 load steps on specimen 2.5

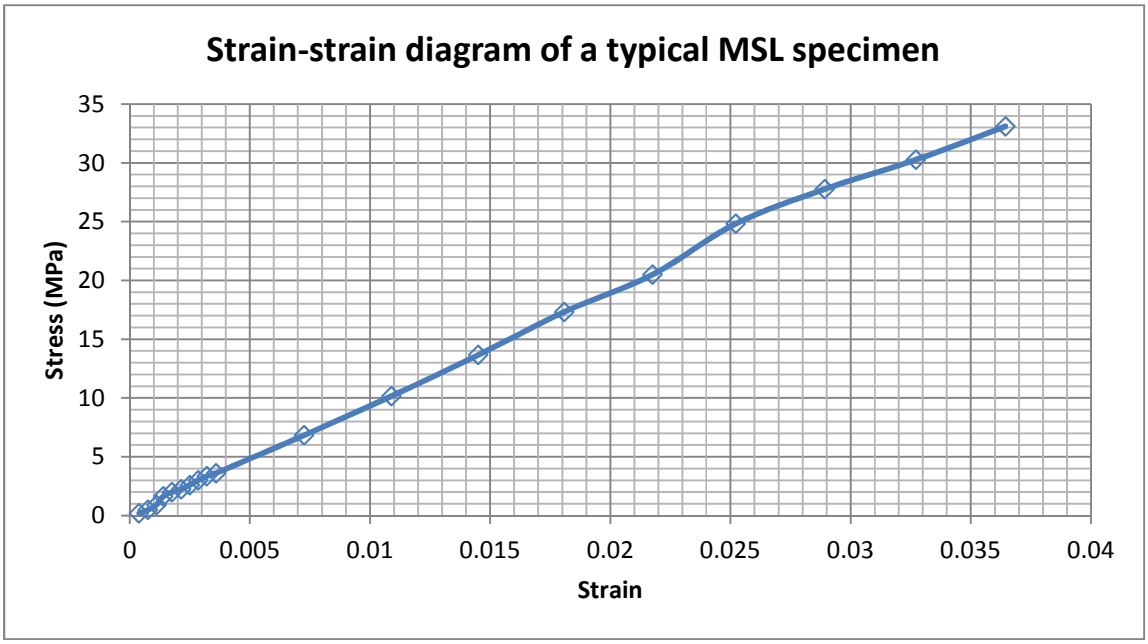

Figure 6.4: Tensile test result on specimen 2.5

6.3.1 Tensile tests on specimens of different sizes

Specimens of different sizes (specimens 2.1-2.6) were fabricated and tested using the new tensile test-rig to investigate the potential size effects on the mechanical properties of thin MSL specimens. As discussed in the previous section, the dimensional error can directly affect the resulting stiffness of specimens (See Equation 6.1). Despite of the near 2%¬3% uncertainties in dimensional measurement, the stress-strain curve of test beams showed steadily and consistent slope (See appendix D for details). The stress-strain diagram of these specimens is shown in Figure 6.5.

Figure 6.5 summarises the size dependence of the mechanical behaviour of thin test beams made of Envisiontec R11 resins. A clear size-dependence on the mechanical behaviour of MSL test beams fabricated under the same conditions can be observed. Test beams with smaller dimensions (Specimen 2.5 and 2.6) had significantly higher values of

Young's modulus than specimens 2.1-2.4 (Table 6.5). The elastic behaviour of specimens 2.1-2.4 was largely consistent. A significant difference occurred between specimen 2.4 and specimen 2.5 where the thickness was decreased from 0.2 to 0.1 mm. A similar, slightly smaller, jump in mechanical properties happened when the width was changed from 0.5 to 0.2 mm. Besides, The Young's module of specimen 2.1 ~2.4 had a higher repeatability than those of specimen 2.5 and 2.6, suggesting that the smaller specimens (2.5 and 2.6) were more susceptible to stress or damage either during the fabrication or during the measurement.

Table 6.5: The Young's modulus of specimens of different sizes (repeatability is quoted at one standard deviation)

	Measured Young's modulus of specimens (MPa)					
	Specimen2.1	Specimen2.2	Specimen2.3	Specimen2.4	Specimen2.5	Specimen2.6
Dimensions (L/W/T mm)	5/2/0.5 (5/1.94/0.38)	2/1/0.2 (2/0.98/0.16)	1/1/0.2 (1/0.98/0.16)	1/0.5/0/2 (1/0.48/0.16)	1/0.5/0.1 (1/0.48/0.087)	1/0.2/0.1 (1/0.19/0.095)
0.5% strain	301 (± 2.18%)	320 (± 1.98%)	340 (± 2.56%)	360 (± 1.78%)	920 (± 3.26%)	1200 (± 3.44%)
1% strain	322 (± 2.23%)	310 (± 2.04%)	321 (± 2.45%)	380 (± 2.19%)	915 (± 3.45%)	1220 (± 3.08%)
1.5% strain	306 (± 2.02%)	323 (± 2.11%)	322 (± 2.55%)	370 (± 1.97%)	940 (± 3.30%)	1200 (± 3.15%)
2% strain	/	/	305 (± 2.34%)	380 (± 2.18%)	950 (± 3.11%)	1250 (± 3.88 %)

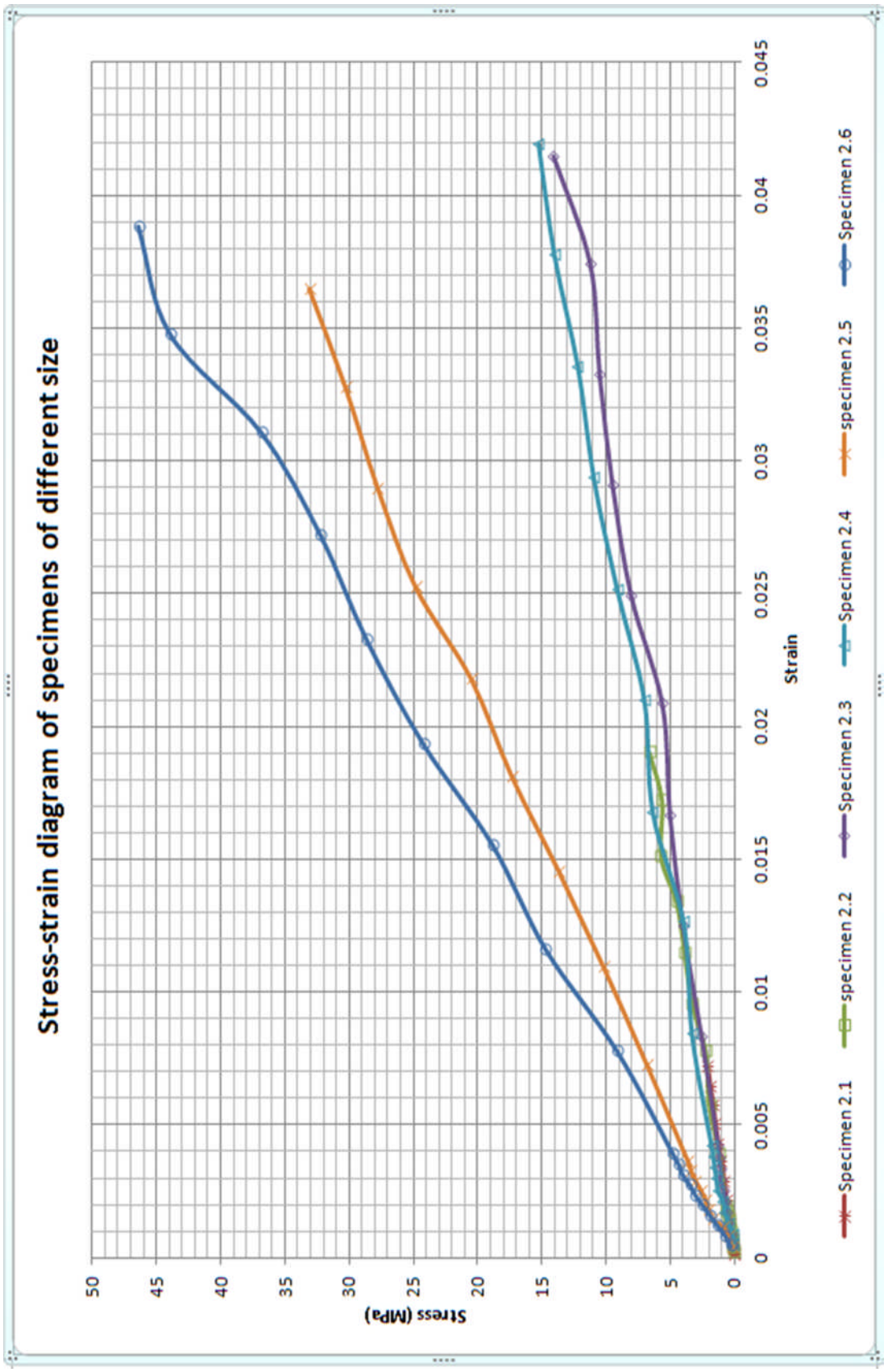

Figure 6.5: The stress-strain diagram of specimens of different size

This size effect could also be verified by using the Deben microtest module. Due to the stringent requirement of high flatness, specimens with same dimensions as specimen 2.1-2.5 but with 9.5 s UV exposure for both curing layers and burn-in range layers were fabricated to repeat the test (test beams equivalent to specimen 2.6 were too delicate and usually broken during the hard clamping process in Deben machine). The result of Deben tests on size effects is given in Figure 6.6. Regardless of the scattering of measurement values, a rough trend could be observed that the smaller test beams had higher modulus than the bigger ones. There was also a trend for smaller beams to have higher strength: smaller test beams (specimen 2.3, 2.4 and 2.5) had a similar fracture strain of about 74%, which was significantly larger that these of larger beam (specimen 2.1: 40%, specimen 2.2: 61% and specimen 2.3: 58%).

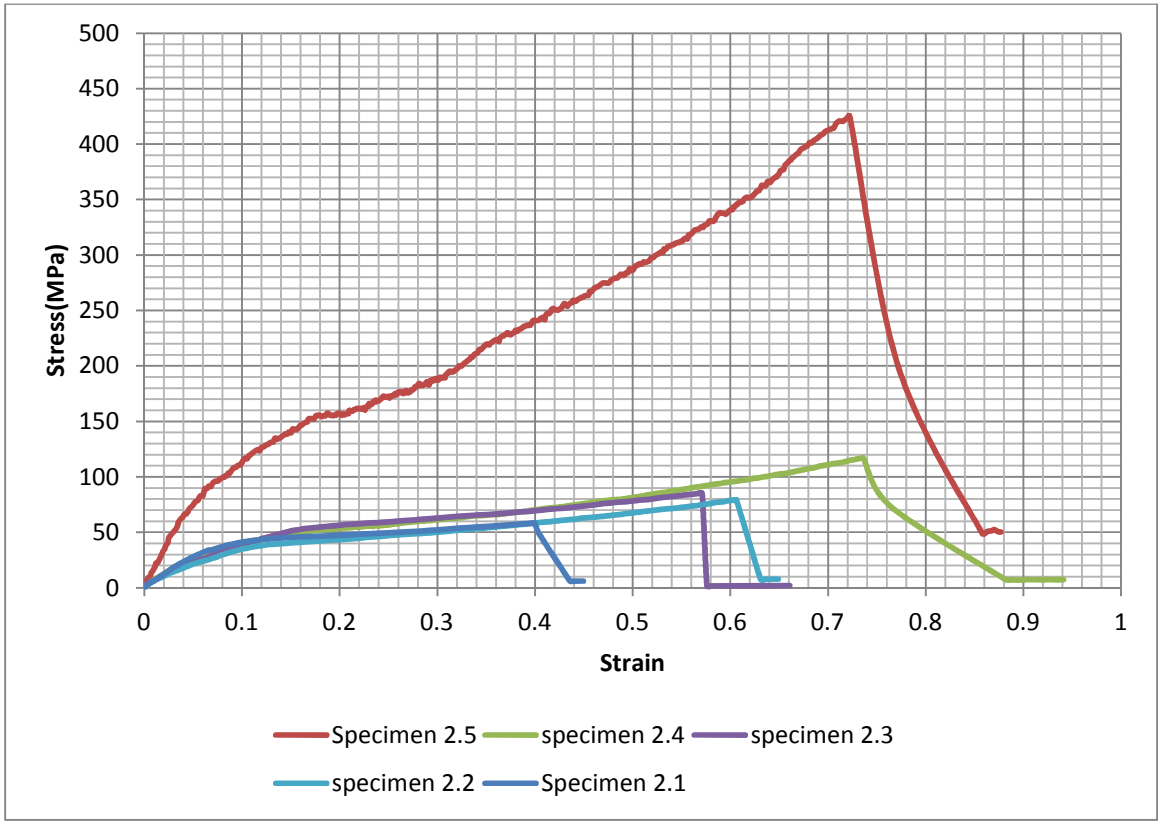

Figure 6.6: The stress-strain diagram using Deben machine

For the explanation of the size dependency on the mechanical properties, the combination of two factors may be considered. First, specimens with larger dimension (particularly the length) had difficulty in forming the first layers of test beam hanging over the two bulk ends. This mis build phenomenon (see 6.2.2) tended to decrease the success of building layers of large specimens and weaken the specimen. Moreover, MSL specimens were made in layer by layer style where the curing layer introduced peeling stress to the layer below during the thermal expansion and cooling stage. This peeling effect becomes more prominent for thicker specimens. A more detailed discussion will be provided in Chapter 7.

6.3.2 Tensile tests on specimens under different UV exposure

The UV exposure of MSL resins was a crucial factor which directly affected the mechanical properties of resulting specimens. The curing layers absorbed more energy when higher UV exposures were used, resulting in a higher cure ratio of resin and higher strength. Similar to the approach in section 6.3.1, specimens under different exposures (specimen 2.5, 2.7-2.12) were fabricated and measured for resulting geometry. There was a 4%-10% shrinkage ratio in width and 12% and 25% in thickness. The stress-strain curve of these specimens is given in Figure 6.7.

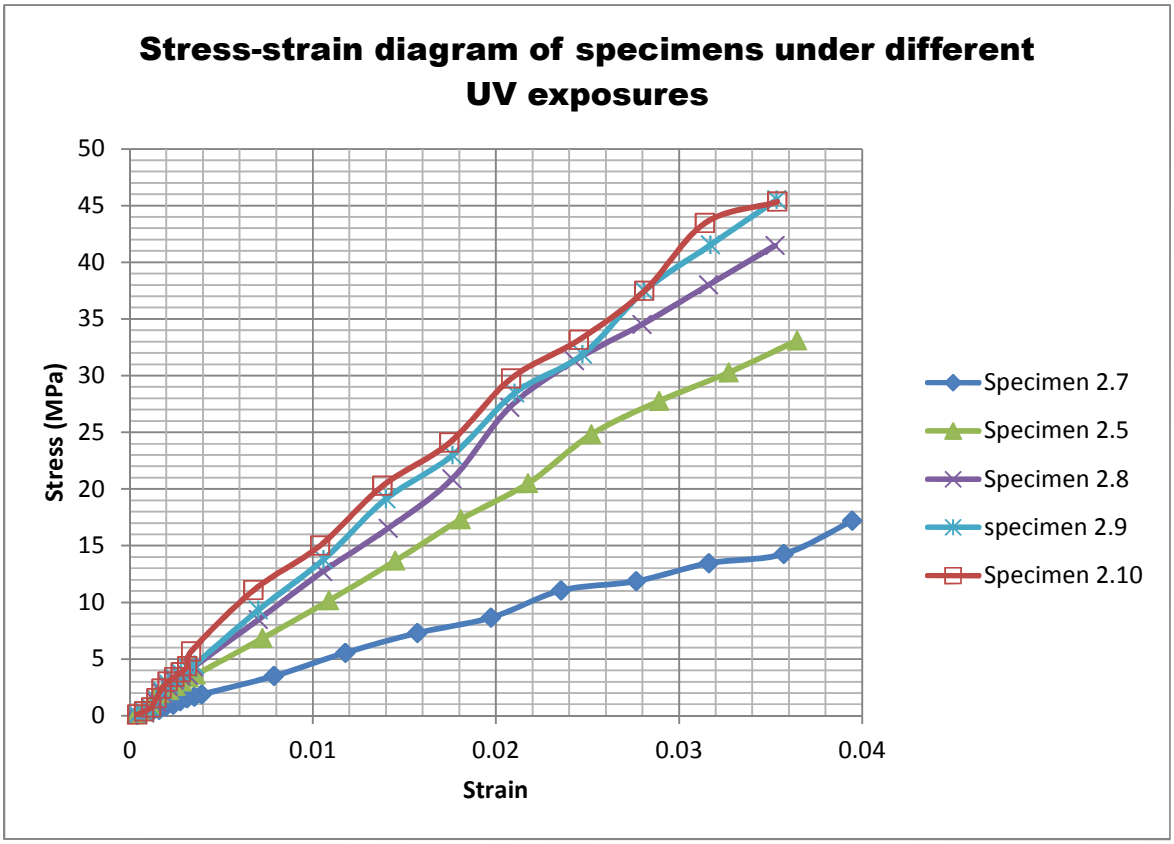

Figure 6.7: The stress-strain diagram of specimens under different UV exposures

Specimens 2.5, 2.7-2.10 were fabricated using UV exposures from 3.0 s to 9.5 s and a standard 9.5 s for burn-in range layers. Figure 6.7 shows that specimens using higher UV exposures were stiffer than those at lower exposures (specimen 2.5 and 2.7). The values of Young's modulus of each specimen are given in Table 6.6. The Young's modulus of the 3.0 s exposure specimen was only half of the standard curing process (specimen 2.5). After 4.0 s, the Young's modulus of higher specimens slowly increased which indicated a near saturation of UV absorption. In all, the recommend 3.5 s seemed a little low for fabricating small size specimens.

Table 6.6: The Young's modulus of specimens under different UV exposures (repeatability is quoted at one standard deviation)

	Young's modulus of specimens under different UV exposures (MPa)				
	Specimen 2.7	Specimen 2.5	Specimen 2.8	Specimen 2.9	Specimen 2.10
UV exposure	3.0 s	3.5 s	4.0 s	6.0 s	9.5 s
0.5% strain	420 (±5.33%)	980 (±3.26%)	1210 (±3.13%)	1270 (±2.03%)	1450 (±2.45%)
1% strain	445 (±4.72%)	930 (±3.45%)	1200 (±3.11%)	1320 (±2.31%)	1400 (±2.24%)
1.5% strain	468 (±4.66%)	933 (±3.30%)	1166 (±2.88%)	1333 (±1.98%)	1433 (±2.11%)
2% strain	435 (±4.21%)	945 (±3.11%)	1266 (±2.92%)	1380 (±2.12%)	1520 (±1.92%)

Specimen 2.11 and specimen 2.12 were fabricated using lower burn-in range exposures (6.0 s). In Figure 6.8, both 2.11 and 2.12 showed relative lower strength than their counterpart using higher burn-in exposure. The curl distortion phenomenon was more severe in them since they were relatively weak in strength and tend to suffer removal stress after curing. However, specimen 2.12 (6.0 6.0 s) showed a closer stiffness with specimen 2.9 (6.0 9.5 s) and 2.10 (9.5 9.5 s) which further confirmed that the radiation absorption is near to saturation absorption after 6.0 s.

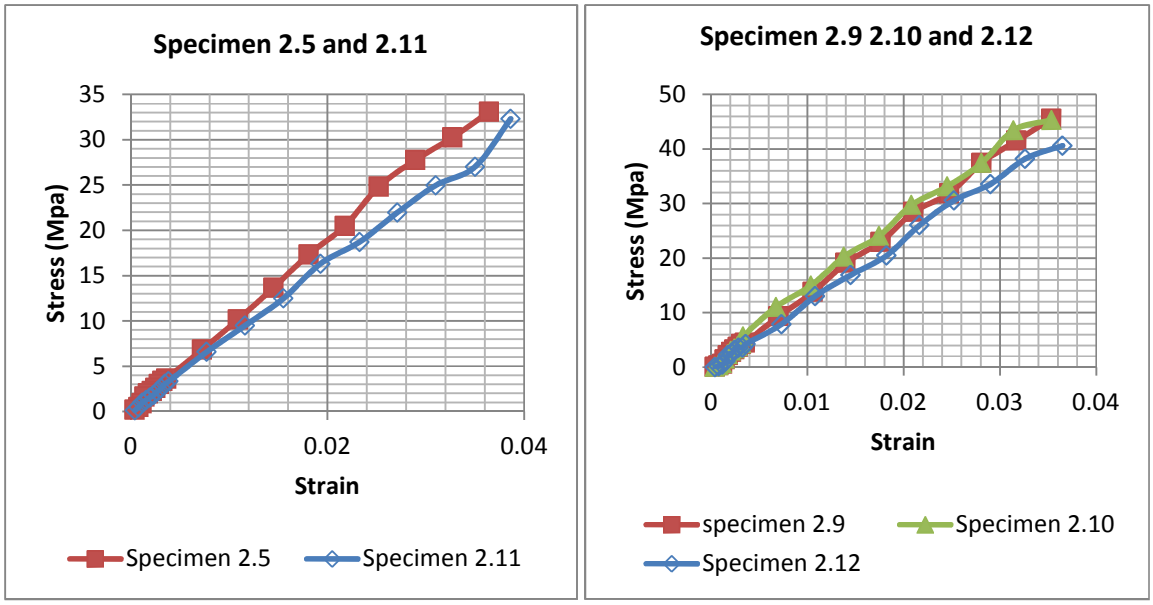

Figure 6.8: Stress-strain diagram of specimens of different burn-in range exposures

6.3.3 The degeneration of R11 resin

The ageing of R11 resin had been observed after using a stock for a few months. The recommended life of R11 resin was 3～5 months and was much dependent on the frequency of use and environment conditions. The aged resin was usually pre-polymerised and has a lower polymerisation ratio which results in significant issues such as low mechanical strength, high shrinkage ratio, significant curl distortion, *etc*. Even more significantly, small beams (specimen 2.5 and 2.6) were extremely hard to fabricate without failure during the removal process. These test beams also tended to break when curl distortion occurred.

The performance of degenerate resin could be seen by comparing tensile test results of specimens made of brand new resin and specimens made with an old resin (used longer

than 5 months). The standard specimen design (specimen 2.5) was used. The dimensions of resulting specimens were 1-0.46-0.77 and 1-0.48-0.87 mm for the degenerated specimen and the specimen made of new resin. The performance of two specimen tests are given in Figure 6.9. The degenerated specimen had only approximately 60 % of the Young's modulus of the specimen made of new resin.

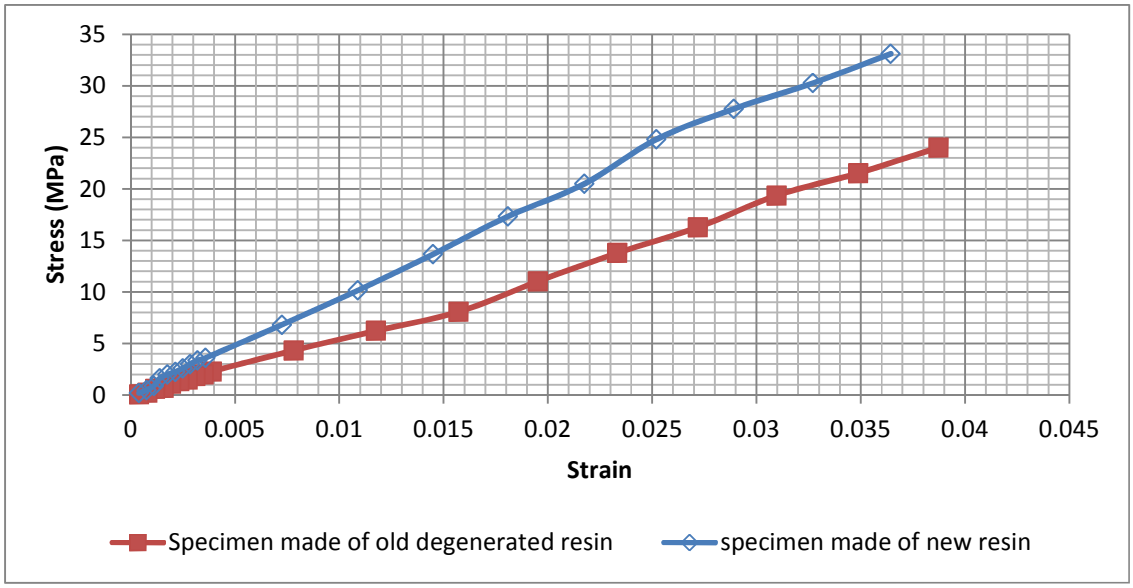

Figure 6.9: The comparison between two specimens made of degenerated resin and new resin

The degeneration performance of R11 was also tested using the Deben microtest. Specimens of high exposure (Specimen 2.10) were used since Deben microtest could not properly handle specimens with considerable curl distortion. Three series of Deben tensile test were taken. The first series of specimens was made using brand new Envisiontec resin R11 (S01) while the latter two specimens were taken about four months (S02) and six months (S03) later. Figure 6.10 plots the three results of the Deben tensile test showing a significantly decrease of Young's modulus. Thus, the degeneration of R11 resin further decreased the fabrication stability of MSL specimens.

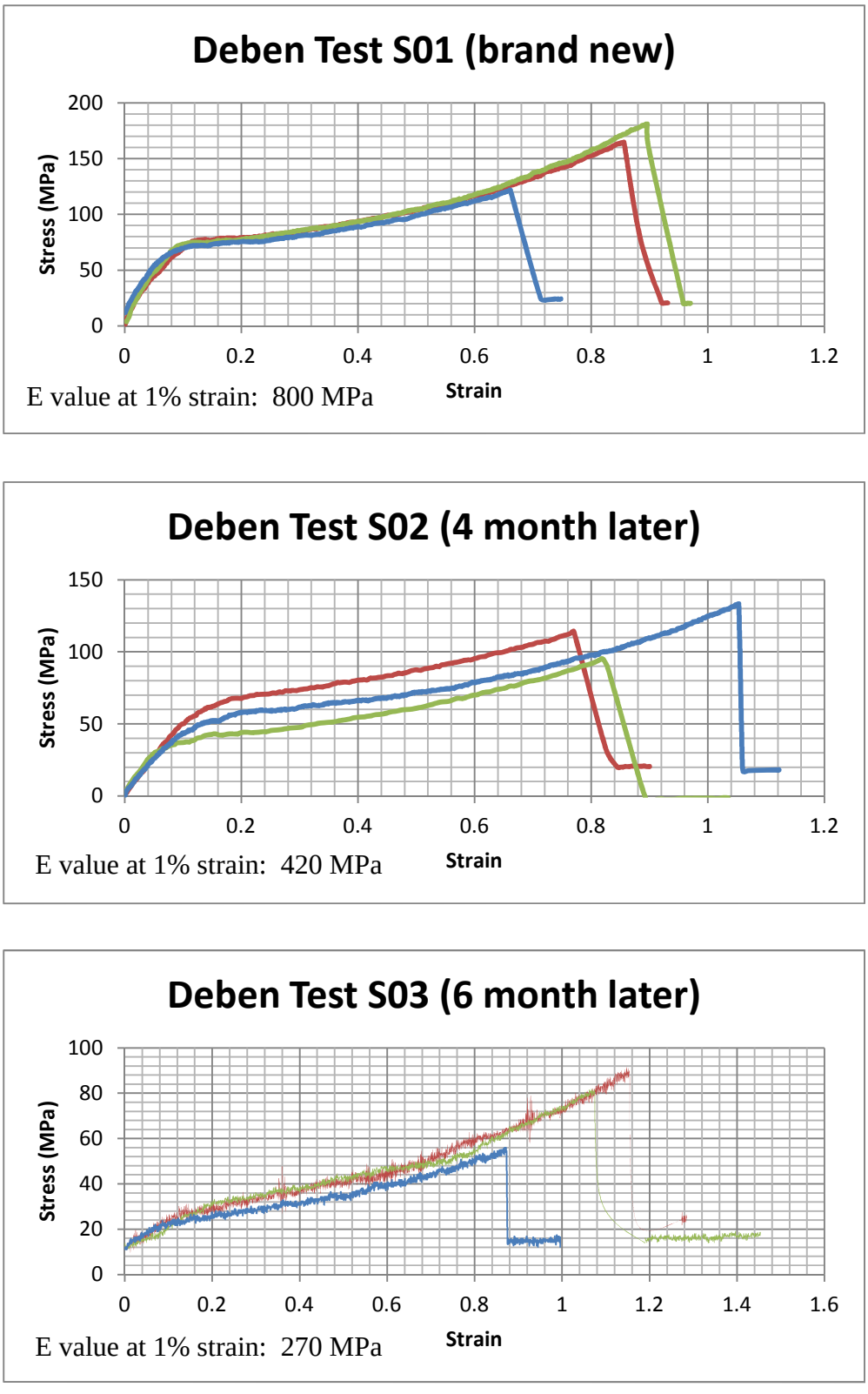

Figure 6.10: The Deben results on specimens made of R11 at different time

6.4 Conclusion

Specimens of different sizes and made under different UV exposures have been examined using the new tensile test-rig. Most of the specimens had a substantial reduction in width and thickness due to the shrinkage and curl distortion effect. The result of dimensional measurement on the final specimens suggested that high UV exposure specimens had a high shrinkage ratio, particularly in thickness. The tensile test on specimens of different sizes revealed a clear size-dependence of the mechanical behaviour of R11 resin. Smaller test beams (less than 1 mm) had significantly higher strength (the largest beam in specimen 2.1 (5/2/1) had a Young's modulus of only 25% of that of the smallest beam in specimen 2.6 (1/0/2/0.1)). The tensile test also confirmed that the mechanical strength of small specimens of the same nominal size increased with the UV exposures (over the range 3.0 to 9.5 s) and suggested a near saturation of 6.0 s for small specimens. Besides, it was also observed that the R11 resin degenerated after using it for a few months, resulting in significantly decreased Young's modulus, severe curl distortion and high risk of failure during manufacturing. Further detailed discussion about the fabrication process of MSL specimens and the tensile test-rig will be given in Chapter 7.

References

Huang, Y-M. and Jiang C-P. (2003). "Curl distortion analysis during photopolymerisation of stereolithography using dynamic finite element method," *Int. J. Adv. Manuf. Technol*, **21**,586-595.

Hunziker, M. and Leyden, R. (1992). "Basic polymer chemistry," Chapter 2 in *Rapid prototyping and manufacturing: Fundamentals of stereolithography*, 1st edition, Society of Manufacturing Engineering, Dearborn, MI.

Narahara, H., Tanaka, F., Kishnami, T., Igarash, S. and Saito, K. (1999). "Reaction heat effect on initial linear shrinkage of stereolithography resins," *Rapid Prototyping Journal*, **5**(3), 120-128.

Simon, G. and Weippert, Ch., Dual, J. and Vill. J (2005), "Size effects in tensile testing of thin cold rolled and annealed Cu foils," *Materials science and Engineering*, **A 416**, 290-299.

Chapter 7: MSL fabrication and the tensile test-rig

7.1 Overview

Micro-Stereolithography (MSL) is a relatively new manufacturing technique which now attracts great interest for fabricating MEMS parts. More functional MEMS components such as micro-sensors (Leigh 2011), micro-actuators (Kang 2006), micro-fluidic parts (King 2009) have been prototyped to investigate the enormous potential of this free-form technique. However, insufficient knowledge of materials (particularly under small scales) and the influence of process parameters on the resultant mechanical behaviour has been a major hurdle; more research work on the mechanical characterisation is called for.

A special form of tensile test-rig has been designed and built to test small MSL specimens fabricated by an Envisiontec Perfactory system using a commercial R11 resin. The main process limitations in fabricating small size specimens (less than 1 mm) were the significant shrinkage and curl distortion in the resulting specimen during the fabrication process. This flawed performance of MSL specimens came from both the MSL system and materials aspect, making the resultant specimens extremely delicate and hard to process and measure in conventional measuring systems due to either insufficient precision or harsh environmental requirements. Thereby, a special form of tensile test-rig with a compatible special specimen design for the small scale measurement needed to be designed and built. The strategy was to use stiffly constrained mounting and loading surfaces, so protecting against parasitic motions during the test in combination with high-sensitivity capacitive micrometry. This tensile test-rig was primarily designed to address the small-scale measurement of elastic properties on MSL materials, but it could also be applied to other MEMS materials.

In this chapter, the performance from both the Envisiontec Perfactory MSL system and the R11 resin aspects will be summarised and discussed. The tensile results on R11 specimens also provide basic mechanical properties of this material in terms of size-dependency and relationship between Young's modulus and UV exposures. Then, discussion on the metrology of the prototype tensile test-rig is given, with suggestions for further improvement. The emphases are on the parallel springs design, clamping strategy and capacitive micrometry design. A comparison of performance of this test-rig and a commercial Deben microtest module is given at the end.

7.2 Issues concerning the MSL specimen fabrication

A customized Envisiontec Perfactory SXGA+ system used for the present studies was an effective projection-based stereolithography system which was capable of producing large (at the order of tens mm) and complex functional MEMS components rapidly and cheaply (King 2009 and Leigh 2011). However, this system had difficulties in fabricating small size specimens (less than 1 mm) in terms of dimensional accuracy and curl distortion. This inaccuracy of the resulting MSL specimens was the co-product of system accuracy and the properties of materials and it became more crucial in producing high-aspect-ratio specimens.

7.2.1 Fabrication performance of the Envisiontec Perfactory MSL system

The dimensional accuracy of the MSL system depended on machine set-up, materials and control factors while being ultimately limited by its different planar and vertical

resolution due to its particular layer accumulation method. The Envisiontec Perfactory system was a projection-based system, therefore the planar resolution was determined by the minimum size corresponding to a pixel in the dynamic mask. It had a projector resolution of 1400 x1050 with a building size of 27.96 × 20.98 mm, giving an X/Y resolution of near 20 µm per pixel. This resolution could be improved to about 10 µm by using the integrated Enhanced Resolution Module (ERM).

The vertical dimensional accuracy of the MSL system depended largely on the minimum thickness of the curing layer. Theoretically, it is determined by the accuracy of motion stage in Z-direction (near micrometre precision). The thickness of the curing layer in principle could be controlled to be as low as 10 µm. However, the initial trials of fabricating tensile test specimens using a small layer thickness of 10 µm indicated that such small tensile beams (typical 1/0/5/0.1 mm) are extremely fragile and often fall-apart during the fabrication process due to the insufficient mechanical strength of curing layers. A compromise of 25 µm curing thickness, therefore, was made to ensure a reliable fabrication of small-size test beams.

The tensile specimen design had the central test beam formed between two bulk ends. For specimens with large length and width (particularly length), the first few layers were at significant risk of falling off the platform or being distorted (See 6.2.2). This was because test beams with larger length and width were weaker and more subjected to the vertical stress when the platform was lifting up for curing successive layers since the thickness of the curing layer was only 25 µm. Moreover, thin and long curing layers were more vulnerable to the shearing stress arising from the peeling effect. This mis build behaviour of the MSL system would significantly reduce the thickness of long-span test

beams. Non-uniform cross-section test beams were more likely to be fabricated for specimens with large length and width which would introduce complicated analytical effects into the mechanical characterisation of tensile tests.

The vertical resolution of the Envisiontec Perfactory system was further limited by the calibration offset. The calibration process was completed by firmly clamping a 2 mm thickness calibration plate between a platform and a resin tray and measuring the gap. This hard clamping had usually resulted in a slight indentation in the rubber resin tray (Figure 7.1). This calibration offset was often nulled by constructing a few solid base layers before starting the actual specimen building (burn-in layers).

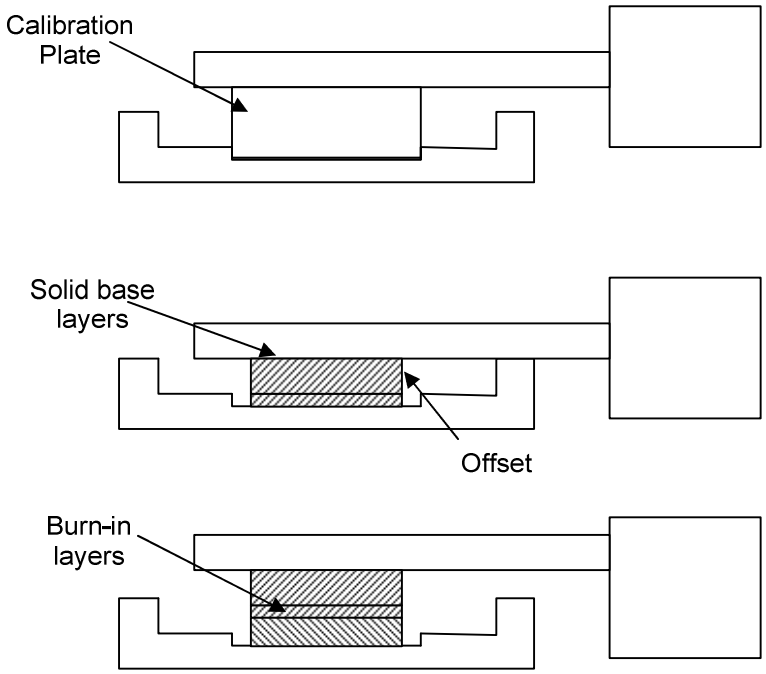

Figure 7.1: The calibration offset in Envisiontec Perfactory system

However, for thin specimens with delicate test beams in the central region, it was undesirable to have a bulk solid base of about 0.6~0.7 mm for the 2 mm calibration plate (according to Envisiontec 2003) since the designed tensile specimen cells were only up to 2 mm thickness. This calibration offset was only empirically adjusted leaving a substantial uncertainty in the curing thickness of specimen cells. However, this calibration offset would not affect the fabrication thickness of test beams as the thickness of test beams was only integral multiple of the thickness of the curing layer.

7.2.2 The fabrication performance of Envisiontec R11 resin

The properties of R11 resin was another factor in building accurate small-size parts. In order to determine the properties of R11, the MSL system must achieve high dimensional accuracy due to the interdependence of the MSL system and the material. From the result of dimensional measurement in section 6.2, the resulting geometry of specimen was significantly worse than the fabrication accuracy of the Envisiontec MSL system (10~20 μm). Since the results also showed some time-dependent shrinkage, it was thereby assured that the resulting dimensional accuracy of the MSL specimens was seriously dependent on properties of the resin formulation.

For production MEMS parts, the MSL materials must be able to produce small parts with high dimensional precision for various applications; otherwise these parts would be only suitable for visualization purposes. Precise fabrication of small MSL parts required resins with low linear shrinkage ratio and curl distortion. The R11 resin was a commercial acrylic resin, which polymerised via a free-radical mechanism. The photospeed of R11

resin was quite high comparing to other epoxy or vinylether polymers systems. However, this acrylate-based resin was more susceptible to linear shrinkage and curl distortion than epoxy-base resins (Jacob 1996). These effects were clearly revealed in the dimensional measurement on the resultant specimens made of R11 resin (see section 6.2.2).

The shrinkage and curl distortion on the resultant specimens had been major limitation in producing small size specimens using R11 resin. The shrinkage was generally within 5% in the width of test beams (presumably it would be similar in the length without the bulk ends), and could be generally minimized by adding another calibration. The main idea of this calibration to minimize the shrinkage effects was to determine the shrinkage factor of the down-scaled specimens and to scale up by this factor for producing normal specimens. The first step of this calibration was to perform a geometry measurement on a specimen cell contains various test-beams in different orientations (Figure 7.2) to determine the shrinkage factor. The shrinkage factor was then calculated and the normal building envelope size was downscaled by this factor in the Perfactory system. As a result of the reduced normal pixel size, more pixels could be used to fill the part region. This led to an up-scaled specimen in the *X*-*Y* direction since the actual building envelope of the machine was not changed. However, the shrinkage effects on thickness of specimen could not be adjusted in this method.

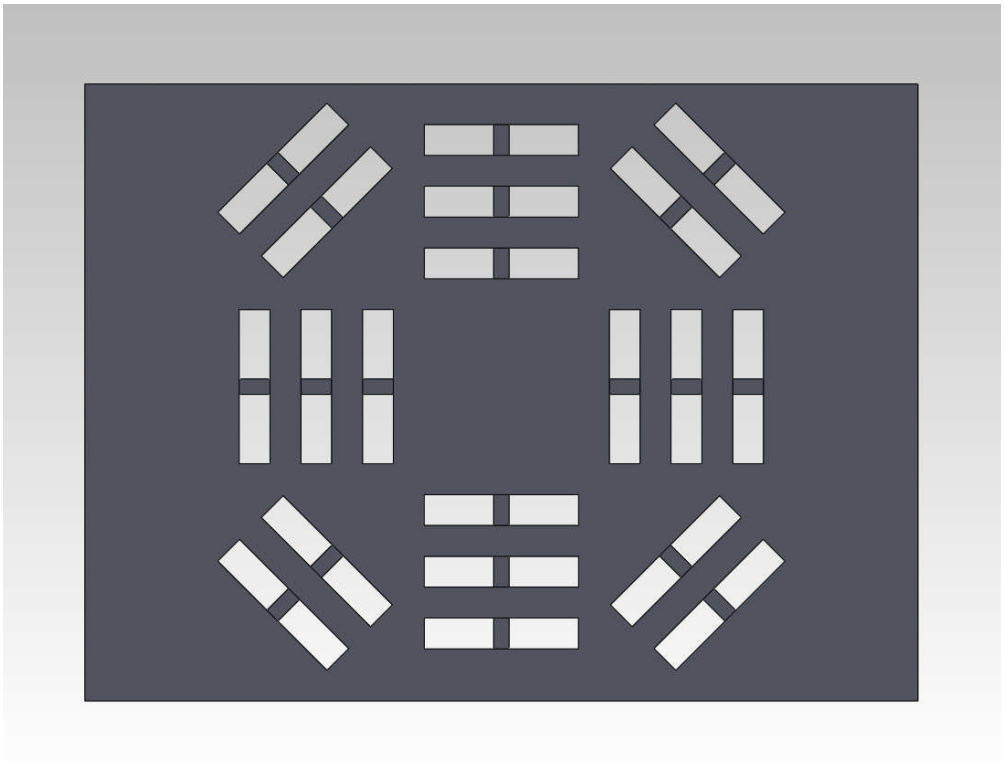

Figure 7.2: Proposed specimen models for calculating the shrinkage factor

The curl distortion on R11 resin was not only another issue significantly limiting the dimensional accuracy, but it also introduced a significant uncertainty for the tensile specimens. Early trials of building the specimen onto a rigid silicon plate stuck to the building platform and releasing the specimen after two days of cool storage suffered from removal problems and these specimens were still subjected to severe curl distortion a long time after the curing processes. It was suggested that the residual internal stress still led to a delayed warp known as GCD (Green creep distortion) (Jacob 1996) after removing the specimen from the silicon plate.

There were only a few published works explaining curl distortion and proposing potential solutions to reduce it. Marutani (1989) suggested a few predictions on how the curl

distortion could be reduced which have largely been confirmed by later experimental results (Jacobs 1992). His proposals included using high exposure, using resins with faster rates of polymerisation, using a low shrinkage resin and increasing layer thickness to increase strength. Since the acrylic R11 resin was the only currently available material for fabricating small specimens and the layer thickness was set to be 25 μm for a balance between reliable fabrication with low curl distortion and Z-directional fabrication accuracy, it was practical to use high UV exposures to increase the mechanical strength and reduce the curl distortion. Specimens with high exposures underwent less curl distortion due to the increased mechanical strength. This was particularly so when the curing exposure was high and close to the burn-in range exposure. From section 4.5.2, the difference between curing exposure and burn-in range was a significant factor contributing to the curl distortion in thin specimens. It was also found that using thicker bulk ends in the design could significantly decrease the curl distortion.

In practice, the dimensional properties of the resultant specimens (accuracy and dimensional stability) were largely dependent on the availability of high-quality resin formulations. As there was a lack of commercial MSL resin formulations designed specifically for fabrication small specimens of less than 1 mm thickness, the good all-round acrylate-based R11 resin formulation was the primary choice for fabricating them despite its relatively large shrinkage and curl distortion. It was imperative to thoroughly inspect the dimensional accuracy actually achieved by any other MSL materials before proceeding with their mechanical characterisation.

7.2.3 Tensile test results of R11 specimens

It was generally difficult to judge the quality of MSL specimens because the resulting properties of specimens may vary to a substantial extent with particular combinations of MSL system and its materials. Moreover, the considerable number of factors affecting the resulting properties of MSL specimens made it difficult even to determine the resultant properties. It was not within the scope of this research to attempt to build precise models to determine the properties of MSL materials. The aim was first to develop and demonstrate a reliable methodology for testing small-scale behaviour and so to gain better understanding and useful perspectives based on the mechanical characterisation results of MSL specimens fabricated by a representative Envisiontec projection MSL system with a commercial acrylate-based R11 resin.

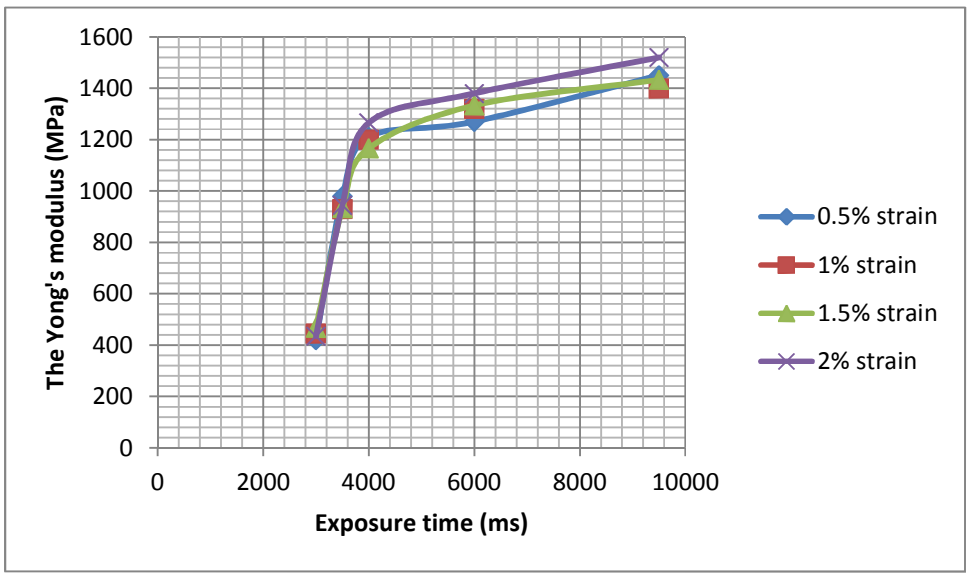

Figure 7.3: The relationship between Young's modulus assessed over various strains and exposure time

In order to reliably fabricate specimens with sufficient stiffness, the UV exposure of R11 resin should be larger than 3.0 s and 6.0 s for curing exposure and burn-in range exposure respectively (see section 4.5.2). Figure 7.3 plots the Young's modulus of specimens at different curing exposures (adapted from results in Table 6.6). Specimens with high-exposure showed a higher stiffness corresponding to their high cure-ratio. The Young's modulus of R11 increased rapidly when the curing exposure rises from 3.0 to 4.0 s, and then became moderate. It suggested that the saturation absorption of exposure energy occurs after 6.0 s and the manufacturer recommendation of standard exposure of 3.5 s was a little short for fabricating small size specimens.

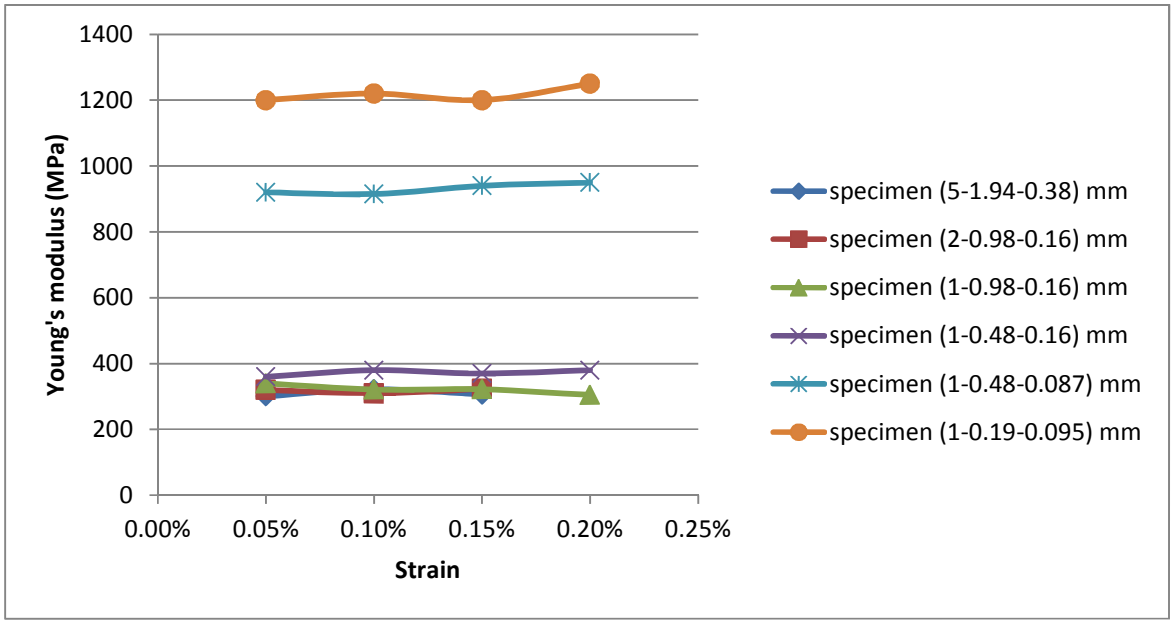

Figure 7.4: The Young's modulus of specimens of different sizes assessed over various strain

Another important result of the tensile tests was that the size of specimens had a significant influence on their mechanical properties in the size region that had been

investigated. From Figure 7.4 (adapted from the tensile test results of Table 6.5), a clear size dependence can be observed. Smaller test beams displayed a significantly higher Young's modulus than larger ones. The large test specimens exhibited a largely consistent stress-strain curve, while a significant leap in mechanical properties could be observed when the thickness reduced from 0.2 to 0.1 mm. There was also a smaller jumping of increased values of Young's modulus when the width was further reduced from 0.5 to 0.2 mm. It was suggested that the size effects in the Young's modulus were likely to be important when the size is less than 1/0.5/0.1 (L/W/T) mm.

Several effects may be responsible for the size dependence of Young's modulus. As already reported in section 6.2.2, the first few layers of larger dimension specimens underwent severe vertical stress during the lifting up phase. These layers were usually weak or may even fall off during the building process. Moreover, MSL specimens were made in layer by layer style where the curing layer introduced peeling stress to the layer below during the thermal expansion and cooling stage. This peeling effect became more prominent for thicker specimens where thicker parts were stiffer and not flexing much to accommodate stresses in the new layers, resulting relatively higher stress and lower values of Young's modulus in the thicker specimens.

The non-uniform cross-sections of test beams (particularly on small size beams) would also give a length-dependent systematic error. The design using two bulk ends made the smaller central test-beams more vulnerable to the curl distortion (Figure 7.5). The smaller test beams were more distorted and the strain mostly occurred at the smaller cross-section over a little shorter effective gauge length l_2. Since the strain used to

calculate Young's modulus was based on the large value of nominal gauge length L_2, so the Young's modulus of small beams would probably be overestimated a little.

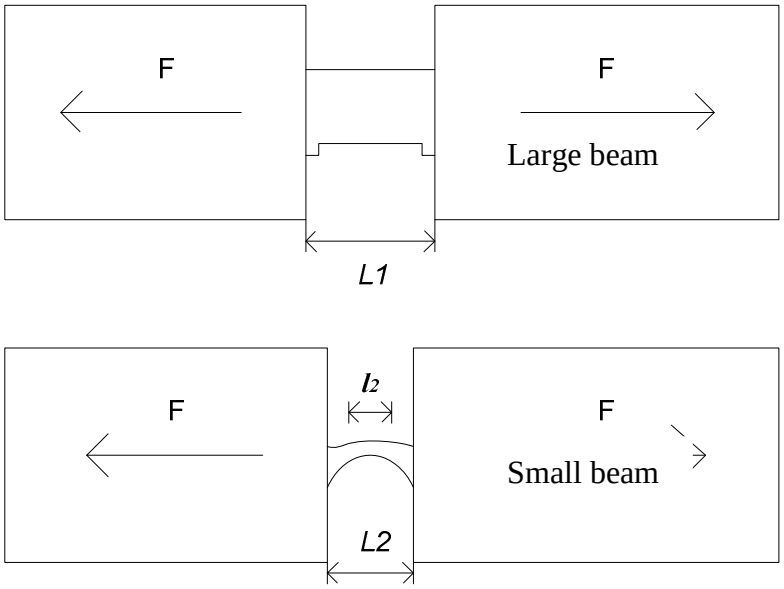

Figure 7.5: The tensile test on specimens of different size

7.3 The metrology of the tensile test-rig

In this section, an overview of system performance is firstly given, followed by analysis and discussion about crucial parts of the test-rig: the clamping issue and capacitive micrometry. Finally, a comparison and discussion of the performance of this test-rig and a commercial Deben microtest module is given.

7.3.1 The overview of tensile test-rig

The typical MEMS specimens usually featured small and fragile structures with dimensions less than 1 mm, making them difficult to handle and test. Moreover, the practical fabrication accuracy of MSL specimens was usually limited because the tolerance ranges of these fabrication processes were relatively large. These uncertainties in the dimensional accuracy usually produced tolerances more than 10% of the nominal values and it was often very expensive to improve the process accuracy (Shavezipur 2008). Thus testing under axial load was preferred to, e.g., bending because it offered simpler uncertainty models against the dimensional variations of specimens. On the other hand, as one of the representative MEMS fabrication techniques, a free-form MSL technique was used to fabricate tensile specimens firstly, allowing a flexible design of specimens and offering more potentially practical solutions for a robust specimen handling strategy.

A special tensile test-rig designed for the mechanical characterisation of a compatible specimen fabricated by MSL had therefore been built. The actual test beam was incorporated monolithically within a much larger specimen structure which gave it protection during fabrication, storage and mounting onto the tensile tester. The strategy of the test-rig was to use stiffly constrained mounting and loading surfaces and a flexure guideway in combination with high-sensitivity capacitive micrometry, so protecting against parasitic motions during the test. Deadweight was used here for simple and reliable force applications, but it could be conveniently replaced by a linear voice-coil force actuator. The specimen was clamped onto the surface of the flexure and shares the tensile load with the flexure spring. The same displacement shared by the flexure and the

specimen was measured by compact capacitive micrometry, chosen for its ease in integrating into the test-rig and high sensitivity. Similar small capacitive probes were also employed to investigate the clamping conditions.

This tensile test-rig was primarily built for polymeric MSL specimens, but it could also be applied for characterisations of other MEMS materials. The notch flexure spring was monolithically manufactured and designed to have a relatively high stiffness of about 200 kN/m in order to protect the MSL specimens (and was still suitable for other MEMS specimens stiffer than polymeric MSL ones). The typical sensitivity of the capacitive gauge was about 20 mV/μm, and a typical noise level of 2 mV could be obtained at 50 Hz. Thus, an effective resolution of sub-micrometre could be achieved readily in the test-rig.

7.3.2 The two parallel springs design

In operation, the flexure acted both as a spring in parallel sharing the same displacement with the specimen and as a linear guideway for applying the tensile load (Figure 7.6). This increased stability and protected the specimen from transient load changes at the cost of slightly increased uncertainty in the force actually applied to the specimen. The stiffness of the notch hinge design was balanced between loading measurement accuracy and robust protection. A typically sized (1/0.5/0.1 mm L/W/T) polymeric specimen having an elastic modulus of a few GPa would have an axial stiffness in the order of 100 kN/m, therefore the notches for the prototype were designed to give the flexure a stiffness, λ_f, of around 200 kN/m. Only about one third of the tensile load would then be

distributed to the specimens. From the test results in section 6.3, the R11 resin specimens usually had Young' modulus of less than 1 GPa and so were less stiff than expected. Hence, a larger portion of the applied load would be taken by the flexure and decrease the accuracy of measurement to some extent. However, this flexure design still had satisfactorily robust performance and suitable for general characterisation of MEMS materials since many of them have stiffer mechanical behaviour than polymers.

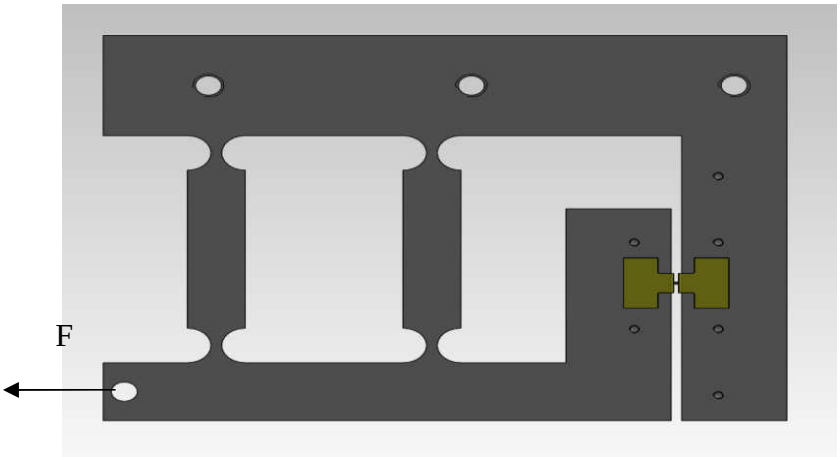

Figure 7.6: The parallel spring design

The parallel spring paths had very little effect on the uncertainty compared to direct application and measurement of force and displacement. From Equation 5.3 in section 5.2, the Young's modulus of the specimen was given by

$$E = (\frac{F}{\delta} - \lambda_f)\frac{l}{A}$$

where F, δ, l and A represented the applied force, elongation, length and area of cross-section respectively. From the analysis in section 5.4, the uncertainties associated with δ (other than from the capacitor gauge itself) would not be significant since the lateral parasitic motion is less than 0.05% of the displacement in the driving direction (section

5.4). The uncertainty in the tensile force was also quite small since the force was directly applied to the flexure by the deadweight. The only extra uncertainty introduced by the parallel spring approach was the stiffness of flexure, λ_f, and that could be kept relatively small with a good calibration.

The flexure spring also provided a rigid reference frame for specimen clamping and alignment. The clamping devices were mounted on the flanged side of the flexure where the specimens are clamped. This parallel-motion action allowed a practical compromise of building in an approximately 30 mm Abbe offset to keep the extension gauge conveniently clear of the sample mounting area. The lateral parasitic motion of the flexure was only tens of nanometres for a typical testing and the Abbe error was also limited within a few tens of nanometres.

7.3.3 The specimen design and clamping strategy

The MSL specimens were fabricated using an acrylate-based R11 resin which curved significantly when used at small scales. The test-section (typically $1\times0.5\times0.1$ mm^3), was too delicate to handle easily. It was therefore made integrally within a larger carrier. The bulk of the specimen provided bases for hard, frictional, clamping. To prevent the delicate sample being pre-stressed or damaged during mounting and alignment, it was fabricated integrally with protection structures on both sides: they were gently cut by a sharp knife through once it was properly positioned and fixed onto the flexure.

Since the MSL specimens fabricated were curved and delicate, a robust and reliable clamping was one of the most crucial factors in the tensile test. An initial attempt was

made using a pin-block method to avoid directly clamping on curved specimens. This arrangement was kinematically under-constrained and depended on friction plus pin indentation to stabilize the contact. However, small pins with high stiffness were genuinely difficult to be fabricated and embedded into the clamping device. Moreover, the specimen sometimes glided over the pins, introducing shear stress to the specimen and significant uncertainties in specimen mounting. This led to a preference for friction gripping by hard-clamping to the flats of the test rig using screws on slightly flexible brackets. Small areas on the bulk ends were used for point clamping. Moreover, the bulk ends could be made thicker to reduce the curvature of the specimen. The Envisiontec Perfactory system using the R11 resin formulation could produce high quality up-facing and down-facing surfaces for the bulk ends for specimen clamping and aligning. Thus, this screw-driven clamping approach could provide robust specimen mounting but extra pre cautions should be paid to the clamping condition, particularly in slip. The clamping condition was further verified by using two pairs of small capacitive electrodes glued on the specimens and flexures to compare the actual elongation of the specimen and the stage displacement. The smooth and consistent patterns of two capacitive gauge results during the back and forth stage motion indicated no sudden slipping during the cyclic loading and no pattern consistent with steady creep at the clamps, even for relatively heavy loads over 30 μm movements. A repeatability test also confirmed the consistent clamping: even with possible variation in tightness of the screws, the divergence across all tests is within a range of ±3.5 % of the mean. The later tensile test results in section 6.3 exhibited smooth and linear stress-strain curves which further confirm that a reliable clamping condition was most likely to be achieved in this arrangement.

The specimen alignment in this arrangement was less critical than clamping since the flexure functioned as a linear guide for the specimens. The alignment of specimens was completed by aligning the edge of the bulk ends to be parallel with the loading axis by eye to fiducial lines. Slightly misalignment would not significantly affect the measurement results and the shear force on the specimen was much less than 1% of the uniaxial tensile force even with over a large 5º misalignment.

7.3.4 The capacitive micrometry design

The flexure displacement, taken as a measure of specimen extension, was monitored by a capacitive gauge comprising a pair of thin gold electrodes (8×5 mm^2) deposited on glass pads and glued between the stage and base. The wire was silver painted to the electrodes and connected to Queensgate Instruments NS2000S conditioner for output.

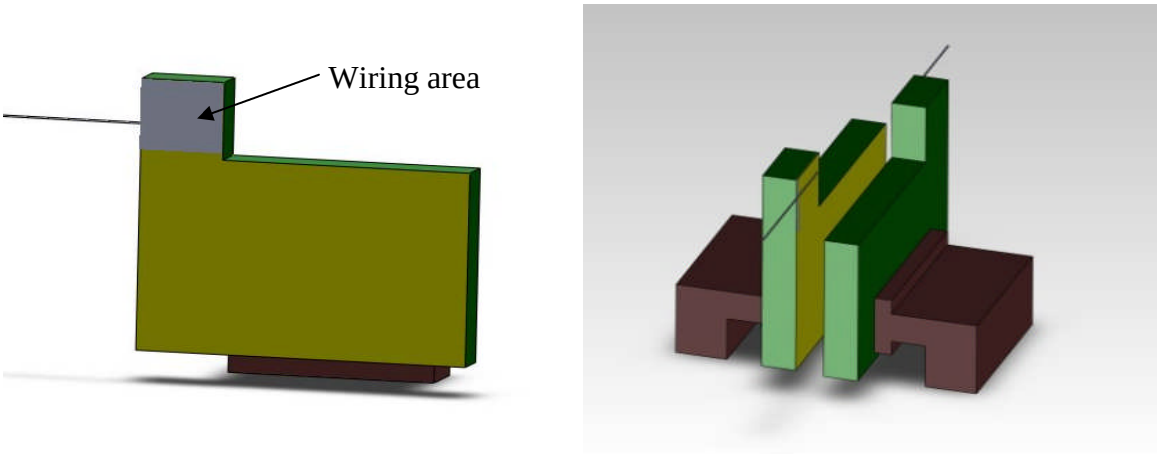

Figure 7.7: The capacitive electrodes arrangement

The capacitive electrodes were small and could be conveniently integrated into the test-rig without introducing significant effects on the measurement loop. The nominal gap between the two capacitive electrodes was a crucial factor in installing the capacitive micrometry. It should be kept as small as possible to obtain high sensitivity. A nominal gap of a few hundred micrometres was usually established to keep conveniently clear of the wiring area (Figure 7.7). This could be improved by re-making the wiring area further away from the capacitive electrodes and reducing the nominal gap down to 100 micrometres.

The typical sensitivity of the capacitive gauge was calibrated to be around 20 mV/μm with linearity error less than 0.8% up to 40 μm. The noise level at 50 Hz corresponded to 100 nm, which placed a limit on the working resolution of this test-rig 100 nm. As a rough empirical rule, capacitive micrometry was best used with a displacement range of ±50% of the nominal gap *G*, which was kept relatively larger on the prototype for easy construction. For example, most of the case G was nearly 200 μm. The typical elongation measurement on the typical size of specimen would be over no more than 20 μm. The whole system would often, therefore, only be using less than 10% of maximum gauge range and so the resolution of the actual elongation was restricted quietly severely by the noise. Reassembly with smaller capacitive electrodes placed closer together would improve the sensitivity to overcome this limit at extra construction cost. Although not ideal, continuing with the first prototype built was considered a better strategy for this project.

The current capacitive gauge was capable of sub-micrometre resolution (0.1 μm) measurement. This resolution was not inherent to the design. The 50Hz bandwidth used here was the minimum setting of the conditioner. Because the tensile instrument was normally used quasi-statically, extra filtering/averaging to roughly 1Hz bandwidth might give about 7 times improvement. An approximately 20 nm resolution could then be achieved with relatively little effort. It could be further improved by re-making and re-installing the capacitive pads with smaller nominal gap, which would significantly increase the sensitivity and decrease the noise level.

7.3.5 Comparison between the new tensile test-rig and Deben module

A commercial Deben microtest module was also employed to verify the test results of the new tensile rig using a broadly similar methodology. It employed a stepping motor to apply the tensile load by asserting displacement while a custom miniature load cell was embedded into one end of the moving stage to provide the force reading. The specimen was hard clamped by mechanical jaws at each end of the specimen, between two stages. A dual threaded leadscrew drove the jaws symmetrically in opposite directions, keeping the specimen centrally aligned. This Deben microtest module allowed real time observations of the mechanical behaviour of different specimens. A maximum tensile load of 600 N could be directly applied to the specimens with stage travel range up to ~20 mm. This instrument had a linear motion stage for elongation measurement and optical encoders for speed control from 0.55 to 6.67μm/s with sample time from 100 ms to 5 s. From section

5.10, the Deben microtest module produces results of Young's modulus closely agreed with results from the tensile test-rig, nearly 1 GPa.

The Deben tensile module could produce a full range of tensile stress-strain diagrams of different specimens (by using different calibrated loadcells) where the new tensile test-rig has limited force range of a few newtons on the MSL specimen because large part of load was distributed to the a relatively high stiffness flexure spring. Furthermore, this Deben microtest stage was a robust design insensitive to the environmental factors. It was easy to apply this Deben tensile module for a general testing while installing the new tensile test-rig was slow and requires substantial calibration work. Of course, the commercial system had such setting and calibration in-built on delivery and reflected in its sale price.

The most prominent limitation in the Deben microtest modules in testing MSL specimens was that it required a high flatness of the specimen surfaces. The large face-to-face mechanical jaw clamping arrangement in the Deben machine required an extremely high flatness of test specimens; otherwise it introduced significant stress or even severe damage to the central test beam during the clamping (Figure 7.8 left). This requirement conflicted with the commonly curved nature of thin MSL specimens and so the Deben tensile test could only be used to test R11 specimens with high flatness (2 mm thicker and 9500 over-cure ones). Thus, the Deben tensile test was only used as a general confirmation of test results from the tensile test-rigs. In the new tensile test-rig, point clamping with soft material as a cushion was used to ensure that specimens with some curvature would be unaffected by the directly clamping (Figure 7.8 right). The main concerns in this arrangement were slip and creep rather than the stress or damage brought by the clamping. The tensile results from a verification experiment using an extra pair of

small capacitive electrodes on specimens and a repeating clamping test revealed no evidence of slippage or creep sufficient to degenerate the elongation measurement, suggesting a relatively robust clamping is likely to be established in this clamping arrangement.

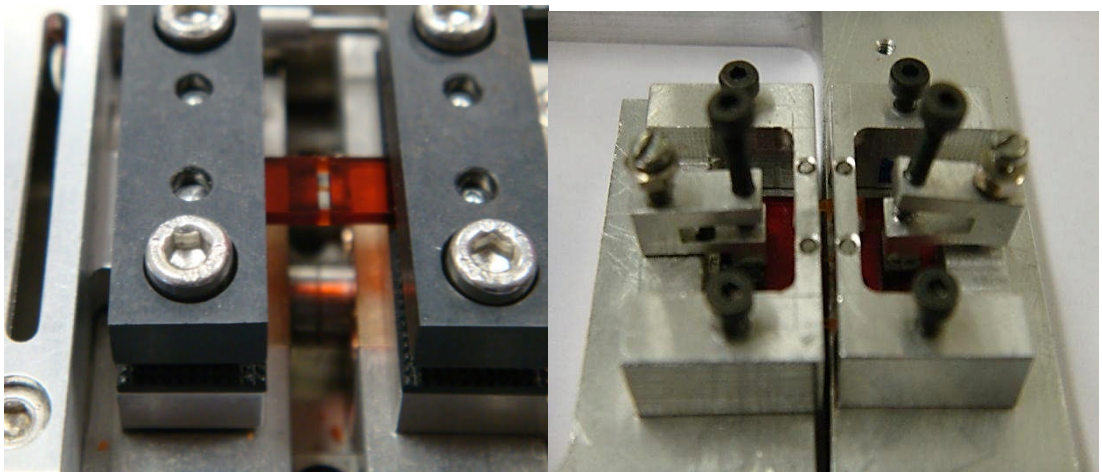

Figure 7.8: The two clamping arrangement (Left: Deben machine. Right: new built test-rig)

The Deben microtest module was designed to be suitable for measurement under SEM (scanning electron microscope), optical microscopy or AFM (Atomic force microscopy). Without them, the accuracy of this method was limited by the step-motor precision which is only at the micrometre level. On the other hand, the tensile test-rig using the high sensitivity capacitive micrometry was convenient to have a sub-micrometre resolution with plenty of potential for further improvement. At the scale being considered here, directly asserting forces and measuring elongation provided better and flexible control of the process.

7.4 Conclusion

An Envisiontec projection-based MSL system using a compatible acrylate-based R11 resin was used here to investigate the properties of resulting specimens. The mechanical properties of the R11 specimen were depend largely on the UV exposure as expected and a clear size dependency trend had been observed when the dimension of test beam reduced less than 1 mm. As the influence of many parameters needed to be taken into account for this size effect, more experimental characterisation works are required for further study of this material.

A special prototype of a new tensile rig was also presented and used for the mechanical characterisation of the small scale MSL materials. The strategy was to use stiffly constrained mounting and loading surfaces, so protecting against parasitic motions during the test in combination with high-sensitivity capacitive micrometry. Its abilities of robust and reliable specimen clamping and sub-micrometre measurement resolution made it qualified for general characterizing small MSL (and other MEMS) specimens where the conventional systems were experiencing difficulties in handling small delicate specimens and insufficient accuracy. A few sections of this test-rig could be further improved and will be discussed in Chapter 8.

References

Envisiontec (2003). Envisiontec Perfactory manual, Edition 2003, Envisiontec GmbH, Gladbeck, Germany.

Jacobs, P.F. (1992). *Rapid prototyping and manufacturing: Fundamentals of stereolithography*, 1st edition, Society of Manufacturing Engineering, Dearborn, MI. ISBN: 0872634256.

Jacobs, P.F. (1996). *Stereolithography and other RP&M Technologies*, Chapter 2, 27-73. Society of Manufacturing Engineering, Dearborn, MI. ISBN: 0872634671.

Kang, K.W., Lee, I.H. and Cho, D.W. (2006) "Development of a micro-bellows actuator using micro-stereolithography technology," *Microelectronic Engineering*, 83, 1201-1204.

King, P. and Covington, J.A. (2009). "A novel monolithic microactuator fabricated by 3D rapid direct manufacture," *Proceedings of Eurosensors XXIII conference, Procedia chemistry*, **1**, 1163-1166.

Leigh, S.J., Purssell, C.P., Hutchins, D.A., Covington, J.A. and Billson, D.R. (2011). "A miniature flow sensor fabricated by micro-stereolithography employing a magnetite/acrylic nanocomposite resin," *Sensors and Actuators A: Physical*, **168**(1), 66-71.

Marutani, Y. and Nakai, T. (1989). *Laser research*, **17**, 410-480.

Shavezipur, M., Ponnambalam, K., Khajepour, A. and Hashemi, S.M. (2008). "Fabrication uncertainties and yield optimization in MEMS tunable capacitors," *Sensors and Actuator A*, **147**, 613-622.

Chapter 8: Summary, conclusions and future work

8.1: Summary of the work

Micro-stereolithography (MSL) has attracted more and more research interest and has become an important technique for fabricating small size 3D MEMS (Micro-Electro-Mechanical System) structures and micro-devices. One major impediment to realizing the full potential of this free-form technique is limited material choices and poor current knowledge of their mechanical properties. Moreover, the mechanical characterisation of small-sized specimens is generally challenging for conventional instruments. Therefore, this research mostly addresses three areas currently constraining the commercial viability of MEMS techniques: better understanding of the mechanical properties of the polymers at small scales; better knowledge of MSL fabrication processes and the development of new metrology techniques to gain this data.

Chapter 1 introduced the background of disruptive MEMS technologies. It briefly covered the basic information about fabrication techniques, materials and applications of MEMS. The enormous potential of MEMS technologies requires better understanding of basic engineering data about the material properties as well as the manufacturing technologies themselves. Current challenges and interests in MEMS had been briefly described, indicating that more characterisation work should be carried out to further understand the fabrication process and fully explore the potential of MEMS.

Chapter 2 gave a literature-based overview of an important MEMS fabrication technique: Micro-stereolithography (MSL). It firstly dealt with the principles of the MSL system and then with new developments of MSL apparatus in different arrangements and MSL

materials. According to the literatures, the main technical limitations in MSL technology are its relatively slow fabrication speed (except for TNO micro-stereolithography machines) and the limited material choice with insufficient knowledge about their mechanical properties. It identified the urgent need for precise mechanical characterisations at small scales.

Chapter 3 reviewed various testing methods for mechanical characterisation of small scale specimens. It stressed that the main challenge and difficulty in these measurements was dealing with small fragile specimens in terms of robust specimen handling and precise measurement. A comparison of tensile and bending tests was given and discussed, leading to a practical preference to the uniaxial tensile test because it offered simpler uncertainty models against the dimensional variations of samples. A systematic overview of mechanical characterisation at small scales on was presented. Several design aspects (e.g., specimen design, specimen mounting and alignment, strain measurement) were reviewed and discussed to provide a useful perspective for the later construction of the tensile test-rig.

Chapter 4 described the procedures for fabrication of MSL specimens. A projection-based Envisiontec Perfactory SXGA+ system with a commercial R11 acrylate-based resin was employed. During fabrication, significant shrinkage and curl distortion was observed on thin MSL specimens (1 mm thickness).

Chapter 5 dealt with a prototype tensile test-rig and a compatible MSL specimen design for lateral mechanical characterisation. The specimens were made integrally with a robust carrier that is separated after mounting on the instrument to protect the delicate test beams. The tensile test-rig used stiffly constrained mounting and loading surfaces, so

protecting against parasitic motions during the test in combination with high-sensitivity capacitive micrometry. Alternative methods for the crucial issue of specimen holding were investigated and verification tests carried out to ensure robust specimen clamping. The preliminary tensile results indicated that the standard MSL specimen had a Young's modulus of approximately 1 GPa, which largely agreed with test results from a commercial Deben tensile module.

Chapter 6 presented the tensile test results for the MSL specimens. The results of dimensional measurement on the resulting specimens were firstly given, with comments on the shrinkage of thin specimens. The tensile test results on specimens of different sizes revealed a clear size-dependence where smaller test beams exhibited higher stiffness than larger beams. The Young's modulus of specimens increased when higher UV exposure time was employed. The degenerated performance of old R11 resin was observed during tensile tests, causing weaker, lower stiffness specimens.

Chapter 7 discussed the tensile test results of MSL specimens with comments on fabrication processes. The mechanical behaviour of the MSL specimens was illustrated and explained while the performance of tensile test-rigs were also analysed and compared to the performance of the Deben machines, a commercial instrument marginally suited to the present test regime.

8.2 Conclusions

This study addressed the mechanical characterisation of MSL specimens via building a prototype tensile test-rig. The following conclusions were hereby derived from the MSL system aspect, material aspect and tensile test-rig aspect.

8.2.1 The performance of MSL system and material

The projection-based Envisiontec Perfactory system using a commercial acrylate-based R11 could produce small MSL specimens rapidly and at low unit cost. The X/Y fabrication resolution of the MSL system could be down to 10~20 μm where the minimum layer thickness (vertical accuracy) should be larger than 25 μm for reliable fabrications. The acrylate-based R11 resin was the best choice available for producing small tensile loaded parts at high speed. However, substantial shrinkage and curl distortion had been observed, which could greatly reduce the fabrication accuracy of the MSL specimens.

From the results of dimension measurements on the fabricated specimens, most of the shrinkage occurred simultaneously with the curing process. Due to the bulk end design, the length of test beams was hardly affected while the width and thickness was significantly reduced. There was approximately 5% reduction in the width and 10%~15% in thickness on a typical size specimen (1/0/5/0.1 mm) with a standard exposure of 3.5 s. Specimens produced with higher UV exposures (large than 6 s) had a higher shrinkage ratio, and specimens with larger dimensions (particularly length) suffered more reduction in the thickness due to the mis building layers in the MSL processes. Curl distortion

usually occurred after the post-curing. Thin specimen cells (with thickness less than 1 mm) were observed regularly with severe curl distortion, while specimen cells with thickness of 2 mm exhibited a satisfactory flatness for the tensile test. Also specimens with lower UV exposures (less than 6 s) were more susceptible to curl distortion due to their weaker mechanical strength and the greater internal stress introduced by the different UV exposures in curing layers and burn-in range layers.

The mechanical properties of the R11 specimen largely depended on the UV exposure, as expected. The Young's modulus increased rapidly when the curing exposure rose from 3.0 to 4.0 s, and then increased only moderately after 6.0 s. It suggests that the saturation absorption of exposure energy was around 6.0 s and the manufacturer recommendation of a standard exposure of 3.5 s was a little short for fabricating small size specimens. A clear size-dependency trend had been observed: the larger test beams exhibited a largely consistent stress-strain curve while a significant leap in Young's modulus could be observed when the thickness was reduced from 0.2 to 0.1 mm (from 380 MPa to 920 MPa). This could be explained by the severe peeling effects and mis building layers phenomenon on large specimens. The severe curl distortion on small specimens could also result in a high stiffness in the measurement.

8.2.2 The performance of tensile test-rig

This study addressed small-scale measurements of elastic properties via building a special form of test-rig and a compatible special design for the MSL specimens. Since the MSL specimen was particularly delicate and tended to become curved, the main concern

was to ensure that MSL specimens can be made and then transferred to and aligned on the tester without significant damage. The specimens were made integrally with a robust carrier that was separated after mounting on the instrument. A robust notch hinge flexure functioned both as a stiff spring in parallel with the specimen to share the tensile load and protect specimens and as a parallel motion guide to allow a large area for specimen clamping and ease the task of measuring very small elongations on small and delicate specimens. Deadweight loading was employed here for its simplicity and high reliability, but the design was fully suitable for use with an electromagnetic actuator that would be more practical for routine measurement work.

The clamping condition was a crucial factor for tensile test at small scales. Initial trials of a pin-block method experienced practical difficulties in producing small pins of high stiffness in a constrained space, leading to a preference for friction gripping by hard-clamping to the flats of the test rig using screws acting through slightly flexible brackets. The two bulk ends on each side of the test beam provided spaces for robust clamping and loading surfaces as well as giving a reference base for alignment. Further verification tests on the clamping conditions showed no significant evidence of sudden slip or creep, which further confirms that reliable clamping was likely to be established by the proposed method.

The geometry of MSL specimens needed to be fully measured post-production due to shrinkage and curl distortion. The length and width of a test beam were measured by placing the specimen cell under a Nikon digital microscope and the thickness was gauged by a Keyence confocal laser sensor. Capacitive micrometry was used to measure the stage motion, deemed as the elongation of specimens since reliable clamping was most

likely to be realized. The typical sensitivity of the capacitive gauges was calibrated to be approximately 20 mV/μm with linearity error less than 0.8% up to 40 μm. The noise level at 50 Hz corresponded to around 0.1 μm. The tensile test-rig used here was an initial prototype intended partly to assess the overall feasibility of the instrumentation and methodology. It therefore incorporated several compromises to ease manufacture and to allow the mounting of extra sensing for its evaluation. The displacement resolution can be readily improved by re-making the capacitive electrodes and reducing the nominal gap and using heavy noise filtering.

Overall, the general literature study of MSL technology suggested a promising future of fabricating MEMS devices but also pointed out a growing need for improved understanding of fabrication processes and mechanical properties of materials. It was difficult to carry out mechanical characterisation of MEMS specimens under small scales (less than 1 mm) particularly due to the practical difficulties in handling and mounting the small and fragile specimens. Tensile approach was finally chosen for its simple data conversion and relatively low requirement on the dimensional accuracy of specimens. A few tensile designs were studied in searching for a reliable tensile approach for mechanical characterisation of MSL specimens. The early trial specimens fabricated by Envisiontec Perfactory machine using acrylate-based R11 resin exhibited substantial shrinkage and curl distortion. Therefore, MSL specimens needed to be carefully addressed in designing the test-rig and the form of the specimen.

A novel form of tensile test-rig and a compatible specimen design were built for mechanical characterisation of small MSL specimens. In order to carefully deal with the

small specimen, this test-rig employed a ‘two parallel spring design’ and the tensile force was applied through a notch hinge flexure, which it also functioned as a robust guide. A clamping strategy using stiffly strained mounting surface was employed and verified, indicating a robust specimen mounting and clamping was most likely to be achieved with no evidence of sudden slip and creep. The strain of specimen was obtained by measuring the dimension of specimens through optical resorts (Nikon microscope for length and width measurement and Keyence sensor for thickness measurement) and the deflection of flexure (treated as the elongation of specimen) through capacitive gauges separately. The capacitive gauges showed sub-micrometre resolution and could be further improved by optimising the capacitive design. The characterisation results of R11 resins showed that the Young’s modulus was a little smaller than expected (0.9 GPa) and certainly dependent on both size and process parameters.

8.3: Future work

A large part of this study had been concerned with developing new metrology for testing the tensile properties of MSL materials. The approach now has proven feasibility and while further refinement is needed to gain better performance, it is technologically straightforward. It has, so far, only been practical to use this method for a small study of the basic mechanical properties of R11 specimens with different sizes and different UV exposures. Since a considerable number of variables in the fabrication processes might affect the resulting mechanical properties of specimens, much more characterisation work on MSL specimens under different fabrication conditions (e.g. different UV source, using ERM module (1/2 pixel shifting), different layer thickness and different

temperature/humidity) should be carried out for better understanding of the fabrication processes (including their statistical variability) of MSL systems.

The mechanical behaviour of MSL specimens is also expected to vary with different combinations of MSL systems and materials. It is recommended to use scanning MSL systems and epoxy-based resin to produce MSL specimens with high fabrication accuracy, while projection-based Envision Perfactory system and acrylate-based resin was the only currently available equipment for fabricating specimens with small sizes.

The results of mechanical characterisation of small MEMS material may be sensitive to different measurement approaches. For example, some MSL processes produce relatively large surface structure compared to the thin beam that might be required in functioning MEMS. A bending test should be designed and built to give more information about the mechanical properties of MEMS specimens. An elementary attempt at using the existing facilities in bending mode led to early specimen failure, attributed to limitations with the production process. However, bending tests on improved specimen designs fabricated using other combination of materials and MEMS techniques should be followed to provide more engineering data about MEMS processes and materials.

Appendix:

A: Preliminary test results of a typical MSL specimen

The dimension of the specimen was measured to be 1.00/0.48/0.087 (L/W/T) mm (see Table 5.2) and the sensitivity of capacitive gauge was 20.48 mV/µm.

	Capacitive gauge Reading (mV)						
Overall Tensile load	Test 1	Test 2	Test 3	Test 4	Test 5	Test 6	Test 7
0.098 N	5.16	6.08	4.77	6.83	5.43	6.05	6.42
0.196 N	11.78	12.88	11.13	14.95	11.57	13.47	14.28
0.294 N	19.25	20.98	18.27	22.74	19.27	19.83	22.17
0.392 N	26.52	28.53	26.14	29.61	26.73	27.12	28.92
0.49 N	35.91	36.97	34.14	38.51	35.43	37.22	37.84
0.588 N	42.67	43.67	41.12	45.22	42.13	43.86	45.7
0.686 N	50.12	51.22	48.62	52.3	49.1	51.62	51.9
0.784 N	57.16	58.77	56.13	60.42	57.3	58.22	59.57
0.882 N	65.25	65.78	63.1	67.49	64.52	66.71	66.93
0.98 N	71.11	71.42	68.25	72.32	70.22	69.21	71.75

B: The dimensional measurement of specimens at different stages (Specimen1.1-1.5):

Specimen 1.1 (Exposure 3.0 s and 9.5 s)

Designed dimension (1.0/0.5/0.1 mm)	**Measured specimen dimension (L/W/T mm)**		
	After build curing	After post-curing	After 2 days
Specimen Set 1	1.00/0.46/0.082	1.00/0.44/0.080	1.00/0.39/0.077
	1.00/0.46/0.082	1.00/0.43/0.082	1.00/0.38/0.076
Specimen Set 2	1.00/0.47/0.082	1.00/0.42/0.081	1.00/0.39/0.079
	1.00/0.48/0.083	1.00/0.43/0.081	1.00/0.39/0.078
Specimen Set 3	1.00/0.46/0.083	1.00/0.42/0.081	1.00/0.38/0.074
	1.00/0.46/0.082	1.00/0.43/0.080	1.00/0.38/0.075
Specimen Set 4	1.00/0.46/0.081	1.00/0.45/0.080	1.00/0.40/0.078
	1.00/0.45/0.082	1.00/0.44/0.081	1.00/0.39/0.077
Specimen Set 5	1.00/0.47/0.079	1.00/0.44/0.077	Broken
	1.00/0.46/0.078	1.00/0.44/0.075	Broken

Specimen 1.2 (Exposure 3.5 s and 9.5 s)

Designed dimension (1.0/0.5/0.1 mm)	**Measured specimen dimension (L/W/T mm)**		
	After build curing	After post-curing	After 2 days
Specimen Set 1	1.00/0.45/0.080	1.00/0.45/0.079	1.00/0.40/0.077
	1.00/0.45/0.081	1.00/0.45/0.079	1.00/0.40/0.076
Specimen Set 2	1.00/0.45/0.080	1.00/0.45/0.079	1.00/0.40/0.078
	1.00/0.46/0.080	1.00/0.46/0.079	1.00/0.41/0.077
Specimen Set 3	1.00/0.45/0.079	1.00/0.45/0.078	1.00/0.40/0.077
	1.00/0.45/0.080	1.00/0.45/0.078	1.00/0.40/0.076
Specimen Set 4	1.00/0.46/0.079	1.00/0.46/0.077	1.00/0.42/0.075
	1.00/0.45/0.079	1.00/0.45/0.079	1.00/0.40/0.077
Specimen Set 5	1.00/0.46/0.080	1.00/0.45/0.077	1.00/0.41/0.076
	1.00/0.45/0.080	1.00/0.45/0.077	1.00/0.40/0.076

Specimen 1.3 (Exposure 4.0 s and 9.5 s) Designed dimension (1.0/0.5/0.1 mm)	Measured specimen dimension (L/W/T mm)		
	After build curing	After post-curing	After 2 days
Specimen Set 1	1.00/0.45/0.075	1.00/0.45/0.072	1.00/0.43/0.071
	1.00/0.46/0.075	1.00/0.46/0.073	1.00/0.44/0.071
Specimen Set 2	1.00/0.46/0.077	1.00/0.46/0.074	1.00/0.44/0.072
	1.00/0.46/0.075	1.00/0.46/0.072	1.00/0.44/0.070
Specimen Set 3	1.00/0.46/0.075	1.00/0.46/0.072	1.00/0.44/0.071
	1.00/0.45/0.076	1.00/0.45/0.073	1.00/0.43/0.071
Specimen Set 4	1.00/0.44/0.075	1.00/0.44/0.072	1.00/0.43/0.069
	1.00/0.46/0.077	1.00/0.45/0.073	1.00/0.43/0.072
Specimen Set 5	1.00/0.44/0.075	1.00/0.44/0.072	1.00/0.42/0.070
	1.00/0.45/0.076	1.00/0.45/0.073	1.00/0.42/0.071

Specimen 1.4 (Exposure 6.0 s and 9.5 s) Designed dimension (1.0/0.5/0.1 mm)	Measured specimen dimension (L/W/T mm)		
	After build curing	After post-curing	After 2 days
Specimen Set 1	1.00/0.45/0.071	1.00/0.44/0.070	1.00/0.43/0.068
	1.00/0.44/0.071	1.00/0.44/0.069	1.00/0.42/0.066
Specimen Set 2	1.00/0.45/0.070	1.00/0.44/0.070	1.00/0.43/0.068
	1.00/0.46/0.070	1.00/0.45/0.070	1.00/0.44/0.068
Specimen Set 3	1.00/0.45/0.070	1.00/0.44/0.070	1.00/0.43/0.068
	1.00/0.46/0.071	1.00/0.45/0.071	1.00/0.44/0.069
Specimen Set 4	1.00/0.46/0.071	1.00/0.45/0.070	1.00/0.44/0.068
	1.00/0.45/0.071	1.00/0.44/0.070	1.00/0.43/0.068
Specimen Set 5	1.00/0.44/0.070	1.00/0.43/0.068	1.00/0.42/0.067
	1.00/0.45/0.070	1.00/0.44/0.070	1.00/0.43/0.068

Specimen 1.5 (Exposure 9.5 s and 9.5 s)			
Designed dimension			
(1.0/0.5/0.1 mm)	**Measured specimen dimension (L/W/T mm)**		
	After build curing	After post-curing	After 2 days
Specimen Set 1	1.00/0.45/0.072	1.00/0.45/0.072	1.00/0.43/0.071
	1.00/0.45/0.072	1.00/0.45/0.071	1.00/0.43/0.071
Specimen Set 2	1.00/0.45/0.072	1.00/0.45/0.072	1.00/0.43/0.071
	1.00/0.45/0.071	1.00/0.45/0.071	1.00/0.43/0.070
Specimen Set 3	1.00/0.45/0.072	1.00/0.45/0.072	1.00/0.43/0.071
	1.00/0.44/0.072	1.00/0.44/0.072	1.00/0.42/0.071
Specimen Set 4	1.00/0.46/0.072	1.00/0.46/0.072	1.00/0.44/0.071
	1.00/0.46/0.072	1.00/0.45/0.072	1.00/0.43/0.070
Specimen Set 5	1.00/0.45/0.072	1.00/0.44/0.072	1.00/0.43/0.070
	1.00/0.44/0.072	1.00/0.44/0.072	1.00/0.42/0.071

C: The dimensional measurement of specimens fabricated under different conditions (Specimen 2.1-2.12):

Specimen 2.1 (Exposure 3.5 s and 9.5 s)	
Designed dimension (5.0/2.0/0.5 mm)	**Measured specimen dimension (L/W/T mm)**
Specimen Set 1	5.00/1.96/0.375
	5.00/1.94/0.380
Specimen Set 2	5.00/1.95/0.395
	5.00/1.95/0.355
Specimen Set 3	5.00/1.96/0.392
	5.00/1.95/0.380
Specimen Set 4	5.00/1.96/0.380
	5.00/1.95/0.345
Specimen Set 5	5.00/1.95/0.335
	5.00/1.94/0.343

Specimen 2.2 (Exposure 3.5 s and 9.5 s)	
Designed dimension (2.0/1.0/0.2 mm)	**Measured specimen dimension (L/W/T mm)**
Specimen Set 1	2.00/0.98/0.157
	2.00/0.98/0.160
Specimen Set 2	2.00/0.98/0.149
	2.00/0.97/0.166
Specimen Set 3	2.00/0.98/0.158
	2.00/0.98/0.172
Specimen Set 4	2.00/0.97/0.155
	2.00/0.98/0.153
Specimen Set 5	2.00/0.98/0.158
	2.00/0.96/0.147

Specimen 2.3 (Exposure 3.5 s and 9.5 s) Designed dimension (1.0/1.0/0.2 mm)	Measured specimen dimension (L/W/T mm)
Specimen Set 1	1.00/0.98/0.168
	1.00/0.98/0.167
Specimen Set 2	1.00/0.97/0.164
	1.00/0.98/0.169
Specimen Set 3	1.00/0.98/0.165
	1.00/0.98/0.167
Specimen Set 4	1.00/0.97/0.167
	1.00/0.98/0.168
Specimen Set 5	1.00/0.97/0.166
	1.00/0.98/0.167

Specimen 2.4 (Exposure 3.5 s and 9.5 s) Designed dimension (1.0/0.5/0.2 mm)	Measured specimen dimension (L/W/T mm)
Specimen Set 1	1.00/0.48/0.169
	1.00/0.48/0.165
Specimen Set 2	1.00/0.48/0.168
	1.00/0.47/0.165
Specimen Set 3	1.00/0.48/0.168
	1.00/0.47/0.168
Specimen Set 4	1.00/0.48/0.167
	1.00/0.48/0.164
Specimen Set 5	1.00/0.47/0.165
	1.00/0.48/0.167

Specimen 2.5 (Exposure 3.5 s and 9.5 s) Designed dimension (1.0/0.5/0.1 mm)	Measured specimen dimension (L/W/T mm)
Specimen Set 1	1.00/0.48/0.085
	1.00/0.48/0.087
Specimen Set 2	1.00/0.48/0.087
	1.00/0.47/0.086
Specimen Set 3	1.00/0.47/0.085
	1.00/0.48/0.086
Specimen Set 4	1.00/0.47/0.086
	1.00/0.48/0.087
Specimen Set 5	1.00/0.47/0.086
	1.00/0.48/0.087

Specimen 2.6 (Exposure 3.5 s and 9.5 s) Designed dimension (1.0/0.2/0.1 mm)	Measured specimen dimension (L/W/T mm)
Specimen Set 1	1.00/0.19/0.095
	1.00/0.19/0.095
Specimen Set 2	1.00/0.18/0.093
	1.00/0.19/0.094
Specimen Set 3	1.00/0.19/0.095
	1.00/0.19/0.094
Specimen Set 4	1.00/0.19/0.094
	Broken
Specimen Set 5	Broken
	Broken

Specimen 2.7 (Exposure 3.0 s and 9.5 s)	
Designed dimension (1.0/0.5/0.1 mm)	**Measured specimen dimension (L/W/T mm)**
Specimen Set 1	1.00/0.48/0.083
	1.00/0.47/0.085
Specimen Set 2	1.00/0.44/0.082
	1.00/0.46/0.084
Specimen Set 3	1.00/0.48/0.088
	1.00/0.46/0.081
Specimen Set 4	1.00/0.48/0.083
	1.00/0.47/0.083
Specimen Set 5	1.00/0.44/0.082
	1.00/0.47/0.085

Specimen 2.8 (Exposure 4.0 s and 9.5 s)	
Designed dimension (1.0/0.5/0.1 mm)	**Measured specimen dimension (L/W/T mm)**
Specimen Set 1	1.00/0.47/0.085
	1.00/0.47/0.084
Specimen Set 2	1.00/0.47/0.085
	1.00/0.48/0.087
Specimen Set 3	1.00/0.47/0.085
	1.00/0.46/0.084
Specimen Set 4	1.00/0.47/0.082
	1.00/0.47/0.083
Specimen Set 5	1.00/0.46/0.085
	1.00/0.47/0.086

Specimen 2.9 (Exposure 6.0 s and 9.5 s)	
Designed dimension (1.0/0.5/0.1 mm)	**Measured specimen dimension (L/W/T mm)**
Specimen Set 1	1.00/0.45/0.080
	1.00/0.45/0.082
Specimen Set 2	1.00/0.45/0.080
	1.00/0.44/0.080
Specimen Set 3	1.00/0.45/0.081
	1.00/0.44/0.080
Specimen Set 4	1.00/0.44/0.082
	1.00/0.45/0.082
Specimen Set 5	1.00/0.44/0.081
	1.00/0.45/0.081

Specimen 2.10 (Exposure 9.5 s and 9.5 s)	
Designed dimension (1.0/0.5/0.1 mm)	**Measured specimen dimension (L/W/T mm)**
Specimen Set 1	1.00/0.45/0.080
	1.00/0.45/0.082
Specimen Set 2	1.00/0.45/0.080
	1.00/0.44/0.079
Specimen Set 3	1.00/0.45/0.081
	1.00/0.44/0.080
Specimen Set 4	1.00/0.45/0.080
	1.00/0.44/0.080
Specimen Set 5	1.00/0.44/0.079
	1.00/0.45/0.082

Specimen 2.11 (Exposure 3.5 s and 6.0 s) Designed dimension (1.0/0.5/0.1 mm)	Measured specimen dimension (L/W/T mm)
Specimen Set 1	1.00/0.40/0.068
	1.00/0.41/0.070
Specimen Set 2	1.00/0.39/0.068
	1.00/0.38/0.064
Specimen Set 3	1.00/0.40/0.067
	1.00/0.42/0.072
Specimen Set 4	1.00/0.39/0.067
	1.00/0.41/0.070
Specimen Set 5	1.00/0.39/0.065
	1.00/0.41/0.069

Specimen 2.12 (Exposure 6.0 s and 6.0 s) Designed dimension (1.0/0.5/0.1 mm)	Measured specimen dimension (L/W/T mm)
Specimen Set 1	1.00/0.45/0.075
	1.00/0.44/0.073
Specimen Set 2	1.00/0.45/0.075
	1.00/0.44/0.074
Specimen Set 3	1.00/0.45/0.076
	1.00/0.44/0.075
Specimen Set 4	1.00/0.43/0.071
	1.00/0.44/0.072
Specimen Set 5	1.00/0.44/0.075
	1.00/0.45/0.076

D: The tensile results on specimens of different conditions (Specimen 2.1-2.12)

Specimen 2.1 (5.00/1.95/0.368 mm L/W/T)					
Deadweight (g)	Tensile load (N)	Elongation (μm)	Stress (MPa)	Strain	E (MPa)
1000	9.8	35.68	2.171014493	0.007136	304.2340937
900	8.82	32.05	1.973871237	0.00641	307.9362305
800	7.84	28.53	1.741318283	0.005706	305.1732007
700	6.86	24.84	1.563489409	0.004968	314.7120389
600	5.88	21.3	1.337374582	0.00426	313.9376953
500	4.9	17.95	1.050097547	0.00359	292.5062806
400	3.92	14.25	0.875487737	0.00285	307.1886796
300	2.94	10.64	0.671906355	0.002128	315.7454673
200	1.96	7.13	0.436134337	0.001426	305.8445559
100	0.98	3.55	0.222895764	0.00071	313.9376953
90	0.882	3.21	0.195777592	0.000642	304.9495202
80	0.784	2.84	0.178316611	0.000568	313.9376953
70	0.686	2.49	0.154417503	0.000498	310.0753068
60	0.588	2.12	0.136956522	0.000424	323.0106645
50	0.49	1.77	0.113057414	0.000354	319.3712249
40	0.392	1.43	0.085939242	0.000286	300.4868599
30	0.294	1.1	0.055602007	0.00022	252.736394
20	0.196	0.76	0.028483835	0.000152	187.3936514
10	0.098	0.39	0.011022854	0.000078	141.3186405

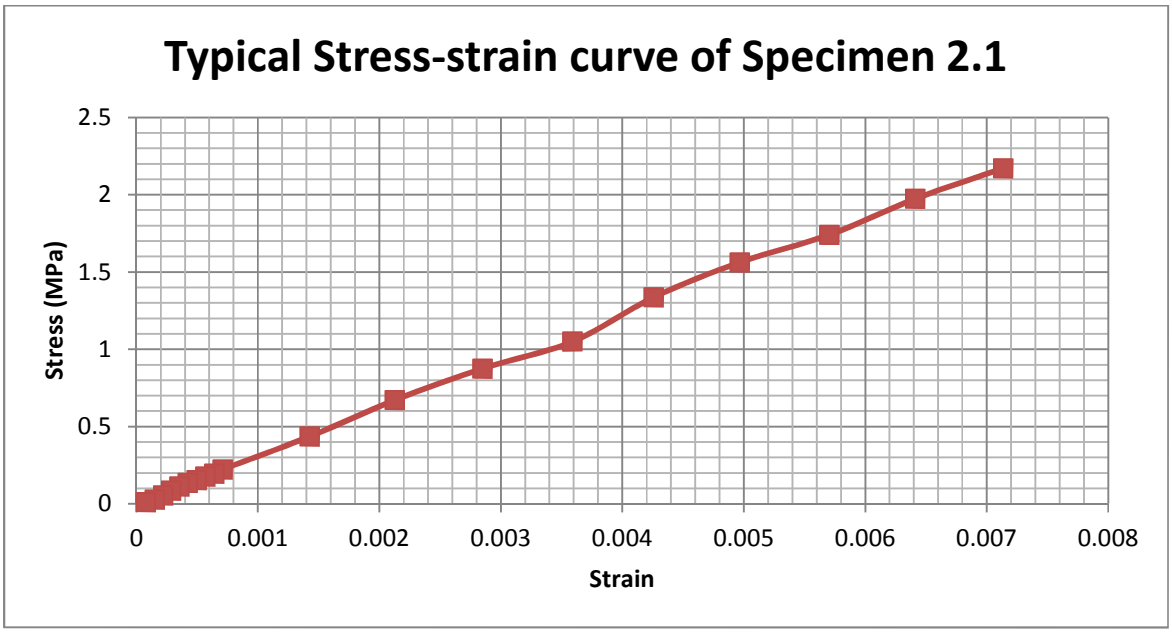

Specimen 2.2 (2.00/0.98/0.158 mm L/W/T)					
Deadweight (g)	Tensile load (N)	Elongation (μm)	Stress (MPa)	Strain	E (MPa)
1000	9.8	38.02	6.570524412	0.01901	345.6351611
900	8.82	34.42	5.612115732	0.01721	326.0962076
800	7.84	30.14	5.668173599	0.01507	376.1229992
700	6.86	26.71	4.456148282	0.013355	333.6689092
600	5.88	22.88	3.840867993	0.01144	335.7402092
500	4.9	19.03	3.255424955	0.009515	342.1360961
400	3.92	15.49	2.207504521	0.007745	285.0231789
300	2.94	11.44	1.920433996	0.00572	335.7402092
200	1.96	7.72	1.141048825	0.00386	295.6085038
100	0.98	3.82	0.630198915	0.00191	329.9470759
90	0.882	3.44	0.564195298	0.00172	328.0205223
80	0.784	3.07	0.483273056	0.001535	314.8358671
70	0.686	2.69	0.417269439	0.001345	310.2375014
60	0.588	2.29	0.381103074	0.001145	332.8411128
50	0.49	1.92	0.300180832	0.00096	312.6883665
40	0.392	1.55	0.21925859	0.000775	282.914309
30	0.294	1.18	0.138336347	0.00059	234.4683851
20	0.196	0.78	0.102169982	0.00039	261.9743126
10	0.098	0.4	0.036166365	0.0002	180.8318264

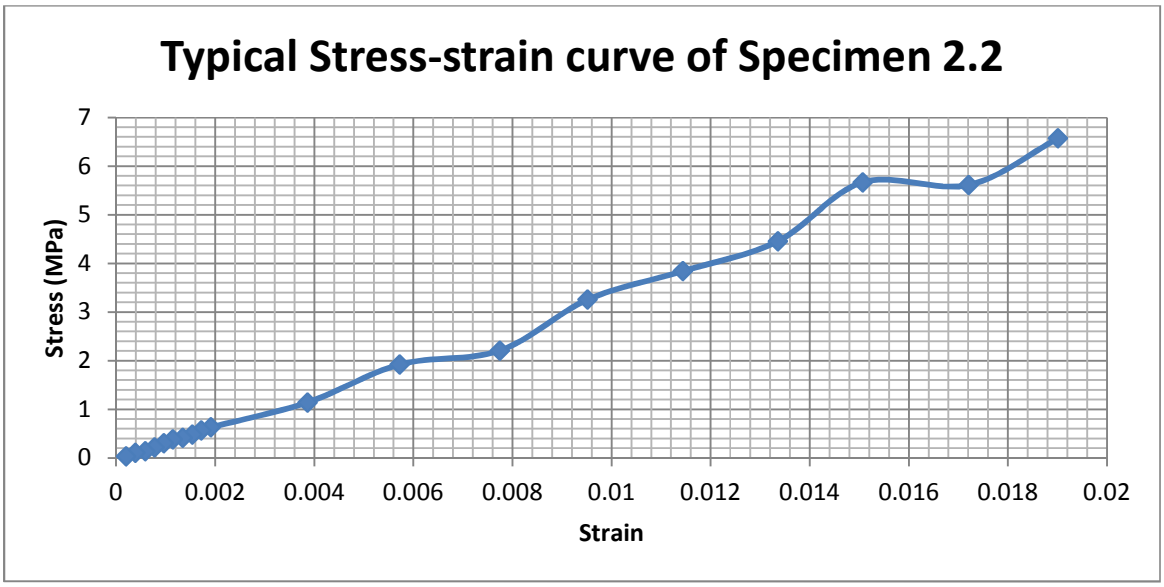

Specimen 2.3 (1.00/0.98/0.167 mm L/W/T)					
Deadweight (g)	Tensile load (N)	Elongation (µm)	Stress (MPa)	Strain	E (MPa)
1000	9.8	41.42	14.17450813	0.04142	342.2141025
900	8.82	37.38	11.31736527	0.03738	302.765256
800	7.84	33.19	10.5774166	0.03319	318.6928772
700	6.86	29.02	9.555175364	0.02902	329.2617286
600	5.88	24.88	8.109495295	0.02488	325.9443447
500	4.9	20.81	5.675791275	0.02081	272.7434538
400	3.92	16.61	5.076988879	0.01661	305.6585719
300	2.94	12.44	4.054747648	0.01244	325.9443447
200	1.96	8.3	2.609067579	0.0083	314.3454915
100	0.98	4.15	1.30453379	0.00415	314.3454915
90	0.882	3.73	1.24465355	0.00373	333.6872788
80	0.784	3.315	1.114200171	0.003315	336.1086489
70	0.686	2.89	1.124893071	0.00289	389.2363567
60	0.588	2.485	0.853293413	0.002485	343.3776311
50	0.49	2.07	0.722840034	0.00207	349.1980842
40	0.392	1.65	0.662959795	0.00165	401.793815
30	0.294	1.24	0.461933276	0.00124	372.5268357
20	0.196	0.83	0.260906758	0.00083	314.3454915
10	0.098	0.416	0.116338751	0.000416	279.6604593

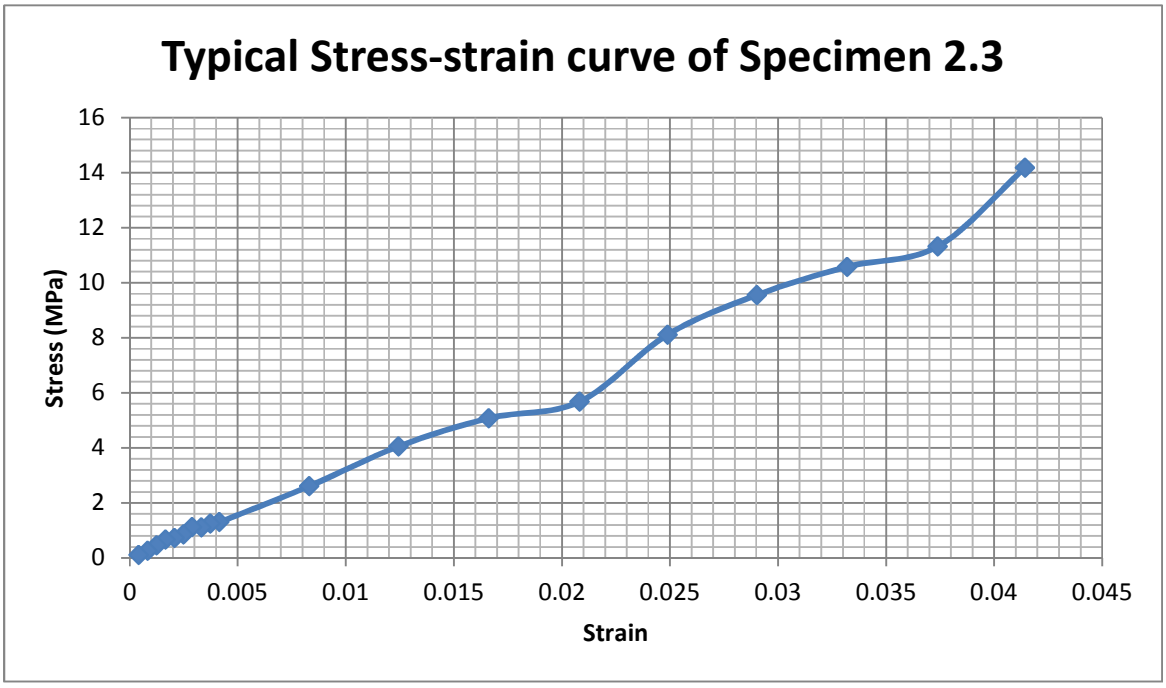

Specimen 2.4 (1.00/0.48/0.167 mm L/W/T)					
Deadweight (g)	Tensile load (N)	Elongation (μm)	Stress (MPa)	Strain	E (MPa)
1000	9.8	41.9	15.10728543	0.0419	360.5557382
900	8.82	37.7	13.88473054	0.0377	368.2952398
800	7.84	33.52	12.08582834	0.03352	360.5557382
700	6.86	29.32	10.86327345	0.02932	370.5072801
600	5.88	25.14	9.064371257	0.02514	360.5557382
500	4.9	20.97	6.977295409	0.02097	332.7274873
400	3.92	16.75	6.331087824	0.01675	377.9753925
300	2.94	12.59	3.955838323	0.01259	314.2047914
200	1.96	8.37	3.309630739	0.00837	395.4158588
100	0.98	4.18	1.798902196	0.00418	430.3593769
90	0.882	3.76	1.676646707	0.00376	445.9166773
80	0.784	3.34	1.554391218	0.00334	465.3865921
70	0.686	2.92	1.432135729	0.00292	490.4574413
60	0.588	2.5	1.30988024	0.0025	523.9520958
50	0.49	2.09	0.899451098	0.00209	430.3593769
40	0.392	1.67	0.777195609	0.00167	465.3865921
30	0.294	1.257	0.453218563	0.001257	360.5557382
20	0.196	0.842	0.186876248	0.000842	221.9432868
10	0.098	0.42	0.122255489	0.00042	291.0844977

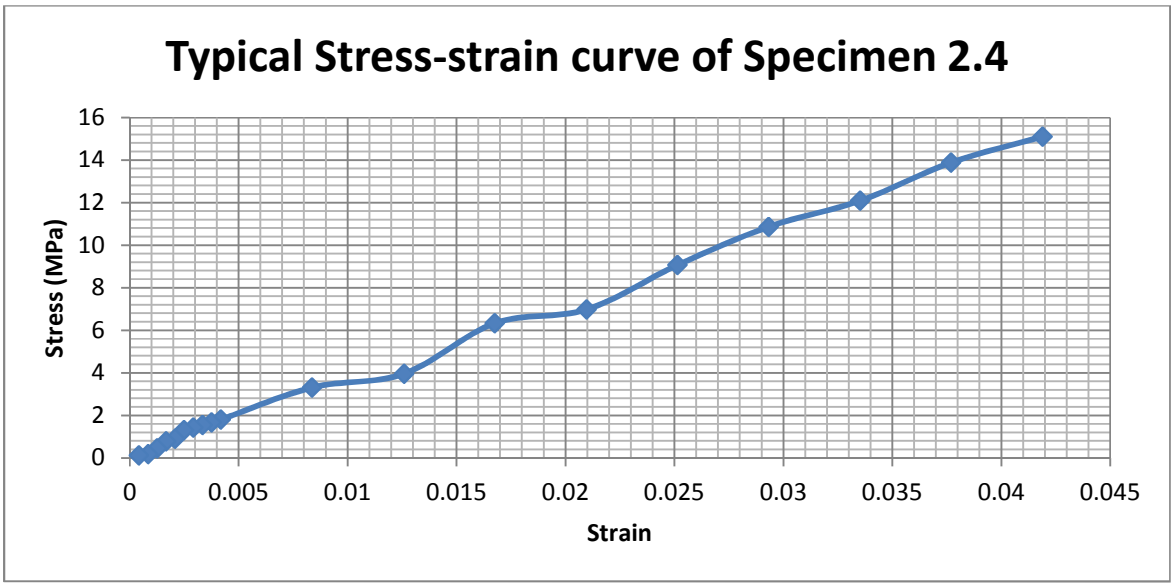

Specimen 2.5 (1.00/0.48/0.086 mm L/W/T)					
Deadweight (g)	Tensile load (N)	Elongation (µm)	Stress (MPa)	Strain	E (MPa)
1000	9.8	36.44	33.4874031	0.03644	918.9737404
900	8.82	32.71	30.61991279	0.03271	936.1025005
800	7.84	28.92	28.08817829	0.02892	971.2371471
700	6.86	25.21	25.10876938	0.02521	995.9845053
600	5.88	21.75	20.73037791	0.02175	953.1208233
500	4.9	18.08	17.52713178	0.01808	969.4210057
400	3.92	14.5	13.82025194	0.0145	953.1208233
300	2.94	10.89	10.28125	0.01089	944.1000918
200	1.96	7.25	6.910125969	0.00725	953.1208233
100	0.98	3.59	3.650920543	0.00359	1016.96951
90	0.882	3.21	3.403343023	0.00321	1060.231471
80	0.784	2.85	3.043846899	0.00285	1068.016456
70	0.686	2.5	2.628391473	0.0025	1051.356589
60	0.588	2.14	2.268895349	0.00214	1060.231471
50	0.49	1.76	2.021317829	0.00176	1148.476039
40	0.392	1.4	1.661821705	0.0014	1187.015504
30	0.294	1.11	0.910610465	0.00111	820.3697884
20	0.196	0.76	0.495155039	0.00076	651.5197878
10	0.098	0.39	0.191618217	0.00039	491.3287617

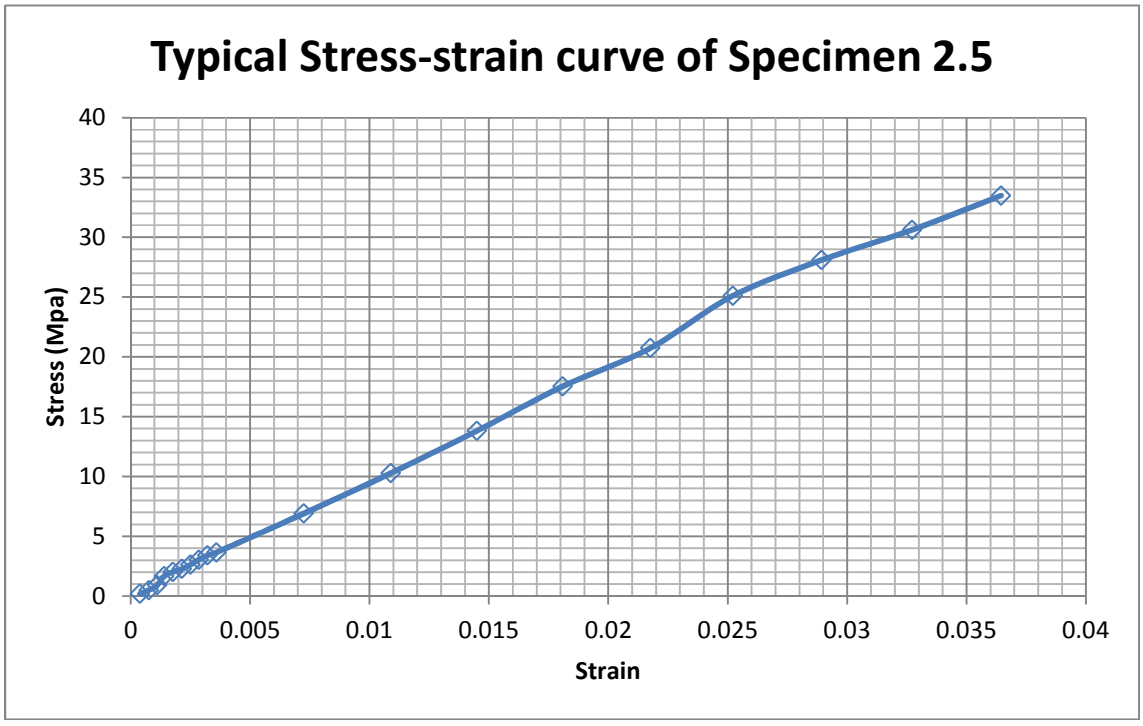

Specimen 2.6 (1.00/0.19/0.095 mm L/W/T)					
Deadweight (g)	Tensile load (N)	Elongation (µm)	Stress (MPa)	Strain	E (MPa)
1000	9.8	38.8	46.38227147	0.0388	1195.419368
900	8.82	34.75	43.91966759	0.03475	1263.875326
800	7.84	31.06	36.8498615	0.03106	1186.408934
700	6.86	27.18	32.21163435	0.02718	1185.122677
600	5.88	23.22	28.59722992	0.02322	1231.577516
500	4.9	19.32	24.21495845	0.01932	1253.362239
400	3.92	15.5	18.80886427	0.0155	1213.475114
300	2.94	11.58	14.68254848	0.01158	1267.923012
200	1.96	7.77	9.148476454	0.00777	1177.410097
100	0.98	3.87	4.766204986	0.00387	1231.577516
90	0.882	3.48	4.327977839	0.00348	1243.671793
80	0.784	3.08	4.017728532	0.00308	1304.457316
70	0.686	2.7	3.451523546	0.0027	1278.342054
60	0.588	2.31	3.013296399	0.00231	1304.457316
50	0.49	1.93	2.447091413	0.00193	1267.923012
40	0.392	1.55	1.880886427	0.00155	1213.475114
30	0.294	1.17	1.31468144	0.00117	1123.659351
20	0.196	0.793	0.710083102	0.000793	895.4389691
10	0.098	0.4	0.310249307	0.0004	775.6232687

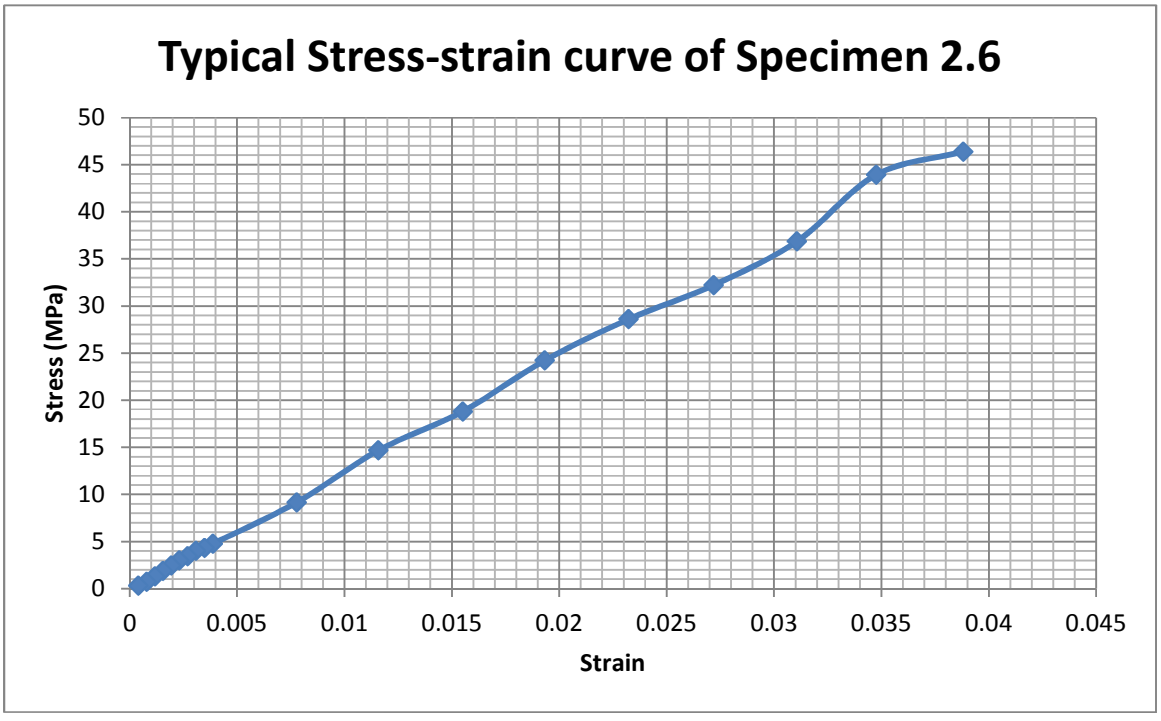

Specimen 2.7 (1.00/0.47/0.084 mm L/W/T)					
Deadweight (g)	Tensile load (N)	Elongation (µm)	Stress (MPa)	Strain	E (MPa)
1000	9.8	39.46	17.34397163	0.03946	439.5329861
900	8.82	35.72	14.40425532	0.03572	403.2546282
800	7.84	31.62	13.57092199	0.03162	429.1879186
700	6.86	27.65	11.97695035	0.02765	433.1627615
600	5.88	23.55	11.14361702	0.02355	473.1896824
500	4.9	19.72	8.730496454	0.01972	442.7229439
400	3.92	15.71	7.370567376	0.01571	469.1640596
300	2.94	11.77	5.60106383	0.01177	475.8762812
200	1.96	7.88	3.539007092	0.00788	449.1125752
100	0.98	3.92	1.886524823	0.00392	481.2563323
90	0.882	3.53	1.686170213	0.00353	477.6686155
80	0.784	3.13	1.544326241	0.00313	493.3949652
70	0.686	2.75	1.285460993	0.00275	467.4403611
60	0.588	2.38	0.968085106	0.00238	406.7584481
50	0.49	1.98	0.826241135	0.00198	417.2935024
40	0.392	1.61	0.508865248	0.00161	316.0653716
30	0.294	1.21	0.367021277	0.00121	303.3233691
20	0.196	0.81	0.225177305	0.00081	277.9966728
10	0.098	0.412	0.071631206	0.000412	173.8621497

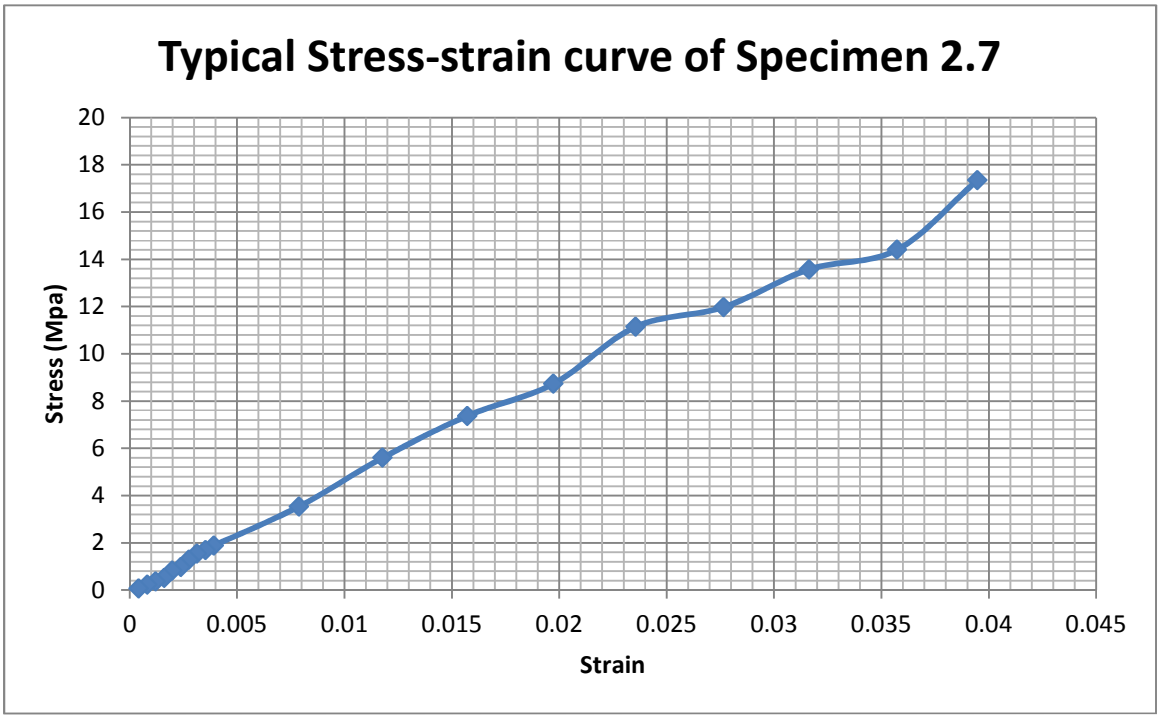

Specimen 2.8 (1.00/0.47/0.085 mm L/W/T)					
Deadweight (g)	Tensile load (N)	Elongation (μm)	Stress (MPa)	Strain	E (MPa)
1000	9.8	35.25	41.48310388	0.03525	1176.825642
900	8.82	31.61	37.99974969	0.03161	1202.143299
800	7.84	27.97	34.51639549	0.02797	1234.050608
700	6.86	24.28	31.32215269	0.02428	1290.039238
600	5.88	20.75	27.20275344	0.02075	1310.976069
500	4.9	17.6	20.88610763	0.0176	1186.710661
400	3.92	14.11	16.53541927	0.01411	1171.893641
300	2.94	10.53	12.70513141	0.01053	1206.565187
200	1.96	7.02	8.47008761	0.00702	1206.565187
100	0.98	3.5	4.292866083	0.0035	1226.533166
90	0.882	3.2	3.574468085	0.0032	1117.021277
80	0.784	2.79	3.492115144	0.00279	1251.654173
70	0.686	2.43	3.120650814	0.00243	1284.218442
60	0.588	2.1	2.57571965	0.0021	1226.533166
50	0.49	1.78	1.972966208	0.00178	1108.407982
40	0.392	1.5	1.138923655	0.0015	759.2824364
30	0.294	1.17	0.593992491	0.00117	507.6858894
20	0.196	0.81	0.22252816	0.00081	274.7261237
10	0.098	0.41	0.082352941	0.00041	200.8608321

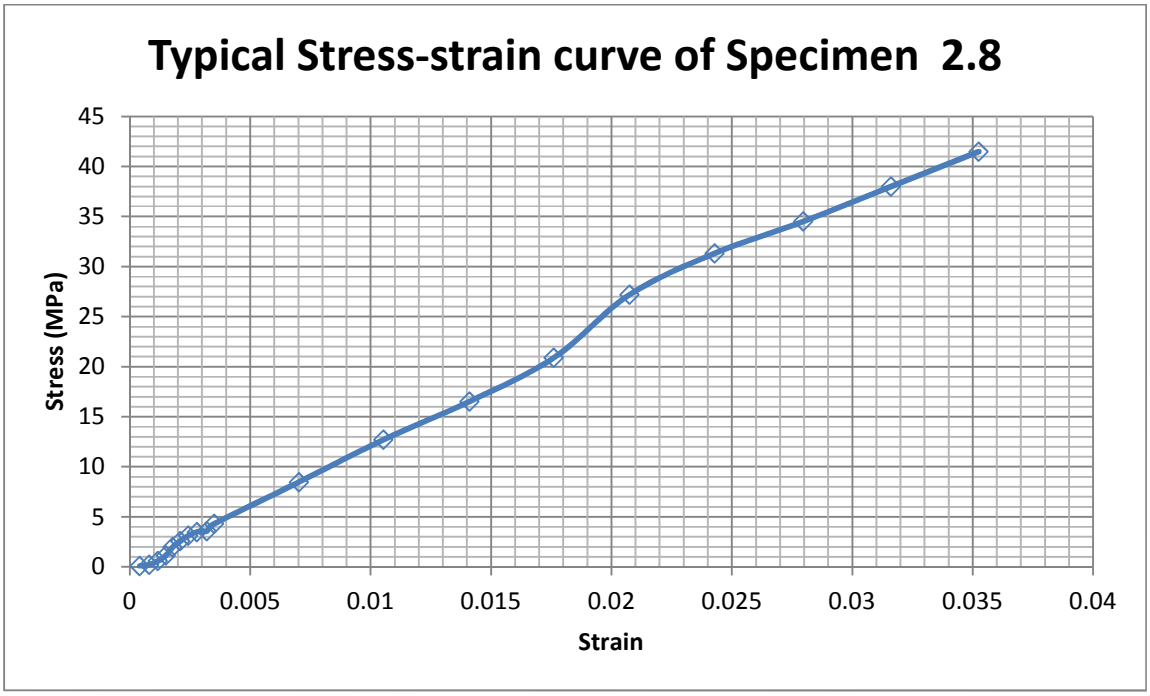

Specimen 2.9 (1.00/0.45/0.081 mm L/W/T)					
Deadweight (g)	Tensile load (N)	Elongation (µm)	Stress (MPa)	Strain	E (MPa)
1000	9.8	35.33	44.95939643	0.03533	1272.555801
900	8.82	31.71	41.01481481	0.03171	1293.434715
800	7.84	28.1	37.00685871	0.0281	1316.970061
700	6.86	24.73	31.47791495	0.02473	1272.863524
600	5.88	21.02	28.1037037	0.02102	1336.998273
500	4.9	17.63	22.70150892	0.01763	1287.66358
400	3.92	13.99	18.88367627	0.01399	1349.798161
300	2.94	10.58	13.60823045	0.01058	1286.22216
200	1.96	7.03	9.220027435	0.00703	1311.525951
100	0.98	3.54	4.451577503	0.00354	1257.507769
90	0.882	3.16	4.171193416	0.00316	1319.997916
80	0.784	2.81	3.700685871	0.00281	1316.970061
70	0.686	2.46	3.230178326	0.00246	1313.080621
60	0.588	2.11	2.759670782	0.00211	1307.900844
50	0.49	1.78	2.162414266	0.00178	1214.839475
40	0.392	1.47	1.438408779	0.00147	978.5093736
30	0.294	1.18	0.587654321	0.00118	498.0121364
20	0.196	0.8	0.307270233	0.0008	384.0877915
10	0.098	0.41	0.090260631	0.00041	220.1478805

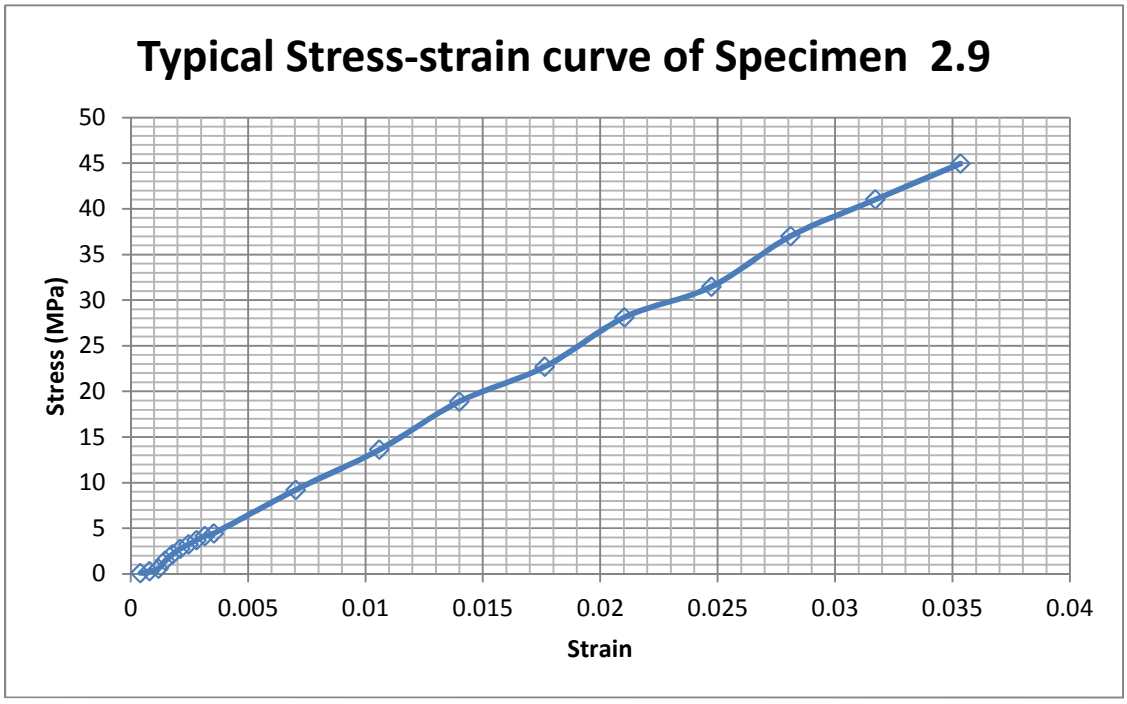

Specimen 2.10 (1.00/0.45/0.080 mm L/W/T)					
Deadweight (g)	Tensile load (N)	Elongation (µm)	Stress (MPa)	Strain	E (MPa)
1000	9.8	35.36	45.32888889	0.03536	1281.925591
900	8.82	31.41	43.4525	0.03141	1383.397007
800	7.84	28.1	37.46944444	0.0281	1333.432187
700	6.86	24.53	33.15472222	0.02453	1351.598949
600	5.88	20.82	29.73833333	0.02082	1428.354147
500	4.9	17.46	24.07611111	0.01746	1378.929617
400	3.92	13.81	20.27472222	0.01381	1468.118915
300	2.94	10.39	14.9975	0.01039	1443.455245
200	1.96	6.76	11.06777778	0.00676	1637.245233
100	0.98	3.36	5.662222222	0.00336	1685.185185
90	0.882	3.14	4.351666667	0.00314	1385.881104
80	0.784	2.8	3.811111111	0.0028	1361.111111
70	0.686	2.44	3.398888889	0.00244	1392.98725
60	0.588	2.08	2.986666667	0.00208	1435.897436
50	0.49	1.75	2.381944444	0.00175	1361.111111
40	0.392	1.46	1.520555556	0.00146	1041.476408
30	0.294	1.16	0.723333333	0.00116	623.5632184
20	0.196	0.79	0.375277778	0.00079	475.0351617
10	0.098	0.41	0.091388889	0.00041	222.899729

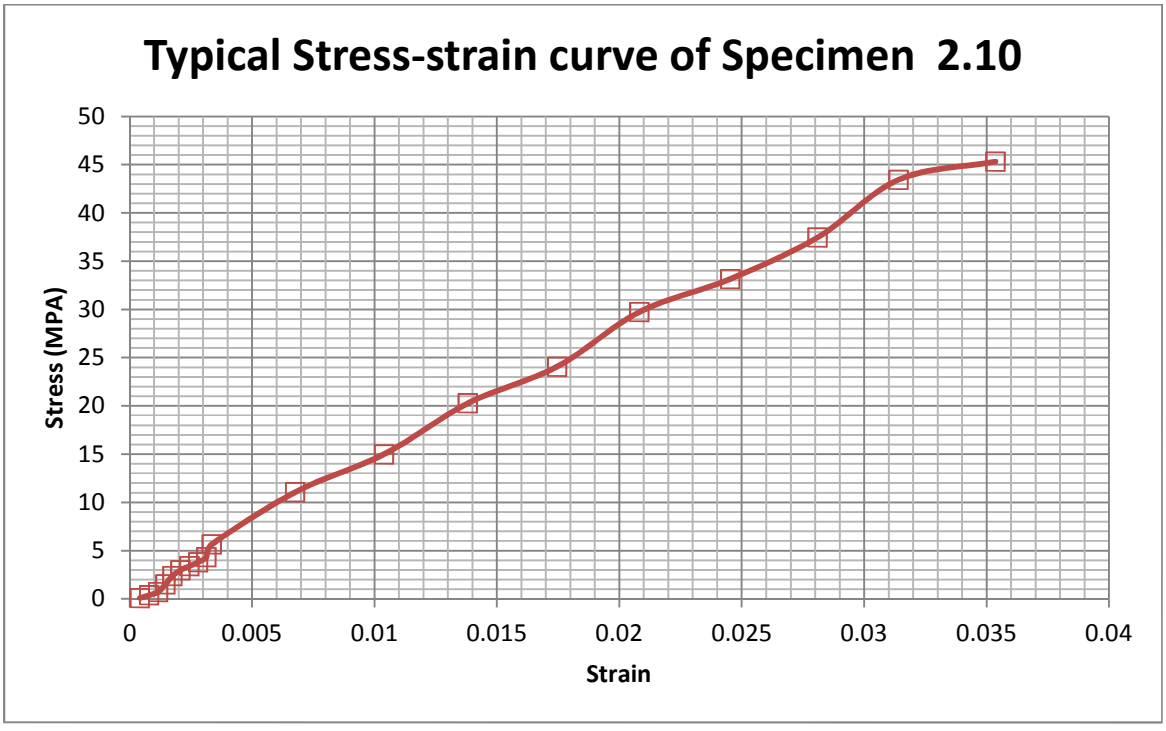

Specimen 2.11 (1.00/0.40/0.068 mm L/W/T)					
Deadweight (g)	Tensile load (N)	Elongation (μm)	Stress (MPa)	Strain	E (MPa)
1000	9.8	38.62	32.30808824	0.03862	836.5636519
900	8.82	35	27.02205882	0.035	772.0588235
800	7.84	31	24.96323529	0.031	805.2656546
700	6.86	27.11	21.97022059	0.02711	810.4102024
600	5.88	23.25	18.72242647	0.02325	805.2656546
500	4.9	19.29	16.32389706	0.01929	846.2362394
400	3.92	15.5	12.48161765	0.0155	805.2656546
300	2.94	11.61	9.488602941	0.01161	817.2784618
200	1.96	7.71	6.580514706	0.00771	853.5038529
100	0.98	3.85	3.332720588	0.00385	865.6417112
90	0.882	3.46	3.041911765	0.00346	879.1652499
80	0.784	3.09	2.58125	0.00309	835.3559871
70	0.686	2.71	2.205514706	0.00271	813.8430649
60	0.588	2.33	1.829779412	0.00233	785.3130523
50	0.49	1.94	1.538970588	0.00194	793.2838084
40	0.392	1.55	1.248161765	0.00155	805.2656546
30	0.294	1.16	0.957352941	0.00116	825.3042596
20	0.196	0.79	0.496691176	0.00079	628.7230082
10	0.098	0.41	0.120955882	0.00041	295.0143472

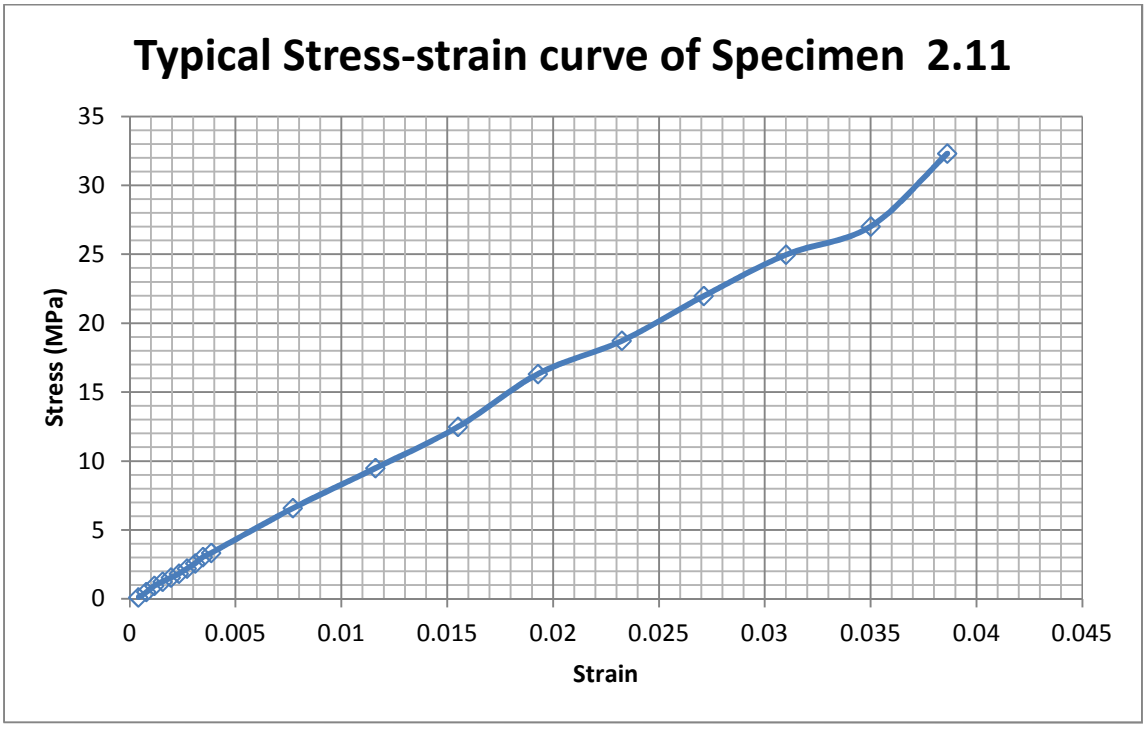

Specimen 2.12 (1.00/0.44/0.074 mm L/W/T)					
Deadweight (g)	Tensile load (N)	Elongation (µm)	Stress (MPa)	Strain	E (MPa)
1000	9.8	36.49	42.10104423	0.03649	1153.769368
900	8.82	32.6	39.6007371	0.0326	1214.746537
800	7.84	29.03	34.83015971	0.02903	1199.798819
700	6.86	25.23	31.69133907	0.02523	1256.097466
600	5.88	21.65	26.99170762	0.02165	1246.730144
500	4.9	18.22	21.22788698	0.01822	1165.087101
400	3.92	14.5	17.52149877	0.0145	1208.379226
300	2.94	10.82	13.53132678	0.01082	1250.58473
200	1.96	7.33	8.193181818	0.00733	1117.760139
100	0.98	3.62	4.415847666	0.00362	1219.847422
90	0.882	3.29	3.747235872	0.00329	1138.977469
80	0.784	2.87	3.717137592	0.00287	1295.169893
70	0.686	2.5	3.332309582	0.0025	1332.923833
60	0.588	2.17	2.663697789	0.00217	1227.510502
50	0.49	1.79	2.349815725	0.00179	1312.746215
40	0.392	1.53	1.18458231	0.00153	774.2368036
30	0.294	1.2	0.515970516	0.0012	429.97543
20	0.196	0.82	0.202088452	0.00082	246.4493318
10	0.098	0.42	0.03009828	0.00042	71.66257166